Looking for new physics

Muhammad Ansar Iqbal

Search for anomalous gauge couplings in WW and WZ production using the CMS experiment

ETP-KA/2020-23

Karlsruher Institut für Technologie

LOOKING FOR NEW PHYSICS: SEARCH FOR ANOMALOUS GAUGE COUPLINGS IN WW AND WZ PRODUCTION IN LEPTON + JET EVENTS IN PROTON-PROTON COLLISIONS AT $\sqrt{s} = 13$ TEV WITH THE CMS EXPERIMENT

Zur Erlangung des akademischen Grades eines
DOKTORS DER NATURWISSENSCHAFTEN

von der KIT-Fakultät für Physik des
Karlsruher Instituts für Technologie (KIT)
genehmigte

Dissertation

von

M.Sc. Muhammad Ansar Iqbal
aus Sargodha

Mündliche Prüfung: 26. Juni 2020

Referent: Prof. Dr. Thomas Müller
Institut für Experimentelle Teilchenphysik

Korreferent: Dr. Ashfaq Ahmad
National Centre for Physics, Islamabad

Eidesstattliche Versicherung gemäß § 13 Absatz 2 Ziffer 3 der Promotionsordnung des Karlsruher Instituts für Technologie (KIT) für die KIT-Fakultät für Physik:

1. Bei der eingereichten Dissertation zu dem Thema

   Looking for new physics: Search for anomalous gauge couplings in WW and WZ production in lepton + jet events in proton-proton collisions at $\sqrt{s}$ = 13 TeV with the CMS experiment

   handelt es sich um meine eigenständig erbrachte Leistung.

2. Ich habe nur die angegebenen Quellen und Hilfsmittel benutzt und mich keiner unzulässigen Hilfe Dritter bedient. Insbesondere habe ich wörtlich oder sinngemäß aus anderen Werken übernommene Inhalte als solche kenntlich gemacht.

3. Die Arbeit oder Teile davon habe ich bislang nicht an einer Hochschule des In- oder Auslands als Bestandteil einer Prüfungs- oder Qualifikationsleistung vorgelegt.

4. Die Richtigkeit der vorstehenden Erklärungen bestätige ich.

5. Die Bedeutung der eidesstattlichen Versicherung und die strafrechtlichen Folgen einer unrichtigen oder unvollständigen eidesstattlichen Versicherung sind mir bekannt.

Ich versichere an Eides statt, dass ich nach bestem Wissen die reine Wahrheit erklärt und nichts verschwiegen habe.
Karlsruhe, den 26. Juni 2020

....
(Full name)

Abstract

The LHC Run 2, with a centre-of-mass energy of 13 TeV, has opened new avenues for searching possible effects of physics beyond the standard model. Such new physics can be parametrised by adding additional operators to the standard model Lagrangian in a model-independent effective field theory approach. In this thesis, a search is presented for three operators that would lead to anomalous WWγ or WWZ couplings. They are constrained by studying proton-proton collision events, recorded by the CMS experiment, in which two vector bosons are produced; a W boson which decays into a charged lepton and the corresponding neutrino, and a W or Z boson which decays into hadrons that are reconstructed as a single, large-radius jet. Using reconstructed kinematic variable distributions, one- and two-dimensional 95% confidence intervals are obtained for the anomalous coupling parameters. The obtained limits, $-1.58 < c_{\mathrm{WWW}}/\Lambda^2 < 1.59\ \mathrm{TeV}^{-2}$, $-2.00 < c_{\mathrm{W}}/\Lambda^2 < 2.65\ \mathrm{TeV}^{-2}$, and $-8.78 < c_{\mathrm{B}}/\Lambda^2 < 8.54\ \mathrm{TeV}^{-2}$, are the strictest bounds on these parameters to date.

The analysis presented in this thesis has been published in the Journal of High Energy Physics [1].

There are more things in heaven and earth,
Horatio,
Than are dreamt of in your philosophy.

……

– William Shakespeare, Hamlet

Introduction

A prelude —

This mini-chapter serves as a preamble, and gives a taste of things to come. The basic idea is discussed, followed by an overview of the strategy used in this search. The introduction concludes by giving a glimpse of the final results and briefly summarising the contents of the chapters in this thesis.

0

A complete understanding of the basic constituents of matter has been the holy grail for researchers and scientists over the ages. Our efforts to attain this understanding have culminated in the standard model (SM) of particle physics. Whist the SM describes elementary particles and their interactions quite precisely, it is inherently incomplete. It does not include a description of the interaction that holds planets, stars, solar systems, and galaxies together — gravity. Furthermore, there are several issues that it cannot accommodate, including a description of dark matter [2,3] and dark energy [4–6], the protection of the Higgs mass from the Planck scale (the Hierarchy problem) [7], the observation of neutrino oscillations and nonzero neutrino masses [8], and the asymmetry in observed amounts of baryonic matter and antimatter [9].

A plethora of beyond SM (BSM) models and extensions to the SM have been introduced to address these issues. Most of these models add new physics at scales larger than the electroweak scale, and it may or may not be within the reach of our current particle colliders to directly produce and observe new heavy BSM particles. It is however much more plausible to measure the impact of such new physics, if it exists, on the interactions of the SM particles. This impact can be parametrised by higher-order operators within an effective quantum field theory.

In 2015, the Large Hadron Collider (LHC) at CERN started colliding protons at a centre-of-mass energy of 13 TeV. This enhanced centre-of-mass energy allows for a much larger reach to look for the effects of physics beyond the SM. In the electroweak sector, these effects can be expected to show up in vector boson final states. The analysis described in this thesis looks for modifications to the production of WW and WZ final states, and searches for anomalous WWγ and WWZ triple gauge couplings. The results, published in the Journal of High Energy Physics [1], are derived from data recorded by the Compact Muon Solenoid (CMS) experiment at the CERN LHC in proton-proton collisions during 2016, corresponding to an integrated luminosity of 35.9 fb^{-1}. The results are also demonstrated to show improvement by adding data recorded in 2017 and 2018.

Events with WW and WZ final states are considered for analysis, wherein a W boson decays into a charged lepton and the corresponding neutrino, and the other W or Z boson decays into hadrons. This semileptonic final state has the advantage of having a large branching ratio compared to the fully leptonic final state, as well as the possibility of a better reconstruction because of the presence of only one neutrino. When compared with the fully hadronic final state, which suffers from the presence of background processes with much larger cross sections, the semileptonic final state is much cleaner. The semileptonic final state thus offers a perfect balance between purity and efficiency.

The effect of anomalous triple gauge couplings (aTGCs) is most pronounced in the tails of kinematic distributions, at large momenta of the vector bosons and diboson invariant masses. It is therefore natural to consider the scenario where the two jets coming from the hadronically decaying W or Z boson have a significant Lorentz boost and will overlap in the detector. The two jets are therefore reconstructed as a single, large-radius, “fat” jet, and jet substructure techniques are used to improve sensitivity to gauge boson decays, and to reject other background processes.

For the final signal extraction, a specially constructed two-dimensional fit is performed to the (soft drop jet mass m_{SD}, diboson mass m_{WV})-distribution in data. The effect of presence of a signal is modelled using parametric functions, which take into account contributions from different anomalous triple gauge couplings and their interference, as well as the interference between the standard model contribution and each anomalous coupling. Background processes are estimated using a mix of Monte Carlo (MC) simulation and data-driven techniques.

The dominant background process, W+jets, is estimated in the signal region by transferring normalisation and shape of the contribution from a W+jets-enriched sideband region. The shape of top quark pair production ($\mathrm{t\bar{t}}$) is estimated from simulation in the m_{SD} component and from data in the m_{WV} component, whilst the normalisaion is fixed from data. Minor contributions, standard model WW and WZ and single top quark processes, are estimated from simulation. Systematic uncertainties are included as nuisance parameters in the final fit for contributions obtained from simulation.

One- and two-dimensional 95% confidence intervals are obtained for the anomalous coupling parameters using profile likelihood distributions. Two-dimensional limits on the anomalous coupling parameters obtained from this analysis are shown in Figure 0.1.

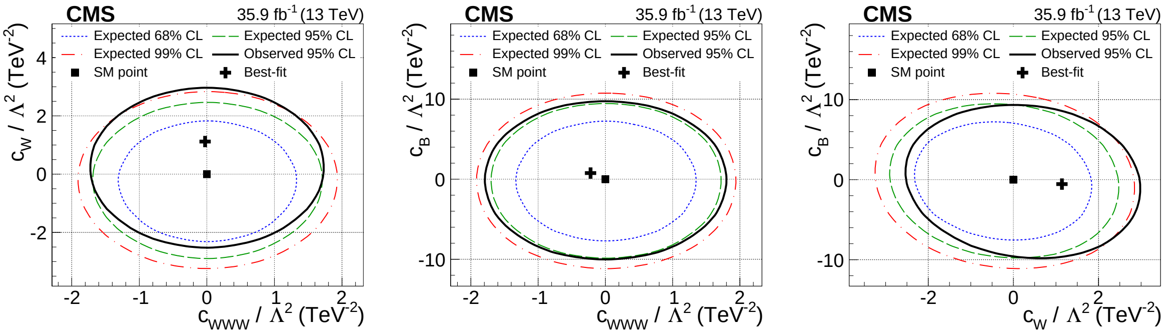

Figure 0.1: Simultaneous limits on two aTGC parameters, with the third being fixed to zero. Limits for the combinations $c_{\mathrm{WWW}}/\Lambda^2$–$c_{\mathrm{W}}/\Lambda^2$ (left), $c_{\mathrm{WWW}}/\Lambda^2$–$c_{\mathrm{B}}/\Lambda^2$ (centre), and c_{W}/Λ^2–c_{B}/Λ^2 (right) are shown. Expected 95% CL contours are shown in dashed green, whilst the dotted blue and dot-dashed red represent the 68 and 99% CL contours, respectively. Contours for the observed 95% CL are shown in solid black. The SM expectation is marked with the black squares, while the observed best-fit points are shown by the black crosses. This figure has been published in Reference [1].

Previous searches for anomalous gauge couplings by the CMS and ATLAS experiments have focused on fully leptonic final states [10–28]. Semileptonic final states were used for studies performed with data taken at centre-of-mass energies of 7 and 8 TeV [29–32]. A comparison of the 95% confidence limits obtained from the search presented in this thesis with contemporary and historical measurements in other processes and final states is presented in Figure 0.2. The constraints from this search are the most stringent limits on these parameters ever reported.

This thesis is structured as follows: The theoretical foundation is laid down in Chapter 1,

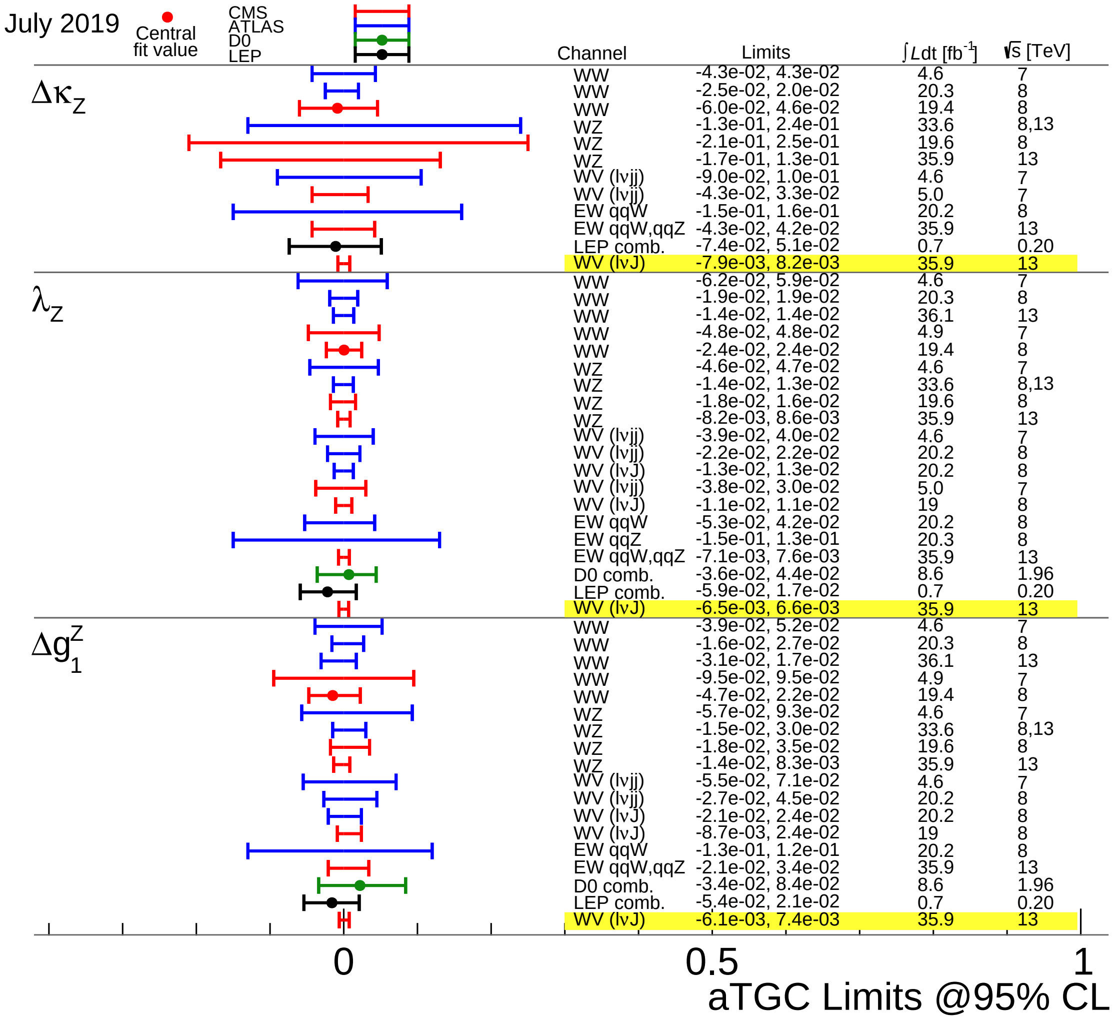

	Channel	Limits	$\int L dt$ [fb^{-1}]	$\sqrt{s}$ [TeV]
$\Delta\kappa_Z$	WW	-4.3e-02, 4.3e-02	4.6	7
	WW	-2.5e-02, 2.0e-02	20.3	8
	WW	-6.0e-02, 4.6e-02	19.4	8
	WZ	-1.3e-01, 2.4e-01	33.6	8,13
	WZ	-2.1e-01, 2.5e-01	19.6	8
	WZ	-1.7e-01, 1.3e-01	35.9	13
	WV (lvjj)	-9.0e-02, 1.0e-01	4.6	7
	WV (lvjj)	-4.3e-02, 3.3e-02	5.0	7
	EW qqW	-1.5e-01, 1.6e-01	20.2	8
	EW qqW,qqZ	-4.3e-02, 4.2e-02	35.9	13
	LEP comb.	-7.4e-02, 5.1e-02	0.7	0.20
	WV (lvJ)	-7.9e-03, 8.2e-03	35.9	13
λ_Z	WW	-6.2e-02, 5.9e-02	4.6	7
	WW	-1.9e-02, 1.9e-02	20.3	8
	WW	-1.4e-02, 1.4e-02	36.1	13
	WW	-4.8e-02, 4.8e-02	4.9	7
	WW	-2.4e-02, 2.4e-02	19.4	8
	WZ	-4.6e-02, 4.7e-02	4.6	7
	WZ	-1.4e-02, 1.3e-02	33.6	8,13
	WZ	-1.8e-02, 1.6e-02	19.6	8
	WZ	-8.2e-03, 8.6e-03	35.9	13
	WV (lvjj)	-3.9e-02, 4.0e-02	4.6	7
	WV (lvjj)	-2.2e-02, 2.2e-02	20.2	8
	WV (lvJ)	-1.3e-02, 1.3e-02	20.2	8
	WV (lvjj)	-3.8e-02, 3.0e-02	5.0	7
	WV (lvJ)	-1.1e-02, 1.1e-02	19	8
	EW qqW	-5.3e-02, 4.2e-02	20.2	8
	EW qqZ	-1.5e-01, 1.3e-01	20.3	8
	EW qqW,qqZ	-7.1e-03, 7.6e-03	35.9	13
	D0 comb.	-3.6e-02, 4.4e-02	8.6	1.96
	LEP comb.	-5.9e-02, 1.7e-02	0.7	0.20
	WV (lvJ)	-6.5e-03, 6.6e-03	35.9	13
Δg_1^Z	WW	-3.9e-02, 5.2e-02	4.6	7
	WW	-1.6e-02, 2.7e-02	20.3	8
	WW	-3.1e-02, 1.7e-02	36.1	13
	WW	-9.5e-02, 9.5e-02	4.9	7
	WW	-4.7e-02, 2.2e-02	19.4	8
	WZ	-5.7e-02, 9.3e-02	4.6	7
	WZ	-1.5e-02, 3.0e-02	33.6	8,13
	WZ	-1.8e-02, 3.5e-02	19.6	8
	WZ	-1.4e-02, 8.3e-03	35.9	13
	WV (lvjj)	-5.5e-02, 7.1e-02	4.6	7
	WV (lvjj)	-2.7e-02, 4.5e-02	20.2	8
	WV (lvJ)	-2.1e-02, 2.4e-02	20.2	8
	WV (lvJ)	-8.7e-03, 2.4e-02	19	8
	EW qqW	-1.3e-01, 1.2e-01	20.2	8
	EW qqW,qqZ	-2.1e-02, 3.4e-02	35.9	13
	D0 comb.	-3.4e-02, 8.4e-02	8.6	1.96
	LEP comb.	-5.4e-02, 2.1e-02	0.7	0.20
	WV (lvJ)	-6.1e-03, 7.4e-03	35.9	13

Figure 0.2: Comparison of the observed limits on aTGC parameters from different measurements. The highlighted rows represent the limits obtained from the measurement presented in this thesis. This figure has been published in Reference [1].

along with a synopsis of experimental results available on anomalous triple gauge couplings; and the experimental setup is described in Chapter 2, which introduces the LHC and the CMS experiment at the LHC. Chapter 3 discusses the matter of alignment of the CMS tracker, which is pivotal in doing physics, and presents the alignment and validation for legacy reprocessing of all of 13 TeV data. Monte Carlo simulation, object reconstruction, and boosted topology techniques are elucidated in Chapter 4; event selection is discussed in Chapter 5; and signal modelling and background estimation are presented in Chapter 6, shedding light on the approach used to extract different contributions. Chapter 7 details the statistical model and presents the results of this search; and Chapter 8 demonstrates the improvement in results from inclusion of 2017 and 2018 data. The thesis concludes with Chapter 9 with suggestions for future work on the topic.

Contents

I do not know what I may appear to the world, but to myself I seem to have been only like a boy playing on the seashore, and diverting myself in now and then finding a smoother pebble or a prettier shell than ordinary, whilst the great ocean of truth lay all undiscovered before me.

……

– Isaac Newton

1

Theoretical underpinning

Earth, water, air, fire —

This chapter briefly describes the evolution of ideas regarding the basic building blocks of matter, culminating in the standard model of particle physics. Theoretical basis for the standard model is presented along with the particles included in various families and generations. Theoretical and experimental shortcomings of the standard model are brought to light and the idea of an effective field theory is discussed. The chapter concludes by giving an overview of the experimental results available on anomalous coupling parameters in the effective field theory, which are the topic of this thesis.

Since times immemorial, our ancestors have speculated about the material nature of things around us. These inferences were first passed on from generation to generation by word of mouth, but the development of writing enabled humans to keep track of this knowledge and advance on it. One of the earliest characterisations of what everything is made up of was in the form of classical elements. The Greek philosopher Empedocles established the concept of four elements, depicted in Figure 1.1, which were earthly and corruptible. Aristotle, in his treatise "On Generation and Corruption", furthered this notion of elements and added a fifth element, aether, which he hypothesised is pure and comprised the stars. Similar ideas about the nature of matter were also present in ancient cultures in Persia, Babylon, China, Japan, Tibet, and India.

In parallel, the notion that matter is made up of tiny discrete units was also put forth since the ancient times. The Greek philosophers Leucippus and Democritus coined the term "atomos" ("ατομος" in Greek) meaning "indivisible", from which the term atom has been derived. This concept of atomism was, however, quite different from the current idea of atoms. The atoms of Leucippus and Democritus were eternal and came in infinite shapes and forms. The idea of atomism and underlying similarity at a finer level in substances that behaved similarly was furthered in the early middle ages by Arab philosophers and scientists. Jabir Ibn Hayyan made a table to classify the chemical elements into groups of metals, non-metals and substances that can be distilled. This table later served as a first step towards Mendeleev's periodic table of elements.

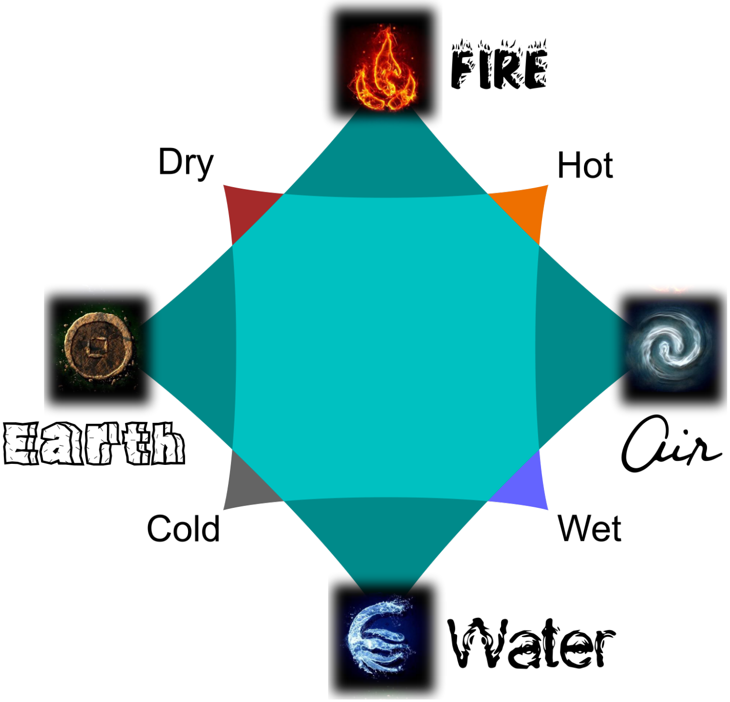

Figure 1.1: The ancient concept of elements. It was hypothesised by Aristotle that fire is hot and dry, earth is dry and cold, water is cold and wet, and air is wet and hot.

At the turn of the seventeenth century, Descartes and Newton pioneered the idea that light is made of tiny corpuscles which travel in a straight line with finite speed and possess momentum. A century later, John Dalton and Robert Brown proved experimentally that matter does indeed consist of discrete packets, which later became known as atoms and molecules.

In 1897, J. J. Thomson discovered the first subatomic particle by measuring the mass of cathode rays and showing that they were made of electrically charged particles. At the start of the twentieth century, Max Planck and Albert Einstein discovered the photon by explaining the results of blackbody radiation and the photoelectric effect. In 1909, Rutherford discovered the nucleus and proposed his model of the atom. Niels Bohr presented a semiclassical model in 1913 to remedy some of the issues in Rutherford's model.

With the advent of quantum mechanics, the field of atomic and subatomic physics was turned on its head and people proposed radical new ideas and discovered lots of particles. The discovery of mesons, the proposal of antiparticles by Dirac and their discovery later on, and the idea of neutrinos from Fermi are all wonderful stories in their own right. Towards the second half of the twentieth century, elementary particles were being discovered so frequently that it was crucial to find a way to organise them based on their symmetries. This was done in 1961 by Murray Gell-Mann and George Zweig, who introduced the eightfold way and the quark model, which was later expanded and improved to form the standard model (SM) of particle physics.

1.1 Particle content of the standard model

The SM of particle physics is our current theory describing elementary particles and their interactions with one another. Fundamental particles in the SM are either fermions, following Fermi-Dirac statistics [33, 34] and having half-integer spins; or bosons, following Bose-Einstein statistics [35,36] and having integer spins. The fermions comprise three generations of quarks and leptons, and their antiparticles, while the bosons consist of force-carrying gauge bosons and the recently discovered Higgs boson [37,38].

1.1.1 Fermions

Fundamental fermions of the SM can be broadly divided into quarks and leptons. Quarks are the elementary particles that combine to form hadrons, which may be mesons formed by combining a quark and an antiquark, baryons formed by combining three quarks, or more exotic states like pentaquarks [39].

There are six quarks in the SM forming three generations. The up and down quarks make up the first generation and have an electric charge of $+(2/3)$e and $-(1/3)$e, respectively, where e is the magnitude of charge on an electron. The up quark is the lightest quark in the SM with a mass of around 2.16 MeV [40]. The second generation consists of the up-like charm quark and the down-like strange quark, both being heavier than their first generation counterparts. The third generation consists of the top quark and the bottom quark. The top quark is the heaviest of all quarks with a mass of around 173 GeV [40] and is different from the other quarks in that its small decay time does not allow it to hadronise before it decays, enabling us to study properties of the bare quark. The six quarks along with their properties and year of prediction and discovery are summarised in Table 1.1.

Table 1.1: Properties of the SM quarks along with their prediction and discovery years. Electric charge is given in units of electron charge. Masses are taken from Reference [40].

Quark	Symbol	Electric charge (e)	Mass	Predicted	Discovered
Up	u	$+2/3$	$2.16^{+0.49}_{-0.26}$ MeV	1964	1968
Down	d	$-1/3$	$4.67^{+0.48}_{-0.17}$ MeV	1964	1968
Charm	c	$+2/3$	1.27 ± 0.02 GeV	1970	1974
Strange	s	$-1/3$	93^{+11}_{-5} MeV	1964	1968
Top	t	$+2/3$	173.1 ± 0.9 GeV	1973	1995
Bottom	b	$-1/3$	$4.18^{+0.03}_{-0.02}$ GeV	1973	1977

Each lepton generation consists of a charged lepton and a corresponding neutral neutrino. The neutrinos are massless in the SM, although recent discoveries of neutrino flavour oscillations [8] have confirmed nonzero neutrino masses. The electron is the lightest of the charged leptons, having a mass of 0.511 MeV [40]. The muon is almost 200 times heavier than the electron and the tau is even heavier. The SM leptons along with their properties and year of prediction and discovery are summarised in Table 1.2.

Table 1.2: Properties of the SM leptons along with their prediction and discovery years. Electric charge is given in units of electron charge. Masses are taken from Reference [40].

Lepton	Symbol	Electric charge (e)	Mass	Predicted	Discovered
Electron	e	-1	0.511 MeV	1874	1897
Electron neutrino	ν_e	0	< 2 eV	1930	1956
Muon	μ	-1	105.6 MeV	-	1936
Muon neutrino	ν_μ	0	< 0.19 MeV	~1940	1962
Tau	τ	-1	1.78 GeV	~1970	1975
Tau neutrino	ν_τ	0	< 18.2 MeV	~1970	2000

1.1.2 Gauge bosons

The SM incorporates three of the four fundamental interactions: electromagnetic, strong and weak nuclear interactions. These are mediated by the photon, eight gluons, and the $W^\pm$ and Z bosons, respectively. The photon and the gluons are massless whilst the $W^\pm$ and Z bosons possess mass owing to electroweak symmetry breaking (EWSB) and the Brout-Englert-Higgs (BEH) mechanism [41,42], which is discussed in Section 1.2. Fundamental bosons in the SM along with their properties and year of prediction and discovery are summarised in Table 1.3.

The $W^\pm$ and Z bosons, also called intermediate vector bosons (IVBs), play a pivotal role in the analysis presented in this thesis. They were predicted in 1968 by Sheldon Glashow, Steven Weinberg, and Abdus Salam [43–45], and discovered in 1983 by the UA1 (led by Carlo Rubbia) and UA2 (led by Pierre Darriulat) experiments at CERN [46–49]. Owing to

Table 1.3: Properties of the SM fundamental bosons along with their prediction and discovery years. Electric charge is given in units of electron charge. Masses are taken from Reference [40].

Boson	Symbol	Electric charge (e)	Mass (GeV)	Predicted	Discovered
Photon	γ	0	0	~1700	~1900
Gluons	g	0	0	1962	1978
W bosons	$W^{\pm}$	±1	80.379 ± 0.012	1968	1983
Z boson	Z	0	91.188 ± 0.002	1968	1983
Higgs boson	H	0	125.10 ± 0.14	1964	2012

their large decay width — or equivalently, short lifetime — it is not possible to detect them directly but only via their decay products. Both bosons decay dominantly into hadrons, more than two thirds of the times, and less than one third of the times into leptons.

This analysis is interested in events in which a pair of vector bosons is produced. The branching fractions of a WW or WZ boson pair are shown in Figure 1.2. The largest fraction is the one with only hadrons in the final state. This final state, however, suffers from huge backgrounds coming from interactions between quarks and gluons. The cleanest final state is the one with only leptons. However, this final state has the smallest branching fraction. The state where one of the vector bosons decays into hadrons and the other into leptons offers a good balance between a decent branching fraction and manageable background contamination. Because of this reason, this analysis focuses on the final state with one vector boson decaying hadronically and the other leptonically.

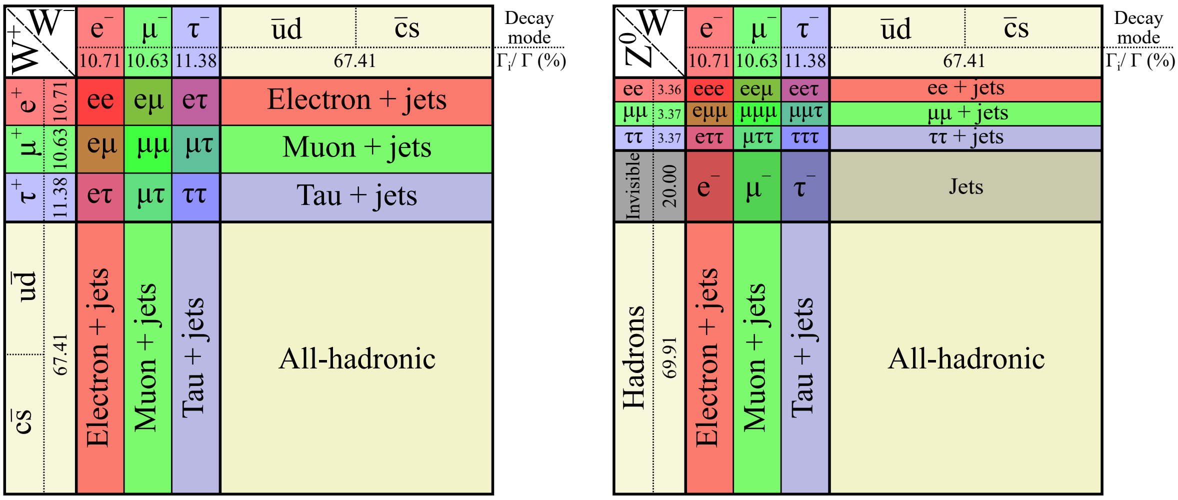

Figure 1.2: Branching fractions of a WW (left) and WZ (right) pair. Branching fractions are taken from Reference [40]. Only decays with significant branching fractions are included.

1.1.3 The Higgs boson

The only scalar fundamental particle in the SM is the Higgs boson. The existence of the Higgs boson was predicted in 1964 as the particle corresponding to the Higgs field, which was proposed to resolve the problem of gauge boson masses via electroweak symmetry breaking [41, 42]. This topic of electroweak symmetry breaking and the Brout-Englert-Higgs mechanism is discussed in detail in Section 1.2. The discovery of this illusive final piece in the SM had to wait several decades until the Large Hadron Collider at CERN started to collect and analyse data. This discovery of the Higgs boson was announced by the ATLAS and CMS collaborations at CERN simultaneously on July 4, 2012 [37, 38], marking it as one of the most valuable milestones in the history of modern science.

1.2 Mathematical framework of the standard model

The standard model is a quantum field theory, wherein fields are the fundamental quantities. All particles can be interpreted as excitations of these fields. In the Lagrangian formalism, the central quantity is the Lagrangian density (generally referred to as the Lagrangian):

$$\mathcal{L} = \mathcal{L}\left(\phi(x), \partial_\mu \phi(x)\right), \tag{1.1}$$

where x is the spacetime four-vector, ϕ is the spacetime dependent field, and $\partial_\mu = \frac{\partial}{\partial x^\mu}$, with $\mu = 0, 1, 2, 3$. The principle of stationary action states that the variation in action

$$\mathcal{S} = \int \mathrm{d}^4x \ \mathcal{L}(\phi, \partial_\mu \phi) \tag{1.2}$$

must vanish ($\delta\mathcal{S} = 0$). It can be shown that this is equivalent to the condition that the Lagrangian satisfies the Euler-Lagrange equation:

$$\frac{\partial \mathcal{L}}{\partial \phi} - \partial_\mu \frac{\partial \mathcal{L}}{\partial(\partial_\mu \phi)} = 0. \tag{1.3}$$

As a demonstration, we consider the postulated Lagrangian of a real scalar (spin-0) field without any interaction:

$$\mathcal{L} = \frac{1}{2}(\partial_\mu \phi)(\partial^\mu \phi) - \frac{1}{2} m^2 \phi^2, \tag{1.4}$$

where, in literature, the first term is generally called the kinetic term and the second term the mass term. Putting this Lagrangian in the Euler-Lagrange equation gives us the Klein-Gordon equation:

$$(\partial_\mu \partial^\mu + m^2)\phi = 0, \tag{1.5}$$

or sometimes written as:

$$(\Box + m^2)\phi = 0, \tag{1.6}$$

where $\Box = \partial_\mu \partial^\mu$ is the d'Alembert operator. On the same footing, we can consider the postulated Lagrangian of spin-½ fermions without any interaction (generally called the Dirac Lagrangian):

$$\mathcal{L} = \overline{\psi}(i\not{\partial} - m)\psi, \tag{1.7}$$

where $\not{\partial} = \gamma^\mu \partial_\mu$, and ψ and $\overline{\psi} = \psi^\dagger \gamma^0$ are the Dirac spinor and the adjoint spinor, respectively. The γ^μ used here are the gamma matrices. Plugging this Lagrangian in the Euler-Lagrange equation gives us the Dirac equation:

$$(i\not{\partial} - m)\psi = 0, \tag{1.8}$$

and its conjugate. The Dirac equation has been held up by many as the most beautiful equation in all of physics.

The SM is a gauge theory, implying that the Lagrangian is invariant under local gauge transformations (in addition to being invariant under Lorentz transformations) of the type:

$$\psi(x) \mapsto \psi' = e^{i\alpha(x)} \cdot \psi(x), \tag{1.9}$$

where $\alpha(x)$ is an arbitrary function of spacetime. The symmetry group of the SM is $\mathrm{SU}(3)_\mathrm{C} \otimes \mathrm{SU}(2)_\mathrm{L} \otimes \mathrm{U}(1)_\mathrm{Y}$, corresponding to a transformation of the type:

$$\psi(x) \mapsto \psi' = U(x) \cdot \psi(x), \tag{1.10}$$

where

$$U(x) = e^{i\beta(x)} \cdot e^{\frac{i}{2}\sum_{j=1}^{3} \alpha^j(x)\sigma^j} \cdot e^{\frac{i}{2}\sum_{k=1}^{8} \epsilon^k(x)\lambda^k}. \tag{1.11}$$

Here $\beta(x)$, $\alpha^j(x)$, and $\epsilon^k(x)$ are arbitrary real-valued functions of spacetime; σ^j are Pauli matrices, generators of $\mathrm{SU}(2)_\mathrm{L}$; and λ^k are Gell-Mann matrices, generators of $\mathrm{SU}(3)_\mathrm{C}$. The standard model Lagrangian contains terms corresponding to quantum electrodynamics, weak interaction, electroweak symmetry breaking, Yukawa couplings, and strong interaction. These contributions are discussed one by one in the following sections.

1.2.1 Quantum electrodynamics

The quantum relatavistic version of electrodynamics is known as quantum electrodynamics (QED). QED is the first theory in which a full agreement was achieved between the theory of special relativity and quantum mechanics. It aims at describing the interaction between matter and light. QED is an extremely precise theory and Richard Feynman famously called it "the jewel of physics" [50].

In order to develop the mathematical formalism, we start by considering the Dirac Lagrangian of Equation 1.7. As previously mentioned, the SM Lagrangian has to be gauge invariant. We therefore introduce the gauge transformation:

$$\begin{aligned} \psi(x) &\mapsto \psi' = e^{-iq\varphi(x)} \cdot \psi(x), \\ \overline{\psi}(x) &\mapsto \overline{\psi}' = e^{iq\varphi(x)} \cdot \overline{\psi}(x), \end{aligned} \tag{1.12}$$

where q represents electric charge and $\varphi(x)$ represents an arbitrary phase, and notice that there is an extra term $q\overline{\psi}\gamma^\mu\psi\partial_\mu\varphi$ in the transformed Lagrangian. In order to restore gauge invariance, a gauge field is introduced into the Lagrangian such that its transformation gives a term which cancels the extra term. The new Lagrangian becomes:

$$\mathcal{L} = \overline{\psi}(i\partial\!\!\!/ - m)\psi - q\overline{\psi}\gamma^\mu\psi \mathrm{A}_\mu, \tag{1.13}$$

with A_μ transforming as:

$$\mathrm{A}_\mu(x) \mapsto \mathrm{A}'_\mu(x) = \mathrm{A}_\mu(x) + \partial_\mu\varphi(x). \tag{1.14}$$

Equation 1.13 can be written nicely if we repackage the derivative and the newly added gauge field into the covariant derivative:

$$\mathrm{D}_\mu = \partial_\mu + iq\mathrm{A}_\mu. \tag{1.15}$$

This restores gauge invariance but now we also want to add the kinetic and the mass terms for the new gauge field. The mass term of the form $m_\mathrm{A}^2 \mathrm{A}_\mu \mathrm{A}^\mu$ would not be gauge invariant.

This implies that the mass of the QED gauge boson has to be zero, and indeed the photon is massless. After adding the kinetic term formed from the electromagnetic field strength tensor $F_{\mu\nu} = \partial_\mu A_\nu - \partial_\nu A_\mu$, the final QED Lagrangian becomes:

$$\begin{aligned}\mathcal{L}_{QED} &= \overline{\psi}(i\not{D} - m)\psi - \frac{1}{4}F_{\mu\nu}F^{\mu\nu} \\ &= \overline{\psi}(i\not{\partial} - m)\psi - q\overline{\psi}\gamma^\mu\psi A_\mu - \frac{1}{4}F_{\mu\nu}F^{\mu\nu}.\end{aligned} \tag{1.16}$$

The first term describes the dynamics of a spin-½ particle, the third term the kinematics of the photon field and the second term represents the interaction between the two.

1.2.2 Weak interaction

In order to incorporate the weak interaction, we can follow similar steps to the ones in QED. We start by again considering the Dirac Lagrangian:

$$\mathcal{L} = \overline{\psi}(i\not{\partial} - m)\psi, \tag{1.17}$$

and note that the Dirac spinor ψ has four components. The SM is a chiral theory, and therefore the Dirac spinor can be split into left- and right-handed components:

$$\psi_{L,R} = \frac{1 \mp \gamma^5}{2}\psi, \tag{1.18}$$

where

$$\gamma^5 = \frac{i}{4!}\varepsilon_{\mu\nu\alpha\beta}\gamma^\mu\gamma^\nu\gamma^\alpha\gamma^\beta, \tag{1.19}$$

with ε being the Levi-Civita symbol. The Dirac spinor thus becomes:

$$\psi = \begin{pmatrix}\psi_L \\ \psi_R\end{pmatrix}. \tag{1.20}$$

The component of the SM symmetry group corresponding to the electroweak interaction is $SU(2) \otimes U(1)$, where the charge corresponding to $SU(2)$ is weak isospin I, and to $U(1)$ is weak hypercharge, defined as:

$$Y = 2(q - I_3), \tag{1.21}$$

where q is the electric charge and I_3 is the third component of weak isospin. It was experimentally established in 1957 by C.S. Wu and her collaborators that the weak interaction does not conserve parity [51]. It is rather maximally violated, and the weak interaction only couples to left chiral spinors. The left-handed components of the Dirac spinor behave as doublets under $SU(2)$ while the right-handed components behave as singlets. The fermions of the SM with respect to $SU(2)$ are therefore:

$$\text{Quarks}: \begin{pmatrix}u \\ d\end{pmatrix}_L \otimes (u)_R \otimes (d)_R, \quad \begin{pmatrix}c \\ s\end{pmatrix}_L \otimes (c)_R \otimes (s)_R, \quad \begin{pmatrix}t \\ b\end{pmatrix}_L \otimes (t)_R \otimes (b)_R, \tag{1.22}$$

and

$$\text{Leptons}: \begin{pmatrix}\nu_e \\ e\end{pmatrix}_L \otimes (e)_R, \quad \begin{pmatrix}\nu_\mu \\ \mu\end{pmatrix}_L \otimes (\mu)_R, \quad \begin{pmatrix}\nu_\tau \\ \tau\end{pmatrix}_L \otimes (\tau)_R. \tag{1.23}$$

In the SM, there are no right-handed neutrinos. For the electroweak interaction, a covariant derivative can be defined in the same way as QED:

$$D_\mu = \partial_\mu - \frac{i}{2}g\sigma_j W^j_\mu - \frac{i}{2}g'YB_\mu. \tag{1.24}$$

Similar to QED, we now want to add the kinetic and mass terms for the newly added gauge fields. The mass terms would again violate gauge invariance, and this time we cannot leave them out since we know that the gauge bosons $W^{\pm}$ and Z are massive. This problem is resolved via electroweak symmetry breaking, which is discussed in the following section. Adding the kinetic terms, the electroweak Lagrangian becomes:

$$\mathcal{L}_{\mathrm{EW}} = \overline{\psi}_{\mathrm{L}} i \not{D} \psi_{\mathrm{L}} + \overline{\psi}_{\mathrm{R}} i \not{D} \psi_{\mathrm{R}} - \frac{1}{4} B_{\mu\nu} B^{\mu\nu} - \frac{1}{4} W^{j}_{\mu\nu} W^{\mu\nu}_{j}, \tag{1.25}$$

where the mass terms for the fermions have been omitted (since they are now not invariant under SU(2) in the chiral SM) and

$$\begin{aligned} B_{\mu\nu} &= \partial_\mu B_\nu - \partial_\nu B_\mu, \\ W^{j}_{\mu\nu} &= \partial_\mu W^{j}_\nu - \partial_\nu W^{j}_\mu + g \varepsilon^{jkl} W^{k}_\mu W^{l}_\nu. \end{aligned} \tag{1.26}$$

It is worth noticing that $W^{j}_{\mu\nu}$ contains a quadratic part and hence the Lagrangian would have terms with cubic (and quartic) gauge self-interactions, which are central to the analysis presented in this thesis. The exact form of these is discussed after introducing the physical gauge bosons following electroweak symmetry breaking.

1.2.3 Electroweak symmetry breaking

Gauge invariance of the electroweak Lagrangian, as discussed in the previous section, dictates that the gauge bosons should be massless. However, we know from experiments that the $W^{\pm}$ and Z bosons are massive. This conflict was resolved by a machanism introduced by Peter Higgs, Robert Brout, François Englert, and others [41, 42] in 1964. The basic idea of this Brout-Englert-Higgs mechanism is to introduce a complex scalar field:

$$\phi = \frac{1}{\sqrt{2}} \begin{pmatrix} \phi^+ \\ \phi^0 \end{pmatrix} = \begin{pmatrix} \phi_1 + i\phi_2 \\ \phi_3 + i\phi_4 \end{pmatrix}, \tag{1.27}$$

which is a doublet under $SU(2)_L$. The Lagrangian corresponding to this field is given by:

$$\mathcal{L}_{\mathrm{Higgs}} = (D_\mu \phi)^\dagger (D^\mu \phi) - V(\phi^\dagger \phi), \tag{1.28}$$

where D_μ is the covariant derivative defined in Equation 1.24 and the potential $V(\phi^\dagger \phi)$ is chosen to be of the form:

$$V(\phi^\dagger \phi) = \mu^2 (\phi^\dagger \phi) + \frac{\lambda}{2} (\phi^\dagger \phi)^2, \tag{1.29}$$

with μ^2 and λ being arbitrary real parameters. The shape of this potential for $\mu^2 < 0$ and $\lambda > 0$ is shown in Figure 1.3. This shape, generally called the Mexican hat potential, is symmetric and has a ring minimum at:

$$\phi_0 = \sqrt{\frac{-\mu^2}{\lambda}} e^{i\varphi}, \quad \varphi \in [0, 2\pi]. \tag{1.30}$$

When we choose a value of φ, the ground state does not inherit the original symmetry of the potential, or equivalently the Lagrangian. This is spontaneous symmetry breaking (SSB) in the context of the electroweak SM. The magnitude of the minumum,

$$v \equiv \sqrt{\frac{-\mu^2}{\lambda}}, \tag{1.31}$$

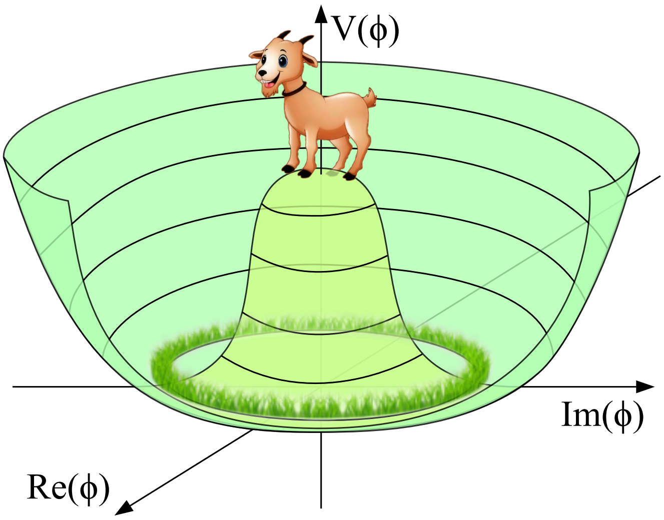

Figure 1.3: The shape of the Higgs potential for $\mu^2 < 0$ and $\lambda > 0$, and a cartoon analogy. The goat on top of the hill likes the grass everywhere and the situation is symmetric as long as he stays there. But in order to eat the grass, he has to come down in one direction. As soon as he does that, the symmetry of the initial terrain is not present in his selected "ground state".

is called the vacuum expectation value (VEV) of the Higgs field, having a value $v = 246$ GeV. It can be shown that by choosing an appropriate gauge, ϕ can be written in terms of a Hermitian field H:

$$\phi(x) = \frac{1}{\sqrt{2}} \begin{pmatrix} 0 \\ v + \mathrm{H}(x) \end{pmatrix}. \tag{1.32}$$

We can now put the ingredients in the Higgs Lagrangian (Equation 1.28), and evaluating it at the vacuum expectation value of the Higgs field finally gives us the physical massive gauge bosons:

$$\mathrm{W}^{\pm}_{\mu} = \frac{1}{\sqrt{2}}(\mathrm{W}^1_\mu \mp i\mathrm{W}^2_\mu), \tag{1.33}$$

and

$$\mathrm{Z}_\mu = \frac{1}{\sqrt{g^2+g'^2}}(g\mathrm{W}^3_\mu - g'\mathrm{B}_\mu), \tag{1.34}$$

and the massless photon:

$$\mathrm{A}_\mu = \frac{1}{\sqrt{g^2+g'^2}}(g'\mathrm{W}^3_\mu + g\mathrm{B}_\mu). \tag{1.35}$$

Noting the structure of Z_μ and A_μ, we can rewrite the Equations 1.34 and 1.35 by introducing the weak mixing angle, also called the Weinberg angle, θ_W ($\sin^2\theta_W = 0.232$ [40]). We identify:

$$\cos\theta_W = \frac{g}{\sqrt{g^2+g'^2}}, \quad \text{and} \quad \sin\theta_W = \frac{g'}{\sqrt{g^2+g'^2}}, \tag{1.36}$$

enabling us to write the weak mixing relations in the form:

$$\begin{pmatrix} A_\mu \\ Z_\mu \end{pmatrix} = \begin{pmatrix} \cos\theta_W & \sin\theta_W \\ -\sin\theta_W & \cos\theta_W \end{pmatrix} \begin{pmatrix} B_\mu \\ W^3_\mu \end{pmatrix}. \tag{1.37}$$

The mass of the Higgs, $W^\pm$, and Z bosons can all be specified in terms of v, λ, g, and θ_W:

$$\begin{aligned} m_H &= \sqrt{\lambda v^2}, \\ m_W &= \frac{gv}{2}, \\ m_Z &= \frac{m_W}{\cos\theta_W}. \end{aligned} \tag{1.38}$$

1.2.4 Cubic gauge self-interactions

Now that we have the gauge bosons, we can try to write the exact form of the Lagrangian consisting of cubic gauge self-interactions. The leading-order (LO) Feynman diagram for such an interaction is shown in Figure 1.4.

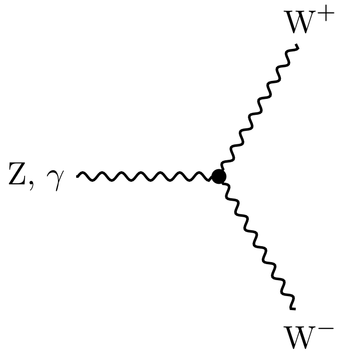

Figure 1.4: The leading-order Feynman diagram for cubic gauge self-interactions

If we define the gauge field strength tensors:

$$\begin{aligned} W^\pm_{\mu\nu} &= \partial_\mu W^\pm_\nu - \partial_\nu W^\pm_\mu, \\ Z_{\mu\nu} &= \partial_\mu Z_\nu - \partial_\nu Z_\mu, \\ A_{\mu\nu} &= \partial_\mu A_\nu - \partial_\nu A_\mu, \end{aligned} \tag{1.39}$$

expanding the kinetic terms in Equation 1.25, we can write the cubic gauge self-interaction Lagrangian as:

$$\begin{aligned} \mathcal{L}_3 = &- ie\cot\theta_W \left(g_1^Z (W^+_{\mu\nu} W^{-\mu} - W^{+\mu} W^-_{\mu\nu}) Z^\nu + \kappa_Z W^+_\mu W^-_\nu Z^{\mu\nu} + \frac{\lambda_Z}{m_W^2} W^{+\nu}_\mu W^{-\rho}_\nu Z^\mu_\rho \right) \\ &- ie \left(g_1^\gamma (W^+_{\mu\nu} W^{-\mu} - W^{+\mu} W^-_{\mu\nu}) A^\nu + \kappa_\gamma W^+_\mu W^-_\nu A^{\mu\nu} + \frac{\lambda_\gamma}{m_W^2} W^{+\nu}_\mu W^{-\rho}_\nu A^\mu_\rho \right), \end{aligned} \tag{1.40}$$

where the first three terms correspond to a WWZ interaction and the last three to a WWγ interaction. The coupling parameters g_1^Z, κ_Z, g_1^γ, and κ_γ are 1 in the SM, and λ_Z and λ_γ are 0. In the analysis presented in this thesis, the deviation of these couplings from this SM prediction is probed.

1.2.5 Yukawa couplings

As stated earlier, in the chiral SM, the Dirac mass term takes the form $m(\overline{\psi}_L\psi_R + \overline{\psi}_R\psi_L)$. This is not allowed since it is not invariant under the $\mathrm{SU}(2)$ structure of the SM. But the newly introduced Higgs field allows us to construct mass terms for fermions by coupling the left- and right-handed spinors via the Higgs field. We therefore include the following type of terms in the SM Lagrangian:

$$\mathcal{L}_{\mathrm{Yukawa}} = -g_f(\overline{\psi}_{\mathrm{L}}\phi\psi_{\mathrm{R}} + \overline{\psi}_{\mathrm{R}}\phi^{\dagger}\psi_{\mathrm{L}}), \tag{1.41}$$

where g_f is the Yukawa coupling of the fermion to the Higgs. The measurement of these Yukawa couplings has been the focus of recent studies, with the ATLAS and CMS collaborations announcing the discovery of Yukawa couplings between the Higgs boson and the third generation fermions in 2018 [52–55].

1.2.6 Quantum chromodynamics

The dynamics of quarks and gluons is governed by the third type of interaction in the SM, the strong interaction. The symmetry group for the strong interaction in the SM is non-abelian $\mathrm{SU}(3)$. The gauge invariant Lagrangian in QCD is given by:

$$\mathcal{L}_{\mathrm{QCD}} = \overline{\psi}_i(i\not{D}_{ij} - m\delta_{ij})\psi_j - \frac{1}{4}G^a_{\mu\nu}G_a^{\mu\nu}, \tag{1.42}$$

where i and j in the quark field ψ run over the three quark generations, and a in the gluon field strength tensor $G^a_{\mu\nu}$ runs from one to eight, corresponding to eight types of gluons. The covariant derivative in QCD is given by:

$$D_\mu = \partial_\mu - \frac{i}{2}g_{\mathrm{S}}\lambda_a\mathcal{A}^a_\mu, \tag{1.43}$$

where $\mathcal{A}^a_\mu$ are the gluon fields, λ_a are the Gell-Mann matrices, and g_{S} is the strength of the coupling. The gluon field strength tensor is given by:

$$G^a_{\mu\nu} = \partial_\mu\mathcal{A}^a_\nu - \partial_\nu\mathcal{A}^a_\mu + g_{\mathrm{S}}f^{abc}\mathcal{A}^b_\mu\mathcal{A}^c_\nu. \tag{1.44}$$

where f^{abc} are structure constants of the group $\mathrm{SU}(3)_C$.

The particles affected by QCD, quarks and gluons, carry colour charge. The charge comes in three flavours, often called red, blue and green, hence the name quantum chromodynamics for the theory. Quarks carry red, blue, or green, and antiquarks carry antired, antiblue, or antigreen. Gluons, which are the mediators of strong force, change colour of quarks and antiquarks for another colour. They therefore carry a pair of colour-anticolour charges. A schematic showing colour charges of quarks, antiquarks and gluons is shown in Figure 1.5.

The strong coupling constant, defined as $\alpha_{\mathrm{S}} = g_{\mathrm{S}}^2/4\pi$, depends on the scale of the process and the momentum transfer. This is why it is generally called a running coupling constant. The strong coupling at four-momentum transfer squared μ^2 can be written as:

$$\alpha_{\mathrm{S}}(\mu^2) = \frac{\alpha_{\mathrm{S}}(\mu_{\mathrm{R}}^2)}{1 + \beta_0\alpha_{\mathrm{S}}(\mu_{\mathrm{R}}^2)\ln(\mu^2/\mu_{\mathrm{R}}^2)}, \tag{1.45}$$

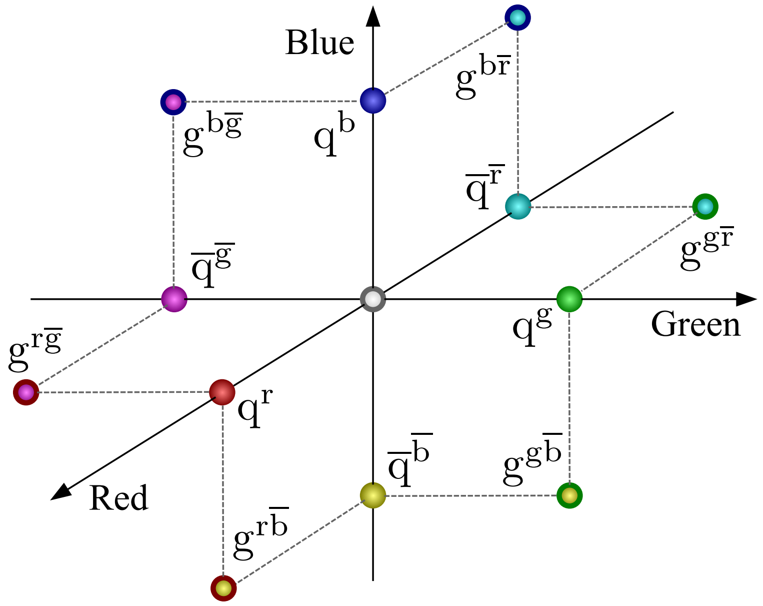

Figure 1.5: Schematic showing colour charges on quarks and gluons. Antiquarks carry the opposite of colour charges red, blue and green, and gluons carry a pair of colour-anticolour charges. Two gluons which have combinations of colour charges summing up to zero are represented at the origin.

with β_0 given by:

$$\beta_0 = \frac{11n_c - 2n_f}{12\pi}, \tag{1.46}$$

where μ_R is a reference scale, called renormalisation scale, at which the value of α_S is known experimentally, n_c is the number of colours, and n_f is the number of quark flavours. Since in the SM the number of colours is 3 and the number of quark flavours is 6, β_0 is positive. This implies that α_S falls with the reciprocal of the logarithm of the four-momentum transfer.

At really high energies — or equivalently, at really small distances — the strong coupling vanishes. This condition is called asymptotic freedom. Since the value of the coupling is small, perturbation theory can be used to give accurate description in terms of higher-order effects. This region of phase space is called the perturbative regime for QCD.

In the exact opposite case, at lower energies — or equivalently, at larger distances — the coupling becomes dramatically strong. It is because of this reason that bare quarks having colour charge do not exist freely. This is called quark confinement. If we try to pull coloured particles apart, the larger potential with increasing distance means that at one point, there is enough energy to create a new quark-antiquark pair. A large value of α_S also means that perturbation series cannot be used at lower energies. This region of phase space is called the non-perturbative regime for QCD.

1.3 Shortcomings of the standard model

The standard model is the most rigorously tested theory and it has, by and large, stood the test of time. There are, however, various shortcomings of the SM. These range from theoretical shortcomings to unexplained phenomena and experimental issues. The major issues with the SM are discussed below.

1.3.1 Gravity

The most obvious interaction that we experience on an everyday basis is gravity. In a stroke of brilliance, in the seventeenth century, Newton “unified” gravity by hypothesising that the force that keeps the moon in orbit is the same as the one that makes an apple fall to the ground, and gave a mathematical framework of it. In the modern age, gravity is explained by Einstein’s general theory of relativity, at the heart of which are the Einstein’s field equations:

$$R_{\mu\nu} - \frac{1}{2} g_{\mu\nu} R - g_{\mu\nu}\Lambda = \frac{8\pi G}{c^4} T_{\mu\nu}, \tag{1.47}$$

where $R_{\mu\nu}$ is the Ricci curvature tensor, which describes the curvature of spacetime; $g_{\mu\nu}$ is the metric tensor; R is the Ricci scalar, obtained by contracting the Ricci tensor; $T_{\mu\nu}$ is the energy-momentum-stress tensor, which is related to energy density and is the source of curvature of spacetime; and G and c are the gravitational constant and the speed of light in vacuum, respectively. The cosmological constant Λ can be added to the left-hand side to give space an accelerated expansion.

The SM has no explanation of gravity. If we make an attempt to do so, divergences occur and the theory is no longer renormalisable. There have been efforts beyond the SM, most notably loop quantum gravity [56] and string theory [57], that hypothesise unifying gravity with the other interactions.

1.3.2 Dark matter and dark energy

Cosmological observations within the last few decades have pointed to the fact that ordinary baryonic matter makes up less than 5% of the energy content of the universe. The rest is postulated to be non-luminous matter and energy.

The first evidence of non-luminous matter was obtained by studying the rotation curves of galaxies. The mass density of a spiral galaxy decreases as a function of distance from the centre of the galaxy. This implies that the galaxy can be modelled as a point mass at the centre, and we can study the effect of the mass of the galaxy on the speed of stars near the edge. This should be decreasing as the distance from the centre increases. However, it was observed by Vera Rubin and her colleagues [3] that the rotation speed stays almost constant with distance. This implies the existence of a lot of “dark” matter in the galaxy. The hypothesis of dark matter has been supported by lots of other observational evidence, like cosmic microwave background and redshift of galaxies and nebulae [2].

Until a few years ago, it was thought that the universe is expanding, but the expansion is slowing down. Riess, Perlmutter, and others observed the exact oppisite, accelerated expansion [4, 5]. This led to the hypothesis that some dark energy is pushing spacetime outwards at an ever increasing rate. It is worth noting that accelerated expansion can be explained by the cosmological constant in Equation 1.47.

The most recent surveys calculate that ordinary baryonic matter constitutes 4.8%, dark matter 25.8%, and dark energy 69.4% of the energy content of the universe [6]. The SM does not give any particle candidates or mathematical plausibility for dark matter or dark energy.

1.3.3 Hierarchy problem and naturalness

As discussed in Section 1.2, the gauge bosons and fermions in the SM get their masses via electroweak symmetry breaking by the introduction of the Higgs field. The Higgs boson has an experimentally measured mass of 125.10 ± 0.14 GeV [40]. Theoretically, the mass-squared parameter of the Higgs boson should get very large radiative quantum corrections. In order to have its value close to the observed value, the bare mass-squared parameter should also be very large, and precisely cancel the quantum corrections to leave behind the observed value. Such fine tuning is considered unnatural by many theorists. This is the hierarchy problem in the context of the VEV of the Higgs field [7].

Another way in which the hierarchy problem is stated, is in terms of strengths of fundamental interactions. It questions why gravity is so much weaker — nearly 40 orders of magnitude — as compared to the other forces. The SM has about 20 free parameters that can be experimentally determined, but not much can be said about the origin of their values. This level of arbitrariness also does not sit well with many theorists.

1.3.4 Matter-antimatter asymmetry

It is a common observation that we live in a matter dominated universe. The question naturally arises about this asymmetry in amounts of matter and antimatter. The SM does not explain this very well. Theoretically, one can add terms in the SM that break CP symmetry in strong interactions. This will relate matter to antimatter; however, this has not been observed, implying that these terms have a very small coefficient. This is, again, considered unnatural and the issue is called the strong CP problem [9].

1.3.5 Neutrino masses

Neutrinos are massless in the SM. This is owing to the fact that in the SM, there are only left-handed neutrinos and thus, we cannot write mass terms of the form in Equation 1.41. There are some ad-hoc techniques via which we can add neutrino masses. The seesaw mechanism is one such technique, in which we add heavy right-handed sterile neutrinos, and the mass of the left-handed neutrinos is inversely proportional to the Majorana mass of the right-handed neutrinos [58].

The presence of nonzero neutrino masses also means that neutrino flavours mix and we have neutrino flavour oscillations. These neutrino flavour oscillations have been experimentally observed [8], confirming that neutrinos must have nonzero masses. The absolute scale of these masses still has to be determined, a task for which the Karlsruhe Tritium Neutrino (KATRIN) experiment has been set up in Karlsruhe, Germany. The first results from the KATRIN experiment were announced in 2019 [59].

1.3.6 Further experimental observations

In addition to the shortcomings described above, there are several experimental observations that the SM does not explain. One of these observations is a deviation in anomalous magnetic dipole moment of the muon from the SM value [60]. This $g-2$ anomaly has been studied at Brookhaven National Laboratory (BNL), and a new experiment called "Muon g−2" [61] is recording data to improve the precision of this measurement. Another inconsistency comes from B meson decays where an excess of 5-sigma from the SM prediction has been reported in 2017 [62].

Keeping in view all these problems, a plethora of beyond the standard model (BSM) theories and models have been proposed. These span a wide range of ideas including, but not limited to, supersymmetry, composite Higgs boson models, different strong dynamics, warped and flat extra dimensions, hidden sector gauge theories, and so on. There has, however, been no evidence of any of these models in our current experiments.

1.4 Effective field theory

As discussed in Section 1.3, the SM has many inconsistencies and unexplained issues. Hundreds, if not thousands, of models have been proposed to rescue the SM from these issues, and offer a more intuitive picture of reality. Many of these models propose resonances, which may or may not be within the reach of our current experiments. While trying to search for physics beyond the SM, it hence becomes a dilemma to choose a model to look for new physics. This can be remedied by choosing a model-independent framework. One of the best such frameworks is the effective field theory (EFT). In the EFT, we parametrise new physics by expanding around the SM, and integrating over degrees of freedom at higher energies. This leads to additional terms in the Lagrangian, supressed by the mass scale of new physics, hereafter referred to as Λ. We therefore form an effective Lagrangian:

$$\mathcal{L}_{\text{eff}} = \mathcal{L}_0 + \sum_{n=1}^{\infty} \sum_i \frac{c_i^{(n+4)}}{\Lambda^n} \mathcal{O}_i^{(n+4)}, \tag{1.48}$$

where $\mathcal{L}_0$ is the SM Lagrangian, $\mathcal{O}_i^{(d)}$ are additional operators of mass-dimension d, and $c_i^{(d)}$ are the respective coupling constants. It should be noted that for the effective field theory expansion to be valid, the scale of the process must be much smaller than Λ.

The first added term consists of dimension-5 operators, which violate lepton number conservation and are relevant at higher energies and in neutrino oscillation studies. The next term comprises dimension-6 operators, and while there is a large number of them, this thesis focuses on CP-conserving operators in the vector boson sector [63, 64]:

$$\begin{aligned} \mathcal{O}_{\text{WWW}} &= \text{Tr}\left[\text{W}_{\mu\nu}\text{W}^{\nu\rho}\text{W}_\rho^\mu\right], \\ \mathcal{O}_{\text{W}} &= \left(\text{D}_\mu\phi\right)^\dagger \text{W}^{\mu\nu} \left(\text{D}_\nu\phi\right), \\ \mathcal{O}_{\text{B}} &= \left(\text{D}_\mu\phi\right)^\dagger \text{B}^{\mu\nu} \left(\text{D}_\nu\phi\right), \end{aligned} \tag{1.49}$$

where ϕ and D_μ are the SM Higgs boson doublet and the electroweak covariant derivative, respectively, defined in Section 1.2, and $W_{\mu\nu}$ and $B_{\mu\nu}$ are now given by:

$$\begin{aligned} W_{\mu\nu} &= \frac{i}{2} g \sigma_j \left(\partial_\mu W^j_\nu - \partial_\nu W^j_\mu + g \varepsilon^{jkl} W^k_\mu W^l_\nu \right), \\ B_{\mu\nu} &= \frac{i}{2} g' Y \left(\partial_\mu B_\nu - \partial_\nu B_\mu \right). \end{aligned} \tag{1.50}$$

After defining these operators, our relevant Lagrangian becomes:

$$\mathcal{L}_{\text{eff}} = \mathcal{L}_0 + \frac{c_{\text{WWW}}}{\Lambda^2} \mathcal{O}_{\text{WWW}} + \frac{c_{\text{W}}}{\Lambda^2} \mathcal{O}_{\text{W}} + \frac{c_{\text{B}}}{\Lambda^2} \mathcal{O}_{\text{B}}, \tag{1.51}$$

and the parameters $\{c_{\text{WWW}}, c_{\text{W}}, c_{\text{B}}\}$, called anomalous triple gauge couplings (aTGC) parameters, control the size of each new contribution. The addition of these aTGCs modifies the cubic gauge self-interaction of Figure 1.4 to the one shown in Figure 1.6.

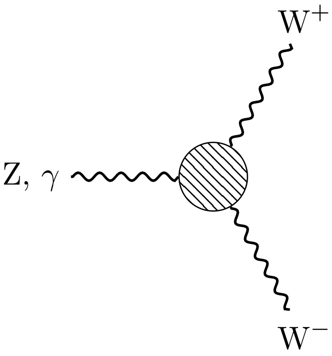

Figure 1.6: Feynman diagram showing anomalous triple gauge couplings between the electroweak gauge bosons

These aTGCs can be linked to the Lagrangian parameters in Equation 1.40 using the following relations [64]:

$$\begin{aligned} \lambda_Z = \lambda_\gamma &= c_{\text{WWW}} \frac{3 g^2 m_W^2}{2\Lambda^2}, \\ \Delta g_1^Z &= c_W \frac{m_Z^2}{2\Lambda^2}, \\ \Delta \kappa_Z &= \left(c_W - c_B \tan^2 \theta_W \right) \frac{m_W^2}{2\Lambda^2}, \\ \Delta \kappa_\gamma &= \left(c_W + c_B \right) \frac{m_W^2}{2\Lambda^2}, \end{aligned} \tag{1.52}$$

where Δ denotes a difference from the SM value of 1.

The newly added terms in Equation 1.51 give contributions proportional to s/Λ^2, where s is the square of the centre-of-mass energy. This means that at higher energies, kinematic variables such as the diboson invariant mass, will show enhanced cross sections. This fact is exploited in this analysis, where deviations from the SM in the tails of diboson invariant mass distributions are examined. It is, however, worth noting that as the newly added contributions become large, they may become large enough to violate unitarity. At high enough energies, where $\sqrt{s}$ starts to become of the order of Λ, EFT is no longer valid. This cutoff scale hence prevents EFT from violating unitarity by construction, and we instead have to talk about EFT validity. On the other hand, if we consider the Lagrangian parameters of Equation 1.40, they do not come equipped with such a cutoff scale, and are prone to unitarity violation. One therefore has to add form-factors to this approach to make sure that the unitary bound is not broken. These form-factors may be overly restrictive, and this shows the inherent advantage of the EFT approach over the other approaches. EFT does not need these form-factors owing to the fact that EFT will always be valid if it fits the data (on the actual scale of the process) since data will never violate unitarity.

As an example, we can consider the predicted differential cross section of WW production, as a function of diboson invariant mass, at $\sqrt{s} = 14$ TeV at the LHC, shown in Figure 1.7. The SM cross section as well as the cross section in the presence of a nonzero aTGC, $c_{\mathrm{WWW}}/\Lambda^2 = (400\ \mathrm{GeV})^{-2}$, is shown. The unitarity bound can also be calculated, and for the scales relevant at the LHC, it is way larger than the cross sections, even in the presence of significant nonzero aTGCs.

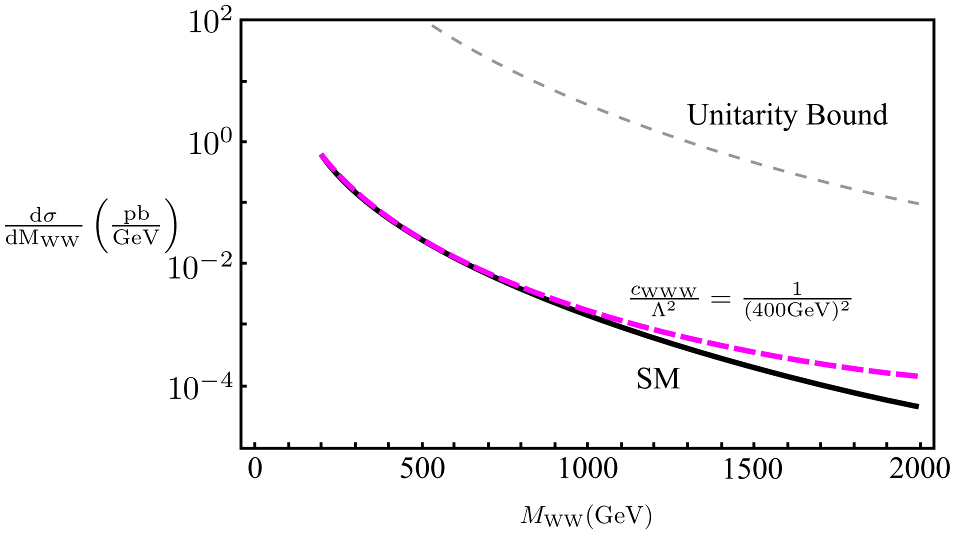

Figure 1.7: Predicted differential cross section of WW production, in the SM case, as well as the case where $c_{\mathrm{WWW}}/\Lambda^2 = (400\ \mathrm{GeV})^{-2}$, at 14 TeV LHC. The calculated unitariy bound is also shown. This figure is taken from Reference [64].

1.5 Synopsis of experimental results

Experimental search for aTGCs has been carried out quite vigourously at particle colliders. Historically, this search was carried out in the Lagrangian formalism and constraints were placed on the Lagrangian parameters of Equation 1.40. Experiments at the Large Electron-Positron (LEP) collider at CERN carried out this search in fully leptonic and semileptonic decay channels [65]. The results of these searches are shown in Table 1.4. The DØ experiment at Fermilab combined the results of $\mathrm{WW} + \mathrm{WZ} \to \ell\nu jj$, $\mathrm{WZ} \to \ell\nu\ell\ell$, $\mathrm{W}\gamma \to \ell\nu\gamma$, and $\mathrm{WW} \to \ell\nu\ell\nu$ final states to constrain these parameters [66]. These constraints are shown in Table 1.5. Owing to considerably less centre-of-mass energies, these experiments were severely limited in sensitivity compared to the experiments of today.

With the advent of the LHC, focus was shifted to the ATLAS and CMS experiments. These experiments are also carrying out an extensive programme of aTGC searches. Most of these searches are in fully leptonic final states [10–28], whilst searches in the semileptonic final state have been carried out at 7 and 8 TeV [29–32]. Recently, as EFT became popular, constraints on aTGCs have been formulated mostly in the EFT parametrisation. The most stringent constraints on charged aTGC parameters — not considering constraints from the analysis presented in this thesis — are from study of electroweak production of a W or Z boson along with two jets [67], and measurement of WZ production cross section in the fully leptonic final state [26], both at $\sqrt{s} = 13$ TeV. These constraints are shown in Table 1.6.

Table 1.4: Historical measurements of charged aTGC parameters, performed at the four LEP experiments [65]. The measurements were performed in fully leptonic and semileptonic decay channels.

Parameter	ALEPH	DELPHI	L3	OPAL	Comb.	95% CL interval
λ_γ	$-0.014^{+0.029}_{-0.029}$	$0.001^{+0.036}_{-0.035}$	$-0.023^{+0.042}_{-0.039}$	$-0.061^{+0.037}_{-0.036}$	$-0.022^{+0.019}_{-0.019}$	$[-0.059,\ 0.017]$
g_1^Z	$0.996^{+0.030}_{-0.028}$	$0.975^{+0.035}_{-0.032}$	$0.965^{+0.038}_{-0.037}$	$0.985^{+0.035}_{-0.034}$	$0.984^{+0.018}_{-0.020}$	$[0.946,\ 1.021]$
κ_γ	$0.983^{+0.060}_{-0.060}$	$1.022^{+0.082}_{-0.084}$	$1.020^{+0.075}_{-0.069}$	$0.899^{+0.090}_{-0.084}$	$0.982^{+0.042}_{-0.042}$	$[0.901,\ 1.066]$

Table 1.5: Historical measurements of charged aTGC parameters, performed at the DØ experiment [66]. The final result is a combination of measurements in fully leptonic and semileptonic decay channels.

Parameter	Minimum	68% CL interval	95% CL interval
λ_γ	0.007	$[-0.015,\ 0.028]$	$[-0.036,\ 0.044]$
g_1^Z	0.022	$[-0.008,\ 0.054]$	$[-0.034,\ 0.084]$
κ_γ	0.048	$[-0.057,\ 0.154]$	$[-0.158,\ 0.255]$

Table 1.6: Best 95% CL intervals on aTGC parameters, not considering the analysis presented in this thesis. These limits were obtained from electroweak W/Z+2-jets analysis [67] and WZ cross-section measurement in the fully leptonic decay channel [26], both at $\sqrt{s} = 13$ TeV.

Parameter	EW W/Z+2-jets (TeV^{-2})	WZ (TeV^{-2})
c_{WWW}/Λ^2	$[-1.8,\ 2.0]$	$[-4.1,\ 1.1]$
c_W/Λ^2	$[-5.8,\ 10.0]$	$[-2.0,\ 2.1]$
c_B/Λ^2	$[-43,\ 45]$	$[-100,\ 160]$

A summary of limits on aTGC parameters — not considering limits from this analysis — is shown in Figure 1.8. In order to easily compare with historical results, such summary plots are often presented in the parametrisation of Lagrangian parameters of Equation 1.40, hereafter called LEP parametrisation. The constraints on all three parameters obtained from the analysis presented in this thesis are the most stringent ones when compared with any of the shown (or otherwise) historical or contemporary measurements. In this thesis, we discuss the procedure used in this analysis, followed by the resulting constraints, and come back to this summary plot in the end.

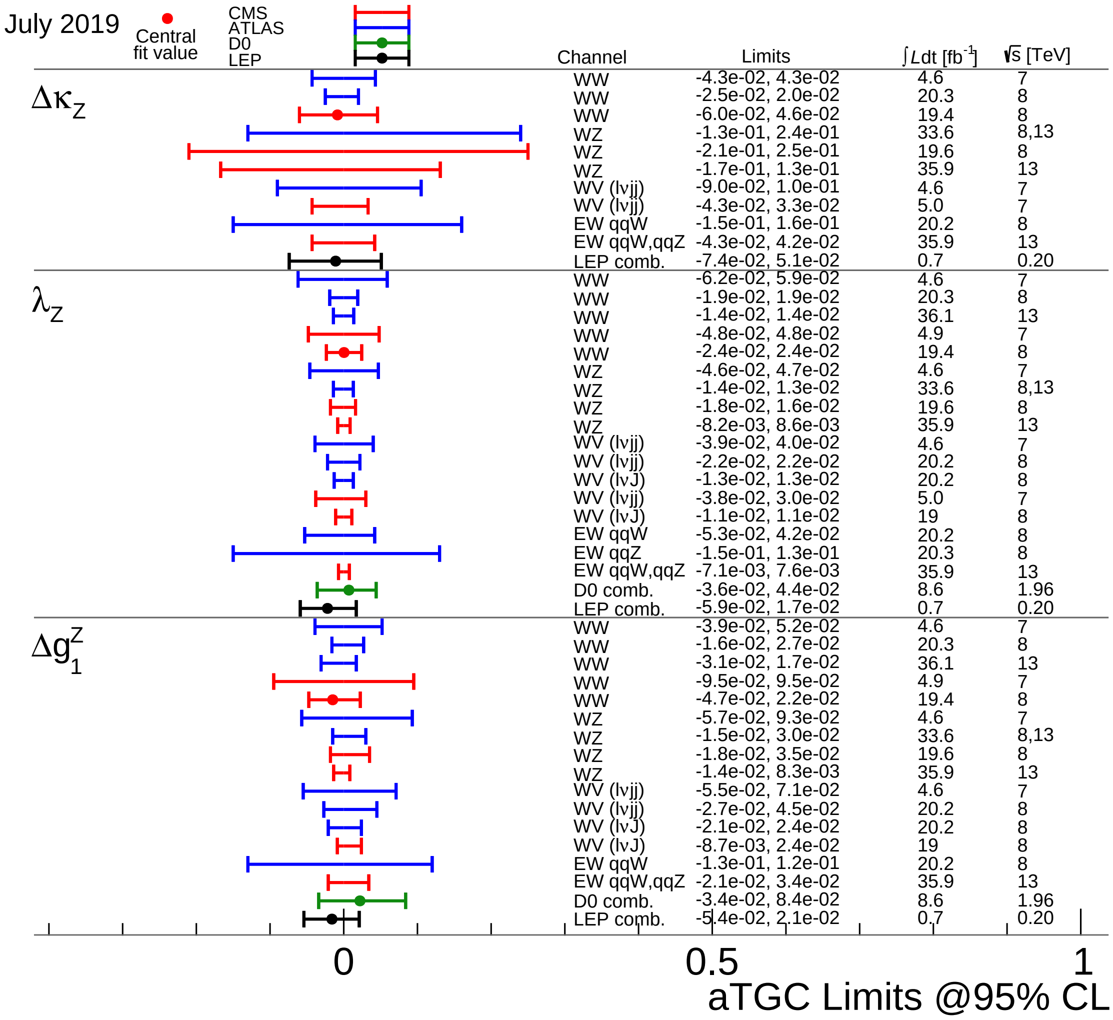

Figure 1.8: Summary of observed limits on aTGC parameters from different measurements, not considering the analysis presented in this thesis. The same summary plot, with the limits derived from this analysis, is shown in Introduction, and again in Chapter 9.

Despite my resistance to hyperbole, the LHC belongs to a world that can only be described with superlatives.

— Lisa Randall,
Knocking on heaven's door

2

The LHC and the CMS experiment

The big bang machine —

This chapter sheds light on the experimental setup of the LHC, followed by an explanation of the CMS experiment, which is used to record data from which the measurement presented in this thesis is derived. Construction and functioning of the subdetectors of the CMS detector are described in detail, along with considerations of performance. The chapter concludes by discussing the CMS trigger system and a distributed computing infrastructure used to share, store and analyse data.

In the year 1897, Ferdinand Braun made the first cathode ray tube, building on the ideas of Geißler and Crookes. The same year, J. J. Thomson discovered the electron using cathode rays. This was a historic landmark in the field of particle physics. It demonstrated that electric and magnetic fields could be used to accelerate, deflect, and hence detect fundamental particles. The idea caught on, and slowly and steadily, people built new and better particle accelerators and detectors. The Large Hadron Collider at CERN is a testament to the ingenuity and effort put into building particle accelerators.

2.1 The Large Hadron Collider

The Large Hadron Collider (LHC) is the flagship accelerator of the European Organization for Nuclear Research (CERN). Located on the border of Switzerland and France, near the town of Meyrin, the LHC is the biggest, most complex machine ever built by man. The LHC is designed to accelerate protons while they circulate in two beams in opposite directions around a ring of circumference 26.7 km, and then collide at specific points along the ring, where experiments have been set up to detect the scattered and newly produced particles.

The LHC started collecting data in 2010, at a centre-of-mass energy of 7 TeV. The so called Run 1 continued for three years, with the centre-of-mass energy raised to 8 TeV in 2012. The Higgs boson was discovered utilising this data [37,38]. In 2013 and 2014, there was a long shutdown of the LHC to make upgrades and improvements. Run 2 started in 2015, with a centre-of-mass energy of 13 TeV, and continued until the end of 2018. 2019 and 2020 are reserved for upgrades, and the LHC will start again for Run 3 in 2021, which will go on for three years. At some point during these three years, the centre-of-mass energy will be shifted to the design value of 14 TeV. For the next few decades, the LHC will be transformed into a high-luminoisty LHC, upgraded drastically to deliver and record many more collisions per second.

The current LHC was built after decommissioning of LEP in 2001. A hierarchy of pre-accelerators at the CERN complex is used to accelerate protons, before they are fed into the LHC. A schematic of the accelerator chain, along with the main experiments, is shown in Figure 2.1. In addition to colliding protons, the LHC also performs Pb-Pb collisions, although they are quite limited in number compared to the proton-proton collisions.

2.1.1 Accelerators feeding the LHC

A cylinder of hydrogen gas is the primary source of protons, which will eventually be used in collisions. Hydrogen atoms are passed through an electric field, which strips them off their electrons leaving behind protons. The protons start their journey at the Linear Accelerator 2 (LINAC 2) [69]. Radio-frequency (RF) cavities are used to accelerate the protons, and when they leave LINAC 2, they are already travelling at one-third the speed of light, having an energy of 50 MeV and gained 5% in mass. LINAC 2 has been working as the starting point of the CERN accelerator complex since 1978, and it will be succeeded by LINAC 4 in 2020.

The protons from LINAC 2 are fed into the Booster [70], which is circular, since linear acceleration is impractical from now on. The Booster has four rings, with a circumference

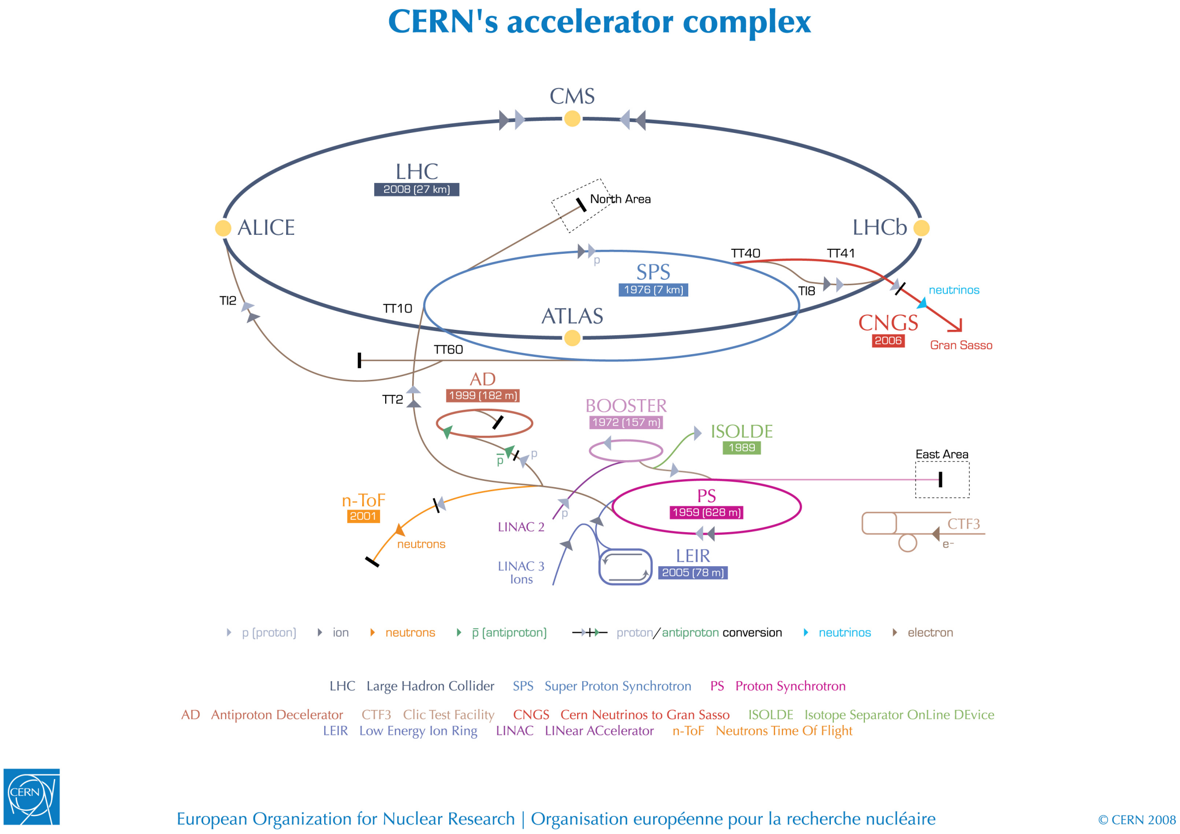

Figure 2.1: Schematic showing the CERN accelerator complex and experiments set up at various points. The largest ring in the centre is the LHC, and the protons travel sequentially through various small accelerators before being injected into the LHC ring. This figure is taken from Reference [68].

of 157 m, to each accelerate one fourth of the packet of protons, hence increasing beam intensity. The Booster accelerates the protons to 92% of the speed of light. Each proton now has an energy of 1.4 GeV.

The next step is the Proton Synchrotron (PS) [71], which is 628 m in circumference, and has been operational since 1959. The protons spend 1.2 s in the PS, and it has 100 dipole magnets to keep the beam following a circular path. At the time of leaving the PS, the protons are travelling at almost the speed of light, and from now on, the increased energy manifests only as increased mass. The energy of protons at the time of leaving the PS is 25 GeV.

Proton beams from the PS are fed into the Super Proton Synchrotron (SPS) [72], which is 7 km in circumference. The SPS has 744 dipole magnets, and protons leave the SPS at an energy of 450 GeV. The SPS is also important historically, since the W and Z bosons were discovered by the UA1 and UA2 collaborations [46–49], using protons and antiprotons accelerated by the SPS.

2.1.2 The LHC ring

Protons from the SPS are injected into the 26.7 km long LHC ring by using kicker magnets. The LHC ring contains two beam cavities, one for protons travelling clockwise and anticlockwise, each. During Run 2, the final energy reached by the protons in the LHC is 6.5 TeV. Each beam consists of 2808 bunches, with the bunches being 25 ns apart, and each bunch contains 10^{11} protons. Travelling at the speed of light, the protons circle around the LHC ring 11,000 times per second.

To accelerate the protons, 16 radio-frequency cavities are placed along the length of the LHC. In order to keep the protons moving in a circular orbit, strong magnetic fields are needed. The current required to generate such magnetic fields is so high that the magnets are made from superconducting niobium-titanium (Ni-Ti) wires, cooled by superfluid liquid helium at 1.9 K. There are 1232 such 15-metre-long dipole magnets along the length of the LHC, which generate a magnetic field of 8.34 T. A cross section of the LHC beam pipe showing the two beam cavities, the dipole magnets, and the cooling and support structures is shown in Figure 2.2. The size, or centre-of-mass energy if we fix the size, of our circular accelerator is primarily determined by the strength of the bending magnetic field. For future accelerators, like the Future Circular Collider (FCC), there is a plan to increase the magnetic field to 12 T, and Ni_3-Sn is being proposed as the superconductor, since it has a higher critical temperature than Ni-Ti.

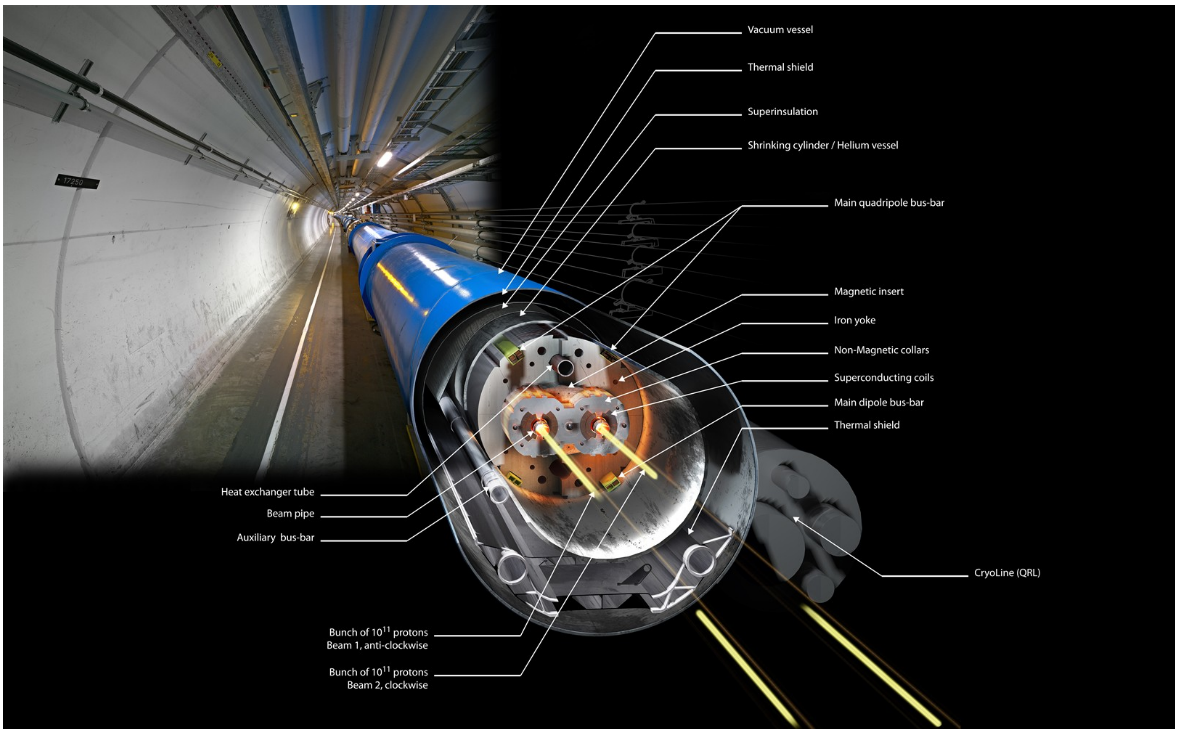

Figure 2.2: Cross section of an LHC beam pipe showing the superconducting dipole magnets used to bend proton beams, along with cooling and support structures. This figure is taken from Reference [73].

2.1.3 Beam dynamics and luminosity

To counter electrostatic repulsion between the protons in a bunch, as well as differences in initial conditions, focusing has to be done to keep the protons as close to the design orbit as possible. This is accomplished by 392 quadrupole magnets along the LHC. A quadrupole magnet which focuses in the horizontal plane defocuses in the vertical plane, and vice versa. Horizontal focusing and defocusing magnets are thus placed alternately, with three dipole magnets following each. This structure is called a FODO cell. Each of the eight arcs of the LHC contains 23 FODO cells.

A detailed discussion of the transverse beam dynamics can be found in Reference [40]. The quadrupole magnets apply a restoring force proportional to the transverse displacement of protons from the design orbit. Using a rotating Frenet-Serret frame, an equation of motion can be written, which turns out to be a Hill's differential equation. The general solutions can be written in terms of a constant of motion called emittance of the beam ε, and a periodic function β, that depends on the properties of the quadrupole lattice. Typically, the distribution of protons in a bunch follows a Gaussian shape, and the one-sigma beam size can be written in terms of emittance of the beam and the beta function, as follows:

$$\sigma_x = \sqrt{\varepsilon \beta_x}. \tag{2.1}$$

We can now define a measure of the interaction rate at the points where the proton beams cross, called instantaneous luminosity, as:

$$\mathscr{L} = f n_b \frac{n_1 n_2}{4\pi \sigma_x \sigma_y} \mathcal{F}, \tag{2.2}$$

where f is the frequency of revolution, n_b is the number of bunches per beam, n_1 and n_2 are the numbers of protons in the colliding bunches, and σ_x and σ_y are the beam sizes in horizontal and vertical directions, respectively, as defined in Equation 2.1. $\mathcal{F}$ is a reduction factor coming from nonzero crossing angle and other effects. The number of events for a specific process can be written as the product of the process cross section and time-integrated luminosity:

$$N_p = \sigma_p \times \int \mathscr{L} \mathrm{d}t. \tag{2.3}$$

Therefore, to obtain statistically significant results for the process we are interested in, against the unwanted backgrounds, it is desirable to have as large an integrated luminosity as possible. The LHC, in all its years of operation, has delivered about 192 fb^{-1} of proton-proton collision data. The growth of integrated luminosity delivered by the LHC, and recorded by the CMS experiment, is shown in Figure 2.3. During Run 1, 45.0 pb^{-1} and 6.1 fb^{-1} of data was collected at 7 TeV, and 23.3 fb^{-1} at 8 TeV, during 2010, 2011 and 2012, respectively. During Run 2, 4.2 fb^{-1}, 41.0 fb^{-1}, 49.8 fb^{-1}, and 67.9 fb^{-1} was recorded at 13 TeV during 2015, 2016, 2017, and 2018, respectively. 35.9 fb^{-1} out of the 41.0 fb^{-1} of 2016 data, which is usable for physics, is utilised in the analysis presented in this thesis.

During Run 3, starting in 2021, the LHC is planned to record more than 300 fb^{-1} of data over a period of three years. With the upgrade to high-luminosity LHC, the goal is to record 3000 fb^{-1} of data in the runs following the upgrade.

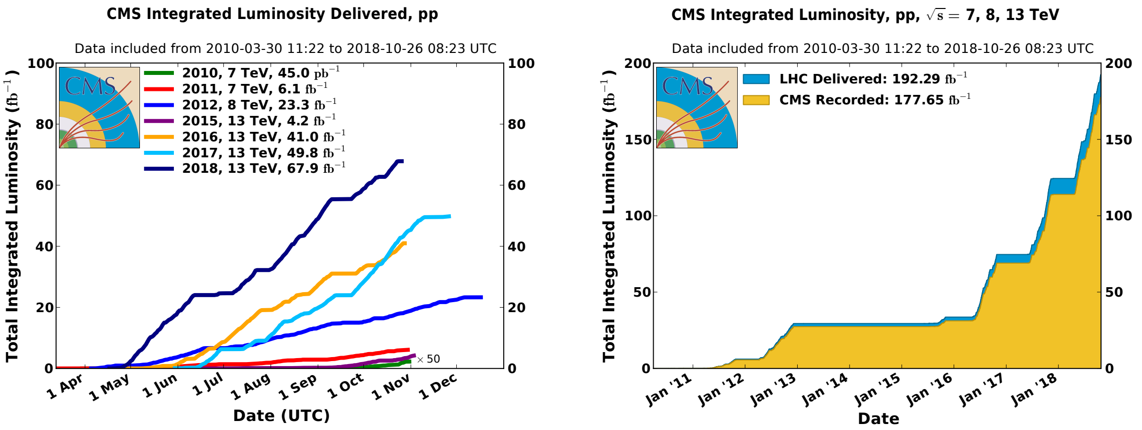

Figure 2.3: Integrated luminosity delivered by the LHC, and recorded by the CMS experiment, as a function of time. The integrated luminosity for different years is shown separately on the left, whilst the cumulative integrated luminosity is shown on the right. These figures are taken from Reference [74].

2.1.4 Experiments at the LHC

Four major experiments have been set up at the LHC, at interaction points where the clockwise and anticlockwise travelling beams cross. Two out of these four, ATLAS and CMS, are general-purpose detectors, while the other two, ALICE and LHCb, have much more specific purposes. In addition, there are several minor experiments, which share their locations with the major experiments.

One of the two general-purpose experiments is ATLAS. Having a length of 46 m, and a diameter of 25 m, ATLAS is the largest detector at the LHC, in terms of volume. The ATLAS detector consists of a complex toroidal magnetic field, tracking detectors, calorimeters, and a muon spectrometer. ATLAS explores a large range of physics, from studying properties of SM particles, including the top quark and the Higgs boson, to resonances searches and searches for supersymmetry and exotica.

The other general-purpose experiment is CMS (Compact Muon Solenoid). Weighing over 14,000 tonnes, the CMS detector is the heaviest detector at the LHC. A detailed explanation of the CMS detector is given in Section 2.2. CMS investigates the same topics as ATLAS, and both experiments work in tandem to give independent measurements regarding the same processes. This ensures that the results quoted by one experiment can be reproduced in another experiment, which is one of the cornerstones of modern scientific philosophy.

ALICE (A Large Ion Collider Experiment) is designed to study heavy ions, and interactions in quark-gluon plasma, similar to the one found just after the Big Bang. The ALICE detector is 26 m long, and 16 m in diameter. To distinguish particles coming from the quark-gluon plasma, ALICE uses a large variety of detectors, including silicon tracking detectors, a time projection chamber (TPC), a transition radiation detector (TRD), a time-of-flight (TOF) detector, a high momentum particle identification detector (HMPID), and calorimeters.

The LHCb (Large Hadron Collider beauty) experiment is designed to study properties and decays of hadrons formed by the bottom quark. An insight into CP violation and matter-antimatter asymmetry can be obtained from such studies. The LHCb detector is an asymmetric forward spectrometer, covering 10–100 mrad in the horizontal and 250 mrad in the vertical direction.

In addition to the above mentioned experiments, the LHCf (Large Hadron Collider forward), TOTEM (TOTal Elastic and diffractive cross section Measurement), and MoEDAL (Monopole and Exotics Detector at the LHC) experiments have been set up alongside ATLAS, CMS, and LHCb, respectively.

2.2 The CMS experiment

The CMS detector is located 100 m below the surface, at Point 5 of the LHC, near the French village of Cessy. It is designed like a cylindrical onion, with layers of detectors, and keeping hermeticity and redundancy in mind. The detector weighs 14,000 tonnes, and is the heaviest detector at the LHC. In terms of dimensions, it is 21.6 m long, and 14.6 m in diameter.

A schematic showing different layers of the CMS detector is shown in Figure 2.4. The innermost component is a silicon based tracking system. Its inner portion consists of pixel detectors while the outer one contains strips. Outside the tracker, there is a lead tungstate ($PbWO_4$) based electromagnetic calorimeter (ECAL), and then a brass and plastic-scintillator based hadron calorimeter (HCAL). The tracker and the calorimeters are housed in a superconducting solenoid magnet, that generates a 3.8 T magnetic field, which is used to curve charged particles for identification and measurement. The outer portion of the CMS detector consists of a muon system, comprising of drift tubes, cathode strip chambers and resistive plate chambers. Return steel yoke structures are placed in between layers of muon detectors to shape the magnetic flux.

All particles produced at the LHC are either stable over the lengths associated with the CMS detector or decay quite rapidly into a handful of particles, which the CMS detector is designed to detect. The interaction of these particles with the CMS detector is demonstrated in Figure 2.5. The pivotal idea is that travelling charged particles bend in presence of a magnetic field, and the curvature depends upon the momentum and charge of the particles. This information, along with the energy deposited in the calorimeters, is used to reconstruct particles, which are then combined to suggest the particles from which they decayed, or scattered. Electrons leave a track in the tracker, owing to their charge, and deposit their energy in the ECAL. Photons on the other hand, do not leave any tracks, and just deposit their energy in the ECAL. Similarly, charged hadrons leave a track and deposit their energy in the HCAL, while neutral hadrons deposit energy without leaving a track. Muons travel the longest, and bend in one direction inside the magnet, and the other outside of it. The CMS detector does not detect neutrinos, and their properties are deduced using momentum conservation.

The CMS experiment uses a right-handed coordinate system, with the x-axis pointing towards the centre of the LHC, and the y-axis upwards. This fixes the z-axis in the direction of the beams. Because of cylindrical symmetry, it is natural to use polar and azimuthal

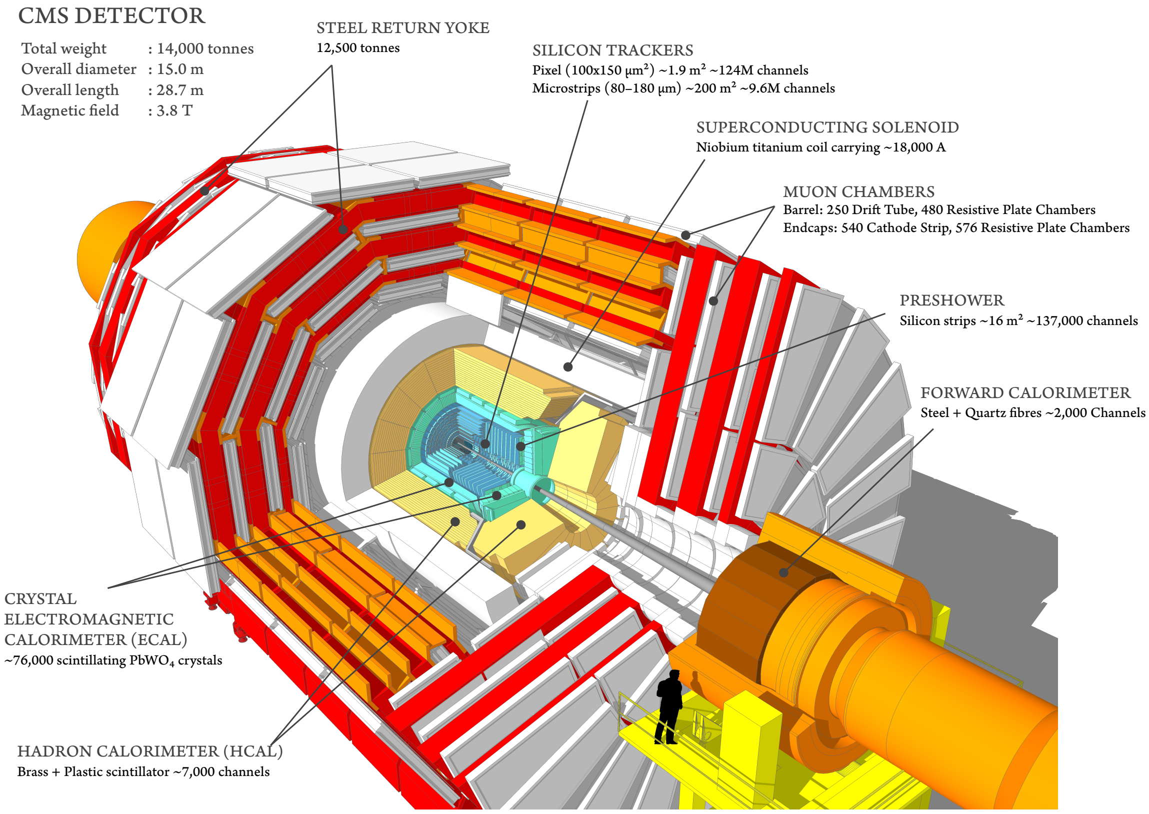

Figure 2.4: A cutaway view of the CMS detector demonstrating the main components. Silicon pixel tracking detectors are closest to the interaction point, followed by silicon strip tracking detectors. Outside these, reside the electromagnetic and hadron calorimeters, respectively. The tracker and the calorimeters are housed in a solenoid magnet, which generates 3.8 T magnetic field. The region outside this is primarily occupied by muon detectors. This figure is taken from Reference [75].

angles. The azimuthal angle ϕ goes from 0 to 2π, from the x-axis, around the z-axis. The polar angle θ is measured from the z-axis. Instead of using the polar angle directly, it is useful to transform this into pseudorapidity, defined as:

$$\eta = -\ln\left(\tan\frac{\theta}{2}\right), \tag{2.4}$$

where η is zero in the transverse direction and diverges as θ approaches zero. It is useful to note that pseudorapidity, written as a function of three momentum:

$$\eta = \frac{1}{2}\ln\left(\frac{|\vec{p}| + p_z}{|\vec{p}| - p_z}\right), \tag{2.5}$$

changes into the usual rapidity:

$$y = \frac{1}{2}\ln\left(\frac{E + p_z}{E - p_z}\right), \tag{2.6}$$

in the relativistic limit. Different components of the CMS detector are described in detail in the following sections.

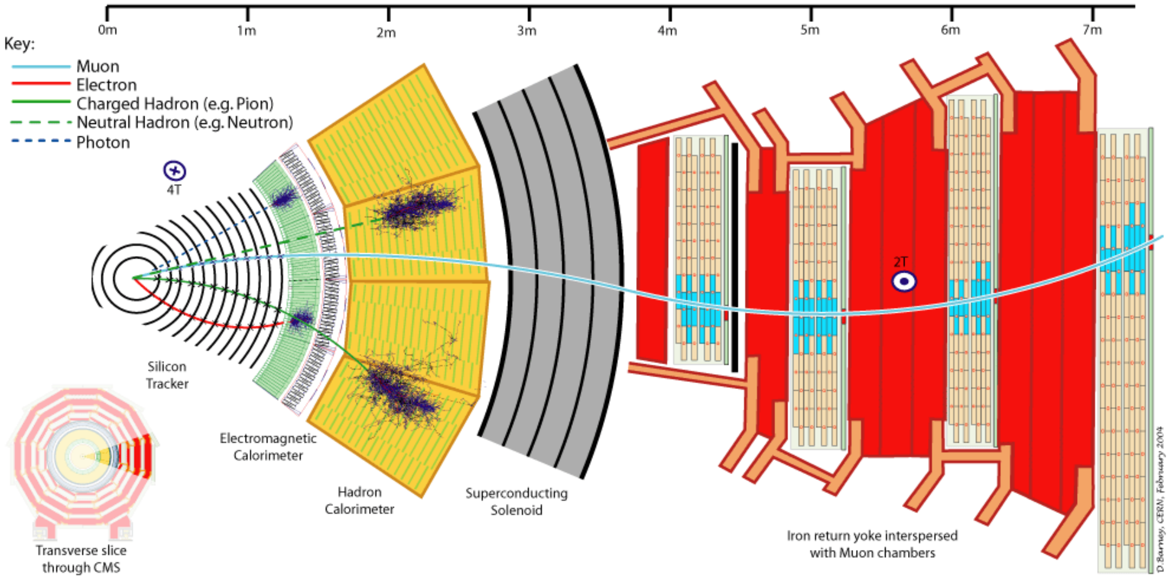

Figure 2.5: A transverse slice of the CMS detector demonstrating the detection of various types of particles. This figure is taken from Reference [76].

2.2.1 Tracker

One of the basic working principles of the CMS detector is that moving charged particles bend in the presence of a magnetic field. The momentum and charge of a particle can be deduced, if we know the trajectory of the particle. Therefore, in order to pinpoint the trajectory of charged particles coming from the interaction point, a tracking detector has been set up at the centre of CMS. The job of the tracker is to record hits from the charged particles at different distances from the centre, and these hits can then be fitted to precisely estimate the trajectory of the particles.

The CMS tracker is made entirely of silicon, and operates on the principle of a *p*-*n* junction diode. A basic module consists of an over-depleted *n*-doped silicon substrate, on which bits of *p*-doped silicon are implanted. When a charged particle passes throught the bulk of the substrate, it generates electron hole pairs which drift in the electric field, and induce a current in the attached metal electrodes. This current is amplified and converted into hits, indicating the passage of a charged particle. Silicon based tracking detectors are faster and much more precise than gaseous detectors and multiwire proportional chambers, but the downside is their high cost. Silicon based tracking has benefitted a lot from the fact that the silicon industry is very well developed because of research for advancements in semiconductor electronics.

The CMS tracker consists of a central pixel detector surrounded by a strip detector. A cutaway view of the tracker, and the layout of different layers of pixel and strip detectors is shown in Figures 2.6 and 2.7, respectively. The pixel detector is the closest of all CMS subdetectors to the interaction point. It thus has to handle large amounts of radiation. In order to cope with increasing luminosity, the pixel detector was given an upgrade during the technical stop between the years 2016 and 2017 [77]. Following the upgrade, the pixel detector consists of four concentric cylindrical layers with radii 30, 68, 109, and 160 mm, respectively, and a length of 548.8 mm, called the barrel pixel (BPIX); and three disks on each side, at a distance of 291, 396, and 516 mm from the centre, called the forward pixel (FPIX). The BPIX is made of 1184 pixel modules, having a total of 79 million $100 \times 150\ \mu\text{m}^2$ pixels. The FPIX has 672 modules, having 45 million pixels in total. The 1856 modules of the pixel detector cover an area of about 1 m^2, and give a coverage up to $|\eta| = 2.5$ and a position resolution of about 15 μm.

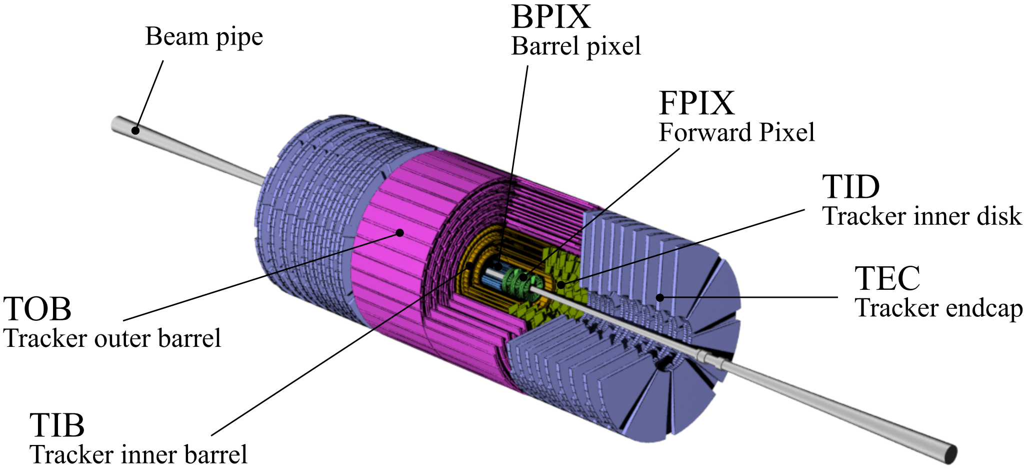

Figure 2.6: A cutaway view of the CMS tracker. This figure has been rendered in 3ds Max [78], after adapting and modifying the original CMS model from Reference [75].

The strip detector is made of 15,148 modules, covering an area of about 210 m^2, comparable to the size of a tennis court, and 9.6 million readout channels are required to get the output from all of the sensors. The modules are arranged in the barrel as tracker inner barrel (TIB) and tracker outer barrel (TOB), and in the endcap as tracker inner disk (TID) and tracker endcap (TEC). TIB extends from 20 to 55 cm from the beam axis, and consists of two layers of single-sided modules and two layers of modules mounted back to back at an inclination of 5.7° with respect to each other, called stereo modules. TOB extends up to 110 cm, and consists of two layers of stereo modules and four layers of single-sided modules. TID and TEC consists of three and nine layers, respectively, on either side the interaction point. The strip detector gives a considerably worse position resolution than the pixel detector, and the resolution can vary between 20 μm and 200 μm, depending on the relevant layer of TIB, TOB, TID, and TEC.

In order to ensure good position resolution of the tracker during data taking, shifts in position, orientation, and surface deformations in the modules have to be taken care of. This is done via software alignment and validation of the tracker modules using information from a large number of tracks. This alignment and validation of the CMS tracker is discussed in detail in Chapter 3.

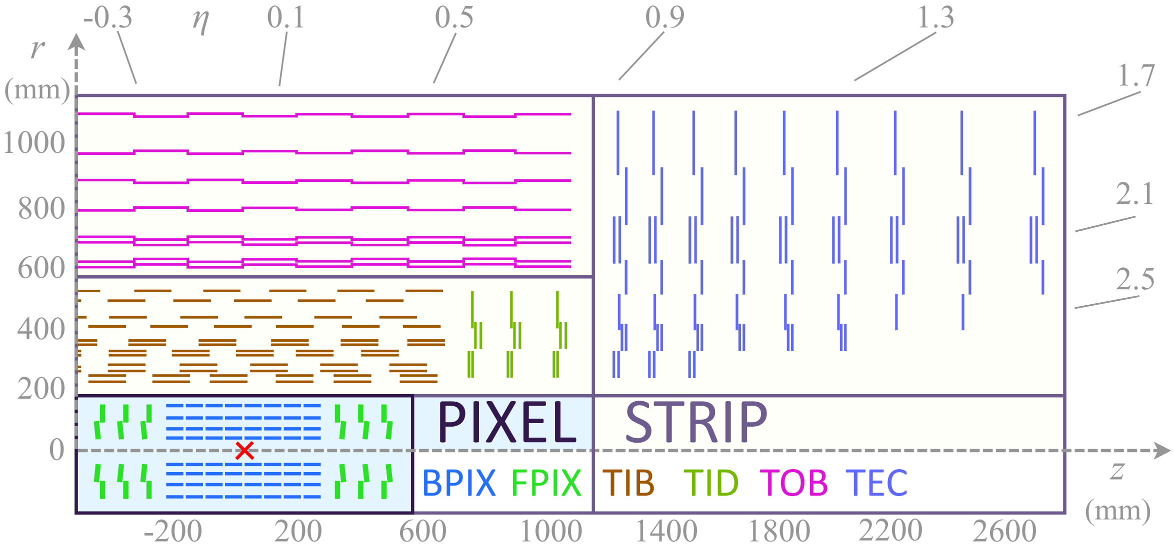

Figure 2.7: A schematic showing layout of the CMS tracker, and the placement of pixel and strip detectors in one quadrant. Following an upgrade at the start of 2017, the pixel detector now consists of four barrel layers (BPIX) and three endcap layers (FPIX). The surrounding strip detector consists of several layers of tracker inner barrel (TIB), tracker inner disk (TID), tracker outer barrel (TOB), and tracker endcap (TEC). Pairs of module lines in the strip detectors indicate double-sided stereo modules.

2.2.2 Electromagnetic calorimeter

In order to measure the energy of particles that interact electromagnetically, an ECAL has been built around the tracker. Particles can interact electromagnetically with a detector material in a few primary ways. They can interact with the atomic electrons of the detector material, causing excitation or ionisation; or they can be deflected or scattered by the nucleus, and may emit bremstrahlung photons in the process. In rarer situations, they might emit Cerenkov radiation, when they enter a material in which the speed of light is smaller than their incident speed; or produce transition radiation while crossing the boundary between different media.

The ECAL works on the principle of electromagnetic showering through bremstrahlung and pair production. Electrons and positrons having energy higher than a certain critical energy generate photons via bremsstrahlung, in the presence of a nucleus with high atomic number, which can then do pair production, and so on, forming a shower. Similarly, incident photons with a high enough energy can initiate pair production, and the resulting electron-positron pair can produce bremstrahlung photons, and so on. When the energy of the photons in the shower becomes smaller than the critical energy necessary for pair production, they are absorbed by the scintillating material, which emits scintillation light. The intensity of the light we get in the end is proportional to the energy of the incident particle; therefore, the energy of the incident particle can be deduced.

Certain characteristics of the stopping material are useful when we want to generate and detect these electromagnetic showers. We can, for instance, benefit from high density and atomic number of a material, short radiation length X_0, and small Molière radius R_M, which describes the spread of the shower in the transverse direction. The CMS ECAL is a homogeneous detector made primarily from lead tungstate ($\mathrm{PbWO_4}$) crystals. $\mathrm{PbWO_4}$ is transparent and has a density of 8.28 $\mathrm{g/cm^3}$, radiation length of 0.89 cm, and Molière radius of 2.2 cm [79]. Furthermore, $\mathrm{PbWO_4}$ has a scintillation decay time such that 80% of the light is emitted in 25 ns. These properties make $\mathrm{PbWO_4}$ a very attractive choice for ECAL absorbing and scintillating material.

The CMS ECAL consists of a central barrel (EB), and a forward endcap (EE) on either side of the interaction point. A cutaway view of the ECAL, and the layout and coverage of the barrel and endcap is shown in Figures 2.8 and 2.9, respectively. The EB consists of 61,200 $\mathrm{PbWO_4}$ crystals, arranged in the form of 36 supermodules. Each supermodule consists of four modules, and is made from 1700 crystals. The crystals have a tapered shape, with an area of $22 \times 22\ \mathrm{mm^2}$ at the front face, and $26 \times 26\ \mathrm{mm^2}$ at the rear face, and are mounted at a small angle (3°) with respect to the vector from the nominal interaction point, to avoid visible gaps. The length of the crystals, 230 mm, is 25.8 times the radiation length, and allows enough material to fully develop the electromagnetic shower. In total, the EB has a crystal volume of 8.14 $\mathrm{m^3}$ and a weight of 67.4 tonnes, and covers the pseudorapidity range $|\eta| < 1.479$. The blue-green scintillation light emitted by the crystals is absorbed using avalanche photodiodes (APDs).

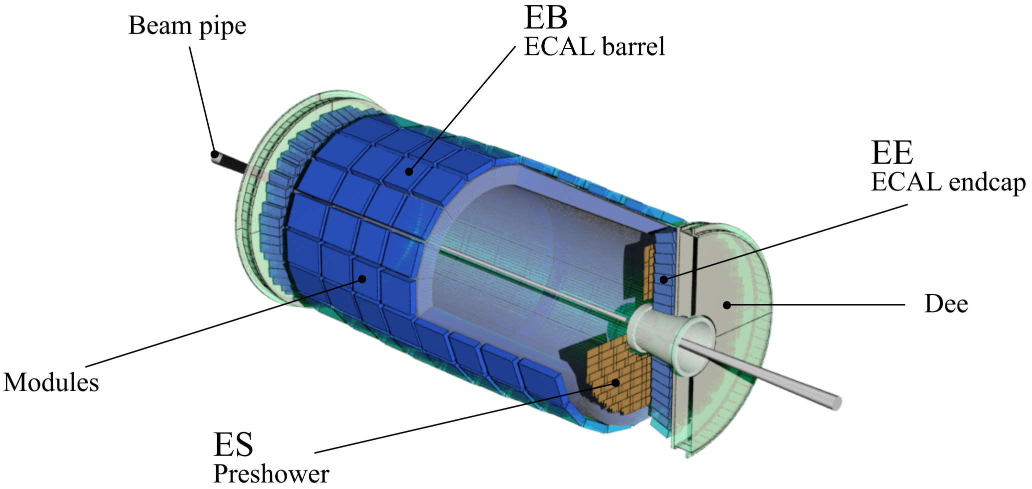

Figure 2.8: A cutaway view of the CMS ECAL. This figure has been rendered in 3ds Max [78], after adapting and modifying the original CMS model from Reference [75].

The EE consists of two halves, called Dees, on either side of the interaction point, each holding 3662 crystals. The EE crystals have a front face area of $28.62 \times 28.62\ \mathrm{mm^2}$ and a rear face area of $30 \times 30\ \mathrm{mm^2}$. The length of EE crystals, 220 mm, is 24.7 times the radiation length. In total, the EE crystals have a volume of 2.90 $\mathrm{m^3}$ and a weight of 24.0 tonnes, and cover the pseudorapidity range $1.479 < |\eta| < 3.0$. The absorption of scintillation light in EE is done using vacuum phototriodes (VPTs).

When a neutral pion decays into two photons, especially in the endcap region where the

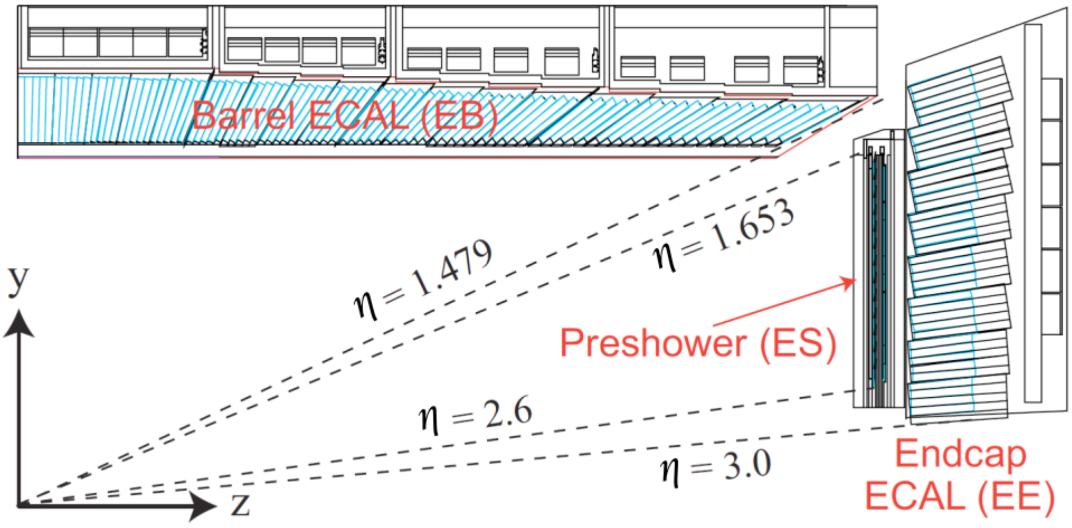

Figure 2.9: A schematic showing layout of the CMS ECAL in one quadrant. ECAL barrel (EB) supermodules cover up to pseudorapidity 1.479, from where the ECAL endcap (EE) extends to 3.0 in pseudorapidity. A preshower detector (ES) is placed in front of the endcap to help differentiate π^0 from γ. This figure is taken from Reference [80].

two photons are highly collinear, it can mimic a high-energy photon in the ECAL. In order to reduce this background, a 20 cm thick preshower (ES) is placed in front of the EE in the pseudorapidity range $1.653 < |\eta| < 2.6$. The ES is a two-layer sampling calorimeter, where each layer consists of lead radiators and silicon strip sensors, which measure the transverse development of the showers induced by the radiators. By looking at the strip sensor hits, when a high-energy photon seems to appear in the ECAL, it can be deduced if the signal was indeed a high-energy photon or a pair of photons from the decay of a neutral pion.

Since the energy measurement in ECAL depends directly on the number of detected photons, which is Poisson distributed, the energy resolution depends on $1/\sqrt{E}$. The statistical fluctuations in the showering process also follow this trend. However, there are other contributions as well. The electronic noise in the readout chain dictates a $1/E$ dependence, since the absolute uncertainty from this source is independent of energy of the incident particle. The resolution also has a constant contribution from instrumentation effects which becomes extremely relevant at higher energies, since the other terms start to become negligible. The combined resolution is the sum in quadrature of these contributions, and they are called stochastic, noise and constant term, respectively. The coefficients of these terms have been measured with electrons of energy 20–250 GeV [81], and thus, the resolution can be given as:

$$\frac{\sigma(E)}{E} = \frac{0.028\,\sqrt{\text{GeV}}}{\sqrt{E}} \oplus \frac{0.12\ \text{GeV}}{E} \oplus 0.003. \tag{2.7}$$

2.2.3 Hadron calorimeter

One important aspect of a high-energy detector, especially one operating at a hadron collider, is measurement of hadron energies. For this purpose, an HCAL has been set up in the CMS detector between the ECAL and the solenoid magnet. In analogy to the ECAL, the HCAL works on the principle of hadronic showering and jets, with the dominant interaction in the showers being the strong nuclear interaction. The HCAL also plays a significant role in the indirect detection of invisible particles, like neutrinos, which appear as "missing" momentum and energy when all other particles and jets are accounted for.

In analogy to the radiation length X_0 in ECAL, a nuclear interaction length λ_0 can be defined for hadronic interaction in a material. Nuclear interaction lengths are typically much larger than radiation lengths. Therefore, in order to have a full shower development, the HCAL is designed as a sampling calorimeter, with alternating layers of dense absorbing and scintillating materials. In the CMS HCAL, the absorbing layers are made from steel and brass. The brass used is composed of 70% copper and 30% zinc, and has a density of 8.53 $\mathrm{g/cm^3}$, radiation length of 1.49 cm, and interaction lenght of 16.42 cm [79]. The scintillating layers are composed of Kuraray SCSN81 plastic, which is chosen owing to its long-term stability and resistance against radiation damage.

The main structure of the HCAL comprises a central barrel (HB) and an endcap (HE) on either side of the interaction point. A cutaway view of the HCAL, and the layout of the barrel and endcap, along with additional forward and outer calorimeters, is shown in Figures 2.10 and 2.11, respectively.

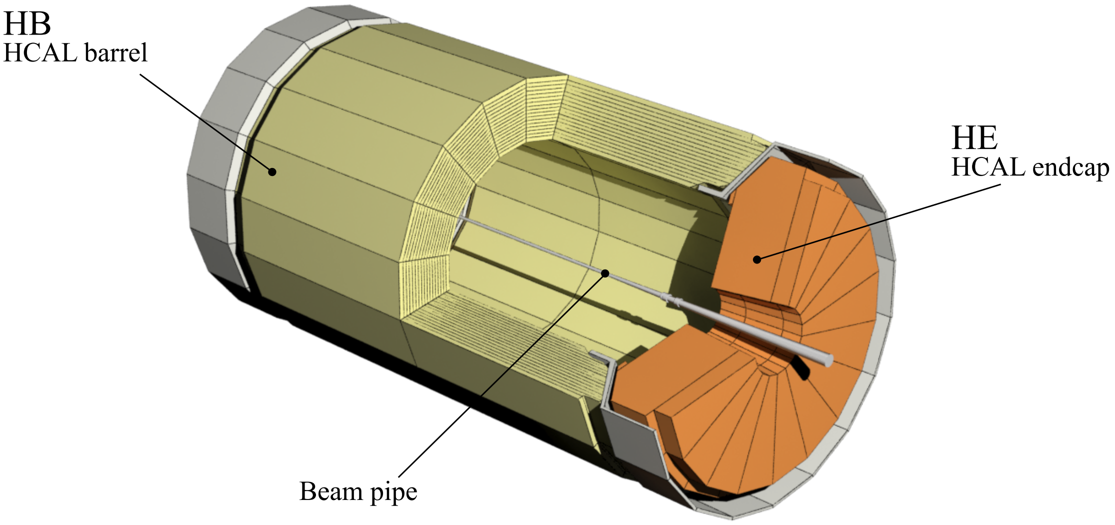

Figure 2.10: A cutaway view of the CMS HCAL inside the superconducting solenoid magnet. This figure has been rendered in 3ds Max [78], after adapting and modifying the original CMS model from Reference [75].

The HB consists of 36 azimuthal wedges, and cover a pseudorapidity range $|\eta| < 1.3$. The wedges are made from flat plates placed parallel to the beam axis. From inside to outside, the wedges contain a 40-mm-thick steel plate, 14 brass plates, eight 50.5 mm thick and six 56.5 mm thick, and a 75-mm-thick steel plate. In the centre, the HCAL offers an absorber

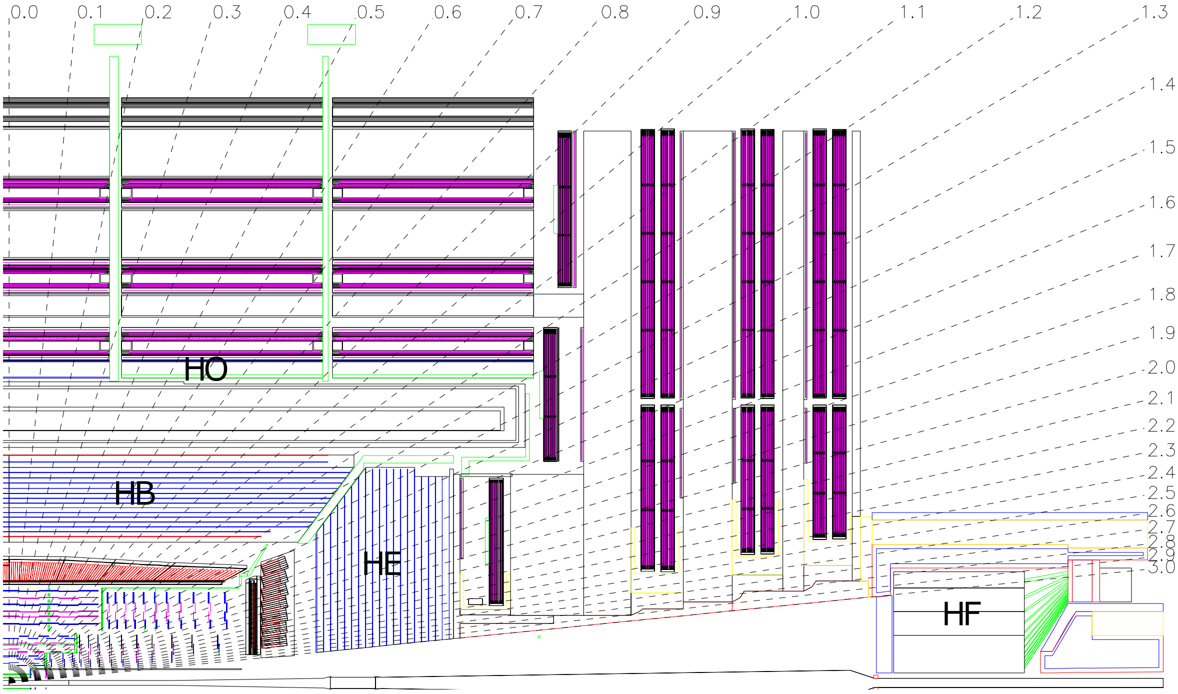

Figure 2.11: A schematic showing layout of the CMS HCAL in one quadrant. In addition to the HCAL barrel (HB) and HCAL endcap (HE), the HCAL is extended outside the solenoid magnet with a tail catcher HCAL outer (HO) calorimeter, to ensure adequate sampling depth. There is also an HCAL forward (HF) calorimeter in the very forward region, which has to endure enormous amounts of particle flux. This figure is taken from Reference [79].

thickness of 5.82 λ_0, while towards the sides, it increases with the reciprocal of the sine of the polar angle. The scintillators consist of 70,000 plastic tiles in total, from which light is collected using wavelength shifting (WLS) fibres, and taken to the readout electronics.

The HE consists of 79-mm-thick brass plates, with 9-mm gaps for the scintillators, and covers a pseudorapidity range $1.3 < |\eta| < 3.0$. This range includes 13.2% of the total solid angle, and contains about 34% of all the produced final state particles. The total length of the HE calorimeters is 10 λ_0.

In the central region, the sampling length of the HCAL is not adequate; therefore, the HCAL is complemented with an outer calorimeter (HO) outside the solenoid magnet. The HO also cleverly uses the solenoid coil as an absorber. The final absorber length after adding the HO is stretched to 11.8 λ_0.

In the very forward region of the detector, at a pseudorapidity range of $3 < |\eta| < 5$, a forward calorimeter (HF) is added to maintain hermeticity of the detector. The HF has to deal with extreme amounts of particles flux, seven to eight times on average as compared to the rest of the detector. Therefore, in order to be robust and endure the harsh environment, the HF is constructed as a Cerenkov detector, with quartz fibres as the active material.

Analogous to the ECAL, the HCAL energy resolution has been measured with pions of energy 20–300 GeV [82], and the resolution can be given as:

$$\frac{\sigma(E)}{E} = \frac{1.15\ \sqrt{\mathrm{GeV}}}{\sqrt{E}} \oplus 0.055. \tag{2.8}$$

2.2.4 Superconducting solenoid magnet

At the heart of the CMS detector, is the idea to bend charged particles using a magnetic field, and deduce their charge and momentum from the curvature. The magnetic field strength required for bending charged particles significantly, at typical LHC energies, is quite high. This is accomplished by a superconducting solenoid magnet. The solenoid is designed to generate up to 4 T magnetic fields, although it is nominally operated at 3.8 T, to ensure a longer lifetime. The field strength generated by the solenoid, as well as predicted field lines, are shown in Figure 2.12.

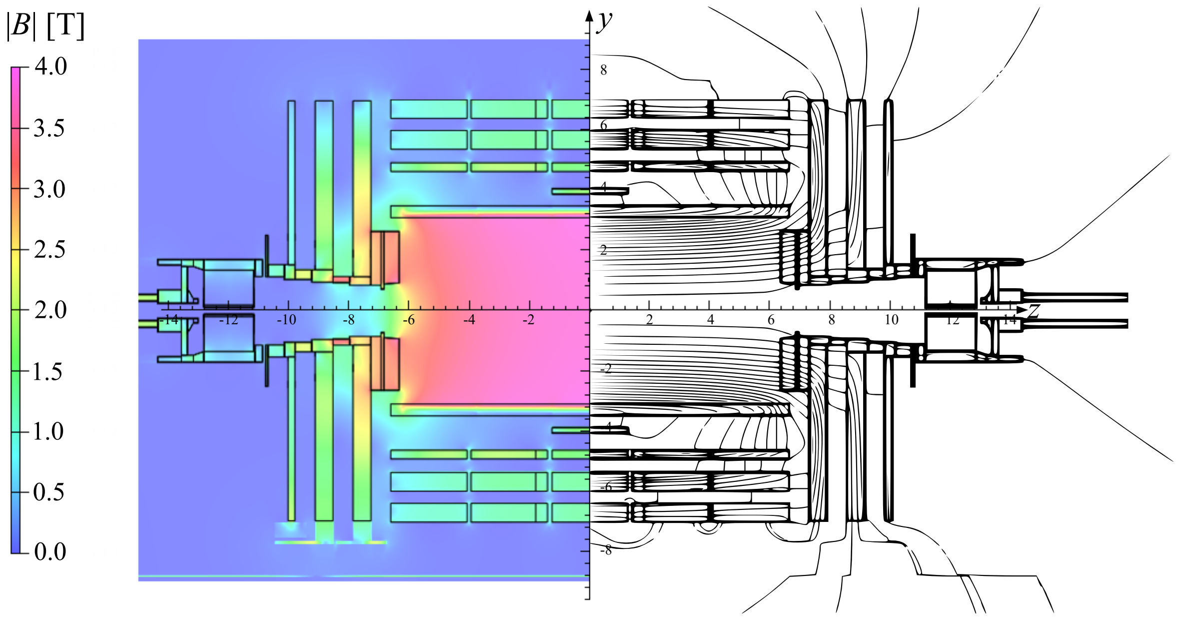

Figure 2.12: Value of magnetic field (left), and field lines (right), projected onto a longitudinal section of the CMS detector, at a central magnetic field of 3.8 T. Each field line shows an increment of 6 Wb in the magnetic flux. This figure is adapted from Reference [83].

The CMS solenoid is 12.5 m long and 6.3 m in diameter, and weighs 220 tonnes. The 4-layer winding is made from Ni-Ti Rutherford cables, co-extruded with pure aluminium, called insert, and an aluminium alloy is used for mechanical reinforcement. To achieve critical temperature for the Ni-Ti superconductor, the coil is operated at 4.5 K, using liquid helium. When operated at the nominal current of 19.14 kA, the coil stores 2.6 GJ of energy.

In order to guide magnetic field lines outside the solenoid, a 10,000-tonne iron return yoke is used. The length of the return yoke in the barrel is 13 m and the outer diameter is 14 m. It is composed of five barrel wheels, each having three layers, and three endcap disks on either side of the interaction point. This modular structure, and easy relative movement, allows an easy access to assemble the inner subdetectors.

2.2.5 Muon system

The above mentioned subdetectors measure and absorb all long-lived SM particles very efficiently, with the exception of muons and neutrinos. Muons are leptons having a mass almost 200 times that of the electron. For this reason, they are not retarded much via bremstrahlung in the ECAL, like electrons. Since they are leptons, they do not take part in strong interaction at all. This has the consequence that muons easily escape the inner detectors, and travel outside the solenoid magnet. In order to detect muons, an extensive muon detector system has been set up.

The muon system consists of various types of subdetectors, placed in an alternating fashion, within the spaces in between the iron return yoke. A longitudinal cross section showing layout of different subdetectors of the muon system, along with a couple of planned improvements for the future is shown in Figure 2.13.

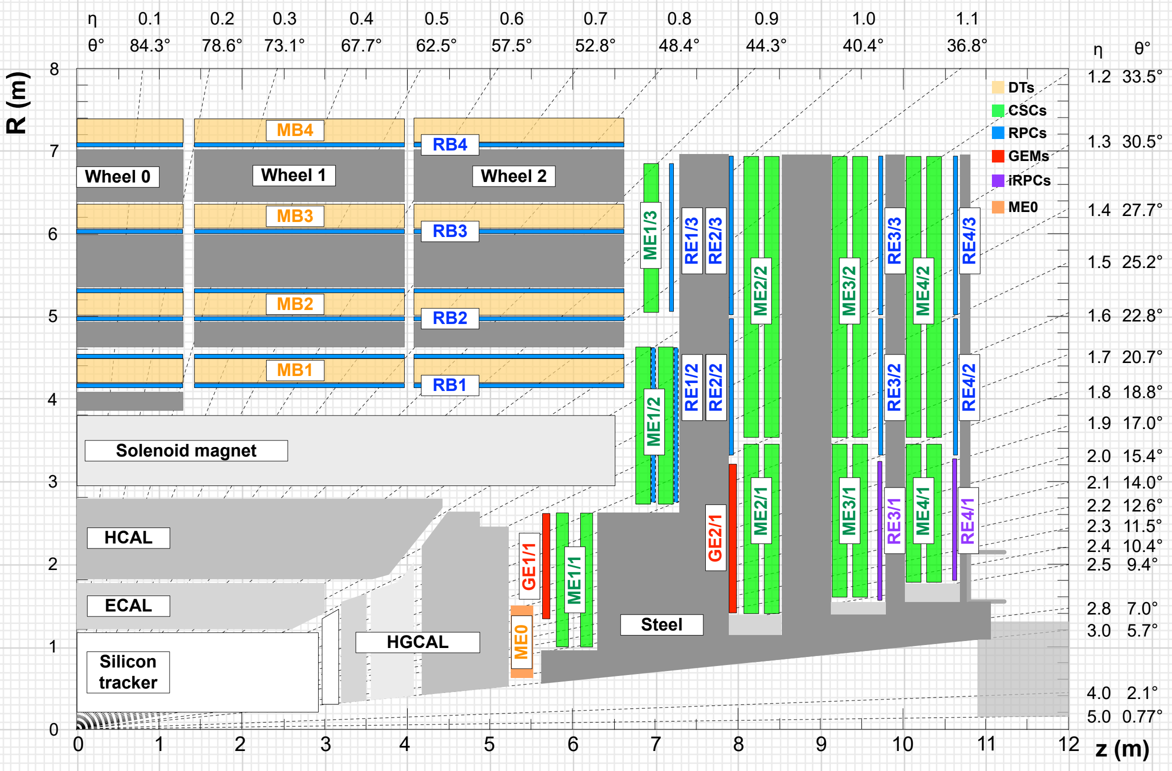

Figure 2.13: A longitudinal cross section showing layout of the current CMS muon system in one quadrant, as well as ongoing upgrades. The barrel consists of drift tubes (DTs or MB in CMS nomenclature, M for muon) and resistive plate chambers (RPCs/RB). The endcap consists of cathode strip chambers (CSCs/ME) and resistive plate chambers (RE). The dark gray area represents the return yoke. As of 2019, the subdetectors ME0, RE3/1, and RE4/1, as well as gaseous electron multipliers (GEMs/GE) are not yet installed, but planned for the so called Phase-2 upgrade for the high-luminosity LHC. This figure is taken from Reference [84].

The first type of detectors used in the muon system is drift tubes (DTs). Each DT consists of a 2.4-m-long wire, in the middle of a tube filled with a gas mixture of 85% argon and 15% carbon dioxide. The wire and alumunium strips along the walls of the tube act as electrodes, and a high voltage, 4800 V, is maintained across them. When a muon passes through the gas, it causes ionisation, and the resulting electrons and ions, while drifting towards the anode wire, trigger more ionisation, causing a Townsend avalanche, which is measured as a current in the wire. DTs are used in the barrel region, where the muon flux is relatively small, and the magnetic field is uniform and mostly contained in the return yoke.

The DTs cover a pseudurapidity region $|\eta| < 1.2$, and are structured in cylindrical layers, called stations (MB1–MB4; M for muon), in each of the five wheels of the muon system barrel. Each wheel is divided into 12 ϕ-sectors. The basic independent functioning unit of DTs is called a superlayer (SL), formed from four layers of rectangular drift cells. Two or three SLs are combined to form a DT chamber, which is installed in a specific wheel, station, and sector. In three-SL chambers, the inner and outer SL have wires parallel to the beam direction, and hence they can measure the ϕ-coordinate, while the middle SL has wires perpendicular to the beam direction, and it measures the z-coordinate. The DT chambers in the outer station do not have this z-measuring middle SL. Reconstructed hit resolutions of 200–300 μm in ϕ-SLs, and 400–1000 μm in θ-SLs was reported in 2016 [85].

In the endcap regions, a high flux of muons and a strong and irregular magnetic field warrant the use of cathode strip chambers (CSCs). CSCs are multiwire proportional chambers, and their principle of operation is similar to DTs, but they use an array of anode wires. The CMS CSCs consist of seven trapezoidal panels, which form six gas gaps. A thin layer of copper on the panels acts as the cathode and layers of anode wire arrays are placed in between the panels. The gas mixture used in CSCs comprises 50% carbon dioxide, 40% argon, and 10% carbon tetraflouride, and a chamber covers 10° or 20° in ϕ.

The CSCs cover pseudorapidity $0.9 < |\eta| < 2.4$, with the range $0.9 < |\eta| < 1.2$ overlapping with the barrel DTs. There are a total of 540 CSCs, arranged in the form of four endcap rings (ME1–ME4) on either side of the interaction point. The total area covered by active planes is about 5000 m^2, the total gas usage is more than 50 m^3, and the total number of wires is about 2 million. Mean spatial resolutions in the range 45–134 μm were reported in 2016, for the CSCs at different station and ring numbers [85].

In order to get a better time resolution, the DTs in the barrel and the CSCs in the endcaps are complemented with resistive plate chambers (RPCs). RPCs are gaseous parallel-plate detectors, with a double gap, operated in avalanche mode, having a central common strip picking up the sum of the signal from both gaps. This double gap mode allows RPCs to run at lower gas gains, and enhanced effective efficiency. The gas mixture used in RPCs consists of 95.2% freon ($C_2H_2F_4$), 4.5% isobutane (i-C_4H_{10}), and 0.3% sulphur hexafluoride (SF_6) [86], although efforts are being carried out to use environment friendly gas mixtures [87].

The RPCs cover a pseudurapidity range $|\eta| < 1.9$. In the barrel, they are arranged in four stations (RB1–RB4), with the first two stations each sandwitching one DT station, whilst the last two are only on the inner sides of DTs. In the endcaps, RPCs are arranged in four rings (RE1–RE4) on either side. RPCs give a time resolution of about 3 ns, which nicely complements the spatial resolutions from DTs and CSCs, and allows the input to be used for a muon trigger.

In addition to the above, several upgrades to the muon system are in progress, or planned for the high-luminosity LHC. These upgrades include addition of a couple of gaseous electron multiplier (GEM) detectors, a new station of CSCs next to the HCAL, and a new station of improved RPCs (iRPC) in rings 3 and 4 each.

2.2.6 Trigger system and data acquisition

The LHC is designed to collide protons at a centre-of-mass energy of 14 TeV and instantaneous luminosity of 10^{34} cm^{-2}s^{-1}. At this luminosity, an average number of 27 interactions were recorded per bunch crossing in 2016 [74], with a bunch crossing every 25 ns. This amounts to data being delivered by the CMS detector at a gigantic rate, and it is not practically possible to save and process all of this data. Keeping this in mind, an elaborate trigger system has been set up at CMS [88], to select potentially interesting events, and discard the rest. The CMS trigger is a two-tiered system, consisting of a Level 1 (L1) trigger and a high-level trigger (HLT). A simplified schematic of the CMS trigger and data acquisition system architecture is shown in Figure 2.14.

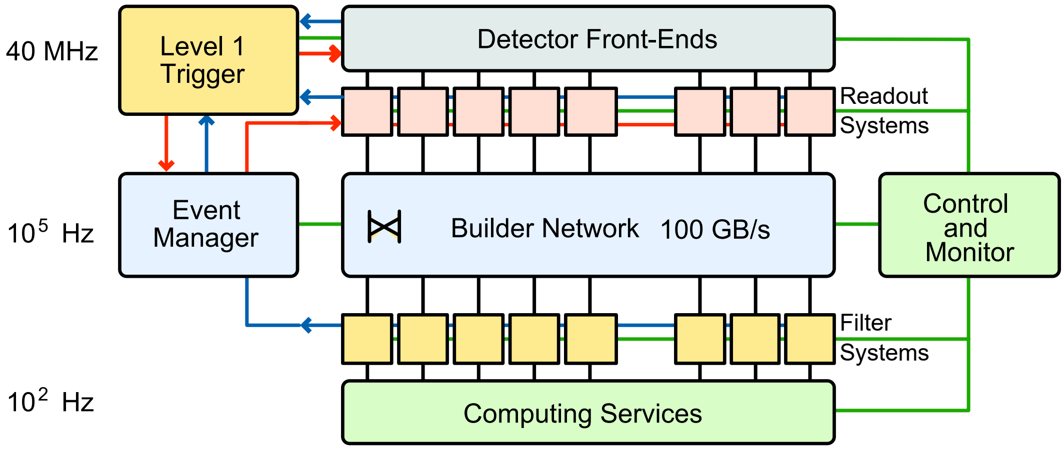

Figure 2.14: A simplified schematic of the CMS trigger and data acquistion system architecture. The L1 trigger reduces the data rate from the original 40 MHz to 100 kHz. The HLT reduces it further to 100 Hz in the original version, and 1 kHz in the currently operating system in Run 2. This figure is taken from Reference [89].

The L1 trigger is implemented using dedicated hardware — field programmable gate arrays (FPGA) and application specific integrated circuits (ASIC) — and gives a fix latency of 4 μs. The structure of the L1 trigger consists of a calorimetric trigger and a muon trigger, which process trigger primitives (TP) from the calorimeters and muon detectors, respectively., in several steps. The calorimeter trigger consists of a regional calorimetric trigger (RCT), which receives energy and quality flags from ECAL and HCAL, and a global calorimetric trigger (GCT) which processes this information further. The muon trigger also consists of a global muon trigger (GMT) which is fed information from RPC pattern comparator, as well as DT and CSC track finders. Information from GCT and GMT is fed into a global L1 trigger (GT) which implements a trigger menu, a set of requirements for HLT algorithms.

The L1 trigger reduces the original data rate of 40 MHz to 100 kHz.

The HLT is implemented in software and runs on a farm of computers. Its implementation is based of the concept of HLT paths, which apply predefined algorithms in a specific order, and perform a rough prompt reconstruction of physics objects, followed by application of selection requirements on these objects The HLT reduces the data rate from 100 kHz to 1 kHz.

In order to make full use of the available resources, the concepts of data parking and data scouting [90] have gained popularity in recent years. Data parking refers to the idea of collecting and storing additional raw data, generally with looser trigger requirements, for reconstruction when data-taking runs have finished, or the resources are free otherwise. Data scouting applies a special strategy, recording limited information of the data that can normally not be recorded on tape due to trigger rate constraints. This limited information can then be used in simple analyses, and if something interesting is found, trigger menus can be changed to look into similar data in more detail in the future.

2.2.7 Computing infrastructure

The data collected by the data acquisition system has to be stored, and processed afterwards. The amount of data, even after reducing it by orders of magnitude using triggers, is still enormous, and impossible for CERN to handle alone. Keeping this in mind, a distributed computing infrastructure has been set up with nodes all around the globe. This computing infrastructure, called Worldwide LHC Computing Grid (WLCG) [91,92], is common to all LHC experiments, to maximise efficiency in resource usage. The WLCG has a tiered structure with four levels. A schematic representation of the WLCG is shown in Figure 2.15.

The CERN computing framework acts as a central Tier-0 (T0). The workflow of data at the T0 site includes acquiring raw data from data acquisition systems of experiments, archiving the raw data to magnetic tapes, distributing a copy to Tier-1 (T1) sites, performing a prompt calibration followed by a first pass prompt reconstruction, and distributing the reconstructed datasets to T1 sites. This distribution of raw and reconstructed data to T1 sites is performed on a 10 Gb/s dedicated optical fibre network, called LHC Optical Private Network (LHCOPN) [93].

T1 consists of 13 sites, located at large national centres. The functions of T1 sites include receiving and archiving a copy of raw data from T0, providing substantial computing resources for reconstruction, calibration, and extraction of data, storing the reconstructed data, and distributing it securely to Tier-2 (T2) sites.

There are around 160 T2 sites in WLCG, and they are generally located in universities and research centres. T2 sites have ample computing resources, but do not have a lot of storage capability. Their purpose is, therefore, to provide computational resources for grid-based analysis as well as generation of simulated event datasets. In addition to the above tiers, additional local and cloud resources can be added as Tier-3 (T3) to enchance the capabilities of the WLCG.

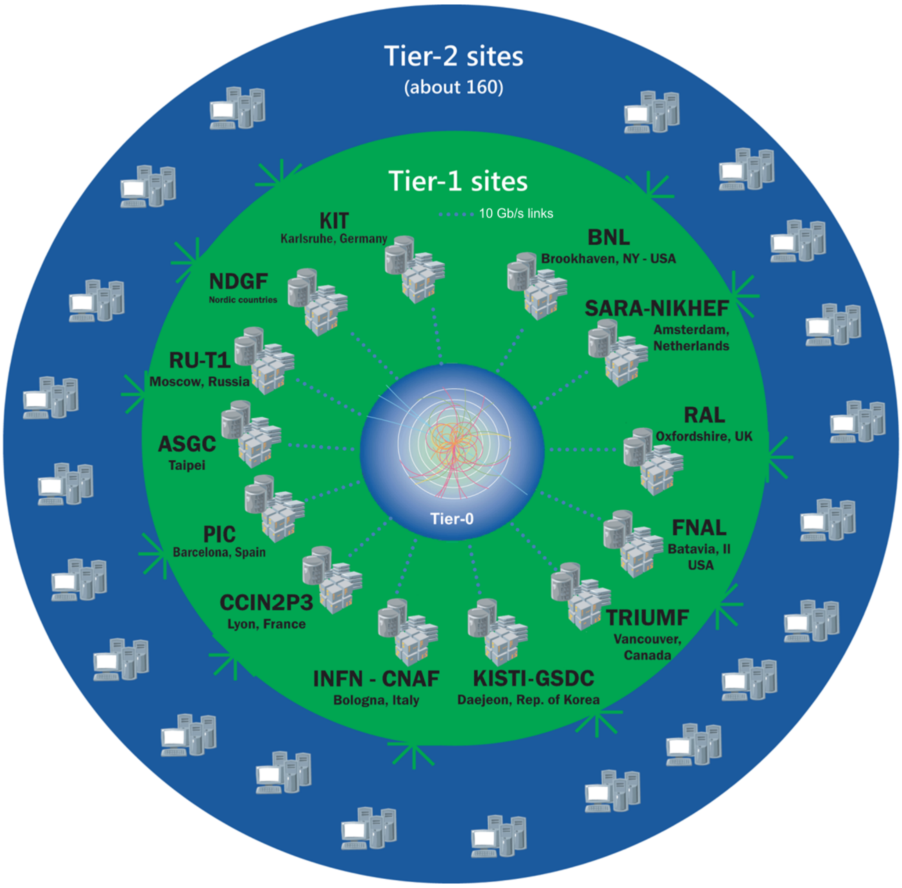

Figure 2.15: A representation of the distributed computing infrastructure used by the CMS experiment. The infrastructure is part of the Worldwide LHC Computing Grid (WLCG), which has a tiered structure. The CERN computing site acts as a central Tier-0, while Tier-1 is comprised 13 dedicated sites in different countries. Tier-2 is made up of nearly 160 sites all around the globe, and further local cloud resources can be added as Tier-3 sites. This figure is taken from Reference [92].

Similarly, many a young man, hearing for the first time of the refraction of stellar light, has thought that doubt was cast on the whole of astronomy, whereas nothing is required but an easily effected and unimportant correction to put everything right again.

……

— Ernst Mach

3

CMS tracker alignment

A hundred thousand corrections —

This chapter discusses offline alignment of the CMS tracker, and explains the techniques used to execute such an alignment. Performance of the alignment conditions derived for data recorded in 2016, 2017, and 2018 is presented, comparing the accuracy of alignments carried out for reconstruction during data taking, at the end of each year, and legacy reprocessing.

As discussed in Chapter 2, at the heart of the CMS detector, is the idea of bending moving charged particles using a magnetic field, and recording their tracks in order to deduce their charge and momentum. According to design specifications, a resolution of 1.5% should be achieved on the transverse momentum p_T for 100 GeV muons. Such p_T resolutions require that the resolution of recorded hit positions when a charged particle passes through the layers of the tracker be accordingly small. This hit-position resolution depends on the intrinsic resolution of the sensors, as well as precise knowledge about geometrical properties of the modules composing the tracker. These geometrical properties may in general be different from the design values, owing to limited mounting precision, effects of strong magnetic field, and so on. A complete set of parameters specifying the geometry of all the tracker modules is referred to as tracker geometry. Tracker geometry is one of the most important inputs to track reconstructrion, and misalignment in tracker geometry can potentially spoil an otherwise good hit-position resolution.

Reconstructed tracks are used in the CMS experiment to calculate momenta of charged particles, identify unwanted particles not coming from the desired primary interaction — called pileup — and form composite objects — called jets — made up of closely related tracks originating from the decay of the same particle. These concepts are discussed in detail in Chapter 4. Most, if not all, physics analyses performed at the CMS experiment are therefore dependent on good track reconstruction, and it is imperative that tracker geometry is aligned precisely. The analysis presented in this thesis also depends heavily on tracks, and tracker alignment is a crucial ingredient to this analysis. The author was involved deeply with the CMS tracker alignment group contributing to several campaigns, including alignments for reconstruction during data taking, at the end of data-taking years, and legacy reprocessing, all of which will be discussed in the following sections.

Owing to the high amount of precision required and limited accessibility inside the CMS detector, physical alignment of the tracker modules is not practically possible. Tracker geometry is therefore determined using a track based alignment procedure [94], and this knowledge is used during reconstruction.

3.1 Track based alignment

In order to understand possible misalignments of the modules in the CMS tracker, let's start by considering a toy tracker, consisting of four one-dimensional layers, as shown in Figure 3.1. In the ideal case, the layers are perfectly aligned, and the track hit positions are accurately known. However, the tracker can be misaligned, and the position, orientation, and shape of one or more layers might be different from the ideal case. Since we do not know these differences a priori, it is impossible to correct for them in advance.

In the CMS tracker, the modules can have three translational shifts, denoted by u, v, and w, and three rotations, denoted by α, β, and γ. In addition, the shape of modules might deviate from the ideal planar surface because of stress after mounting, or single-sided silicon processing. In order to encode deformations in shape, (modified) Legendre polynomials are used to model the shape of sensors, and three additional alignment parameters are added. There are hence nine alignment parameters per sensor, and multiplying this by the number of sensors gives 200,000 alignment parameters in total. The determination of such a large number of parameters requires a large amount of information.

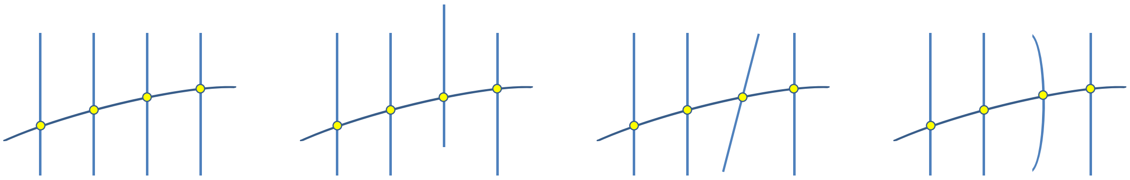

Figure 3.1: A schematic showing possible misalignment scenarios for a simple toy tracker, consisting of four layers. An ideal tracker, with no misalignments, is shown on the left, while trackers with translational, rotational, and shape misalignments are shown on the left-middle, right-middle, and right, respectively.

The idea of track based alignment is to calculate track-hit residuals, as shown in Figure 3.2, and form a χ^2 over many tracks:

$$\chi^2(\mathbf{p},\mathbf{q}) = \sum_j^{\text{tracks}} \sum_i^{\text{hits}} \left(\frac{m_{ij} - f_{ij}(\mathbf{p},\mathbf{q}_j)}{\sigma_{ij}} \right)^2 , \tag{3.1}$$

where $\mathbf{p}$ is the set of alignment parameters that we want to determine, $\mathbf{q}_j$ is the set of parameters describing the j-th track, m_{ij} and f_{ij} are the measured and predicted hit-positions, respectively, and σ_{ij} is the corresponding uncertainty. Forming $\chi^2(\mathbf{p},\mathbf{q})$ over a significantly large number of tracks, and minimising it can determine the sought-after alignment parameters.

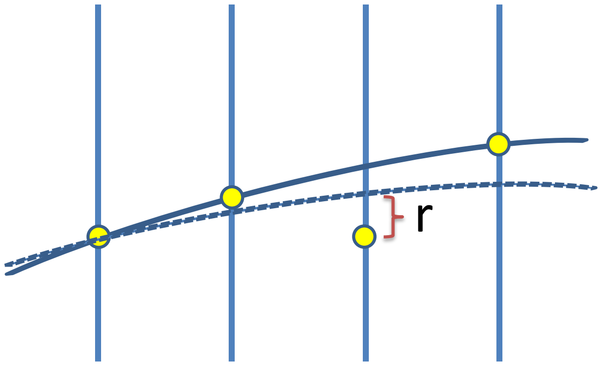

Figure 3.2: A schematic showing calculation of track-hit residuals in the misaligned toy tracker of Figure 3.1 (left-middle). The yellow circles indicate physical hit positions, whilst the solid and dashed curves represent the actual and reconstructed tracks, respectively. Track-hit residuals are calculated as the distance between the physical hit positions and the hit positions predicted by the reconstructed track.

In order to perform a full determination of alignment parameters, information from tens of millions of tracks is required. Therefore, datasets with a large number of tracks are typically used for alignment. Computationally, the problem is linearised, assuming the alignment corrections to be small, and transformed into a system of linear equations. This system is solved using the MILLEPEDE II algorithm [95], which utilises block matrix algebra to benefit from the special structure of the matrices involved. In order to further optimise computational performance, the MILLEPEDE II algorithm proceeds in two steps. Firstly, residuals are calculated for all tracks and the relevant module hits, inside the CMS software framework [96]; this step can be performed in parallel for different tracks. In the second step, these residuals are combined and the minimisation is performed in an experiment-independent program.

Different hierarchical levels of granularity can be selected while performing alignment of the CMS tracker with the MILLEPEDE II algorithm. A high-level alignment only tries to align positions and orientations of the high-level structures, such as half-barrels of the strip tracker and BPIX layers, and FPIX half disks. A module-level alignment, on the other hand, aligns all modules and sensors in addition to the high-level structures. A module-level alignment is much more accurate than a high-level alignment, but executes quite slowly compared to the latter. There is also an intermediate level, called ladder-blade-level, in which the modules are assumed to be fixed, whilst the ladders and blades on which the modules are mounted are aligned, in addition to the high-level structures.

3.1.1 Weak modes

There are certain coherent distortions of the tracker geometry which leave the χ^2 invariant, or almost invariant, in an alignment. This can happen if the change in alignment parameters, $\Delta\mathbf{p}$, is compensated by a change in track parameters, $\Delta\mathbf{q}_j$. These distortions are called weak modes for the alignment. Since geometries transformed by weak modes have the same χ^2, it is hard to identify and remove them via a standard minimisation of χ^2. Weak modes introduce biases in the track model, which may contribute significantly to the systematic uncertainty of kinematic properties derived from the reconstruction of the track.

The most trivial example of a weak mode is a translation of the whole tracker. If tracks were reconstructed under the (rather silly) assumption that the tracker was moved to Paris, without any relative movement between the modules, the residuals would remain unchanged, leaving the χ^2 invariant. Other systematic deformations, which may act as weak modes for an alignment, are shown in Figure 3.3. Owing to the cylindrical symmetry of the tracker, these systematic deformations can be expressed by module displacements Δr, Δz, and $\Delta\phi$ as functions of the coordinates r, z, and ϕ.

Weak modes can be mitigated by including additional constraints and special datasets in the MILLEPEDE II algorithm. One of these is the use of cosmic ray tracks, that break the cylindrical symmetry and help remedy the telescope, layer rotation, elliptical, skew, and sagitta weak modes, shown in Figure 3.3. Straight tracks, recorded with the magnetic field turned off, can be utilised. Other constraints include information about the vertex from which the tracks originated, and knowledge about the invariant mass of the particle whose decay products are recorded as tracks. As a typical example, datasets with events where Z bosons decay into $\mu^+\mu^-$ pairs are employed, and the invariant mass of the Z boson is used as a constraint, to diminish the effect of the twist weak mode, shown in Figure 3.3.

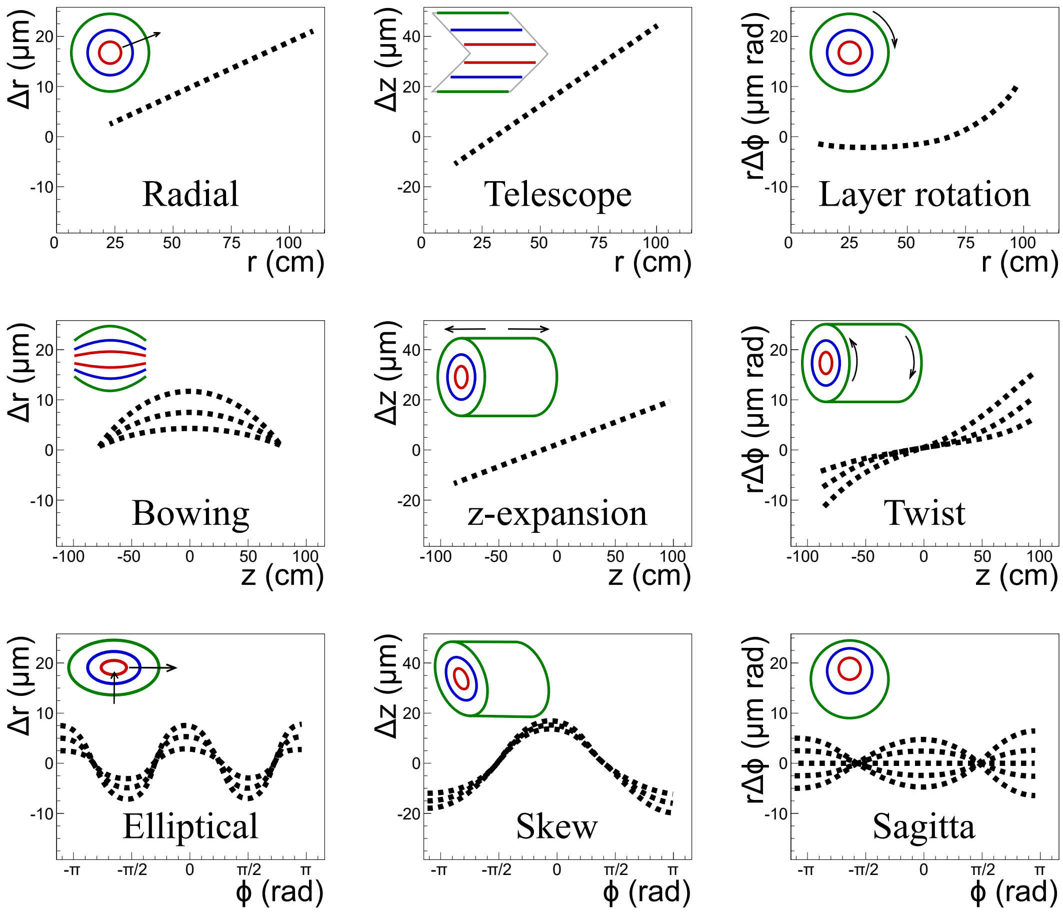

Figure 3.3: Systematic first-order deformations which may act as weak modes for an alignment. Weak modes leave the χ^2 invariant, and are therefore hard to detect. They can be remedied by using special datasets and additional constraints during alignment.

3.2 Alignment performance during Run 2

During Run 2 of the LHC operation, the CMS tracker was aligned regularly, with varying levels of granularity and complexity, depending on the amount of available time and resources. The most frequently executed alignment is a high-level alignment of the pixel tracker — in an automated framework called prompt calibration loop (PCL) [97] — which is performed while collision events are being recorded. Better alignments are required after mechanical movement of modules, or changes in tracker pixel calibration. At the end of each data-taking year, a more detailed alignment was carried out for re-reconstruction of recorded events. At the end of Run 2 in 2018, the CMS experiment started a campaign for legacy reprocessing of datasets compiled during Run 2. For this purpose, an improved alignment was performed for data recorded during 2016, 2017, and 2018, building on the complexity of the end-of-year alignments.

In order to assess the performance of an alignment, various validation techniques are used. Some of these validation techniques, along with performance of Run 2 alignments carried out for reconstruction during data taking, at the end of each data-taking year, and legacy reprocessing, are discussed in the following sections. The author was part of the effort to investigate the performance of Run 2 alignments, and most of the results presented in the following sections are publicly available in Reference [98].

3.2.1 Geometry comparison

A comparison between tracker geometries before and after alignment can give useful information about how the geometry changed, following an alignment. As an example, differences between module positions after legacy reprocessing alignment and alignment during data taking, as functions of the coordinates r, z, and ϕ, are shown in Figure 3.4. Erratic spread of points indicates random misalignments between the two geometries, whilst patterns in the distributions of differences, like the modulations visible in the ϕ-distributions, might indicate weak modes that have been remedied in the legacy reprocessing alignment.

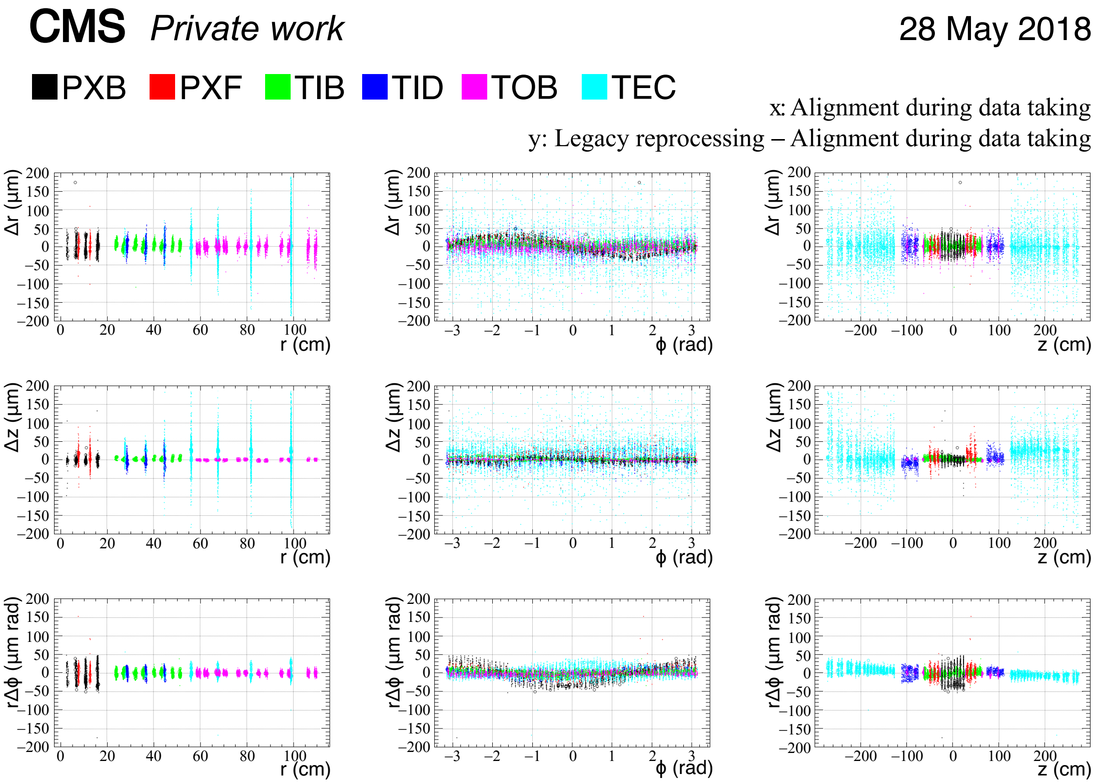

Figure 3.4: Comparison of tracker geometries, derived for reconstruction during data taking and legacy reprocessing, for 28 May 2018. Each point represents a module, and the colours correspond to different subdetectors. General spread of the points indicates random misalignments between the two geometries, whilst correlated patterns, like the modulations visible in the ϕ-distributions, may hint towards weak modes that have been fixed in the legacy reprocessing alignment.

3.2.2 Distribution of the median of the residuals (DMR)

Since the Millepede II algorithm minimises a χ^2 formed from the residuals, the precision and accuracy of an alignment can be assessed by utilising information from residuals calculated for tracks not used in alignment. Residuals are calculated over millions of tracks, and for each module, the median of the residuals is chosen. Measures of goodness of the alignment can be derived from the distribution of these medians over all the modules. As an example, the distribution of the median of the residuals for alignments during data taking, end-of-year re-reconstruction, and legacy reprocessing, on a day in summer 2017, is shown in Figure 3.5. A narrow distribution peaking at zero indicates a good alignment, and the distributions clearly indicate better performance of the legacy reprocessing alignment, especially in pixel subdetectors, which are more sensitive to changes in external conditions.

Evolution of the mean value of the DMRs μ, and the difference in mean values for the modules with electric field pointing radially inwards or outwards $\Delta\mu$, during Run 2 of the LHC, is shown in Figure 3.6. μ is an index of accuracy of the alignment, whilst $\Delta\mu$ is an index of goodness in recovering Lorentz angle effects. The trends clearly indicate the improved accuracy and stability of the legacy reprocessing alignment compared to alignments during data taking and end-of-year re-reconstruction.

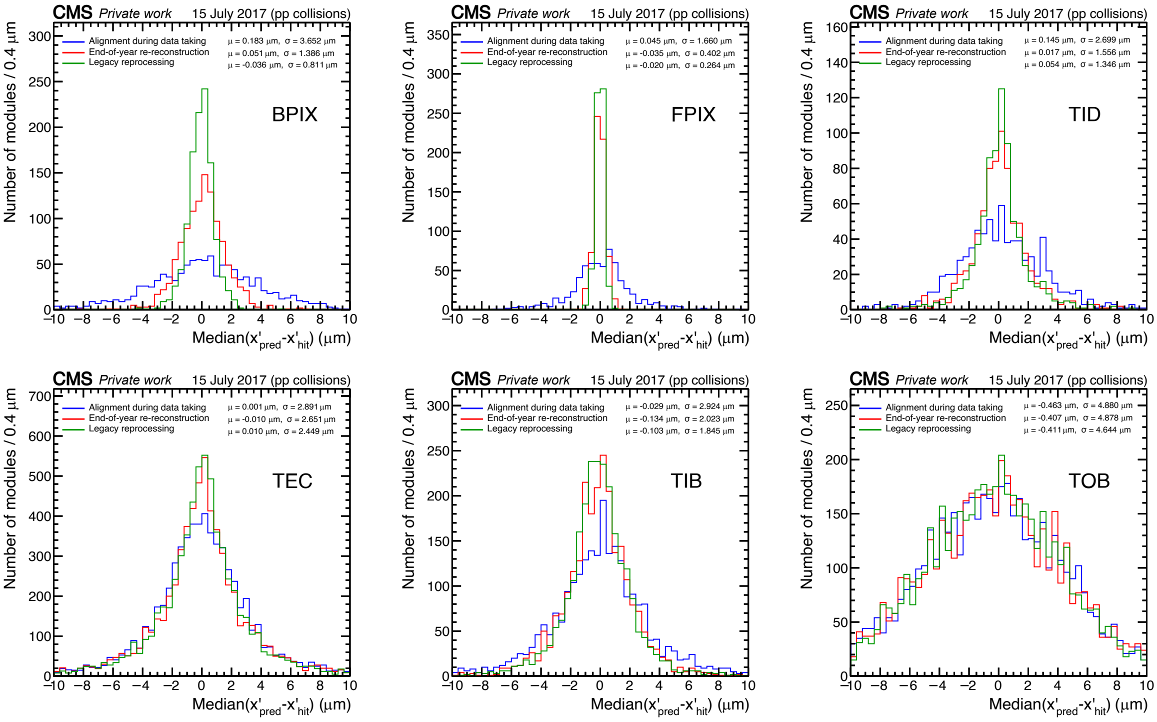

Figure 3.5: Distribution of the median of the residuals, as a function of the local x-coordinate, for the tracker subdetectors, during 15 July 2017. The blue, red, and green distributions correspond to alignments for data taking, end-of-year re-reconstruction, and legacy reprocessing, respectively. A Gaussian is fitted to the distributions, and the means μ and standard deviations σ are quoted in the legend. The distributions demonstrate the improvement of legacy reprocessing alignment compared to alignments during data taking and end-of-year re-reconstruction.

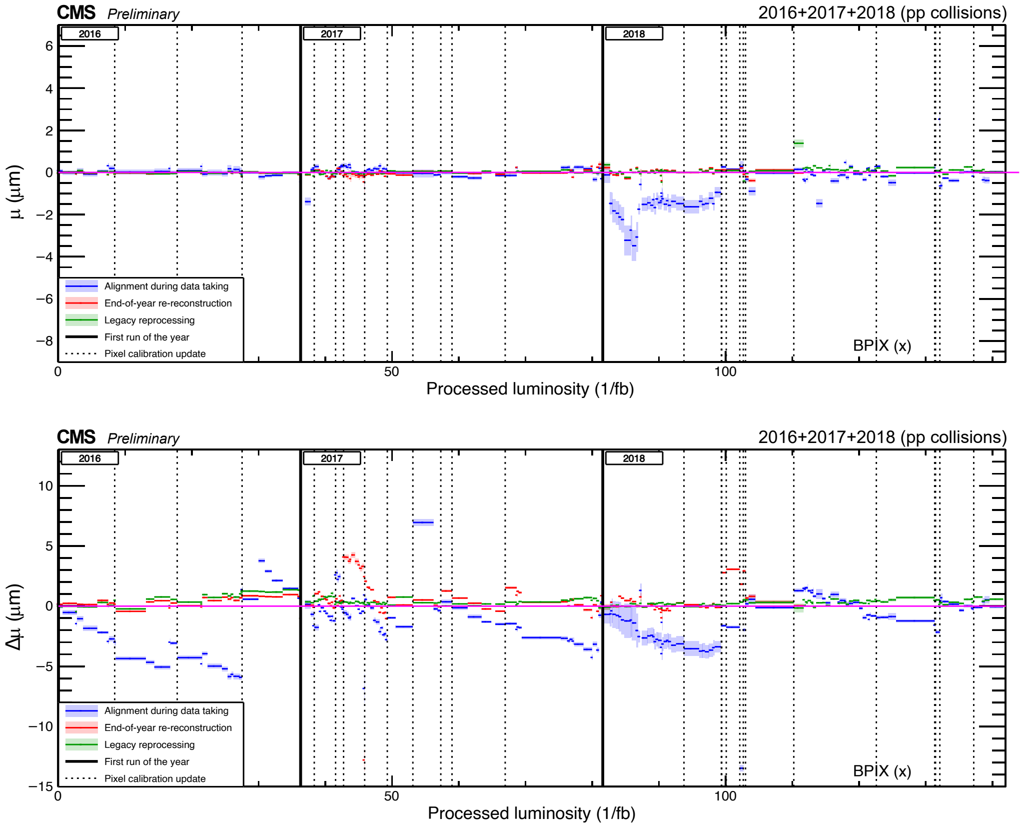

Figure 3.6: Evolution of the mean value of the DMRs (top), and the difference in mean values for the modules with electric field pointing radially inwards or outwards (bottom), with processed luminosity. The blue, red, and green trends correspond to alignments for data taking, end-of-year re-reconstruction, and legacy reprocessing, respectively. The solid vertical lines indicate the start of a new data-taking year, whilst the dotted vertical lines represent changes in pixel calibration conditions. The trends demonstrate the improved accuracy for legacy reprocessing alignment compared to the other alignments. This figure is publicly available in Reference [98].

3.2.3 Primary vertices validation

In the primary vertices validation method, a track is selected, and the primary vertex is reconstructed after removing this track. The impact parameter of the selected track is then calculated with respect to the newly reconstructed primary vertex. This is done for all tracks, and the means of the impact parameters in the transverse plane d_{xy}, and in the longitudinal direction d_z are recorded in bins of the track azimuth ϕ and pseudorapidity η.

Mean track-vertex impact parameter for alignments during data taking, end-of-year re-reconstruction, and legacy reprocessing, averaged over all data-taking cycles in Run 2, after scaling by the corresponding luminosity is presented in Figure 3.7, whilst Figures 3.8, 3.9, and 3.10 show comparison between impact parameters during different years for each alignment. Evolution of the RMS of the average impact parameter, during Run 2 of the LHC operation, is demonstrated in Figure 3.11.

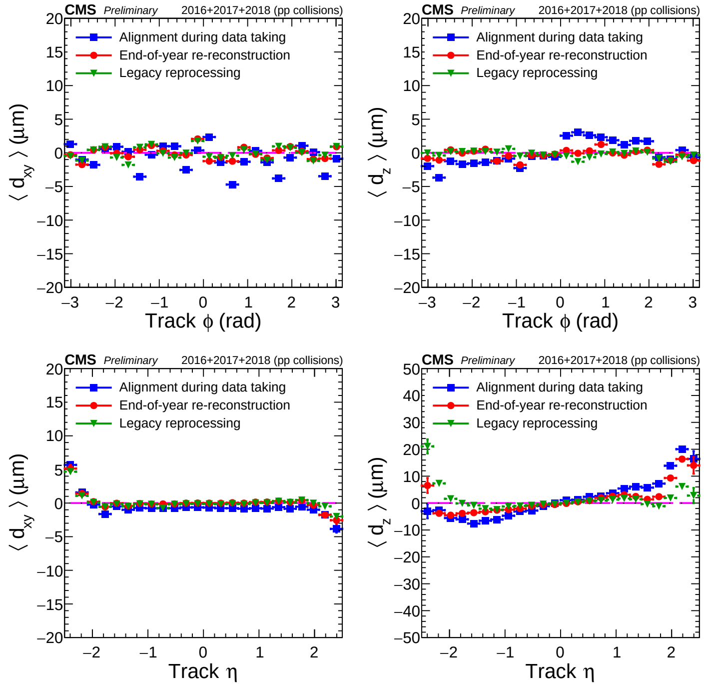

Figure 3.7: Mean track-vertex impact parameter, averaged over all data-taking cycles in Run 2, after scaling by the corresponding luminosity. Modulations visible in the alignments for data taking and end-of-year re-reconstruction are improved by legacy reprocessing alignment. This figure is publicly available in Reference [98].

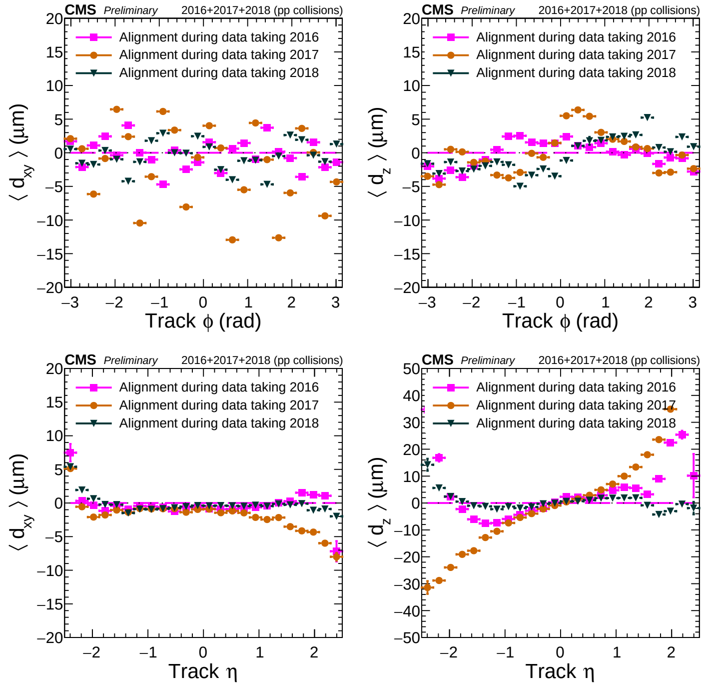

Figure 3.8: Mean impact parameter for alignment during data taking, split into the three years. Tracking performance during 2017 is particularly deficient owing to the commissioning period of the new pixel tracker [77]. This figure is publicly available in Reference [98].

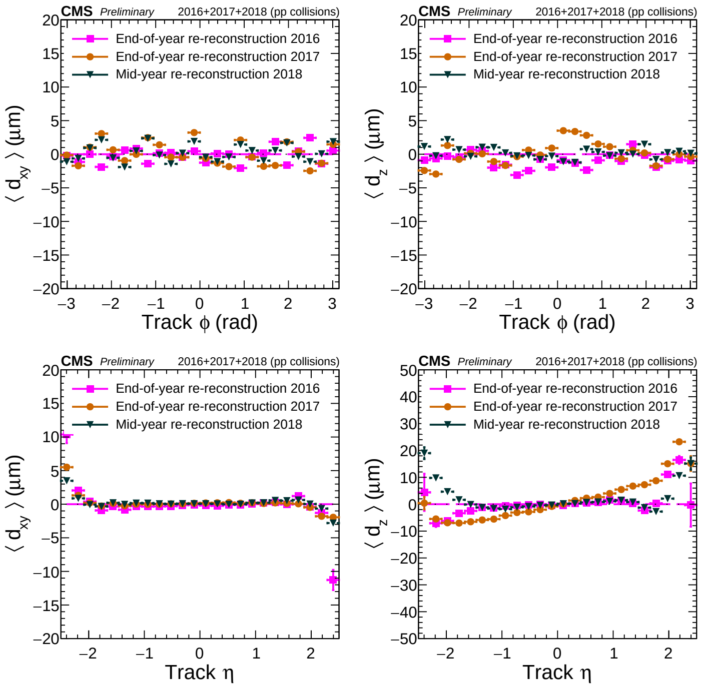

Figure 3.9: Mean impact parameter for end-of-year re-reconstruction alignment, split into 2016, 2017, and 2018. Tracking performance during 2017 is particularly deficient owing to the commissioning period of the new pixel tracker [77]. This figure is publicly available in Reference [98].

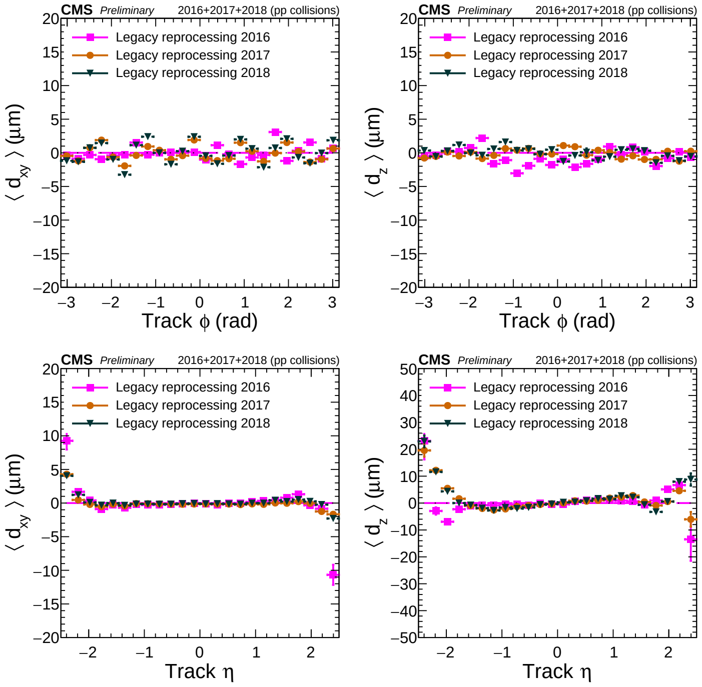

Figure 3.10: Mean impact parameter for legacy reprocessing alignment, split into 2016, 2017, and 2018. Radiation effects in the high pseudorapidity region cannot be fully fixed by alignment. Therefore, there are deviations from the ideal case value of zero. This figure is publicly available in Reference [98].

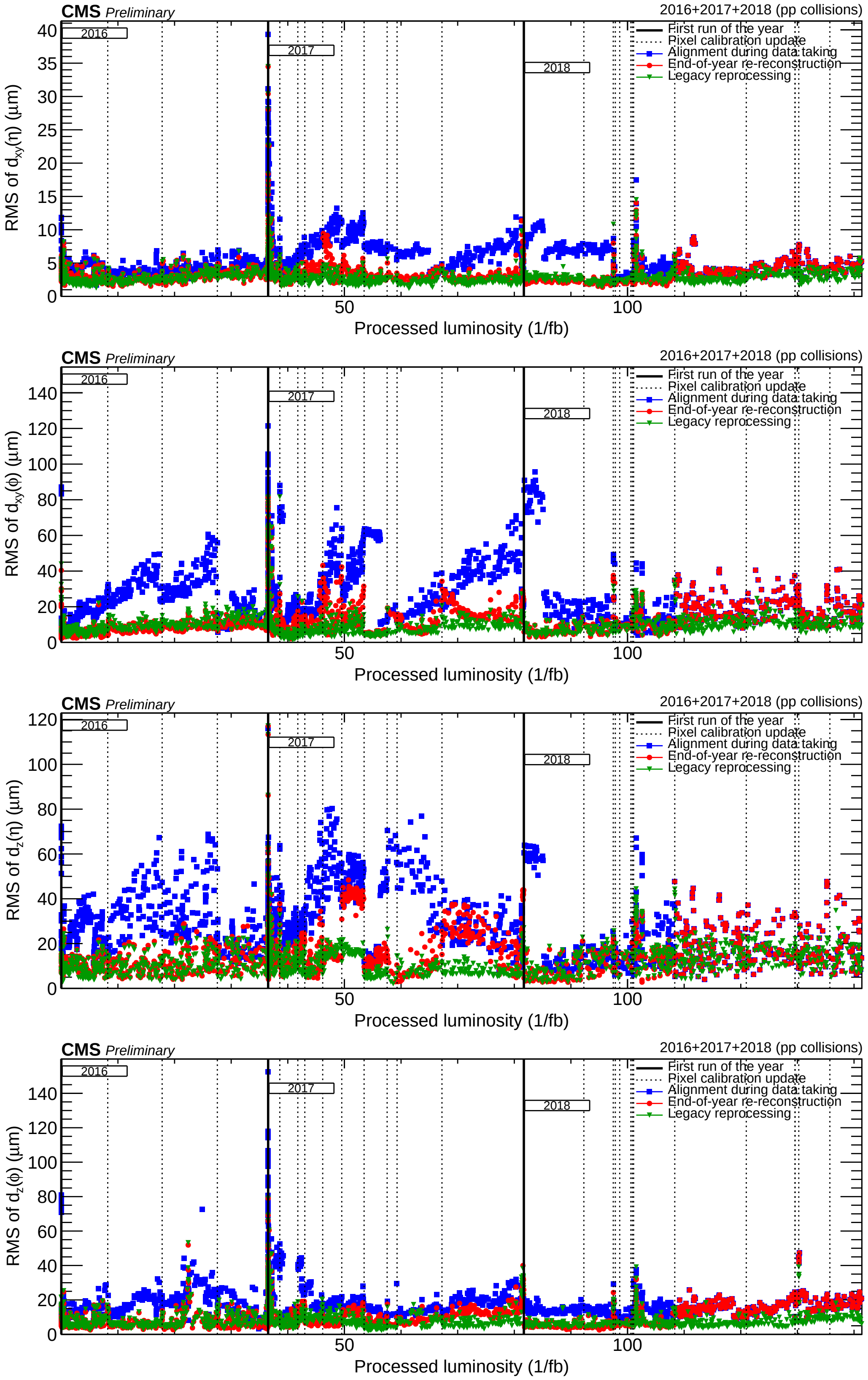

Figure 3.11: Evolution of the RMS of the average impact parameter. The RMS values are significantly lower for legacy reprocessing alignment than the other alignments. Sub-optimal tracking performance, during the commisioning of the new pixel tracker [77], is visible at the start of 2017. This figure is publicly available in Reference [98].

3.2.4 $Z \rightarrow \mu^+\mu^-$ validation

Reconstructing a Z boson using a pair of muon tracks, and studying the reconstructed mass as a function of kinematic variables can give useful infomation about weak modes. Visible modulations in the mean Z boson mass as a function of the angular variables of the muon tracks typically indicate the presence of a twist weak mode. The mean reconstructed Z boson mass for alignments during data taking, end-of-year re-reconstruction, and legacy reprocessing, as a function of various angular variables is shown in Figure 3.12. Uniformity in the reconstructed Z boson mass is improved in the legacy reprocessing alignment compared to the other alignments, indicating mitigation of the twist weak mode.

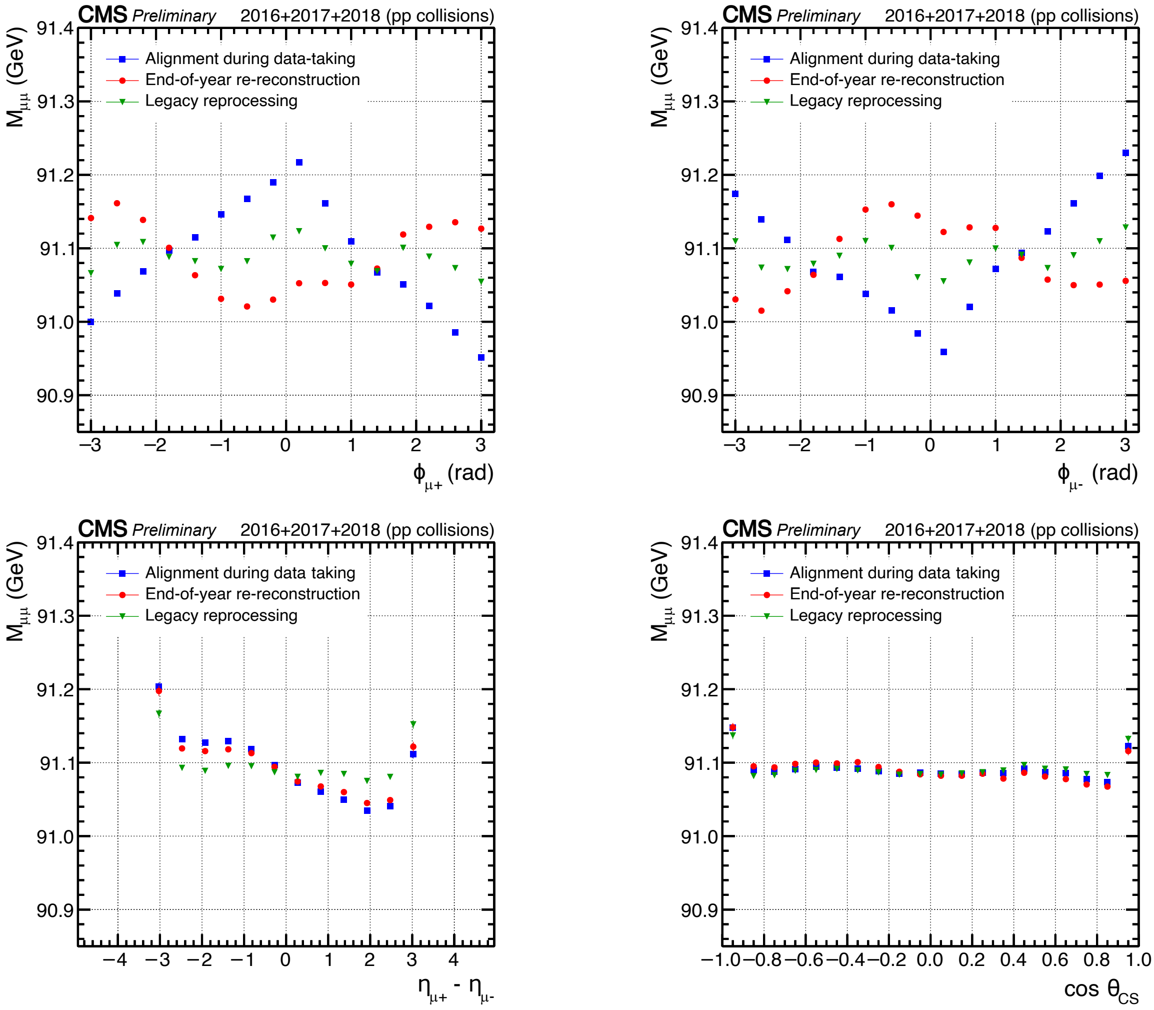

Figure 3.12: Mean reconstructed Z boson mass, in $\mu^+\mu^-$ events, as a function of: the azimuthal angle ϕ of the positively charged muon (top-left) and the negatively charged muon (top-right), the difference in pseudorapidity of the positively and negatively charged muons (bottom-left), and the angle $\cos(\theta_{CS})$ in the Collins-Soper frame of the reconstructed Z boson (bottom-right). Uniformity in the reconstructed Z boson mass is improved in the legacy reprocessing alignment as compared to alignments for data taking and end-of-year re-reconstruction. This figure is publicly available in Reference [98].

Reality is merely an illusion, albeit a very persistent one.

……

– Albert Einstein

4

Event simulation, reconstruction, and boosted topology techniques

A simulation of reality —

This chapter elucidates Monte Carlo simulation of events, and overviews the available event generators. Reconstruction of physics objects from recorded data, using the particle-flow algorithm, is explained. Boosted topology techniques, such as jet grooming and jet substructure, are discussed, keeping in mind their relevance to the analysis presented in this thesis.

The interaction of particles in a high-energy physics collider experiment is inherently non-deterministic in nature. Therefore, in order to understand the processes involved, and compare the predictions of theory with experiment, Monte Carlo (MC) computational algorithms [99] are used to simulate the processes occurring in our detector. The resulting simulated events are processed via the same reconstruction routines as used for physical data from the detector. In this manner, like-for-like comparisons can be made between Monte Carlo simulated events and events recorded by the CMS detector.

4.1 Event simulation

Simulating proton-proton collision events is a complicated task involving many steps. It is therefore not performed within one program, but several programs, each specialising in a component of the simulation process. The components of generating simulated proton-proton collision events are shown in Figure 4.1. At the heart of these components is a hard scattering process between quarks and gluons, called partons, coming from the colliding protons. Parton distribution functions are used to describe the distribution of the proton longitudinal momentum amongst the partons. The final-state partons from the hard process undergo decays and partonic showering, followed by formation of hadrons, which decay into lighter stable hadrons that interact with the detector. In addition to the primary interaction, further partons from the incoming protons may interact to form an underlying event, and particles from other proton-proton interactions in the same, or different, bunch crossing may contaminate the final decay products.

4.1.1 Hard scattering

The essence of the physical theory that we are interested in is encapsulated in the hard scattering process. At high momentum transfer, the hard scattering process can be calculated in perturbation theory using Feynman diagrams. In order to do so, a matrix element $\mathcal{M}$, which is the probability amplitude to transition from a given initial state to a specific final state, is calculated using Feynman rules for the underlying theory.

The matrix element can then be integrated over the Lorentz invariant phase space (LIPS) to obtain the required cross section. For a two to n particle scattering, with four-momenta p_a and p_b, and masses m_a and m_b of the incoming particles, and four-momenta k_i and energies U_i of the outgoing particles, the cross section is given by:

$$\sigma_{\mathrm{ab}\to\mathrm{X}} = \frac{1}{4\sqrt{(p_\mathrm{a}\cdot p_\mathrm{b})^2 - m_\mathrm{a}^2 \cdot m_\mathrm{b}^2}} \int \overline{|\mathcal{M}^2|}(2\pi)^4\delta^4(p_\mathrm{a}+p_\mathrm{b}-k_1-\ldots-k_n)\prod_{i=1}^{n}\frac{\mathrm{d}^3k_i}{(2\pi)^3 2U_i}, \tag{4.1}$$

where $\overline{|\mathcal{M}^2|}$ is the matrix element squared, averaged over unmeasured particle spins; and δ^4 is the four-dimensional delta function.

In addition to the Feynman diagram with the least number of strong interaction vertices, called the leading order (LO) diagram, more complicated diagrams where gluons are radiated, or radiated and reabsorbed forming loops, need to be considered. These diagrams successively increase the number of strong vertices, each of which contributes a power of the strong coupling constant α_S to the calculated cross section. Since α_S is small at high

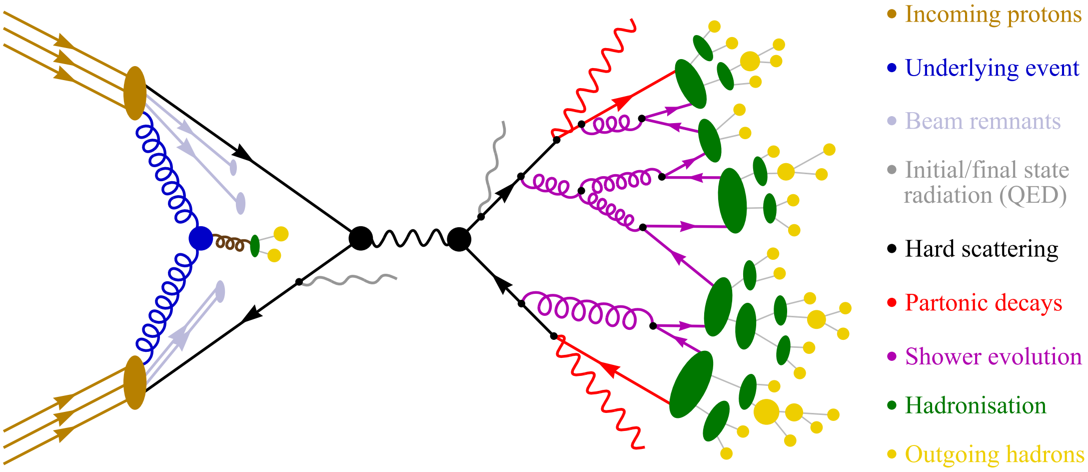

Figure 4.1: Components involved in simulating proton-proton collision events. A hard scattering process (black) occurs between partons from the colliding protons (orange), whilst further interactions between other partons from the protons contribute to the underlying event (blue), and beam remnants (pale blue) are left out. The partons generated from the hard scattering undergo decay (red), and radiate gluons which form a partonic shower (magenta). The shower continues to grow until hadronisation (green) occurs, and the formed hadrons decay into lighter hadrons (yellow) which are detected in the CMS detector. QED radiations (grey) may also be emitted by the initial and final-state partons.

momenta, a perturbation series in terms of α_S can be formed. Including terms with additional powers of α_S gives rise to next-to-leading order (NLO), next-to-next-to-leading order (NNLO), and so on, cross sections. Adding more terms to the calculation not only makes it computationally more expensive, but also introduces divergences that have to be handled carefully.

Analogous orders of calculations can be defined with respect to QED. However, higher order QED corrections are a much smaller effect as compared to QCD, owing to the fact that the fine structure constant α is much smaller than α_S at the relevant energies.

4.1.2 Parton distribution functions

We cannot collide isolated partons in the hard scattering, and collide protons instead, at the LHC. Therefore, the four-momentum of a parton is an unknown fraction of the total proton momentum. Furthermore, as a consequence of the non-deterministic nature, it is impossible to exactly predict the parton momentum fraction. The best we can do is describe the probability density of finding a quark or a gluon with a given longitudinal momentum fraction x. The functions describing the aforementioned probability density for the valence and sea quarks, and gluons, are called parton distribution functions (PDFs).

PDFs cannot be calculated from first principles, and are derived by fitting to data obtained from deep inelastic scattering experiments, as well as other SM processes, at a specific energy scale, and propagating them to the required scale using a set of differential equations called Dokshitzer-Gribov-Lipatov-Altarelli-Parisi (DGLAP) equations. There are many available formulations of PDFs, the most common of which is the neural network based NNPDF set [100, 101]. Figure 4.2 shows the PDFs derived for various quarks and gluons at energy scales 10 GeV^2 and 10^4 GeV^2 in the NNPDF3.1 set. A slightly older version, NNPDF3.0, is used in the generation of simulated events in this analysis.

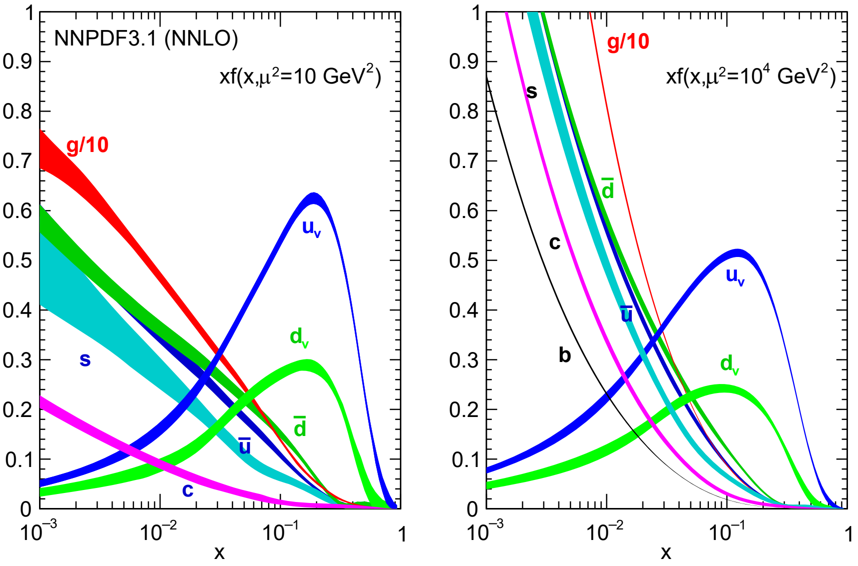

Figure 4.2: Parton distribution functions, evaluated by the NNPDF collaboration, depicting the probability density for finding quarks and gluons with a longitudinal momentum fraction x, at resolution scale 10 GeV^2 (left) and 10^4 GeV^2 (right). This figure is taken from Reference [101].

Using the parton scattering cross section of Equation 4.1 and the derived PDFs, the cross section of producing a final state X from proton-proton collisions is given by:

$$\sigma_{\mathrm{pp}\to\mathrm{X}} = \sum_{a,b} \int \sigma_{ab\to\mathrm{X}}(s, \mu_{\mathrm{R}}^2) \cdot f_a(x_a, \mu_{\mathrm{F}}^2) \cdot f_b(x_b, \mu_{\mathrm{F}}^2) \cdot \mathrm{d}x_a \mathrm{d}x_b, \tag{4.2}$$

where s is the centre-of-mass energy, a and b represent parton flavours, and x_a and x_b are the respective longitudinal momentum fractions. α_{S} entering the matrix element in $\sigma_{ab\to\mathrm{X}}$ is taken at an energy scale called renormalisation scale μ_{R}, as discussed in Section 1.2, and PDFs are evaluated at an energy scale called factorisation scale μ_{F}. The choice of the selection of μ_{R} and μ_{F} is arbitrary, and in general, they are taken to be equal to each other, equal to the combined invariant mass of the final-state particles in an s-channel process, and equal to the transverse momentum in case of massless particles.

4.1.3 Parton showering

The initial and final-state partons can radiate gluons — which possess lower energy than the hard scattering partons — called initial-state radiation (ISR) and final-state radiation (FSR), respectively. These gluons can subsequently radiate more quarks and gluons, and so on, multiplying the number of partons, each having lower energy. This continues until the energy drops down to ~1 GeV, when the partons start combining to form a shower of colourless hadrons. Such a shower, which is generally contained in a cone around the original parton, is called a jet.

In order to compute the shower evolution, a matrix element approach can be used at higher energies. However, at lower energies, perturbation theory is not applicable since α_S becomes large, and Sudakov form factors are used for simulating the shower development [102,103]. The calculation of parton shower can be factorised from the matrix element evaluation, and can therefore be performed separately, irrespective of the hard scattering. Care must, however, be taken when combining a parton shower calculation with a hard scattering evaluated at higher orders. In order to avoid double counting of radiative emissions, merging and matching algorithms, such as MLM [104] and FxFx [105], are utilised.

4.1.4 Hadronisation

As the energy of the partons drops during the shower development, the partons start to cluster into colour-neutral hadrons. At this point, perturbation theory has already fallen apart in describing the strong interactions of the partons. Therefore, in order to describe hadronisation, phenomenological models are used. The most commonly used hadronisation models are the Lund string model [106,107] and the cluster model [108].

The Lund string model assumes that the potential between two colour-charged objects grows linearly with the distance between them. Hence, a string can be imagined between two partons. When the energy of the string crosses a threshold, the string breaks, and a new quark-antiquark pair is formed. The generated partons combine with the already present partons to form colour-neutral hadrons. This processs continues until there are no colour-charged partons remaining in the shower.

The cluster model assumes that all gluons in the shower necessarily decay into quark-antiquark pairs. The neighbouring colour-connected quarks and antiquarks can then be combined to form colourless clusters with a computable mass distribution. The hadrons generated in both schemes include unstable hadrons, and they can decay into secondary stable hadrons that interact with the detector. A number of parameters can be tuned in both hadronisation schemes, to better mimic the production of hadrons that we observe in the data recorded by the CMS detector.

4.1.5 Underlying event

The nuisance of performing experiments with a hadron collider is that hadrons are composite objects. As a consequence, there are secondary interactions amongst further partons from the colliding hadrons, in addition to the ones involved in the hard scattering. These secondary interactions form an underlying event (UE) that needs to be incorporated as well. The UE increases the number of particles in the hadronisation step, and is simulated using phenomenological models that can be tuned to match the data.

4.1.6 Pileup

As discussed in Chapter 2, the LHC collides two bunches of 10^{11} protons every 25 ns in Run 2 of its operation. The event that we are interested in usually comes from one proton-

proton collision. It is, however, quite likely that the recorded event is contaminated by products of additional proton-proton collisions. This effect is called pileup, and it may be because of additional interactions in the same bunch crossing, called in-time pileup, or previous or subsequent bunch crossings owing to a finite temporal resolution, called out-of-time pileup. The effect of pileup is modelled in simulation by adding events passing very loose selection criteria, called minimum bias events, and subsequently adding corrections to simulation to reweight the number of pileup events to the one in the data recorded by the CMS detector.

4.1.7 Monte Carlo event generators

In order to accomplish the complicated simulation tasks discussed above, several Monte Carlo event generators are used. Some of them are generic, and can perform multiple tasks independently. However, most Monte Carlo event simulation routines employ multiple generators working in tandem. Generally, the hard scattering, including the calculation of the matrix element, is computed at NLO precision by specialised frameworks, and the output is interfaced with another framework, simulating parton shower, hadronisation, and underlying event. To make the interfacing seemless, a set of principles, called Les Houches accord [109], has been agreed upon, and a common Les Houches event (LHE) data format is used.

MADGRAPH5_aMC@NLO [110] is one of the most commonly used event generators to compute matrix elements, at LO as well as NLO precision. In order to avoid a possible double counting between real emissions at NLO and hard emissions in the parton shower, a dedicated matching is performed, which may assign negative weights to some events to predict the correct distributions for the full simulation sample. While using MADGRAPH5_aMC@NLO, spin correlations in heavy particle decays can be taken into account by interfacing with a module called MADSPIN. In the analysis presented in this thesis, MADGRAPH5_aMC@NLO v2.4.2 is used to simulate the signal process, whilst v2.2.2 is used to simulate the W+jets process, which serves as a major background. Details of the simulated datasets, along with the event generators used to produce them, are discussed in Chapter 5.

Another common framework used to generate events at NLO precision in QCD is POWHEG (positive weight hardest emission generator) [111–113]. POWHEG circumvents assigning negative weights to events, and needs to be interfaced with a parton shower generator providing p_{T}-ordered showers. In the analysis presented in this thesis, POWHEG v2.0 is used to generate $\mathrm{t\bar{t}}$ and single top quark background processes.

PYTHIA [114,115] is a versatile event generator, which can not only perform matrix element calculation but also parton showering, hadronisation, and underlying event simulation. However, since PYTHIA only allows a LO calculation of matrix elements, the matrix element is calculated in one of the above mentioned generators, and PYTHIA is subsequently used for parton showering, hadronisation, and underlying event simulation. The parton showering in PYTHIA is p_{T}-ordered, the hadronisation is performed in the Lund string model, and different sets of tuning parameters are used. The analysis presented in this thesis utilises PYTHIA v8.212 for parton showering and hadronisation, with CUETP8M1 [116] and CUETP8M2T4 [117] underlying event tunes.

4.1.8 Detector simulation

Once the event generators produce the final state elementary particles and hadrons, their interaction with the detector needs to be simulated. The interactions of the generated particles with the CMS detector — analogous to the interactions of the real particles, as discussed in Chapter 2 — are replicated in the GEANT4 framework [118, 119]. The GEANT4 framework models the CMS detector, and the response of the subdetectors and the readout electronics chain is simulated on the generated events. This process ends up giving data in the same format as is recorded by the CMS data acquisition system, and the same reconstruction routines can be run for like-to-like comparisons.

4.2 Event reconstruction

The signals from the read-out electronics of the subdetectors are in the form of hits. These hits need to be converted into constructs that represent physical objects. In order to do this efficiently, utilising information from all the subdetectors simultaneously, the CMS experiment uses the particle-flow (PF) algorithm [120–122]. The premise of the PF algorithm is that the presence or absence of a signal in the various subdetectors can be linked together to better identify and distinguish physics objects.

The algorithm starts by reconstructing trajectories in the tracker, recreating vertices, and clustering energy deposits in the calorimeters, forming PF elements. PF blocks are then formed by extrapolating and linking the PF elements to one another. The list of blocks thus formed is the input for the iterative reconstruction and identification of particles. Since muons are easily identified, they are reconstructed first, and the corresponding blocks are removed from the subsequent reconstruction steps. Electrons and photons are identified next, and the corresponding blocks are removed from the list, followed by the recontruction of charged and neutral hadrons, and jet clustering can be performed in the final step. Pileup mitigation can be naturally incorporated into the PF algorithm, and excellent reconstruction efficiency can be obtained [120]. The details of the reconstruction of different physics objects is described in the following sections.

4.2.1 Track reconstruction

As discussed in Chapter 3, the essence of the CMS detector is the bending of moving charged particles using a magnetic field, and recording their trajectories, which can then be used to determine their charge and momentum. In order to reconstruct the tracks of charged particles from the hits in the pixel and strip trackers, the combinatorial track finder (CTF) algorithm is used. The CTF algorithm utilises an extended application of Kalman filters [123–125], reconstructing tracks iteratively.

The iteration begins with hits in the innermost pixel tracker layers, and tries to reconstruct tracks with the largest p_{T}. The hits corresponding to the successfully reconstructed tracks in each iteration are removed from the subsequent iterations. Every iteration comprises four steps: The first step produces a track seed, which is a combination of two or three pixel or strip hits. The tracks seed is used to initialise track parameters for the proposed track. The second step utilises Kalman filters to extrapolate tracks to more tracker layers, with the possibility of adding compatible hits and updating the predictions of the Kalman filter. The third step employs a refined Kalman filter to perform a better fit to the selected hits, removing outliers in the process. The final step is quality assessment, in which the tracks that do not satisfy quality requirements, such as a minimum number of hits and a certain χ^2 per degree-of-freedom for the track fit, are removed.

During the reconstruction of the tracks, misalignments in tracker geometry are taken into account by performing an offline tracker alignment, as discussed in Chapter 3.

4.2.2 Beam spot reconstruction

Collisions between protons when the beams cross do not occur at one point, but at different points within a small region near the centre of the detector. Beam spot refers to the luminous region produced by these collisions. The beam spot is characterised by a central position and a spread. Determination of the beam spot is important since it is used, amongst other things, as an input to vertex reconstruction and identification of bottom quarks. The beam spot is calculated using the d_0-ϕ algorithm [126], which is a robust χ^2 fit, utilising the correlation between the track impact parameter d_0 and its azimuthal angle ϕ.

4.2.3 Vertex reconstruction

In order to know the position from where a set of tracks originates, as well as to identify unwanted tracks with a different origin, vertex reconstruction is performed. Vertices are reconstructed in three steps: Firstly, tracks close to the centre of the beam spot and passing quality requirements are selected. The selected tracks are then clustered, using a deterministic annealing (DA) algorithm [127], according to their distance in the z-direction from the centre of the beam spot, at the time of closest approach. Subsequently, the vertex candidates with two or more associated tracks, are fitted using an adaptive vertex fitter (AVF) [128]. As a result of these steps, we obtain the position of the reconstructed vertex as well as probabilities of the corresponding tracks to be associated with the vertex.

The primary vertex (PV) in an event is defined as the vertex with the largest $\sum_i p_{\mathrm{T},i}^2$, where $p_{\mathrm{T},i}$ is the transverse momentum of the i-th track associated with the reconstructed vertex, scaled by the corresponding goodness-of-fit. Vertices other than the PV are useful for mitigation of pileup, since tracks originating from these vertices can be removed, keeping only the tracks from the PV.

4.2.4 Muon reconstruction

Since muons have signatures that can be easily identified, they are reconstructed first. Muons are identified using trajectories reconstructed in the tracker, called tracker tracks, and in the muon system, called standalone-muon tracks. Depending on the order in which these tracks are considered, there can be two approaches to reconstruct muons. In the "inside-out" approach, each tracker track is propagated to the muon sytem, and a compatible matching is found with hits in DT or CSC segments. Muons reconstructed in such a way are called tracker muons. On the contrary, global muons are reconstructed in the "outside-in" approach, where standalone-muon tracks are matched with tracker tracks, using a Kalman filter fit.

The analysis presented in this thesis utilises high-p_T muons, and there are several quality requirements imposed on the selected muon candidates [85]. The candidate must have been reconstructed as a global muon, with at least one muon-chamber hit included in the global-muon track fit, to suppress hadronic punch-through and muons from decays in flight. It is required to have muon segments in at least two muon stations and a relative p_T uncertainty of less than 30%. In order to suppress cosmic muons and further suppress muons from decays in flight, its tracker track is required to have a transverse impact parameter $d_{xy} < 2$ mm and a longitudinal distance $d_z < 5$ mm with respect to the PV. To ensure a good p_T measurement, the candidate is required to have nonzero number of pixel hits and greater than five tracker layers with hits.

In addition, a requirement on the relative isolation of the muon candidate is applied. The muon is considered isolated if the scalar sum of the p_T of tracks from the primary vertex within $\Delta R = \sqrt{(\Delta\eta)^2 + (\Delta\phi)^2} = 0.3$ of the muon is less than one tenth of the p_T of the muon. In order to determine the momentum of the muons, CMS utilises the Tune-P algorithm [86], which has been validated using cosmic ray muons, muons from proton-proton collisions, and MC simulations.

The efficiency associated with the final reconstructed muon object contains several components, including efficiencies of track reconstruction, muon reconstruction and identification, relative isolation, and triggers. The reconstruction, identification, and isolation efficiencies were studied with the tag-and-probe method [85]. The efficiency was found to be above 95% for every case, in the entire range of values of η and ϕ [85].

4.2.5 Electron reconstruction

Since electrons are light compared to muons, and lose a lot of energy in the tracker due to bremsstrahlung, their reconstruction is relatively complicated. However, analogous to the muons, the signatures of electrons include tracker tracks as well as energy deposits in the ECAL crystals, and there are two approaches to reconstruct them. In the ECAL-driven approach, highly energetic ECAL superclusters (SC), as discussed in the paragraphs below, are matched to tracker tracks. The ECAL-driven approach works efficiently for high-p_T electrons. On the other hand, the tracker-driven approach uses tracker tracks and matches them to ECAL superclusters using a calorimeter-unbiased seed algorithm. The tracker-driven approach works effeciently for low-p_T electrons.

The clustering of the energy deposits in the ECAL starts by considering the crystal with the highest energy deposit, which acts as a seed. Seeds are used to form topological clusters that are subsequently grouped together to construct the so-called moustache superclusters. Moustache superclusters are used in both the ECAL-driven and the tracker-driven electron reconstruction. The excessive bremsstrahlung of electrons changes the curvature of the tracks, and only a few hits may be recorded in the tracker. Hence, the track fit has a large χ^2, and it is hard to match the ECAL hits with the tracker tracks using the standard Kalman filter procedure. Therefore, a Gaussian sum filter (GSF) [129] is used, which correctly takes the energy loss into account.

In order to estimate the momentum of electrons, a combination of tracker and ECAL measurements is used [130]. A weight w is defined using a regression technique that combines the track momentum p with the estimated supercluster energy E_{SC} as:

$$p_{\mathrm{comb}} = wp + (1 - w)E_{\mathrm{SC}}. \tag{4.3}$$

The analysis presented in this thesis utilises high energy electron pairs (HEEPv70) identification [130], wherein several quality requirements are imposed on the selected electron candidates. The p_{T} of the candidates is always required to be greater than 35 GeV, and the candidate must be ECAL-driven, whilst slightly different requirements are imposed on other variables based on whether they are reconstructed in the barrel or the endcap regions. Electron candidates in the transition region between the barrel and the endcaps ($1.44 < |\eta| < 1.57$) are rejected, to avoid low quality reconstruction due to a gap where services and cables are housed.

The barrel region extends up to $|\eta| < 1.44$. Electrons reconstructed in the barrel region are required to have the absolute difference between η of the seed cluster and the track η extrapolated from the innermost track position to the position of the closest approach to the supercluster ($\Delta\eta_{\mathrm{in}}^{\mathrm{seed}}$) less than 0.004. The absolute difference in the corresponding ϕ ($\Delta\phi_{\mathrm{in}}^{\mathrm{seed}}$) is required to be less than 0.06. The energy deposited in the HCAL should be less than 1 GeV + 5% of the energy deposited in the ECAL.

The energy deposited in a 2×5 crystal array around the seed crystal should be greater than 0.94 times the energy deposited in the 5×5 array, or the energy deposited in a 1×5 array should be greater than 0.83 times the energy deposited in the 5×5 array. The isolation based on the ECAL and HCAL clusters in the first layer with $\Delta R = 0.3$ should be less than $2 + 0.03p_{\mathrm{T}} + 0.28\rho$, where ρ is the average pileup density in the event. The scalar sum of the p_{T} of the tracks within $\Delta R = 0.3$ of the electron is required to be less than five times the p_{T} of the electron. There should not be more than one lost hits in the inner layer, and the transverse impact parameter is required to be smaller than 0.02 cm.

The endcaps cover a range of $1.57 < |\eta| < 2.5$. Electrons reconstructed in the endcaps are required to have a $\Delta\eta_{\mathrm{in}}^{\mathrm{seed}}$ less than 0.006, and $\Delta\phi_{\mathrm{in}}^{\mathrm{seed}}$ less than 0.06. The energy deposited in the HCAL should be less than 5 GeV + 5% of the energy deposited in the ECAL.

The width of the shower surrounding the electron ($\sigma_{i\eta i\eta}$) should be less than 0.03. The isolation based on the ECAL and HCAL clusters in the first layer with $\Delta R = 0.3$ should be less than $2.5 + 0.28\rho$ for $p_{\mathrm{T}} < 50$ GeV, and less than $2.5 + 0.03(p_{\mathrm{T}} - 50) + 0.28\rho$ otherwise. The track based relative isolation is required to be less than 5, as in the case of barrel electrons. There should not be more than one lost hit in the inner layer, and the transverse impact parameter is required to be smaller than 0.05 cm.

4.2.6 Photon and hadron reconstruction

Since photons are electrically neutral, they do not leave a track inside the tracker. ECAL clusters which cannot be matched to a tracker trajectory, and cannot be associated to bremsstrahlung from a track, are reconstructed as isolated photons. The reconstruction of isolated photons is analogous to electron reconstruction, without any track in the tracker. Subsequently, the remaining ECAL and HCAL energy deposits without any associated tracker trajectories are assumed to be from either neutral hadrons, like neutrons or K^0, or nonprompt photons from decay of π^0. These clusters are made candidates for neutral hadrons, and if any ECAL and HCAL clusters can be linked, they are considered deposits from the same neutral hadron in both detectors.

Energy deposits in the HCAL which can be associated to tracker trajectories are assumed to be from charged hadrons, like protons, $\pi^{\pm}$, or $K^{\pm}$, and the corresponding clusters are reconstructed as charged hadrons if the deposited energy is compatible with the momentum of the associated tracks. In case the energy is significantly lower than the momentum of the associated tracks, the possibility of energy deposits from high-p_T muons is considered, and a second pass at reconstructing previously ill-reconstructed muons is performed.

4.2.7 Jet reconstruction

As discussed in Section 4.1, the quarks and gluons stemming from the hard interaction undergo parton showering and hadronisation, and form a collimated shower of particles which are detected by the CMS detector. In order to deduce the properties of the parent parton, these PF objects are clustered into a jet. Various algorithms can be used to systematically cluster the objects into jets. However, all jet clustering algorithms should obey certain requirements. In particular, the algorithms are required to be infrared and collinear (IRC) safe. Infrared safety refers to the fact that the clustering should be robust against soft emissions, and collinear safety demands that the final clustering output remains invariant following a collinear splitting of the constituents. The necessity for IRC safety is demonstrated in Figure 4.3.

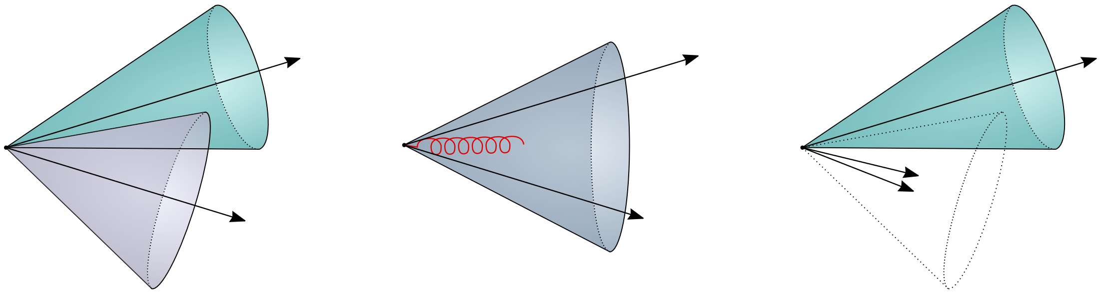

Figure 4.3: An example configuration of jets (left), demonstrating the necessity for infrared and collinear safe jet clustering algorithms. A jet clustering algorithm should be robust against soft emissions which try to merge jets from multiple partons into one (middle), as well as collinear splitting where the energy of a parton is distributed and a jet may even be left out from the reconstruction (right).

There are two major categories of jet clustering algorithms: cone algorithms, like iterative cone (IC) [131] and seedless infrared safe cone (SIScone) [132], which cluster jet constituents assuming a conical spatial distribution; and sequential clustering algorithms, like k_T [133], anti-k_T [134], and Cambridge/Aachen (CA) [135], which iteratively combine objects based on the generalised distance between them. Cone algorithms are easy to implement, but are not favoured since they contain unphysical variables, and are generally IRC unsafe as well. Sequential algorithms, on the other hand, are IRC safe by definition. A comparison of jet clustering algorithms, using a simulated parton-level event, is shown in Figure 4.4.

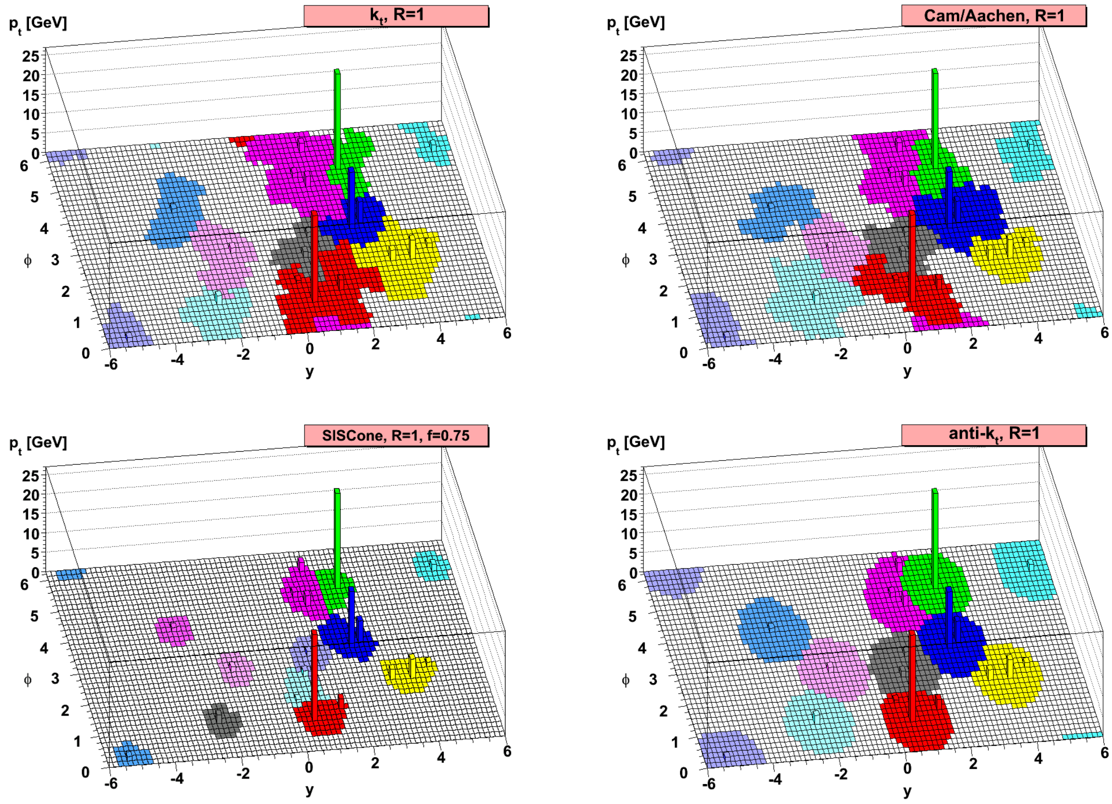

Figure 4.4: Comparison of different jet clustering algorithms, using an example parton-level event, including multiple random soft "ghost" elements. Clustering using the k_T, Cambridge/Aachen, SISCone, and anti-k_T algorithms is shown on the top-left, top-right, bottom-left, and bottom-right, respectively. The anti-k_T algorithm provides the best clustering, whilst the shapes of the k_T and Cambridge/Aachen jets is heavily influenced by the set of ghosts used. This figure is taken from Reference [134].

Sequential jet clustering algorithms define generalised distances d_{ij} between particles i and j, and d_{iB} between particle i and the beam pipe as:

$$\begin{aligned} d_{ij} &= \min(k_{\mathrm{T},i}^{2n}, k_{\mathrm{T},j}^{2n})\frac{\Delta_{ij}^2}{R^2}, \\ d_{iB} &= k_{\mathrm{T},i}^{2n}, \end{aligned} \tag{4.4}$$

wherein

$$\Delta_{ij}^2 = (y_i - y_j)^2 + (\phi_i - \phi_j)^2, \tag{4.5}$$

and $k_{\mathrm{T},i}$, y_i, and ϕ_i are the transverse momentum, rapidity, and azimuthal angle of the particle i, respectively. R is the radius parameter, and n is a characterising feature of the algorithm. The value of n is equal to 1, -1, and 0 for the k_T, anti-k_T, and CA algorithm, respectively. The algorithm proceeds by iteratively merging the closest particles by adding their four-momenta, if d_{ij} is smaller than d_{iB}; otherwise the iteration is terminated, and i is labelled as a jet. The CMS experiment generally uses the anti-k_T jet clustering algorithm with $R = 0.4$ — the corresponding jets are called AK4 jets — and $R = 0.8$ — the corresponding jets are called AK8 jets.

As with the leptons, the jets considered for the analysis presented in this thesis satisfy certain quality requirements. All jets are required to have less than 99% neutral hadron and EM fractions, and strictly more than one constituent. In addition, the central jets ($|\eta| < 2.4$) must have a nonzero charged hadron fraction and charged multiplicity, and less than 99% charged EM fraction.

Jet energy calibration

Jets formed by using jet clustering algorithms are not perfectly representative of the parent partons. There are discrepancies in the energy scale and resolution, due to the effects of pileup and nonlinear response of the detectors. Therefore, the jet energy needs to be calibrated to the actual energy of the partons. This is achieved in the CMS experiment by performing several corrections in a well defined order [136,137]. The jet energy corrections (JEC) applied to jets reconstructed from data and simulation are demonstrated in Figure 4.5.

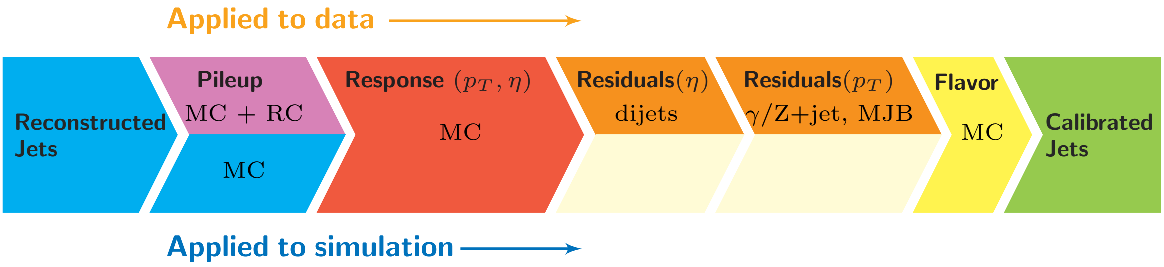

Figure 4.5: A schematic showing the jet energy calibration routine in the CMS experiment. Reconstructed jets are subjected to pileup corrections based on MC simulations, with residual random-cone corrections in case of data. The jets are further corrected for detector response, based on p_T- and η-dependent MC simulations. Consequently, dijet (multijet, γ/Z+jets) events are used to apply residual η (p_T) corrections to jets in data. In the end, flavour-dependent corrections may be added, if required. This figure is taken from Reference [137].

The different levels of jet energy corrections, each intended to mitigate a certain discrepancy, are:

- **L1 pileup:** The contribution from pileup interactions to the measured jet energy is removed. The correction is determined from dijet events, simulated with and without pileup. In addition, a residual correction using a random-cone (RC) method is applied to data [137].
- **L2L3 MC truth:** The reconstructed p_T is corrected to the parton-level p_T, using a simulated QCD sample. The corrections are derived as a function of p_T and η, to ensure uniformity of the detector response.
- **L2L3 residuals:** Residual differences in data are compensated, by using dijet (multijet, γ/Z+jets) events to apply residual corrections as functions of η (p_T).

- **L5 flavour:** Flavour-dependent corrections can be applied, if needed.

Jet energy resolution (JER) is also worse in data than simulation. Therefore, a smearing is applied to the simulated p_T distribution to match it to the observed distribution in data. The details of the specific JER corrections applied for the analysis presented in this thesis are given in Chapter 5.

4.2.8 Mitigation of pileup

Mitigation of pileup is a crucial component of accurate event reconstruction, especially in an environment with a large number of proton-proton interactions. The most widely used technique for mitigation of pileup is charged hadron substraction (CHS) [138]. In the CHS approach, tracking information is used to unambiguously identify charged hadrons from pileup vertices. These charged hadrons are removed from the event, and the remaining PF candidates are clustered to form jets.

The analysis presented in this thesis utilises a more sophisticated technique called pileup per particle identification (PUPPI) [139]. PUPPI makes use of local shape information, event pileup properties, and tracking information to mitigate pileup at the reconstructed particle level. As with the CHS approach, charged particles associated with pileup vertices are discarded. For neutral particles, a local shape variable is defined as:

$$\alpha_i = \log\left(\sum_{j\in\mathrm{event}} \frac{p_{\mathrm{T},j}}{\Delta R_{ij}} \times \Theta(\Delta R_{ij} - R_\mathrm{min}) \times \Theta(R_0 - \Delta R_{ij})\right), \tag{4.6}$$

where $p_{\mathrm{T},j}$ is the transverse momentum of the j-th particle, and ΔR_{ij} is the distance between the particles i and j in the (η,ϕ)-plane. Θ is the Heaviside step function, implying that the particles closer to i than R_min are not considered in the sum; hence R_min acts as a regulator for collinear splitting. Similarly, particles farther from i than cone radius parameter R_0 are not considered in the sum. Using:

$$\chi_i^2 = \frac{(\alpha_i - \bar{\alpha}_\mathrm{PU})^2}{\sigma_\mathrm{PU}^2} \times \Theta(\alpha_i - \bar{\alpha}_\mathrm{PU}), \tag{4.7}$$

where $\bar{\alpha}_\mathrm{PU}$ is the median shape variable for charged pileup particles, and σ_PU^2 is the corresponding mean-squared value, particles are assigned a weight:

$$w_i = F_{\chi^2,NDF=1}(\chi_i^2), \tag{4.8}$$

assuming χ_i^2 is chi-squared distributed, and F_{χ^2} is the cumulative distribution function. The assigned weight — which corresponds to how likely the particle is not from a pileup vertex — is used to rescale the four-momentum of the particle, mitigating the contribution from pileup vertices.

4.2.9 Identification of bottom-quark initiated jets

The identification of jets coming from bottom quarks can be particularly useful, since top quark processes usually contain bottom quarks in the decay products. The procedure used to identify and label bottom quarks is called b tagging. In the analysis presented in this thesis, b tagging is used to estimate and suppress backgrounds that contain bottom quarks.

The combined secondary vertex (CSVv2) algorithm [140, 141] is used to perform the b tagging.

The working principle of the CSV algorithm is demonstrated in Figure 4.6. The hadrons formed by the hadronisation of the bottom quark, like the B meson, have relatively longer lifetimes. This implies that the b hadrons do not decay immediately at the interaction point, but travel a certain distance, typically a couple of millimetres, before decay. When they decay, they form a secondary vertex, and the tracks originating from the secondary vertex have a large impact parameter. The existence of a reconstructed secondary vertex away from the primary vertex, along with a wider shape and a higher multiplicity of the jet, indicates presence of a bottom quark. The CSVv2 algorithm uses multivariate techniques to combine this information into a single discriminant.

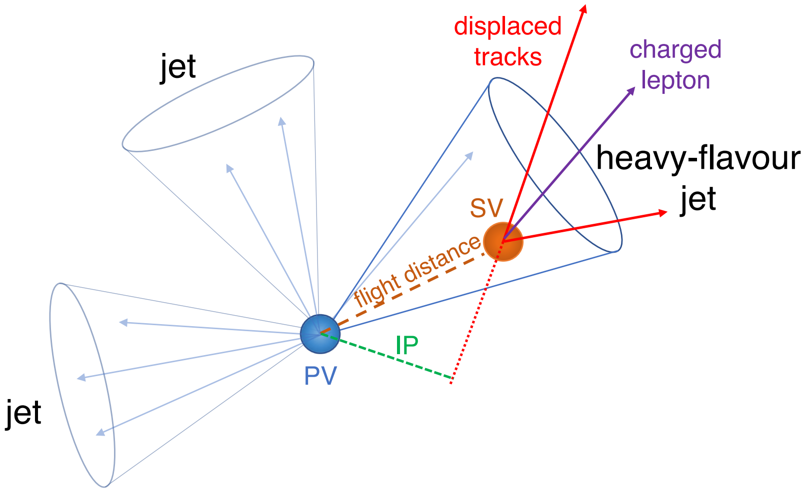

Figure 4.6: Working principle of the combined secondary vertex algorithm. Owing to a longer decay time, B mesons decay at some distance from the primary vertex, and the tracks of the decay products have a large impact parameter. If a set of tracks can be traced back to a certain displaced secondary vertex, it is suggestive of the presence and decay of a b hadron at the secondary vertex. This figure is taken from Reference [141].

The analysis presented in this thesis utilises a "tight" working point of the discriminant (> 0.9535), corresponding to an overall efficiency of 41% for correctly identifying a bottom quark jet, with a 0.1% probability of misidentifying a jet from a light-favour quark or gluon as b tagged.

4.2.10 Missing transverse momentum

The CMS experiment detects most of the stable particles in the final state. However, there are some particles, like neutrinos in the SM and certain dark matter particles in BSM scenarios, which escape the detector without interacting. The presence of such particles can be inferred as missing transverse momentum $p_{\mathrm{T}}^{\mathrm{miss}}$, owing to the fact that the sum of transverse momenta of all final-state particles should add up to zero. In practice, however, several corrections need to be incorporated in this calculation to accurately reconstruct $p_{\mathrm{T}}^{\mathrm{miss}}$ [142].

The raw $\vec{p}_{\mathrm{T}}^{\mathrm{miss}}$ is defined as the negative vector sum of all reconstructed PF particles:

$$\vec{p}_{\mathrm{T}}^{\mathrm{miss,raw}} = - \sum_{i \in \mathrm{PF\ objects}} \vec{p}_{\mathrm{T},i}. \tag{4.9}$$

The final corrected $\vec{p}_{\mathrm{T}}^{\mathrm{miss}}$ is written as:

$$\vec{p}_{\mathrm{T}}^{\mathrm{miss,corr}} = \vec{p}_{\mathrm{T}}^{\mathrm{miss,raw}} + \vec{C}_{\mathrm{T}}^{\mathrm{type\text{-}0}} + \vec{C}_{\mathrm{T}}^{\mathrm{type\text{-}I}}, \tag{4.10}$$

where $\vec{C}_{\mathrm{T}}^{\mathrm{type\text{-}0}}$ is a correction to mitigate the contribution to $\vec{p}_{\mathrm{T}}^{\mathrm{miss}}$ from pileup, and $\vec{C}_{\mathrm{T}}^{\mathrm{type\text{-}I}}$ is the propagation of jet energy corrections to the calculation of $\vec{p}_{\mathrm{T}}^{\mathrm{miss}}$. A type-II correction is also defined for calorimeter based jets, which is not relevant for PF jets.

The calculation of $\vec{p}_{\mathrm{T}}^{\mathrm{miss}}$ is important for the analysis presented in this thesis, since leptonic decay of a W boson is considered, which produces a neutrino that is not detected directly by the CMS detector, and is reconstructed using $\vec{p}_{\mathrm{T}}^{\mathrm{miss}}$.

4.3 Boosted topology techniques

When a hadronically decaying particle is highly boosted, as is the case with the analysis presented in this thesis, the structure of the formed jets starts to differ from conventional jets. In this scenario, it is advantageous to reconstruct the jets utilising techniques developed specifically for boosted jets. These techniques include jet grooming and exploiting jet substructure to help identify the signal and suppress background contributions.

4.3.1 Jet grooming

The formation of jets using jet clustering algorithms is designed to create objects that are representative of the parent particle. However, the output of jet clustering can be contaminated by additional soft contributions from initial-state radiation, underlying event, and pileup. These contributions increase significantly with the radius of the jet, and become a menace when boosted, large-radius jets are reconstructed. Jet grooming refers to the mitigation of these additional contributions by removing soft, wide-angle radiations. The basic idea and routine for jet grooming is shown in Figure 4.7. There are a multitude of jet grooming algorithms, including trimming [143], pruning [144, 145] and soft drop [146], differing in implementation. Soft drop jet grooming is used in the analysis presented in this thesis.

Soft drop is a modified mass-drop declustering algorithm [147, 148]. In the first step, anti-k_{T} jets are reclustered using the CA algorithm, to form a pairwise clustering tree with an angular-ordered structure. The steps of the CA algorithm are then iterated in reverse, declustering the jet into two subjets at each step, and checking for the soft drop condition:

$$\frac{\min(p_{\mathrm{T},1}, p_{\mathrm{T},2})}{p_{\mathrm{T},1} + p_{\mathrm{T},2}} > z_{\mathrm{cut}} \times (\frac{\Delta R_{12}}{R_0})^{\beta}, \tag{4.11}$$

where R_0 is the radius of the jet, and z_{cut} and β are tunable parameters, set to 0.1 and 0, respectively, in this analysis. When the soft drop condition is met, the iteration is stopped,

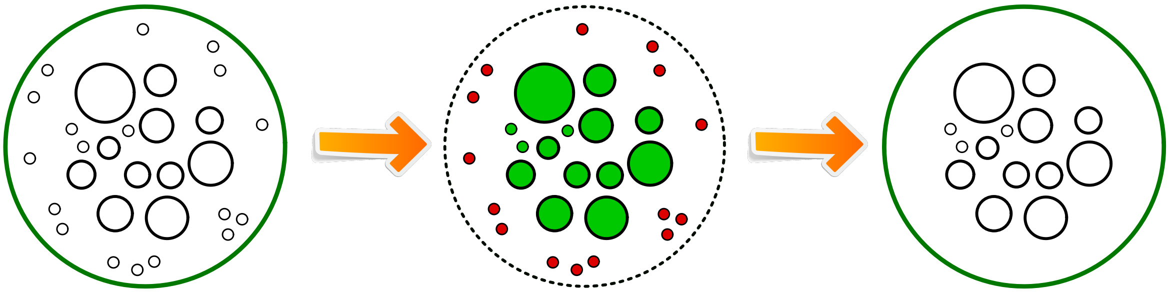

Figure 4.7: A schematic demonstrating the basic repice for jet grooming. Jets are reclustered, removing soft, wide-angle radiation in the process. Jet grooming reduces the mass of jets initiated by single quarks or gluons, and improves the mass resolution for jets initiated by heavy particles.

and the jet is labelled as a soft drop jet. Otherwise the softer subjet is dropped, and the iteration continues on the subjet with the larger p_{T}.

The effect of soft drop jet grooming on W jets and QCD jets is demonstrated in Figure 4.8. The application of jet grooming to the W initiated jets substantially improves jet mass resolution. For the QCD jets, prior to grooming, soft radiations introduce IR divergences, which shift the jet mass peak to a higher value. Removal of the soft divergences by jet grooming reshapes the mass distribution, and helps differentiate it from the more massive W initiated jets.

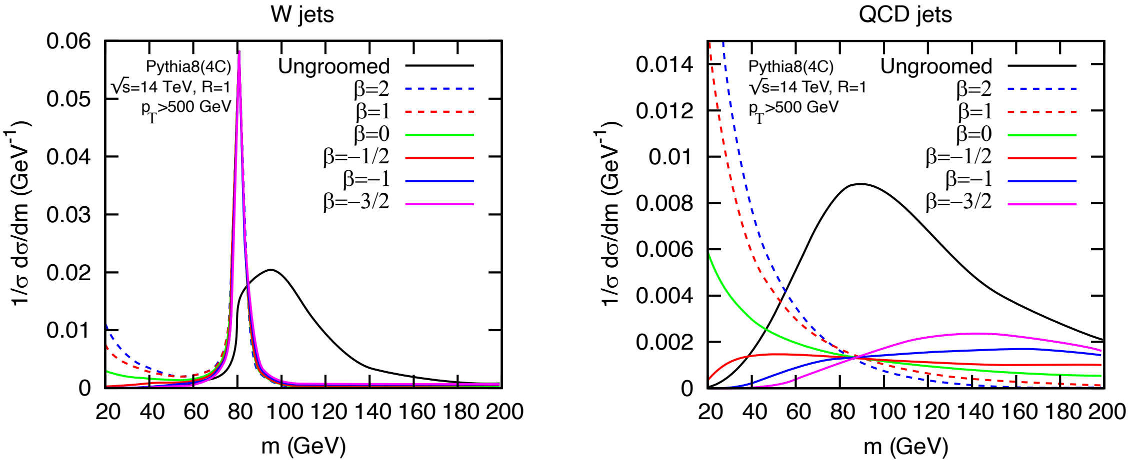

Figure 4.8: Impact of soft drop declustering on the mass distribution of W initiated jets (left) and QCD jets (right). The resolution of the W jets is substantially improved, and the mass of the QCD jets is drastically corrected to their real value. The analysis presented in this thesis utilises $\beta = 0$, which corresponds to the green curves. This figure is adapted from Reference [146].

4.3.2 Jet substructure

The decay of highly boosted hadronically decaying particles generates large-radius jets with a substructure. This substructure can be utilised to identify the parent particle. The basic idea is demonstrated in Figure 4.9. Boosted objects generate jets that can no longer be resolved. However, considering the fact that the jet mass, as well as the number of decay axes inside the large-radius jet, are fixed by the parent particle, new variables can be defined which utilise this information to differentiate between the initial particles. One of the variables which utilises this information is N-subjettiness [149].

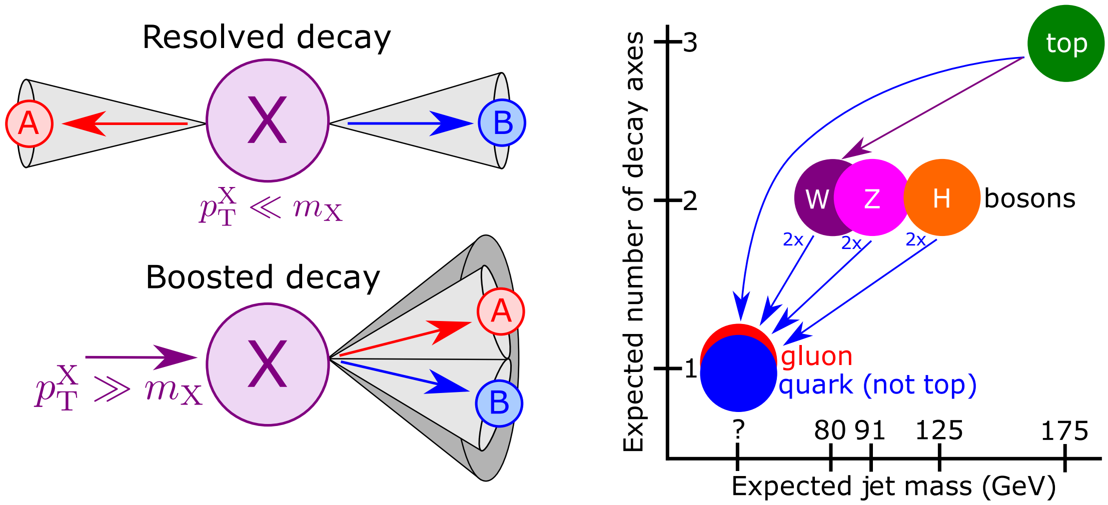

Figure 4.9: Schematics demonstrating the basics of jet substructure. A comparison of resolved and boosted decay topologies is shown on the left, and a map of hadronically decaying SM particles in the (jet mass, number of decay axes)-plane, which can be used to differentiate between the different classes, is shown on the right. This figure is taken from Reference [150].

N-subjettiness τ_N is defined by identifying N candidate subjets, using anti-k_{T} algorithm, within a large-radius jet, and declaring:

$$\tau_N = \frac{1}{d_0} \sum_k \left[p_{\mathrm{T},k} \cdot \min(\Delta R_{1k}, \Delta R_{2k}, ..., \Delta R_{Nk}) \right], \tag{4.12}$$

where the sum is over all constituents of the large-radius jet, $p_{\mathrm{T},k}$ and ΔR_{jk} are the transverse momentum and distance to the j-th candidate subjet axis, respectively, of the k-th particle, and d_0 is a normalisation factor, given by:

$$d_0 = \sum_k \left[p_{\mathrm{T},k} \cdot R_0 \right], \tag{4.13}$$

with R_0 as the original jet radius. τ_N quantifies the likelihood that the jet contains N subjet axes. Smaller values of τ_N imply an agreement with the hypothesis that the radiation is aligned with N subjets, whilst larger values suggest that energy is distributed away from N subjet directions, pointing to more than N subjets.

Instead of using τ_N with various values of N separately, it is often more beneficial to use ratios of τ_N with different values of N [149]. For the analysis presented in this thesis, the ratio of τ_2 and τ_1,

$$\tau_{21} = \tau_2 / \tau_1, \tag{4.14}$$

is used to discriminate between W jets, which have a two-pronged structure, and QCD jets, which have a one-pronged structure. Figure 4.10 (left) shows distribution of τ_{21} in events with W jets and QCD jets, after suitable selection requirements. Application of a selection cut on τ_{21} can separate events of the two types. Figure 4.10 (right) shows a density plot in the (τ_1, τ_2)-plane, for the same set of events. In certain cases, a multivariate cut in the (τ_1, τ_2)-plane can enhance the separation power.

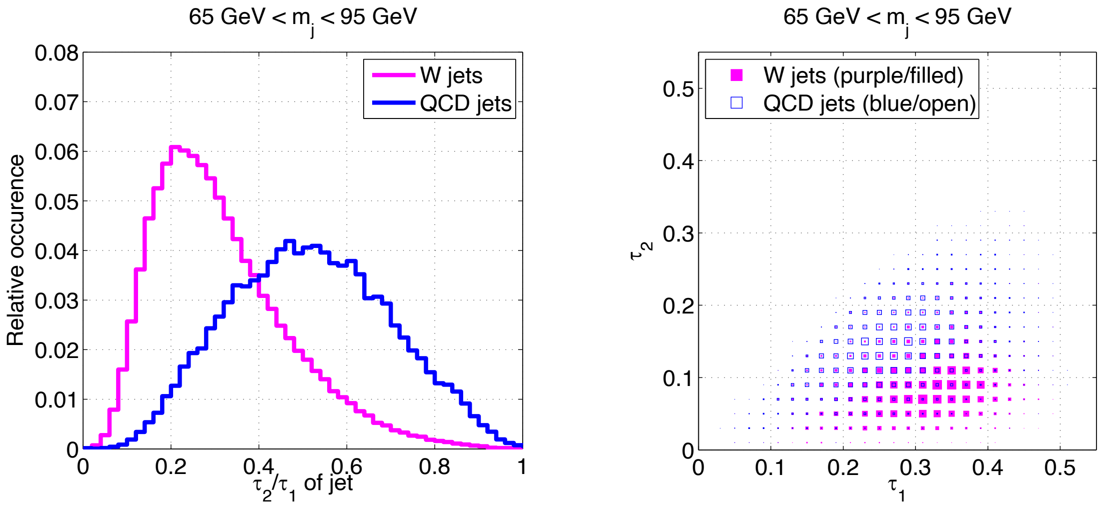

Figure 4.10: Distribution of $\tau_{21} = \tau_2/\tau_1$ for boosted W and QCD jets (left), demonstrating the ability to discriminate between the two; and the corresponding density plot in the (τ_1, τ_2)-plane (right), wherein the marker sizes are proportional to the number of jets in a given bin, demonstrating the possibility of a multivariate cut in the (τ_1, τ_2)-plane to enhace the discriminating power. The events selected for these plots have a set of selections: $65 < m_{\text{jet}} < 95$ GeV on jets of $R = 0.6$, $p_{\text{T}} > 300$ GeV, and $|\eta| < 1.3$ imposed. This figure is taken from Reference [149].

Soft drop groomed jet mass and τ_{21}, along with PUPPI for mitigation of pileup, form a strong discriminant between the signal and background processes for the analysis presented in this thesis.

To be, or not to be, that is the question.

……

– William Shakespeare, Hamlet

5

Event selection

Needle in a haystack —

This chapter introduces the event topology of the signal and background processes, and catalogues data and simulation samples used for analysis. Selection requirements on reconstructed physics objects are presented, leading to the inclusion or omission of the corresponding event. Corrections made to simulation, to enhance imitation of data, are detailed. The chapter concludes by discussing the sources of systematic uncertainty, and the approach used to incorporate them.

The analysis presented in this thesis aims at studying anomalous production of vector boson pairs. However, as already discussed, the production of new particles in collision events is nondeterministic in nature, and additional processes with similar decay products contaminate the desired outcome. These background processes need to be identified and suppressed, to leave a cleaner signature of the signal process. In order to do so, events are subjected to various selection requirements — which are derived based on event topology of the signal and background processes — and discarded if they fail the requirements.

5.1 Event topology

A careful consideration of the event topology of the signal and background processes is critical for any particle physics analysis, since it helps identify characteristic features of the signal process and kinematic distributions, when compared with various background contributions.

5.1.1 The signal process

As discussed in Chapter 1, the analysis presented in this thesis searches for physics beyond the SM in the context of the effective field theory, wherein anomalous gauge couplings manifest themselves in self-interactions of gauge bosons. In this analysis, aTGCs are probed in the process where a pair of vector bosons is produced via a third vector boson. The LO Feynman diagram for the signal process is shown in Figure 5.1.

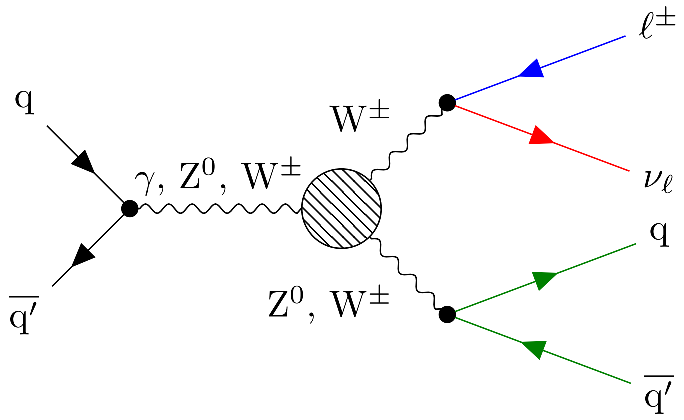

Figure 5.1: The LO Feynman diagram for the signal process involving triple gauge couplings. One of the produced vector bosons (W) decays into leptons, and the other (W/Z) decays into quarks.

In order to achieve optimal balance between efficiency and purity, semileptonic decays of the WW/WZ boson pair are considered, as discussed in Section 1.1. This implies that a W boson in the final state decays into a charged lepton and the corresponding neutrino, and a W/Z boson decays into two quarks. However, since the W/Z boson is highly boosted, the jets formed from the two decay quarks are not reconstructed as resolved jets, but as a single, large-radius jet, utilising the techniques discussed in Section 4.3. The signature of the signal process in an event thus includes a single lepton, missing transverse momentum, and a boosted jet with a two-pronged structure. In addition, systematic deviations in kinematic distributions occur, since the presence of nonzero aTGC parameters modifies the cubic self-interaction, and the kinematic distributions reflect this change.

5.1.2 Background processes

There are several processes, which act as background contributions for this analysis. The relevant background processes, in order of significance, are:

- **W+jets:** The most significant background for this analysis is the production of W bosons in association with jets. LO Feynman diagrams for the W+jets background process are shown in Figure 5.2. A W+jets event can mimic a signal event if the W boson decays into leptons, and one of the jets passes through the selection requirements and appears as a hadronically decaying W or Z boson. Since it is particularly hard to model this process accurately, data-driven methods have been employed in this analysis to estimate the contribution from the W+jets background.
- **Top quark pair production ($\mathrm{t\bar{t}}$):** Another major background is the production of top quark pairs. LO Feynman diagrams for the $\mathrm{t\bar{t}}$ background process are shown in Figure 5.3. A characteristic feature of $\mathrm{t\bar{t}}$ events is that bottom quarks are produced from the decay of top quarks. The bottom quarks can be identified using b tagging, and the event can be discarded. However, since b tagging is not 100% efficient, there is a lot of residual contribution from the $\mathrm{t\bar{t}}$ process.
- **SM diboson production (WW/WZ):** Since the analysis looks for vector boson pairs with modified couplings, production of vector boson pairs in the SM scenario is another background. However, as compared to the W+jets and $\mathrm{t\bar{t}}$ backgrounds, SM WW/WZ is a minor background. LO Feynman diagrams for the SM diboson production in the *s* and *t* channel are shown in Figure 5.4. Since SM WW/WZ production is a minor background, it is mostly estimated from simulation.
- **Single top quark production (t):** Another minor background is the electroweak production of single top quarks. LO Feynman diagrams for single top quark background processes in the *t* channel, associated tW production, and *s* channel are shown in Figure 5.5. Single top quark background is also estimated from simulation.

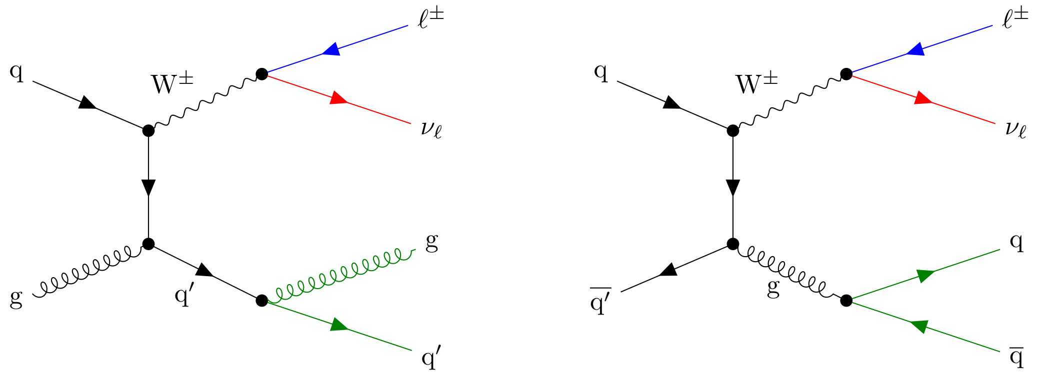

Figure 5.2: LO Feynman diagrams for the W+jets background process. At the LHC, the gluon-initiated process (left) occurs more frequently than the quark-initiated process (right).

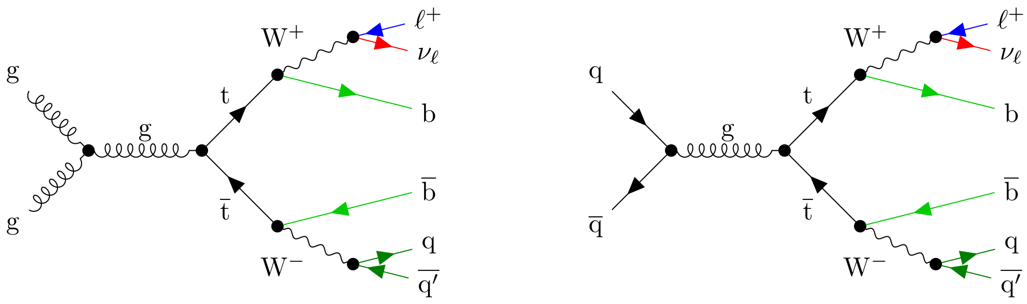

Figure 5.3: LO Feynman diagrams for the top quark pair production ($\mathrm{t\bar{t}}$) background process. At the LHC, $\mathrm{t\bar{t}}$ pairs are mostly produced via gluon fusion (left), and rarely via quark-antiquark annihilation (right). Additional bottom quarks are produced which can be used to identify and suppress the $\mathrm{t\bar{t}}$ background process.

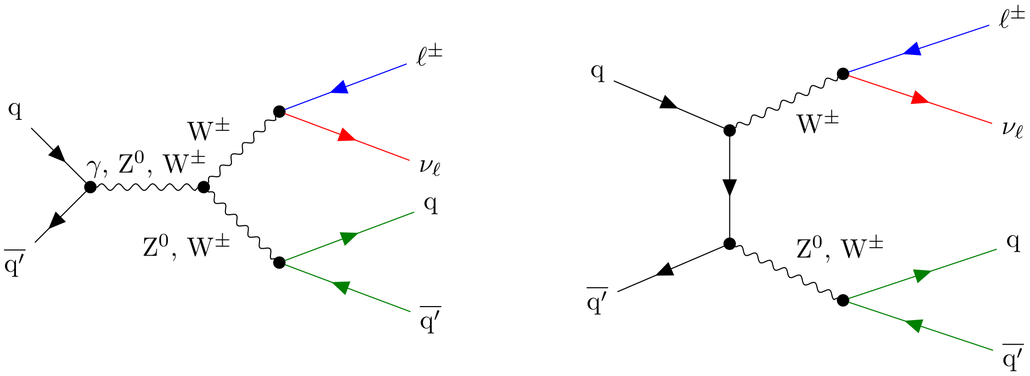

Figure 5.4: LO Feynman diagrams for the SM diboson production. *s*- and *t*-channel are shown on the left and right, respectively.

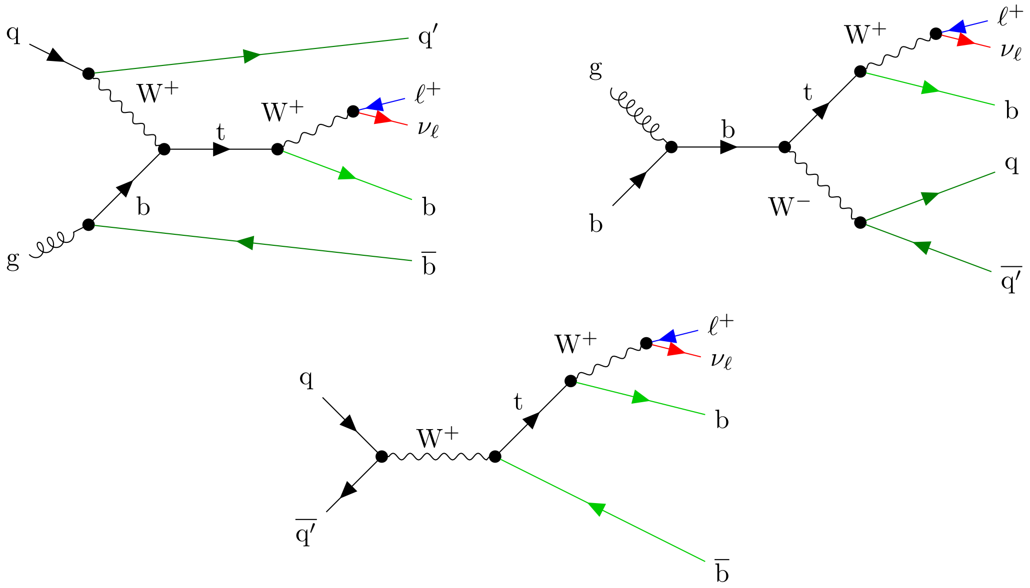

Figure 5.5: LO Feynman diagrams for single top quark (t) processes. Production of top quarks in the *t*-channel, associated tW production, and *s*-channel are shown on the top-left, top-right, and bottom, respectively.

In addition to the above, the contribution from several other processes was checked, and found to be negligible because of events abundantly failing selection requirements or smaller cross sections. These processes include QCD multijet, Z+jets, same-sign WW (vector boson scattering), ZZ, VH, and $W\gamma^*$ production.

5.2 Data and simulated samples

The data and simulated samples used in this analysis correspond to proton-proton collisions with a centre-of-mass energy of 13 TeV and bunch spacing of 25 ns.

5.2.1 Data samples

The data samples comprise data collected by the CMS experiment in proton-proton collisions during 2016 data taking. Single electron and single muon data sets from run periods B to H are used, which have been compiled in the MINIAOD format following the "February 2017" re-reconstruction. Table 5.1 lists the used data sets, along with the integrated luminosity and number of events in each set. The runs passing quality assessment from the data quality monitoring (DQM) are selected only. The used data corresponds to an integrated luminosity of 35.9 fb^{-1}.

Table 5.1: Data sets used in this analysis, along with the corresponding luminosity and number of events. The data accumulated in these data sets was collected by the CMS experiment in proton-proton collisions during 2016, and corresponds to an integrated luminosity of 35.9 fb^{-1}.

Data set	Luminosity (fb^{-1})	Number of events
/SingleElectron/Run2016B-03Feb2017_ver2-v2	5.75	246,440,440
/SingleElectron/Run2016C-03Feb2017-v1	2.57	97,259,854
/SingleElectron/Run2016D-03Feb2017-v1	4.24	148,167,727
/SingleElectron/Run2016E-03Feb2017-v1	4.02	117,321,545
/SingleElectron/Run2016F-03Feb2017-v1	3.10	70,593,532
/SingleElectron/Run2016G-03Feb2017-v1	7.58	153,330,123
/SingleElectron/Run2016H-03Feb2017_ver2-v1	8.65	125,826,667
/SingleElectron/Run2016H-03Feb2017_ver3-v1		3,191,585
/SingleMuon/Run2016B-03Feb2017_ver2-v2	5.75	158,145,722
/SingleMuon/Run2016C-03Feb2017-v1	2.57	67,441,308
/SingleMuon/Run2016D-03Feb2017-v1	4.24	98,017,996
/SingleMuon/Run2016E-03Feb2017-v1	4.02	90,963,495
/SingleMuon/Run2016F-03Feb2017-v1	3.10	65,489,554
/SingleMuon/Run2016G-03Feb2017-v1	7.58	149,916,849
/SingleMuon/Run2016H-03Feb2017_ver2-v1	8.65	169,642,135
/SingleMuon/Run2016H-03Feb2017_ver3-v1		4,393,029

5.2.2 Simulated samples

Simulated samples, used for validating major backgrounds and estimating minor ones, are taken from the `RunIISummer16MiniAODv2-PUMoriond17` campaign. A list of the samples used, along with the cross sections for the corresponding processes, is presented in Table 5.3.

The signal is simulated utilising MadGraph5_aMC@NLO v2.4.2, using the "EWDim6" model, which implements the EFT described in Chapter 1. Events are first generated with the three aTGC parameters set to certain nonzero positive values, and then weights are assigned to different combinations of zero and nonzero values of aTGC parameters using the matrix element event weights computed by MadGraph5_aMC@NLO.

Five possible values are used for each parameter, forming a $5 \times 5 \times 5$ grid in the aTGC space. The set of values used for each parameter is shown in Table 5.2. The values were selected for simulation based on previous knowledge and an expectation of the final limits in such a way that the simulation comfortably covers scenarios well beyond the final limits. The triplet $(c_{\mathrm{WWW}}, c_{\mathrm{W}}, c_{\mathrm{B}}) = (0, 0, 0)$ corresponds to the SM production, and the sample is normalised such that the cross section in this scenario matches the SM NNLO cross section [151, 152].

Table 5.2: Values of aTGC parameters used for simulation. All combinations of the values are used, resulting in 125 scenarios.

Parameter	Used values $\left(\mathrm{TeV}^{-2}\right)$
$c_{\mathrm{WWW}}/\Lambda^2$	$-3.6, -1.8, 0, 1.8, 3.6$
c_{W}/Λ^2	$-4.5, -2.25, 0, 2.25, 4.5$
c_{B}/Λ^2	$-20, -10, 0, 10, 20$

The W+jets process is generated at NLO using MadGraph5_aMC@NLO v2.2.2, and normalised with a k-factor to the inclusive cross section calculated at NNLO using MCFM v6.6 [153]. The $\mathrm{t\bar{t}}$ process is simulated at NLO using Powheg v2.0, and normalised to the NNLO+NNLL cross section calculated using the Top++2.0 program [154]. The SM WW sample is produced using Powheg v1.0, whilst the WZ process is simulated using MadGraph5_aMC@NLO in combination with MadSpin. The samples are normalised to NNLO cross sections [151, 152]. Single top quark processes are simulated using Powheg v2.0, Powheg v1.0, and MadGraph5_aMC@NLO v2.2.2 for the t channel, associated tW production, and s channel, respectively, and the cross sections are calculated at NLO using the Hathor v2.1 program [155].

The parton showering and hadronisation steps for all samples are peformed with Pythia v8.212, with the exception of the single top quark s-channel sample, which uses v8.205. The FxFx merging scheme is used for all samples, with CUETP8M1 underlying event tune, with the exception of the $\mathrm{t\bar{t}}$ sample, which uses the CUETP8M2T4 tune. All events utilise NNPDF 3.0 parton distribution functions, and Geant4 is used for the simulation of the detector response.

Table 5.3: Signal and background simulated samples used in this analysis, along with their cross sections. Additional samples were used to warrant dropping out negligible contributions. The colours set here for the names of the samples will be used to represent their contributions in all the histograms and distributions in the following chapters.

Simulated sample	Cross section (pb)
WWToLNuQQ_MWW-600To800_PtW-180_aTGC_ShowerReconfig_13TeV-amcatnloFXFX-madspin-pythia8	-
WWToLNuQQ_MWW-800_PtW-180_aTGC_ShowerReconfig_13TeV-amcatnloFXFX-madspin-pythia8	-
WZToLNuQQ_MWZ-600To800_PtZ-180_aTGC_ShowerReconfig_13TeV-amcatnloFXFX-madspin-pythia8	-
WZToLNuQQ_MWZ-800_PtZ-180_aTGC_ShowerReconfig_13TeV-amcatnloFXFX-madspin-pythia8	-
WJetsToLNu_Pt-100To250_TuneCUETP8M1_13TeV-amcatnloFXFX-pythia8	$677.8 \times (k = 1.018)$
WJetsToLNu_Pt-250To400_TuneCUETP8M1_13TeV-amcatnloFXFX-pythia8	$24.08 \times (k = 1.018)$
WJetsToLNu_Pt-400To600_TuneCUETP8M1_13TeV-amcatnloFXFX-pythia8	$3.056 \times (k = 1.018)$
WJetsToLNu_Pt-600ToInf_TuneCUETP8M1_13TeV-amcatnloFXFX-pythia8	$0.4602 \times (k = 1.018)$
TT_TuneCUETP8M2T4_13TeV-powheg-pythia8	831.8
WWToLNuQQ_13TeV-powheg	50.00
WZTo1L1Nu2Q_13TeV_amcatnloFXFX_madspin_pythia8	11.46
ST_t-channel_top_4f_inclusiveDecays_13TeV-powhegV2-madspin-pythia8_TuneCUETP8M1	136.0
ST_t-channel_antitop_4f_inclusiveDecays_13TeV-powhegV2-madspin-pythia8_TuneCUETP8M1	80.95
ST_s-channel_4f_leptonDecays_13TeV-amcatnlo-pythia8_TuneCUETP8M1	3.406
ST_tW_antitop_5f_inclusiveDecays_13TeV-powheg-pythia8_TuneCUETP8M1	35.60
ST_tW_top_5f_inclusiveDecays_13TeV-powheg-pythia8_TuneCUETP8M1	35.60

5.3 Selection requirements on physics objects

In addition to the identification criteria and general quality requirements on physics objects discussed in Section 4.2, further requirements are imposed on the p_{T}, η, and other kinematic properties of electrons, muons, jets, and missing transverse momentum. These selection requirements serve to shortlist and consider only those objects which are interesting for this analysis.

5.3.1 Triggers

Since leptonic decay of a W boson is considered in final states containing an electron or a muon, for each channel, events passing a trigger, or a combination of triggers, that target this lepton are selected. Such triggers typically have significantly lower thresholds than a single-jet trigger.

Electrons are required to pass either of the high-level triggers HLT_Ele45_WPLoose_Gsf or HLT_Ele115_CaloIdVT_GsfTrkIdT. The former is seeded by an OR of several Level 1 triggers: L1_SingleEGx, L1_SingleIsoEGy, and L1_SingleIsoEG$z$er, with $x \in \{30, 32, 34, 36, 38, 40\}$, $y \in \{24, 26, 28, 30, 32, 34, 36\}$, $z \in \{22, 24, 26, 28, 30, 32, 34\}$, and requires $p_{\mathrm{T}} > 45$ GeV. The latter is seeded by an OR of L1_SingleEG, SingleJet, and SingleTau triggers, and requires $p_{\mathrm{T}} > 115$ GeV.

Muons are required to pass either HLT_Mu50 or HLT_TkMu50. These are seeded by the Level 1 triggers L1_SingleMu22 OR L1_SingleMu25. The trigger turn-on curve has been measured by the CMS muon physics object group (POG) [85,156], with a minimum muon $p_{\mathrm{T}} > 53$ GeV to be on the plateau.

5.3.2 Electrons

Two electron selections are defined, loose and tight. Both are required to pass the HEEPv70 identification, as discussed in Section 4.2, and have $|\eta| < 2.5$. Loose electrons are required to have $p_{\mathrm{T}} > 35$ GeV, whilst tight electrons have $p_{\mathrm{T}} > 50$ GeV.

5.3.3 Muons

Analogously, two muon selections are defined, loose and tight. Both are required to pass the high-p_{T} muon identification, have $|\eta| < 2.4$ and relative isolation < 0.1, as discussed in Section 4.2. Loose muons are required to have $p_{\mathrm{T}} > 20$ GeV, whilst tight muons have $p_{\mathrm{T}} > 53$ GeV.

5.3.4 Jets

AK8 jets, which are used as candidates for the hadronically decaying vector boson, are required to pass the jet identification requirements in Section 4.2, and have $p_{\mathrm{T}} > 200$ GeV and $|\eta| < 2.4$. AK8 jets are cleaned against tight muon and electron by removing jets that are within $\Delta R < 1$ of any tight muons or electrons. The hardest AK8 jet, which is used for reconstructing the hadronically decaying vector boson, is required to have $\tau_{21} < 0.55$ and $40 < m_{\mathrm{SD}} < 150$ GeV, where m_{SD} is the jet mass following soft drop jet grooming.

AK4 jets, which are used to veto $\mathrm{t\bar{t}}$ events utilising b tagging, are required to have $p_{\mathrm{T}} >$ 30 GeV and $|\eta| < 2.4$. AK4 jets are cleaned against tight muon and electron by removing jets that are within $\Delta R < 0.3$ of any tight muons or electrons. AK4 jets are also cleaned against the highest p_{T} AK8 jet, with a requirement of $\Delta R < 0.8$.

5.3.5 Missing transverse momentum

The missing transverse momentum is reconstructed, as discussed in Section 4.2, and a certain threshold of $p_{\mathrm{T}}^{\mathrm{miss}}$ is required for an event to be considered; this will be elaborated in the following section. In order to eliminate sources of $p_{\mathrm{T}}^{\mathrm{miss}}$ due to detector effects, several filters including noise, beam halo, and good vertices filters are applied according to internal CMS recommendations [157].

5.4 Event selection

The analysis presented in this thesis aims to reconstruct WW and WZ final states, where both vector bosons are heavily boosted. A W boson is reconstructed using its leptonic decay into either an electron or a muon, in combination with $p_{\mathrm{T}}^{\mathrm{miss}}$. Events are therefore divided into two channels based on the flavour of this lepton. Events in the electron (muon) channel are required to have exactly one tight electron (muon), with zero loose muons (electrons). They are also required to have $p_{\mathrm{T}}^{\mathrm{miss}} > 110(40)$ GeV. The motivation for this selection cut is discussed in Section 6.2.

To reconstruct the leptonically-decaying W boson, it is assumed that the event $p_{\mathrm{T}}^{\mathrm{miss}}$ is entirely due to the transverse component of the neutrino momentum. One can then reconstruct the longitudinal neutrino momentum by using the known W boson mass for the invariant mass of the combined lepton and neutrino four-momentum:

$$m_{\mathrm{W}}^2 = (p_\ell + p_\nu)^2\,, \tag{5.1}$$

leading to solutions for the longitudinal momentum of the neutrino:

$$p_{z,\nu} = \frac{\mu \cdot p_{z,\ell}}{p_{\mathrm{T},\ell}^2} \pm \sqrt{\frac{\mu^2 \cdot p_{z,\ell}^2}{p_{\mathrm{T},\ell}^4} - \frac{E_\ell^2 \cdot {p_{\mathrm{T}}^{\mathrm{miss}}}^2 - \mu^2}{p_{\mathrm{T},\ell}^2}}\,, \tag{5.2}$$

with $\mu = \frac{m_{\mathrm{W}}^2}{2} + \vec{p}_{\mathrm{T},\ell} \cdot \vec{p}_{\mathrm{T}}^{\mathrm{miss}}$. In the case of two real solutions, the solution with the smaller absolute value is assigned, whereas in the case of two complex solutions, the real part common to both is instead assigned. The accuracy of this method picking the correct solution is checked in simulated SM diboson samples, and found to be approximately 90%. The reconstructed leptonically decaying W boson is required to have $p_{\mathrm{T}} > 200$ GeV.

For the hadronically decaying vector boson, events are required to have at least one AK8 jet with $p_{\mathrm{T}} > 200$ GeV, and the highest-p_{T} AK8 jet satisfies the selection requirements put forth in the preceding section.

In addition, to target the back-to-back topology of the diboson event, requirements are placed on angles between the reconstructed objects. ΔR between the lepton and the hadronically-decaying vector boson candidate is required to be greater than $\pi/2$; the absolute value of $\Delta\phi$ between the hadronically-decaying vector boson candidate and missing transverse momentum must be greater than 2; and the absolute value of $\Delta\phi$ between the hadronically- and leptonically-decaying vector boson candidates is required to be greater than 2.

For the signal, events are also required to have zero b-tagged AK4 jets to suppress the $t\bar{t}$ background. Additionally, the invariant mass of the diboson system m_{WV} is required to be greater than 900 GeV to restrict the phase space to a region where the background can be described by a monotonically falling parametric function. A summary of the imposed selection requirements is presented in Table 5.4.

Table 5.4: Summary of selection requirements used for this analysis.

Selection cut	Electron channel	Muon channel
Lepton $p_T >$	50 GeV	53 GeV
Lepton $\|\eta\| <$	2.5	2.4
$p_T^{miss} >$	110 GeV	40 GeV
W_{lep} $p_T >$	200 GeV	200 GeV
Jet $p_T >$	200 GeV	200 GeV
Jet $\|\eta\| <$	2.4	2.4
Jet $\tau_{21} <$	0.55	0.55
Jet $m_{SD} \in$	$[40, 150]$ GeV	$[40, 150]$ GeV
$\Delta R(\text{jet}, \text{lep}) >$	$\pi/2$	$\pi/2$
$\|\Delta\phi(\text{jet}, \vec{p}_T^{miss})\| >$	2.0	2.0
$\|\Delta\phi(\text{jet}, W_{lep})\| >$	2.0	2.0
$m_{WV} >$	900 GeV	900 GeV

From the range of the AK8 jet m_{SD} presented above, the region $65 < m_{SD} < 105$ GeV is defined to correspond to signal events. The rest of the interval is used to enrich major background contributions in order to identify and suppress them. Furthermore, in order to better distinguish between WW and WZ events, the signal region is subdivided into WW-sensitive region ($65 < m_{SD} < 85$ GeV) and WZ sensitive region ($85 < m_{SD} < 105$ GeV). In addition to the signal regions, two control regions (CR) are defined, each designed to enrich a specific background contribution in a specific section of phase space:

- **W+jets control region:** The W+jets control region is defined similar to the signal region, but the requirement on m_{SD} is changed to $40 < m_{SD} < 65$ GeV or $105 < m_{SD} < 150$ GeV. The W+jets control region is also dubbed sideband, and the two intervals characterise upper and lower sidebands, respectively.

- **$t\bar{t}$ control region:** The $t\bar{t}$ control region is defined in the interval $40 < m_{SD} < 150$ GeV, but requires at least one b-tagged AK4 jet.

A schematic representation of how these control regions, along with the signal region, occupy the (m_{SD}, number of b tags)-plane is shown in Figure 5.6.

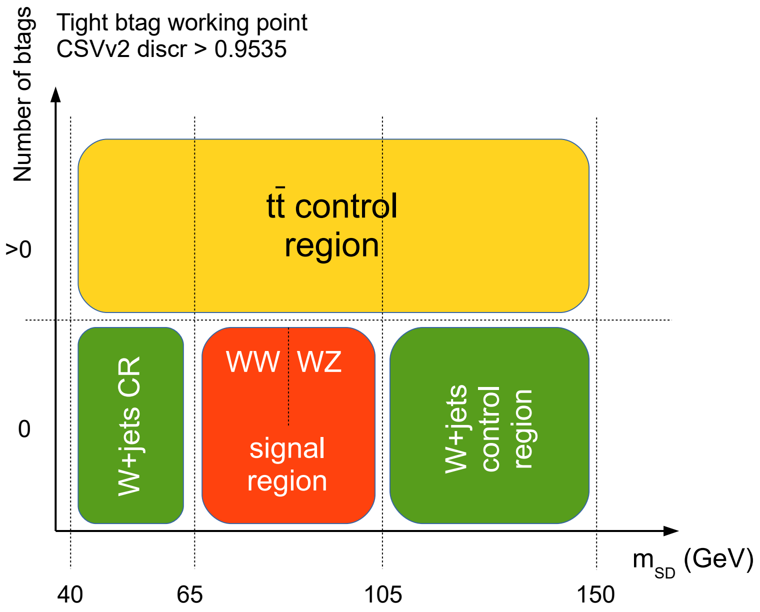

Figure 5.6: Schematic representation of signal and control regions used in this analysis. Control regions are used to identify and suppress the main background contributions.

5.5 Simulation corrections

Despite similar reconstruction and selection requirements, the outputs from data and simulation are not identical owing to differences in luminosity and efficiencies. In order to mitigate the effects of these discrepancies, data-to-simulation scale factors are derived and applied to simulation. The various sources of discrepancies and simulation corrections are discussed below.

5.5.1 Luminosity

The data collected by the CMS experiment in a data-taking period corresponds to an integrated luminosity that depends on the characteristics of the LHC. The number of simulated events is usually determined by the tradeoff between maximising statistics and the amount of available computing resources. The normalisation in the simulated samples is therefore different from the data collected by the CMS detector. In order to do like-for-like comparisons, events in every simulated sample are reweighted using a weight:

$$w_p = \frac{\sigma_p \times \int \mathscr{L}\mathrm{d}t}{N} \tag{5.3}$$

corresponding to the process p, where N is the number of simulated events in the sample, and $\int \mathscr{L} dt$ is the integrated luminosity in the data set.

5.5.2 Number of pileup interactions

The distribution of the number of pileup interactions in data is usually quite different from the one used in simulation. Simulated events are thus reweighted to ensure that their pileup distribution matches that in data. The distribution of the number of pileup interactions in data and simulation for this analysis is depicted in Figure 5.7, wherein there were an average of 23 proton-proton collisions per bunch crossing. The reweighting is performed by comparing the distributions in minimum bias events, where the cross section of minimum bias events is taken to be 69.2 mb [158].

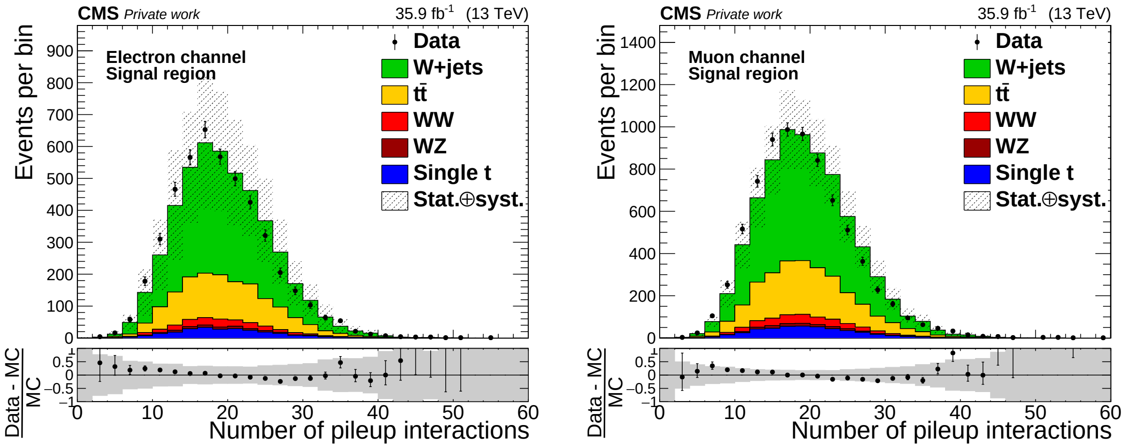

Figure 5.7: Comparison between the number of pileup interactions in data and simulation for the electron (left) and muon (right) channels. The hashed region in the main plots and the grey band in the lower ratio plots represent the combined statistical and systematic uncertainties, with the details of the latter discussed in the following section.

5.5.3 Trigger efficiencies

The efficiencies of triggers are not same in data and simulation. Figure 5.8 shows the efficiencies of the trigger combinations used in this analysis, as a function of p_T and η. The efficiencies were extracted using the tag-and-probe method, starting with HEEP and high-p_T muon identifications. Scale factors are derived as a bin-by-bin ratio of the efficiencies in data to the ones in simulation, and applied to simulated events. This analysis uses the same set of electron and muon triggers as the corresponding resonance search [159], and similar scale factors can be used for both analyses.

5.5.4 Lepton efficiencies

In addition to the triggers, scale factors are also required for the efficiencies of reconstruction and identification of leptons. The total lepton efficiency can be written as:

$$\epsilon^{\ell} = \epsilon^{\ell}_{\mathrm{ID}} \cdot \epsilon^{\ell}_{\mathrm{iso|ID}} \cdot \epsilon^{\ell}_{\mathrm{trigger|iso}}, \tag{5.4}$$

where each factor of efficiency is measured taking as denominator the leptons passing the previous step. The scale factors are generally extracted using the tag-and-probe method.

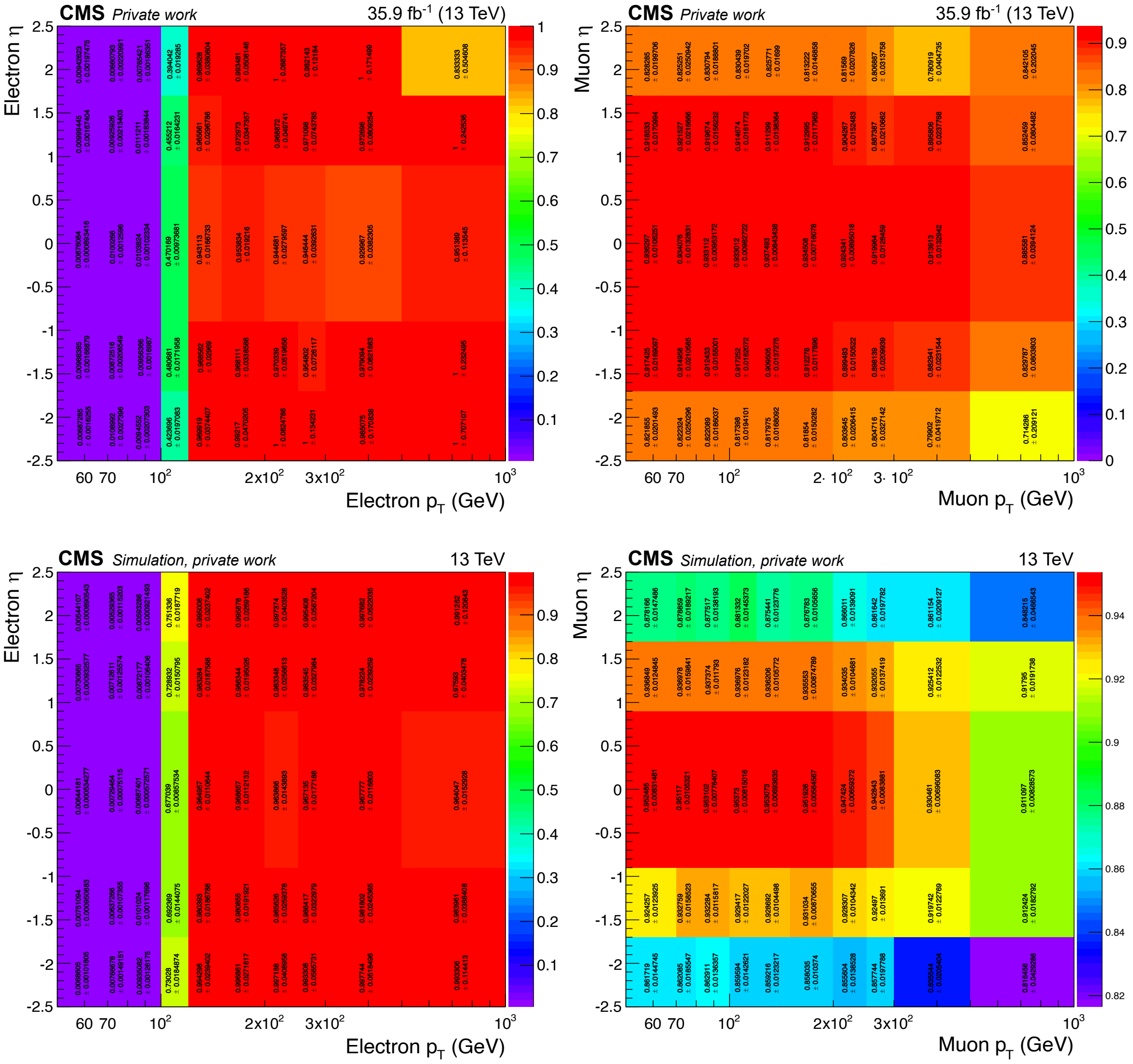

Figure 5.8: Trigger efficiencies as a function of p_T and η, for the combination of the electron (left) and muon (right) triggers used in this analysis. Efficiencies in data and simulation are shown on the top and bottom, respectively. Appropriate scale factors are used to account for the differences in the efficiencies.

For the electrons, scale factors accounting for both reconstruction and HEEP identification efficiency differences are produced [160], and applied to simulation. For the muons, series of run-dependent scale factors are produced [156, 161]. To apply these to simulation, luminosity-weighted averaged scale factors are used, since the running conditions in data-taking eras B–F were different from eras G and H.

5.5.5 Jet energy scale and resolution

In addition to the standard jet energy corrections, discussed in Section 4.2, a "hybrid" method for jet energy resolution correction is used with the recommended scale factors [162]. In the hybrid method, jets are smeared differently depending on if they are matched to a generator-level jet. If there is a matching generator-level jet, the reconstructed jet is scaled by a factor c, where:

$$c = 1 + (s_{\mathrm{JER}} - 1)\,\frac{p_{\mathrm{T}} - p_{\mathrm{T}}^{\mathrm{gen}}}{p_{\mathrm{T}}}, \tag{5.5}$$

where p_{T} and $p_{\mathrm{T}}^{\mathrm{gen}}$ are the transverse momenta of the reconstructed and generator-level jets, respectively, and s_{JER} is the data-to-simulation resolution scale factor. The smearing factor, in case there is no matching generator-level jet, is given by:

$$c = 1 + \mathcal{N}(0, \sigma_{\mathrm{JER}})\sqrt{\max\left(s_{\mathrm{JER}}^2 - 1, 0\right)}, \tag{5.6}$$

where σ_{JER} is the relative p_{T} resolution in simulation, and $\mathcal{N}(0, \sigma)$ represents a number drawn from a Gaussian distribution with mean 0 and standard deviation σ. In both cases, c is constrained to be non-negative, so that the resolution in simulation can only be degraded.

5.5.6 Vector boson identification efficiencies

The identification of hadronically decaying vector bosons using boosted topology variables is also prone to differences in efficiencies for data and simulation. A scale factor of 1 ± 0.0094 is derived for m_{SD} [163], with a double crystal ball fit using Pythia. In addition, m_{SD} in simulation is also smeared using the same procedure as for the jet energy resolution smearing, with $\sigma_{\mathrm{JER}} = 10.1 \pm 0.05$, and $s_{\mathrm{JER}} = 1 \pm 0.2$. A scale factor for the difference in τ_{21} efficiency in data and simulation is calculated as 1.03 ± 0.14 [163], and applied to simulated samples with a real W/Z boson — $\mathrm{t\bar{t}}$, WW, WZ, and associated tW production.

5.5.7 b tagging efficiencies

The efficiencies for identifying b jets differ slightly in data and simulation. In order to account for this effect, the recommended recipe is used [164], wherein simulated events are reweighted using a weight w constructed from the ratio of tagging probabilities in data and simulation :

$$w = \frac{P(\mathrm{data})}{P(\mathrm{MC})}, \tag{5.7}$$

with each probability P being a product over all AK4 jets in the event,

$$\begin{aligned} P(\mathrm{data}) &= \prod_{i \in \mathrm{tagged}} s_i \epsilon_i \prod_{j \in \mathrm{not\ tagged}} (1 - s_j \epsilon_j), \\ P(\mathrm{MC}) &= \prod_{i \in \mathrm{tagged}} \epsilon_i \prod_{j \in \mathrm{not\ tagged}} (1 - \epsilon_j), \end{aligned} \tag{5.8}$$

where ϵ_i is the MC b tagging efficiency, and s_i is the data-to-simulation tagging efficiency scale factor. The scale factors are provided in Reference [165], and require the measurement of b tagging efficiency in simulated samples in the analysis phase space. Therefore, b-tagging efficiencies for b jets and mistagging efficiencies for c and light jets, in simulated events in the phase space considered in this analysis, are measured, shown in Figure 5.9 for the $\mathrm{t\bar{t}}$ sample. Additional figures for b- and mistagging efficiencies in other simulated samples are shown in Appendix A.1.

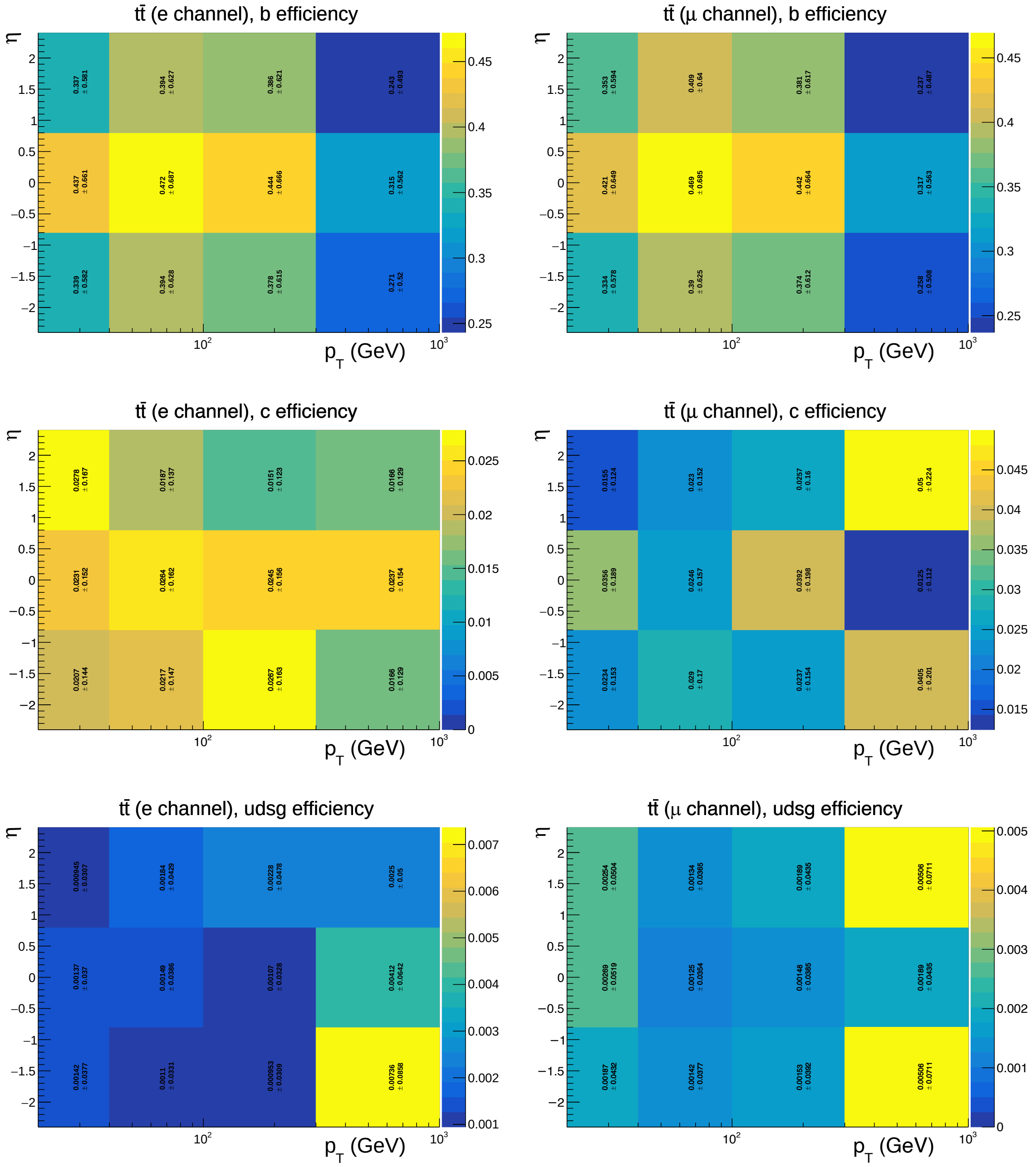

Figure 5.9: b tagging efficiencies as a function of p_{T} and η for the simulated $\mathrm{t\bar{t}}$ sample in the electron (left) and muon (right) channels. b tagging efficiencies for b jets and mistagging efficiencies for c and light jets are shown on the top, middle, and bottom, respectively.

5.5.8 Missing transverse momentum corrections

In addition to the type-0 and type-I corrections to $p_{\mathrm{T}}^{\mathrm{miss}}$, mentioned in Section 4.2, type-XY corrections [166] have to be applied to correct for ϕ-modulation of the $p_{\mathrm{T}}^{\mathrm{miss}}$ direction. This is important since the direction of $p_{\mathrm{T}}^{\mathrm{miss}}$ becomes dependent on ϕ owing to several detector and beam effects. Different type-XY corrections are applied to data and simulation since the required parameters are not identical. The parameters used for the corrections in data-taking eras B–F, G and H, and simulation are detailed in Reference [167].

5.6 Sources of systematic uncertainty

Like any physical measurement, the analysis presented in this thesis is prone to systematic uncertainties from a multitude of sources. The sources include uncertainties from the theory in modelling the signal and background processes, as well as experimental sources in measurement of different constituents. Systematic uncertainties are incorporated into the analysis by propagating the contribution from each source to the normalisation and shape of signal and background models, and using them as constraints in the final fit to data. The most significant sources of uncertainty are discussed below, and the impact of the sources on normalisation and shape parameters is discussed in Chapter 6.

5.6.1 Theoretical sources

The systematic uncertainties from theory arise from the modelling of PDFs and the choice of μ_{F} and μ_{R}.

- **PDF and $\alpha_{\mathrm{S}}(m_{\mathrm{Z}}^2)$:** PDF and $\alpha_{\mathrm{S}}(m_{\mathrm{Z}}^2)$ uncertainties are incorporated by following the PDF4LHC [168] recommendations, wherein 100 variations of the nominal NNPDF3.0 are considered. The corresponding cross sections are reordered in ascending order:

  $$\sigma^{(1)} \leqslant \sigma^{(2)} \leqslant \ldots \leqslant \sigma^{(99)} \leqslant \sigma^{(100)}, \tag{5.9}$$

  and the PDF uncertainty, computed at 68% CL, is given by:

  $$\delta^{\mathrm{PDF}}\sigma = \frac{\sigma^{(84)} - \sigma^{(16)}}{2}. \tag{5.10}$$

  The value of α_{S} and its associated uncertainty is [40]:

  $$\alpha_{\mathrm{S}}(m_{\mathrm{Z}}^2) = 0.1181 \pm 0.0015. \tag{5.11}$$

  In order to incorporate the uncertainty from α_{S}, the predictions are recomputed using upper and lower values of α_{S} for the PDF sets, and the results are added in quadrature.

- **Factorisation and renormalisation scales:** Uncertainties corresponding to the choice of factorisation and renormalisation scales are computed by multiplying/dividing the scales by a factor of two, and quoting the envelope of the output variations as the scale uncertainty. The permutations where one of the scales is increased and the other is decreased simultaneously are not considered per recommendation, since these permutations are excessively pessimistic.

5.6.2 Experimental sources

Uncertainties from various experimental sources are considered, as discussed below.

- **Luminosity:** A 2.5% uncertainty [169] is included to reflect the uncertainty in the integrated luminosity measurement of the 2016 data set.

- **Pileup:** Uncertainty associated with pileup reweighting is calculated based on the input uncertainty (4.6%) in the measurement of the minimum bias cross section [158].

- **Lepton identification:** Uncertainties in the measurement of lepton efficiency and identification scale factors are considered. For the high energy leptons considered in this analysis, additional uncertainties are added to account for the larger uncertainty in the scale factors at higher lepton energies. For the electons in the barrel region, this uncertainty is 1% below 90 GeV, 2% between 90 GeV and 1 TeV, and 3% above 1 TeV; in the endcaps it is 1% below 90 GeV, 2% between 90 and 300 GeV, and 4% above 300 GeV [160]. For the muons, an additional 1% uncertainty is added related to the muon identification criteria, 0.5% related to the isolation requirements, and 0.5% related to the single-muon triggers [161].

- **Lepton energy scale:** An uncertainty is estimated by propagating the effect of varying the lepton energy scale within its uncertainty. The uncertainty in lepton energy scale is estimated to be 1.4% in the electron channel, and a scaling value in the muon channel, where the uncertainty is 0.2% below, and an extra $0.05 \cdot p_{\mathrm{T}}/\mathrm{TeV}$ above 200 GeV.

- **Lepton resolution:** A similar uncertainty in lepton resolution is considered by matching leptons to generator-level leptons, and varying the resolution uncertainty. Uncertainties of 1.16%, 1.61%, and 0.6% are considered for electrons in the barrel and endcap regions, and muons, respectively.

- **Jet energy scale:** W-jet momentum and $p_{\mathrm{T}}^{\mathrm{miss}}$ are recomputed after varying the jet energy scale, within its uncertainty [137], for both AK4 and AK8 jets, simultaneously.

- **Jet energy resolution:** Similarly, the smearing procedure is repeated after varying the resolution scale factor within its uncertainty.

- **Vector boson identification:** A 14% uncertainty on normalisation, arising from uncertainty in jet substructure variables, is considered. This uncertainty corresponds to the mismodelling of the τ_{21} selection efficiency [170].

- **b tagging and mistagging:** The uncertainties in efficiencies of b tagging and mistagging are taken into account. The biggest impact of b tagging uncertainties is on the normalisation of $\mathrm{t\bar{t}}$ and single top quark backgrounds, whilst mistagging uncertainties only have a small impact on all contributions.

- **Missing transverse momentum:** In addition to the propagation of uncertainties from the above mentioned sources to $p_{\mathrm{T}}^{\mathrm{miss}}$, the influence of unclustered energy deposits on $p_{\mathrm{T}}^{\mathrm{miss}}$ are also evaluated and propagated to the final uncertainties.

The impact of the systematic uncertainties on the normalisation and shape parameters of signal and background contributions is discussed in Chapter 6, following the description of the modelling of the respective contributions.

The usual approach of science of constructing a mathematical model cannot answer the questions of why there should be a universe for the model to describe. Why does the universe go to all the bother of existing?

……

– Stephen Hawking,
A brief history of time

6

Signal modelling and background estimation

Crux of the matter —

This chapter elucidates the modelling of signal and background contributions. The modelling of signal distributions, using parametric functions, is first put forth, followed by a description of the impact of systematic uncertainties. Data-to-simulation comparison in control regions is presented, followed by the procedure used for estimating the background contributions. In particular, the estimation of W+jets background from sidebands using a transfer function is explained. The chapter concludes by introducing the setup of a modified two-dimensional fit to data, and highlighting the impact of uncertainties on background contributions.

Kinematic distributions of the diboson system, including softdrop groomed jet mass of the hadronically decaying vector boson m_{SD} and invariant mass of the diboson system m_{WV}, contain indispensable information about signal and background processes. In the analysis presented in this thesis, the aforementioned kinematic distributions are modelled with parametric functions. The signal and background models are first derived from simulation, and then fitted to data to extract the signal and data-driven background contributions.

6.1 Signal modelling

The signal model is constructed realising that additional contributions from anomalous couplings to diboson processes impact the normalisation as well as shape of kinematic distributions, having an especially pronounced effect on the shape of the m_{WV} distribution at high diboson mass. The modelling of the normalisation and shape of the signal distributions is discussed below.

6.1.1 Normalisation

Considering the EFT Lagrangian of Equation 1.51, one can deduce that there are several contributions in case of nonzero aTGCs to the diboson cross section. For each anomalous coupling, these contributions include a term depending on the square of the coupling parameter, an interference term with the SM depending linearly on the coupling parameter, and interference terms with other anomalous couplings. Out of these, the quadratic term dominates at high energies; therefore, additional contributions from anomalous couplings generally enhance the relevant diboson cross section. The impact of nonzero anomalous coupling parameters on the normalisation of simulated WW and WZ m_{SD} distributions is shown in Figure 6.1 and Appendix A.2 for the positive and negative working points, respectively, where the working points for each parameter are taken to be the highest and lowest values considered in simulation, as listed in Table 5.2.

The operators associated with c_{WWW} and c_{W} induce similar contributions to both the WW and WZ processes. However, the operator associated with c_{B} only enhances the WW cross section, with negligible contributions to the WZ cross section. This is visible in the bottom plots in Figure 6.1. It is also the primary reason for splitting the signal region into the WW and WZ sensitive regions, since in the case of nonzero aTGCs, split signal regions would help distinguish between c_{B} and the other two couplings.

Keeping in view the contributions of anomalous couplings to the diboson cross section, as discussed above, the normalisation of the signal can be modelled as:

$$N_{\mathrm{signal}} = N_{\mathrm{SM}} + \sum_i \left(N_{c_i,1} c_i^2 + N_{c_i,2} c_i\right) + \sum_{i<j} \left(N_{c_i,c_j} c_i c_j\right), \tag{6.1}$$

where N_{SM} is the number of events corresponding to the SM cross section including a LO-to-NNLO k-factor, which has already been incorporated when the signal samples were scaled to the NNLO cross section, as discussed in Section 5.2, and c_i and c_j are the anoma-

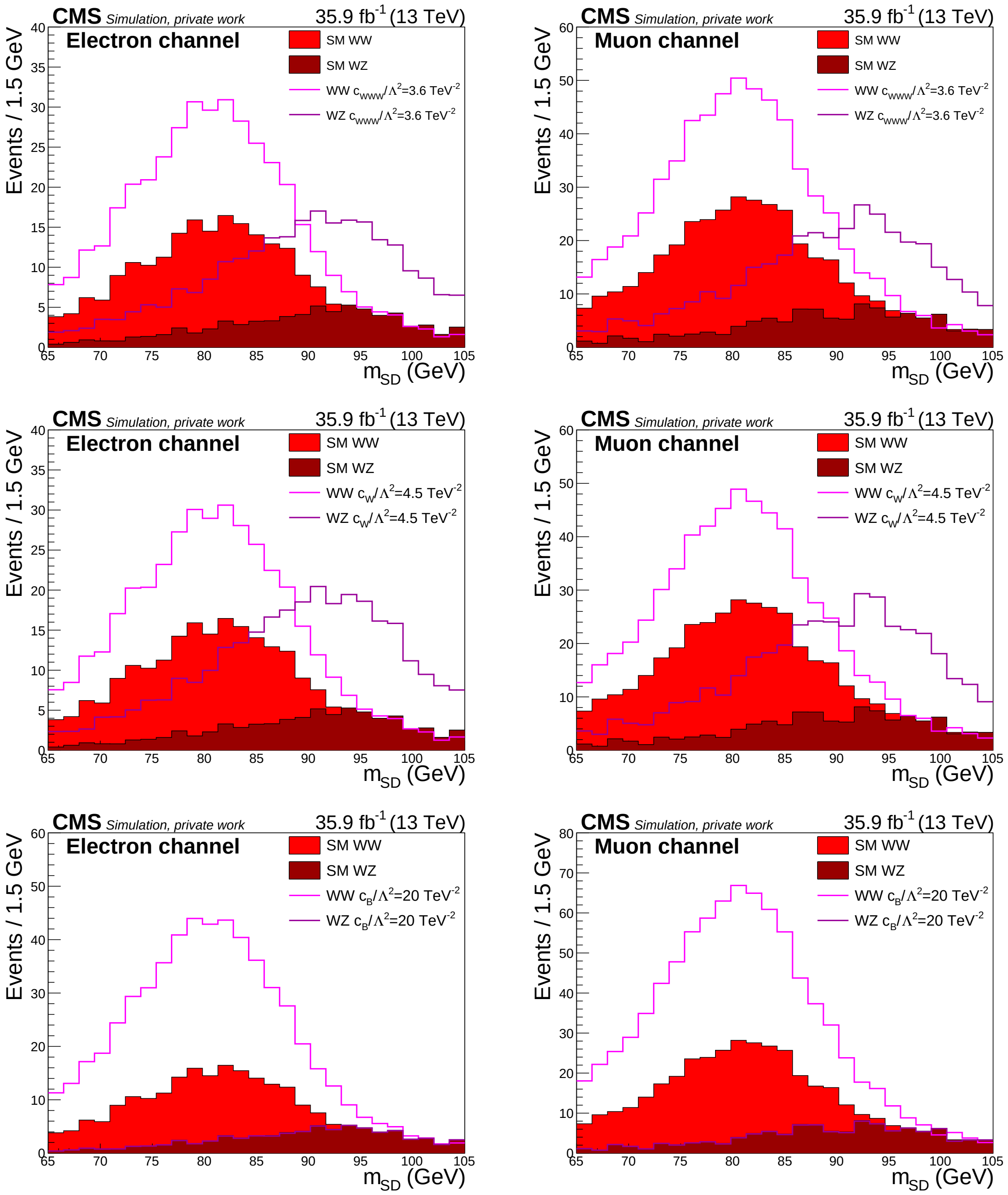

Figure 6.1: Impact of nonzero aTGCs on signal m_{SD} distributions in the electron (left) and muon (right) channels. The impact of $c_{\mathrm{WWW}}/\Lambda^2 = 3.6\ \mathrm{TeV}^{-2}$, $c_{\mathrm{W}}/\Lambda^2 = 4.5\ \mathrm{TeV}^{-2}$, and $c_{\mathrm{B}}/\Lambda^2 = 20\ \mathrm{TeV}^{-2}$ is shown on the top, middle, and bottom, respectively.

lous coupling parameters, normalised to their respective working points:

$$\begin{aligned} c_1 &= \frac{1}{3.6}\frac{c_{\mathrm{WWW}}}{\Lambda^2}, \\ c_2 &= \frac{1}{4.5}\frac{c_{\mathrm{W}}}{\Lambda^2}, \\ c_3 &= \frac{1}{20}\frac{c_{\mathrm{B}}}{\Lambda^2}. \end{aligned} \tag{6.2}$$

The normalisations $N_{c_i,1}$, $N_{c_i,2}$, and N_{c_i,c_j} are extracted from simulation by considering simulated event yields for certain combinations of aTGC parameter values. $N_{c_i,1}$ and $N_{c_i,2}$ are obtained by using simulated event yields $N_{c_i^+}$ and $N_{c_i^-}$ with the parameter c_i equal to positive and negative value of the working point, respectively:

$$\begin{aligned} N_{c_i,1} &= \frac{N_{c_i^+} + N_{c_i^-}}{2} - N_{\mathrm{SM}}, \\ N_{c_i,2} &= \frac{N_{c_i^+} - N_{c_i^-}}{2}. \end{aligned} \tag{6.3}$$

N_{c_i,c_j} are then obtained by utilising the simulated event yield $N_{c_i^+ c_j^+}$ with both parameters equal to their respective positive working points:

$$\begin{aligned} N_{c_i,c_j} &= N_{c_i^+ c_j^+} - N_{\mathrm{SM}} - (N_{c_i,1} + N_{c_i,2}) - \left(N_{c_j,1} + N_{c_j,2}\right), \\ &= \left(N_{c_i^+ c_j^+} + N_{\mathrm{SM}}\right) - \left(N_{c_i^+} + N_{c_j^+}\right). \end{aligned} \tag{6.4}$$

6.1.2 Shape

It is evident from Figure 6.1 that anomalous couplings do not significantly change the shape of the m_{SD} distribution. However, there is a remarkable change in the shape of the m_{WV} distribution, which deviates from the SM contribution quite significantly at high diboson mass. The m_{WV} distribution broadly exhibits an exponentially decaying spectrum, which is the result of the convolution of the intrinsic power spectrum and the steeply falling PDFs. This exponential behaviour is modified by anomalous coupling contributions, including the quadratic, SM-aTGC interference, and aTGC-aTGC interference terms, analogous to the ones in Equation 6.1. These considerations motivate the selection of a signal function, including shape, of the form:

$$\begin{aligned} F_{\mathrm{signal}}(m_{\mathrm{WV}}) =& N_{\mathrm{SM}}\left(e^{a_{\mathrm{SM}} m_{\mathrm{WV}}} + e^{a_{\mathrm{corr}} m_{\mathrm{WV}}}\right) \\ &+ \sum_i \left(N_{c_i,1} c_i^2 e^{a_{i,1} m_{\mathrm{WV}}} \left(\frac{1 + \mathrm{erf}[(m_{\mathrm{WV}} - a_{0,i})/a_{\mathrm{w},i}]}{2} \right) + N_{c_i,2} c_i e^{a_{i,2} m_{\mathrm{WV}}} \right) \\ &+ \sum_{i<j} \left(N_{c_i,c_j} c_i c_j e^{a_{ij} m_{\mathrm{WV}}} \right), \end{aligned} \tag{6.5}$$

where a_{SM}, $a_{i,1}$, $a_{i,2}$, and a_{ij} are the exponential decay constants of the various contributions, and erf is the error function:

$$\mathrm{erf}(x) = \frac{2}{\sqrt{\pi}} \int_0^x e^{-t^2} \mathrm{d}t, \tag{6.6}$$

included to accurately model the turn-on behaviour of the anomalous coupling contributions. The parameters $a_{0,i}$ and $a_{\mathrm{w},i}$ characterise the turn-on threshold and steepness of the error function, and a_{corr} is the decay constant of a small correction term added to account for the deviation of the SM contribution from a simple exponential at higher values of m_{WV}.

The shape parameters are determined from fits to simulated m_{WV} distributions, analogous to the determination of the normalisation constants. First, the SM parameters a_{SM} and a_{corr} are determined from a fit to simulation without anomalous couplings. The SM-aTGC interference parameters $a_{i,2}$ are then extraced by comparing shapes when an aTGC parameter is set to positive and negative working points. Consequently, the pure aTGC parameters $a_{i,1}$, $a_{0,i}$, and $a_{\mathrm{w},i}$ are derived from a simultaneous fit of the pure aTGC and the already obtained

SM and SM-aTGC contributions to simulation where a single aTGC parameter has been set to its working point. Finally, the aTGC–aTGC interference parametes are determined by comparing the simulation with pairs of aTGC parameters set to nonzero values. Some contributions, including SM-c_{WWW} interference, c_{WWW}-c_{B} interference, and the turn on error function for c_{B} in the WZ region are found to be insignificant, and ignored in order to simplify the signal model a bit.

The extracted signal model, with the coupling parameters set to zero and their respective working points, and the corresponding simulated distributions are shown in Figures 6.2 and 6.3 for the WW and WZ categories, respectively. For validation, the extracted signal model with the coupling parameters set to intermediate values is compared to the corresponding simulation, which is different from the ones used to extract the model. Additional figures with the signal model and simulated distributions corresponding to negative working points are given in Appendix A.3.

6.1.3 Impact of systematic uncertainties

Since the parameters of the signal function defined in Equation 6.5 are extracted from simulation, they are affected by systematic uncertainties. In order to calculate the impact of each source of systematic uncertainty discussed in Section 5.6, a simplified signal model, without considering the interference terms, is utilised. The simplified model is first fitted to the simulation with an anomalous coupling parameter set to its working point. The model is then refitted to corresponding simulations where a single source of systematic uncertainty has been varied up and down within its input uncertainty, and the larger difference in the resulting extracted shape parameter is noted. This is done for all the sources, and the final estimate is obtained by considering the sources of uncertainty uncorrelated, and adding their impacts in quadrature.

The estimated total uncertainty on signal shape parameters for both channels and categories is shown in Table 6.1, whilst the impact of individual sources is given in Appendix A.4. The largest impact comes from uncertainty in PDFs and the choice of factorisation and renormalisation scales, with smaller contributions from experimental sources. Uncertainties in luminosity and identification of vector bosons are not considered, since they only affect the normalisation of the process. Figures containing details of shape systematic uncertainties, depicting the nominal model along with the extracted uncertainty band, for the WW and WZ categories are given in Appendix A.4.

Table 6.1: Estimated total uncertainty (%) on signal shape parameters. The effect of a source of uncertainty on the signal shape is calculated by refitting the model to the corresponding variations in simulated samples, and the total uncertainty is obtained by combining the effect of all individual sources.

	WW category		WZ category	
Shape parameter	Electron channel	Muon channel	Electron channel	Muon channel
$a_{c_{\mathrm{WWW}}}$	5.11	5.05	6.55	4.37
$a_{c_{\mathrm{W}}}$	4.19	5.08	5.43	3.68
$a_{c_{\mathrm{B}}}$	3.35	2.35	5.05	4.56

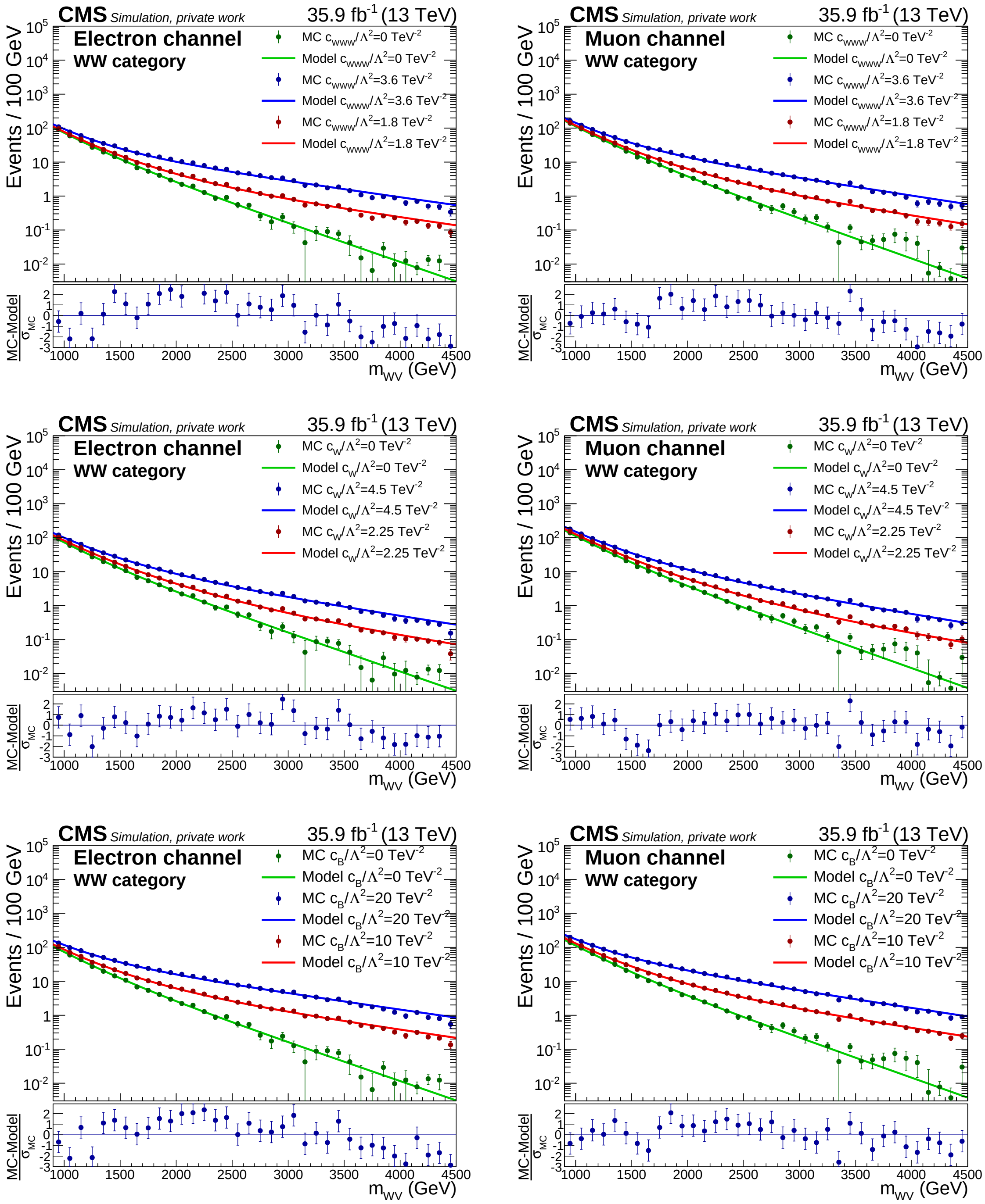

Figure 6.2: Simulated events (points) and the extracted signal model (solid curves) in the electron (left) and muon (right) channels for the WW category. The model is extracted by fitting a parametric function to events without anomalous couplings, shown in green, and with anomalous coupling parameters set to $c_{\mathrm{WWW}}/\Lambda^2 = 3.6\ \mathrm{TeV}^{-2}$ (top), $c_{\mathrm{W}}/\Lambda^2 = 4.5\ \mathrm{TeV}^{-2}$ (middle), and $c_{\mathrm{B}}/\Lambda^2 = 20\ \mathrm{TeV}^{-2}$ (bottom), shown in blue. For further validation, the interpolated model with an intermediate value of the respective aTGC, shown in red, is compared to a corresponding simulated sample, thereby showing good agreement between the model and MC events.

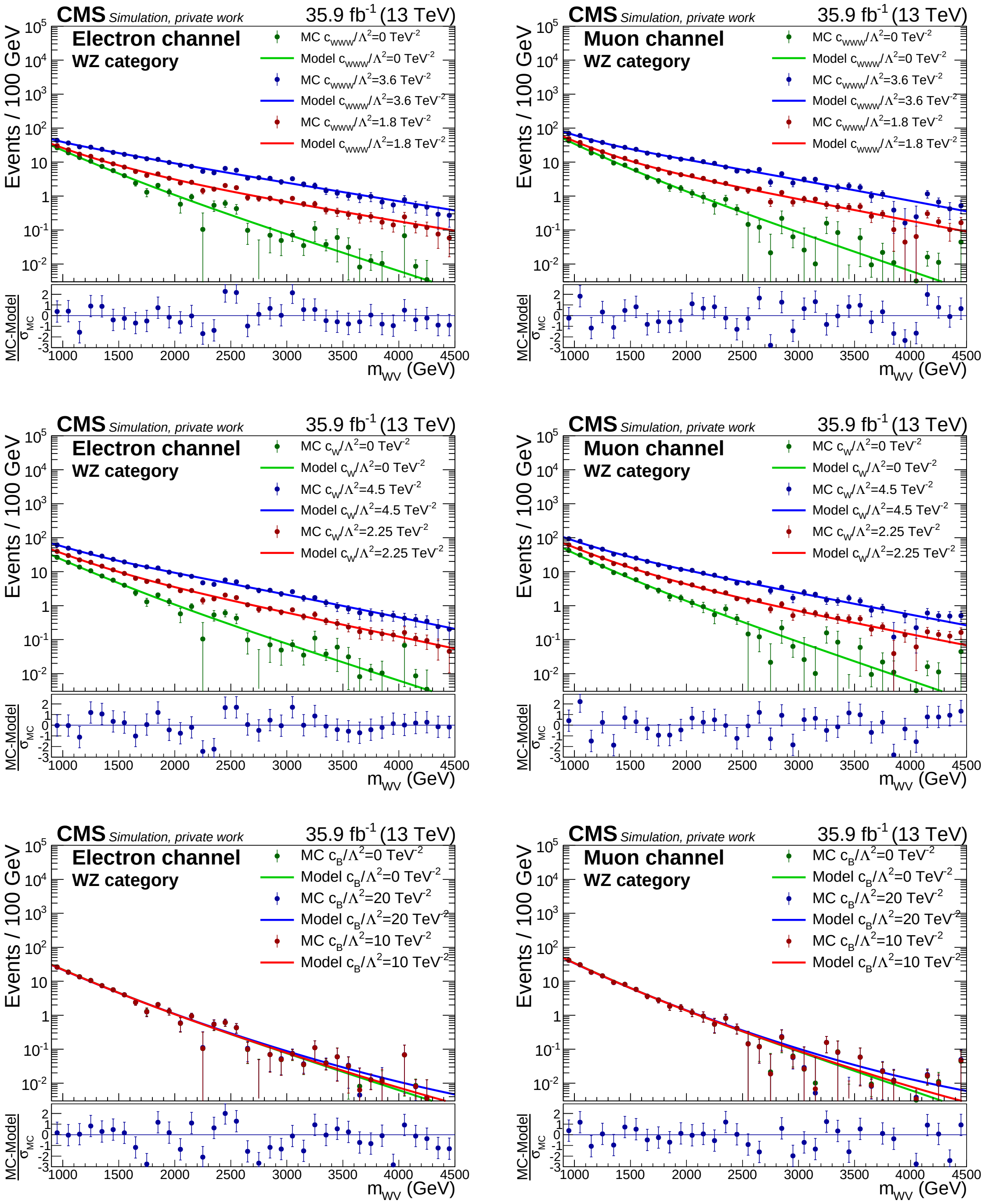

Figure 6.3: Simulated events (points) and the extracted signal model (solid curves) in the electron (left) and muon (right) channels for the WZ category. The model is extracted by fitting a parametric function to events without anomalous couplings, shown in green, and with anomalous couplings, shown in blue. For further validation, the interpolated model with an intermediate value of the respective aTGC, shown in red, is compared to a corresponding simulated sample, thereby showing good agreement between the model and MC events. The bottom plots reiterate the fact that the parameter c_{B} only enhances the cross section of the WW process and leaves the WZ cross section unchanged.

6.2 Background estimation

As discussed in Chapter 5, the signal output is contaminated by various background processes. A multitude of techniques are used to estimate the background contributions. The most significant background, W+jets, is derived entirely from data. For the $\mathrm{t\bar{t}}$ process, the normalisation is fixed in the final fit to data, whilst the shape parameters are first determined by fitting parametric functions to simulation, and the fit uncertainties are used as priors during the final fit. Minor background contributions, SM diboson and single top quark production, are estimated by fitting to simulation, and keeping the derived functions fixed in the final fit. Prior to the fits to simulation and data, MC modelling of the background processes is validated in control regions.

6.2.1 Comparison between data and simulation in control regions

In order to validate the MC modelling of background contributions in the simulated samples, two control regions are defined as discussed in Section 5.4. Each control region is designed explicitly to enrich a certain background contribution, while suppressing contamination from the signal processes. The agreement between data and simulation for various variables, in both the W+jets and $\mathrm{t\bar{t}}$ control regions, is verified by a χ^2 test, with the p-value being greater than 0.99 in all cases.

The W+jets control region is closely related to the signal region, differing only in the selection requirement on m_{SD}. Events in the W+jets control region are required to have m_{SD} smaller than 65 GeV, or larger than 105 GeV. Data-to-simulation comparison for the m_{SD} and m_{WV} distributions in the W+jets control region is shown in Figure 6.4 for both the electron and muon channels. The simulated distributions are normalised to the total integrated luminosity of the data using their respective SM cross sections. The combined effect of a limited number of simulated events and contributions from sources of systematic uncertainty is indicated with the hashed region in the main plots and the grey bands in the ratio plots. The blank space in the m_{SD} distribution in the interval $65 < m_{\mathrm{SD}} < 105$ GeV corresponds to the phase space of the signal region.

Owing to the fact that the efficiency of identifying bottom quark jets, used to veto the $\mathrm{t\bar{t}}$ background process, is 41%, it is evident that there is a significant amount of contribution from the $\mathrm{t\bar{t}}$ process in the distributions in the W+jets control region. Data-to-simulation comparison for the distribution of the p_{T} of the jet, p_{T} of the lepton, τ_{21}, and $p_{\mathrm{T}}^{\mathrm{miss}}$ is shown in Figure 6.6, demonstrating a good agreement between data and simulation. Additional figures depicting data-to-simulation comparison for several other variables can be found in Appendix A.5.

The $\mathrm{t\bar{t}}$ control region differs from the signal region in the number of b-tagged jets, and is designed to enrich events with top quarks. Events are classified as belonging to the $\mathrm{t\bar{t}}$ control region if they contain at least one b-tagged jet. Data-to-simulation comparison for the m_{SD} and m_{WV} distributions in the $\mathrm{t\bar{t}}$ control region is shown in Figure 6.5 for both the electron and muon channels. The simulated distributions are normalised to the total integrated luminosity of the data using their respective SM cross sections.

The small contribution from the W+jets process in the distributions in the $\mathrm{t\bar{t}}$ control region

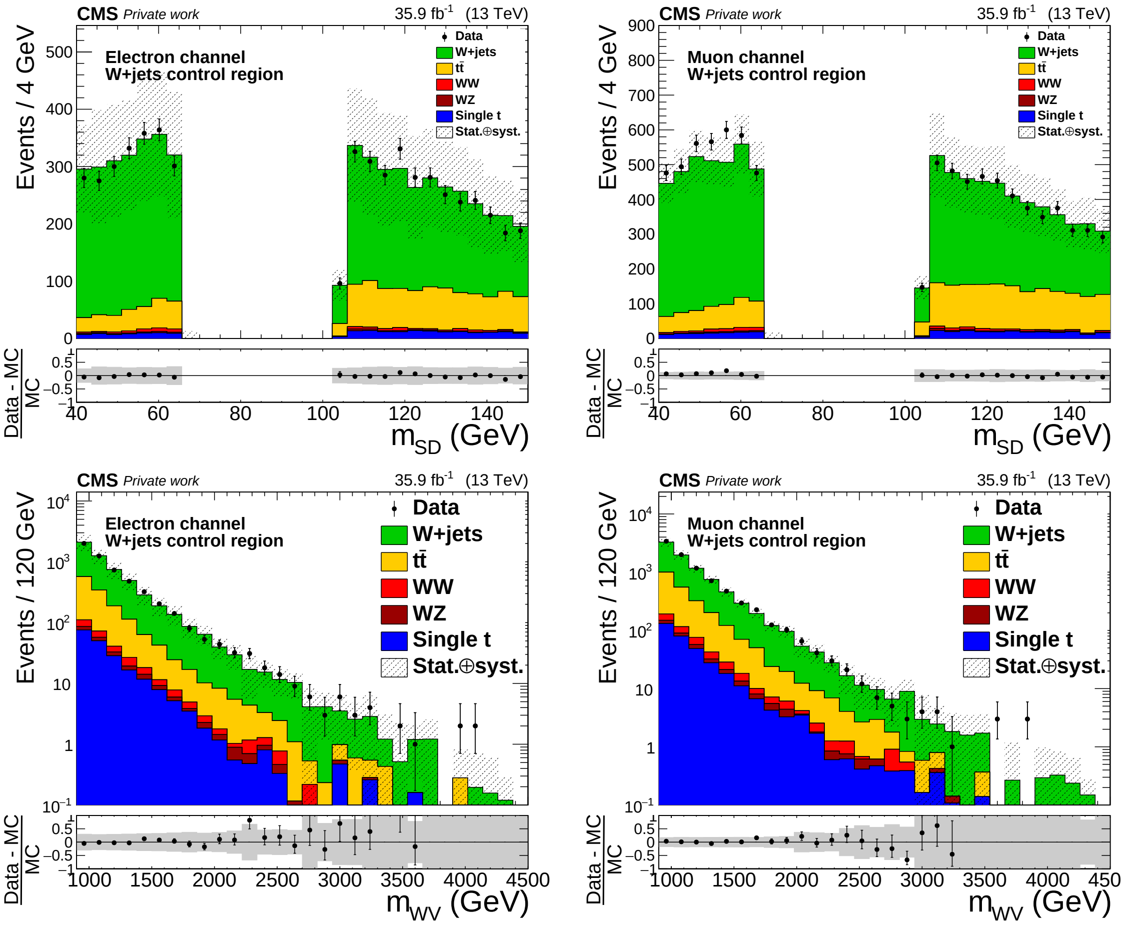

Figure 6.4: Comparison between data and simulation for the m_{SD} (upper) and m_{WV} (lower) distributions in the W+jets control region. The electron and muon channels are shown on the left and right, respectively. The different contributions have been normalised to the luminosity of the data using their respective SM cross sections. The hashed region in the main plots and the grey band in the ratio plots show the combined effect of statistical and systematic uncertainties.

reaffirms the low mistag rate of the b tagging technique used. Data-to-simulation comparison for the distribution of the p_{T} of the jet, p_{T} of the lepton, τ_{21}, and $p_{\mathrm{T}}^{\mathrm{miss}}$ is shown in Figure 6.7, demonstrating a good agreement between data and simulation. Additional figures depicting data-to-simulation comparison for several other variables can be found in Appendix A.5.

Inspite of the good agreement between data and simulation in both the W+jets and $\mathrm{t\bar{t}}$ control regions, some systematic deviations, although within uncertainties, can be observed. These deviations can be attributed to several causes. For instance, it is particulary hard to accurately model the W+jets process and jet substructure. Certain deviations in the muon channel distributions can be attributed to poorly derived scale factors for the high-p_{T} muons used. These concerns motivate the use of data driven techniques, and hence the major backgrounds are not entirely obtained from MC simulation but extracted from data where necessary.

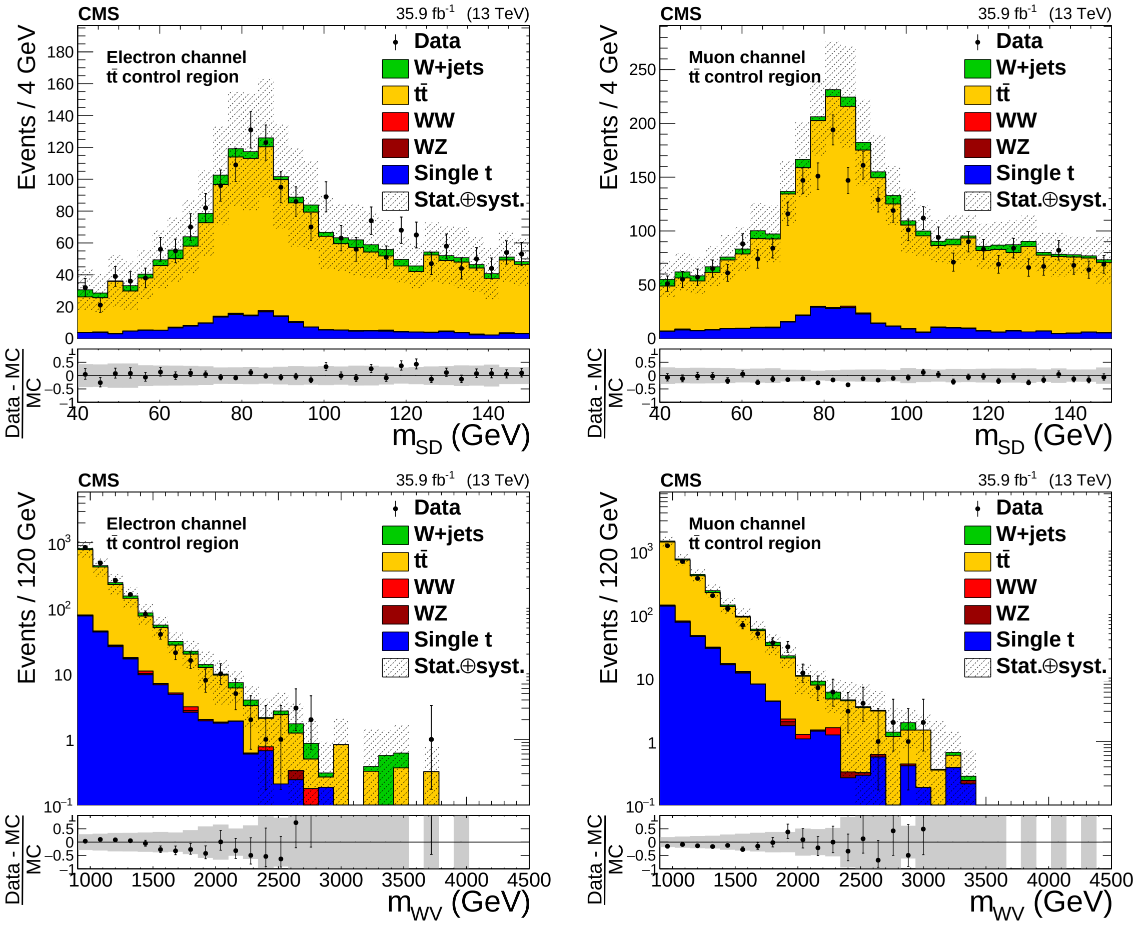

Figure 6.5: Comparison between data and simulation for the m_{SD} (upper) and m_{WV} (lower) distributions in the $\mathrm{t\bar{t}}$ control region. The electron and muon channels are shown on the left and right, respectively. The different contributions have been normalised to the luminosity of the data using their respective SM cross sections. The hashed region in the main plots and the grey band in the ratio plots show the combined effect of statistical and systematic uncertainties. This figure has been published in Reference [1].

A selection requirement is imposed on $p_{\mathrm{T}}^{\mathrm{miss}}$, as discussed in Section 5.4, to suppress certain background processes, including QCD multijet events. The choice of the threshold for the selection requirement is optimised in both the electron and muon channels. Figure 6.8 shows the comparison between data and simulation for the $p_{\mathrm{T}}^{\mathrm{miss}}$ distribution without the final selection cut on $p_{\mathrm{T}}^{\mathrm{miss}}$. A scan is performed using different values of the threshold, and the discrepancy between data and simulation is noted. The final value of the threshold is chosen to be the one where the discrepancy falls below 1%. This value is 110 (40) GeV in the electron (muon) channel.

In addition to the W+jets and $\mathrm{t\bar{t}}$ control regions, more phase space regions are constructed to further validate background contributions. These include another $\mathrm{t\bar{t}}$ control region, wherein $m_{\mathrm{SD}} > 150$ GeV, and QCD enriched regions, as discussed in the next section.

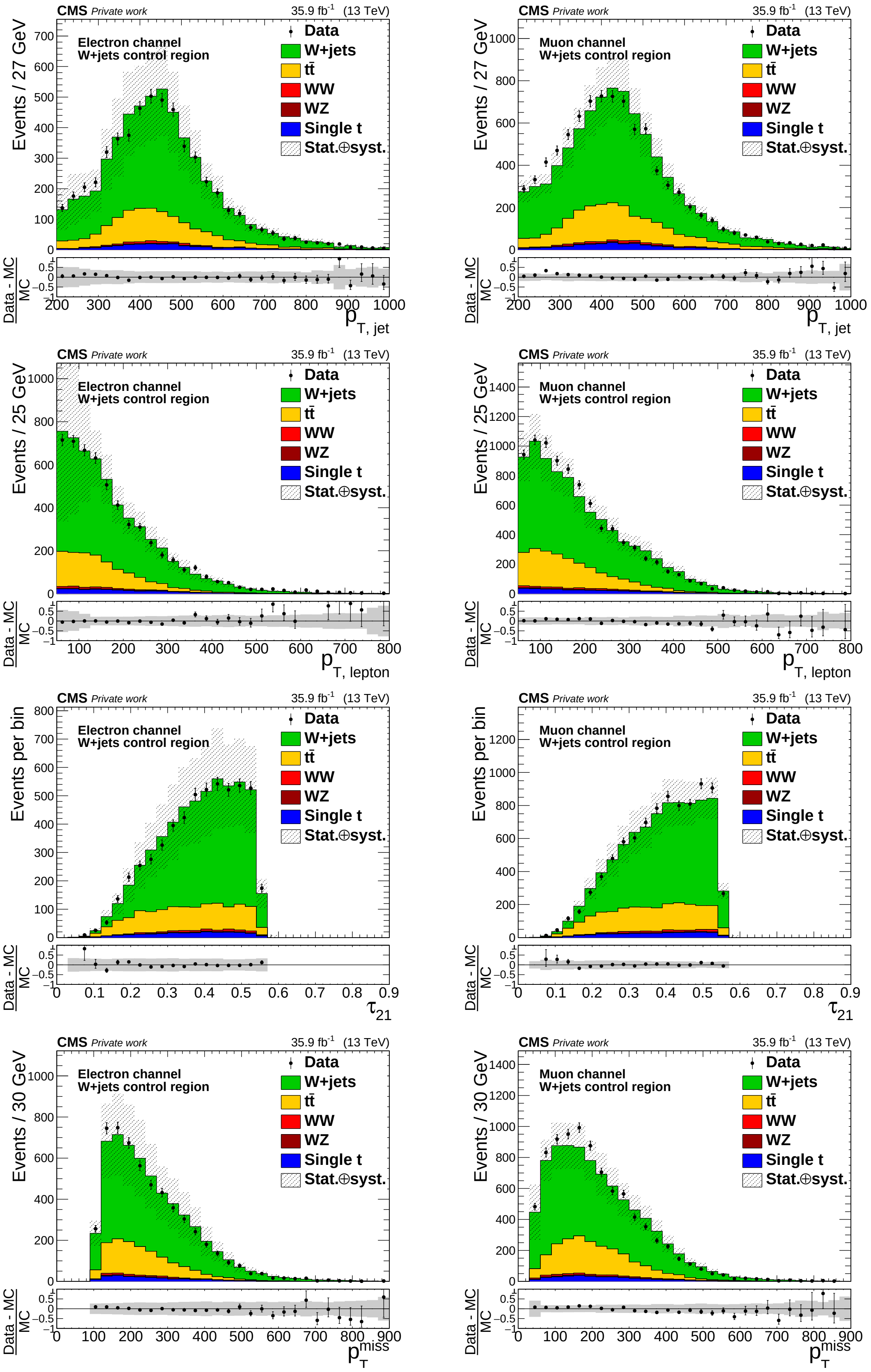

Figure 6.6: Comparison between data and simulation for the $p_{\mathrm{T,jet}}$, $p_{\mathrm{T,lep}}$, τ_{21}, and $p_{\mathrm{T}}^{\mathrm{miss}}$ (top to bottom, respectively) distributions in the W+jets control region. The electron and muon channels are shown on the left and right, respectively.

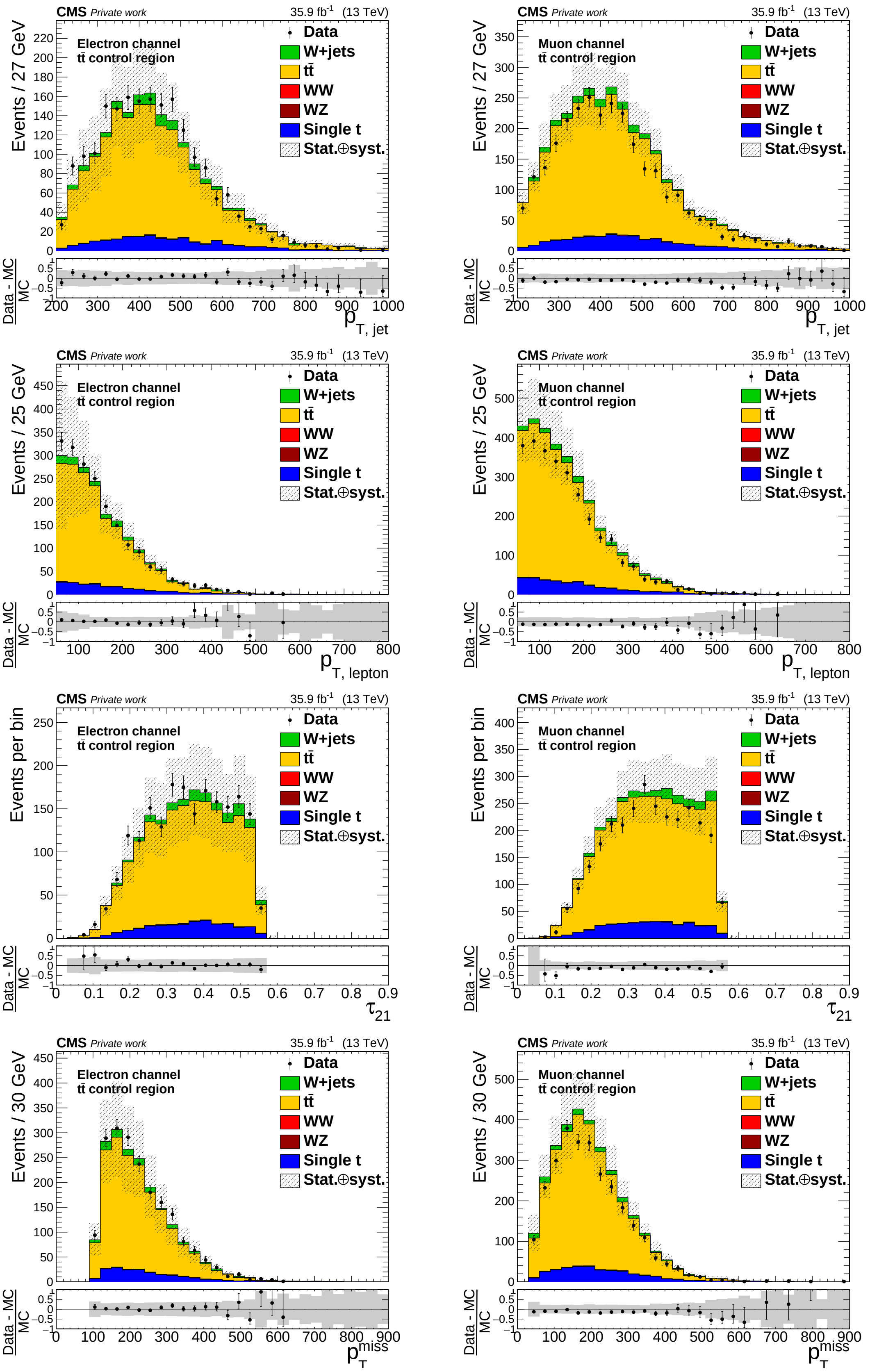

Figure 6.7: Comparison between data and simulation for the $p_{\mathrm{T,jet}}$, $p_{\mathrm{T,lep}}$, τ_{21}, and $p_{\mathrm{T}}^{\mathrm{miss}}$ (top to bottom, respectively) distributions in the $\mathrm{t\bar{t}}$ control region. The electron and muon channels are shown on the left and right, respectively.

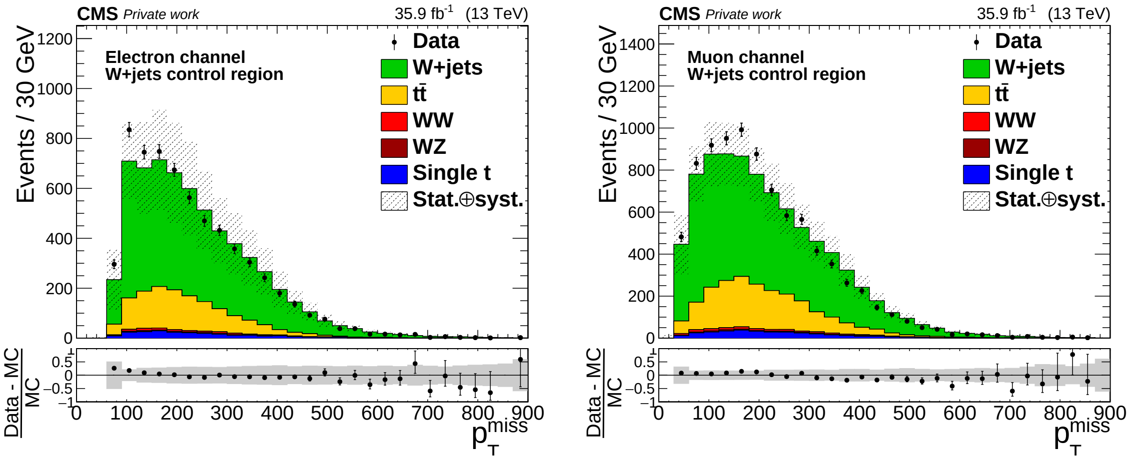

Figure 6.8: Comparison between data and simulation for the $p_{\mathrm{T}}^{\mathrm{miss}}$ distribution without the corresponding selection cut, to demonstrate the motivation for the selection cut. The requirement on $p_{\mathrm{T}}^{\mathrm{miss}}$ is set to be: $p_{\mathrm{T}}^{\mathrm{miss}} > 110(40)$ GeV in the electron (muon) channel.

6.2.2 Validation of negligible backgrounds

The contributions from several potential background processes are checked, and validated to be negligible. These processes either have a tiny cross section compared to the other background contributions or fail selection requirements frequently, resulting in negligible contributions. Simulated samples are used to verify the contribution from the Z+jets process. A comparison between the obtained m_{SD} distributions for the Z+jets and W+jets processes is given in Appendix A.6.

For the QCD multijet process, as a first check, simulated samples are used. Application of all the selection requirements results in less than 1% QCD events as compared to the W+jets contribution. In order to demonstrate that even if a noticable QCD contribution is present, it can be absorbed into the W+jets distribution because of similar shapes, very loosely selected — with selection requirements like a single isolated lepton and one clean AK8 jet only — QCD events are examined. The m_{SD} and m_{WV} distributions of these QCD events compared with the W+jets distributions are shown in Figure A.16. The W+jets fitting functions discussed in the next section are also easily able to absorb these loosely selected QCD events, when fit to the sum of the two contributions.

However, since simulated QCD events do not represent data very accurately, a full data-driven estimation of the QCD contribution is performed. In order to do so, QCD enriched phase space regions are defined. A schematic representation of the regions used for extracting the contribution of the QCD multijet process is shown in Figure 6.9. Side-sideband regions are defined in the m_{SD} interval orthogonal to the signal and sideband regions. Furthermore, QCD enriched control regions are defined by inverting the lepton isolation criteria in the signal and sideband regions.

A QCD fake rate is obtained by taking the ratio of the number of events in the isolated side-sideband region to those in the anti-isolated side-sideband region. The distributions,

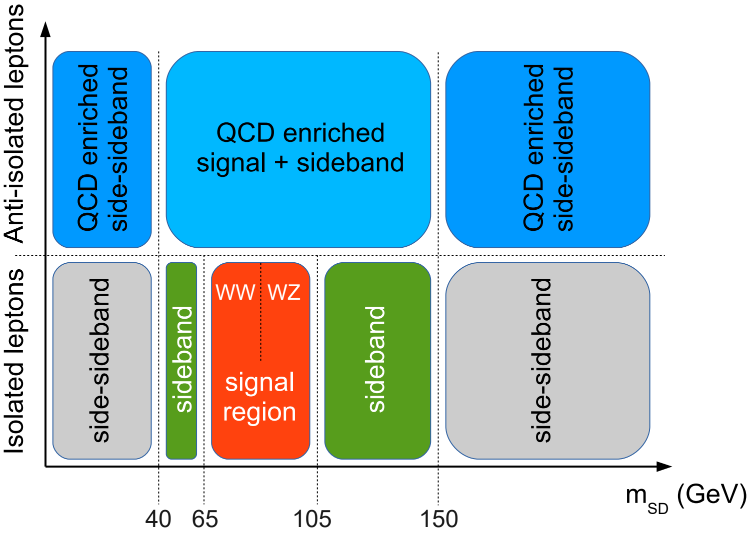

Figure 6.9: Schematic representation of regions used to estimate the contribution of QCD from data. The lepton isolation requirement is inverted to obtain the QCD-enriched regions.

using which the QCD fake rate is calculated, are shown in Figure 6.10. The fake rate is consequently used to transfer the QCD distribution in the anti-isolated signal + sideband region to the interesting signal + sideband region. The application of the fake rate to get the required QCD estimate is shown in Figure 6.11. The extracted QCD distribution is also compared with the W+jets distribution, to demonstrate the insignificance of the QCD multijet process for this analysis, after application of the well designed selection requirements.

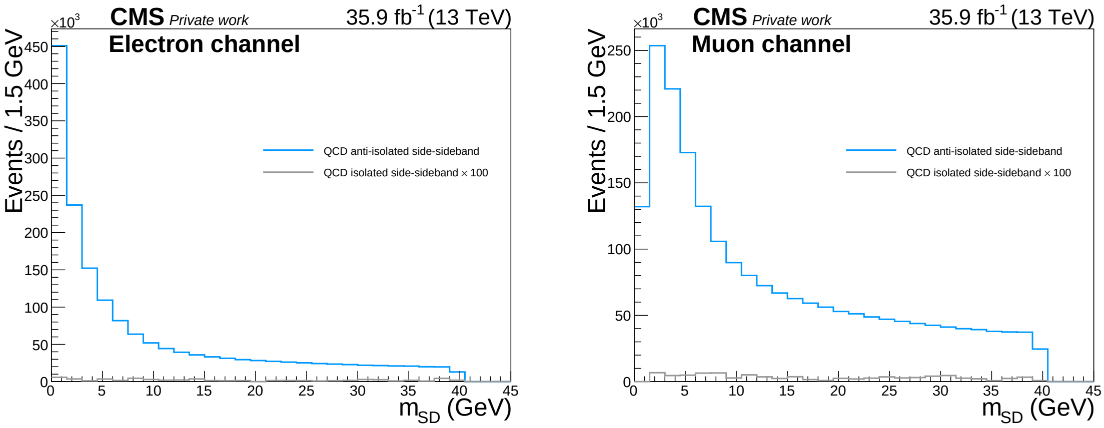

Figure 6.10: Estimation of QCD fake rate in the electron (left) and muon (right) channels. The fake rate is calculated as the ratio of the number of QCD events in the isolated and anti-isolated side-sideband regions.

The relevant numbers for the estimation of the QCD contribution from data are listed in Table 6.2. The final QCD estimate is ~1% when compared with the other backgrounds in both the electron and muon channels. As with the validation using simulated samples, the W+jets fitting functions discussed in the next section are easily able to absorb the

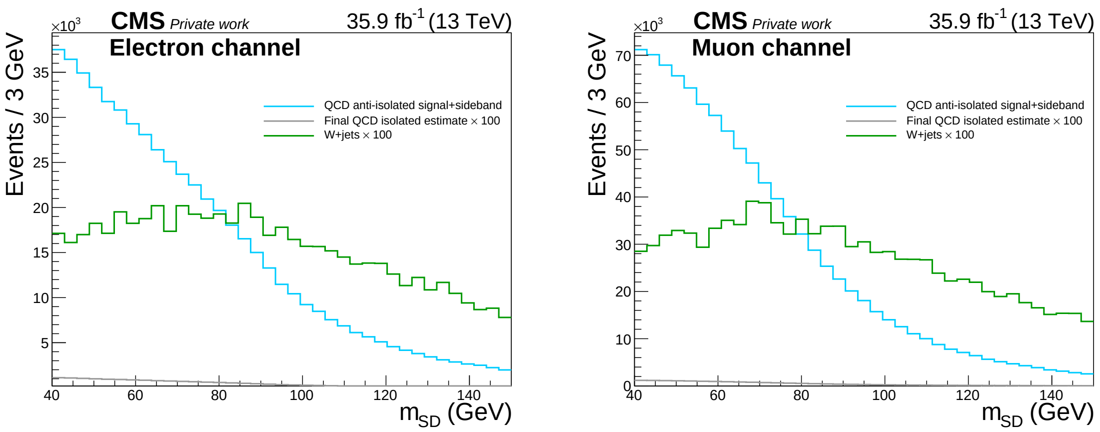

Figure 6.11: Final QCD estimate from data in the electron (left) and muon (right) channels in the interested signal + sideband region, obtained by transferring the QCD distribution from the corresponding anti-isolated region using the fake rate. A comparison with the W+jets distribution is also shown to demonstrate neglecting the QCD contribution.

contribution from QCD multijet events.

Table 6.2: Summary of estimated contribution from QCD events using data from QCD-enriched regions. The final estimate justifies ignoring its contribution in this analysis.

	Electron channel	Muon channel
$N_{\text{QCD}}^{\text{iso,side-sideband}}$	507	352
$N_{\text{QCD}}^{\text{anti-iso,side-sideband}}$	1,700,563	2,121,627
Fake rate (%)	0.0298	0.0166
$N_{\text{QCD}}^{\text{anti-iso,signal+sideband}}$	565,450	1,000,762
$N_{\text{QCD}}^{\text{iso,signal+sideband}}$	169	166

6.2.3 Background modelling

Analogous to signal modelling, the m_{SD} and m_{WV} distributions for the background contributions are modelled using parametric functions, which are first fitted to simulation.

Background m_{SD} distribution

The m_{SD} distribution for the background contributions is modelled using a variety of components. These components are selected considering characteristic features of the shape for each contribution. The details of the functions used, along with the motivation of constructing the specific form of the functions, is as follows:

- **W+jets:** The W+jets distribution contains a broad Sudakov peak of jet masses expected in highly energetic QCD jets. This broad, continuous distribution is modelled using a chi-square function of degree four:

$$F_{\mathrm{W+jets}}(m_{\mathrm{SD}}) = (m_{\mathrm{SD}} - k_{\mathrm{CS1}})e^{k_{\mathrm{CS2}}(m_{\mathrm{SD}}-k_{\mathrm{CS1}})}, \tag{6.7}$$

where k_{CS1} and k_{CS2} are the shape parameters of the χ^2_4 distribution. Since the W+jets process is the most significant background, an alternative fit function is also used to avoid bias from the selection of the specific form of the function. The used alternative fit function is a standardised Bernstein polynomial of degree 3:

$$F^{\mathrm{alt}}_{\mathrm{W+jets}}(m_{\mathrm{SD}}) = k_{\mathrm{BS0}}(1-x^3) + k_{\mathrm{BS1}}x(1-x^2) + k_{\mathrm{BS2}}x^2(1-x) + k_{\mathrm{BS3}}x^3, \tag{6.8}$$

where x is the standardised m_{SD}:

$$x = \frac{m_{\mathrm{SD}} - 40}{110}. \tag{6.9}$$

The difference in normalisation resulting from the use of the alternative fit function is propagated to the uncertainty of the W+jets normalisation. The uncertainty from the alternative function is estimated to be ~10%.

- **Top quark pair production:** For the $\mathrm{t\bar{t}}$ background, the m_{SD} distribution contains a well-defined peak, indicative of real boosted W bosons, emerging from the decay of the top quarks, and decaying hadronically. In addition to the sharp peak, there is a continuous distribution resulting from the case where the W boson and the bottom quark emerging from a top quark are not easily distinguished. Therefore a combination of an exponential times error function and a Gaussian function is used:

$$F_{\mathrm{t\bar{t}}}(m_{\mathrm{SD}}) = e^{k_{\mathrm{EEG1}}m_{\mathrm{SD}}}\left(\frac{1+\mathrm{erf}((m_{\mathrm{SD}}-k_{\mathrm{EEG2}})/k_{\mathrm{EEG3}})}{2}\right) + k_{\mathrm{EEG4}}\mathrm{G}(m_{\mathrm{SD}}, k_{\mathrm{EEG5}}, k_{\mathrm{EEG6}}), \tag{6.10}$$

  with the Gaussian function, having a mean c_{EEG5} and standard deviation c_{EEG6}, modelling the peak, and the exponential times error function modelling the continuous distribution.

- **SM diboson production:** The SM diboson m_{SD} distribution only contains a resonant contribution, with minor tails extending into the sidebands. Hence, a combination of two Gaussian functions is used:

$$F_{\mathrm{WV}}(m_{\mathrm{SD}}) = \mathrm{G}(m_{\mathrm{SD}}, k_{\mathrm{DG1}}, k_{\mathrm{DG2}}) + k_{\mathrm{DG3}}\mathrm{G}(m_{\mathrm{SD}}, k_{\mathrm{DG1}} + k_{\mathrm{DG4}}, k_{\mathrm{DG3}}k_{\mathrm{DG5}}), \tag{6.11}$$

  with the subscript DG denoting "double Gauss".

- **Single top quark production:** The m_{SD} distribution for the single top quark production is quite similar to the $\mathrm{t\bar{t}}$ production, with a resonant contribution from associated tW production, and a continuous distribution from the t-channel production. However, since single top quark processes form a minor background, a somewhat simplified function is used, consisting of a combination of an exponential function and a Gaussian:

$$F_{\mathrm{t}}(m_{\mathrm{SD}}) = k_{\mathrm{EG1}}e^{k_{\mathrm{EG2}}m_{\mathrm{SD}}} + \mathrm{G}(m_{\mathrm{SD}}, k_{\mathrm{EG3}}, k_{\mathrm{EG4}}). \tag{6.12}$$

A table summarising the values of the parameters extracted from the fits to simulation is given in Appendix A.7. Simulated m_{SD} distributions, along with the extracted fit functions, in both the electron and muon channels are shown in Figure 6.12. In order to construct the

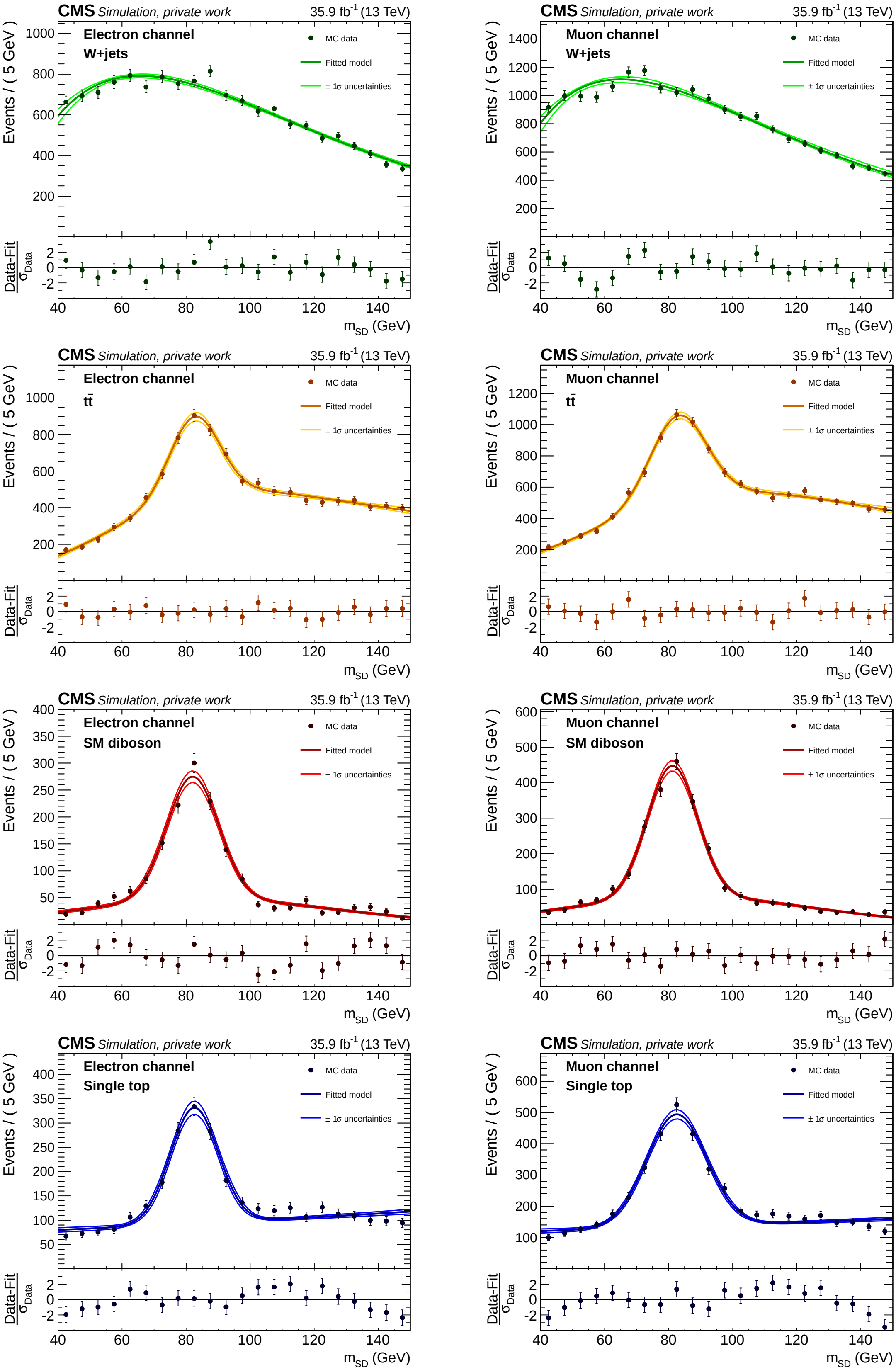

Figure 6.12: Simulated events and fitted parametric functions for the W+jets, $t\bar{t}$, SM diboson, and single top quark (top to bottom, respectively) m_{SD} distributions. The electron channel is shown on the left, whilst the muon channel is shown on the right.

shown 1σ uncertainty bands, the fitted functions are evaluated along the m_{SD}-axis, whereof the extracted parameters are randomised according to their covariance matrix, and the central 68% of the resulting values are selected at every point along m_{SD}.

Figure 6.13 shows the complete background m_{SD} model, formed by combining the functions described above, compared to data before the final fit. In order to avoid personal bias resulting from observing data in the signal region, the signal region in figures like this is kept blinded, and revealed only after details of the analysis have been finalised and approved following various iterations of careful review within the CMS collaboration.

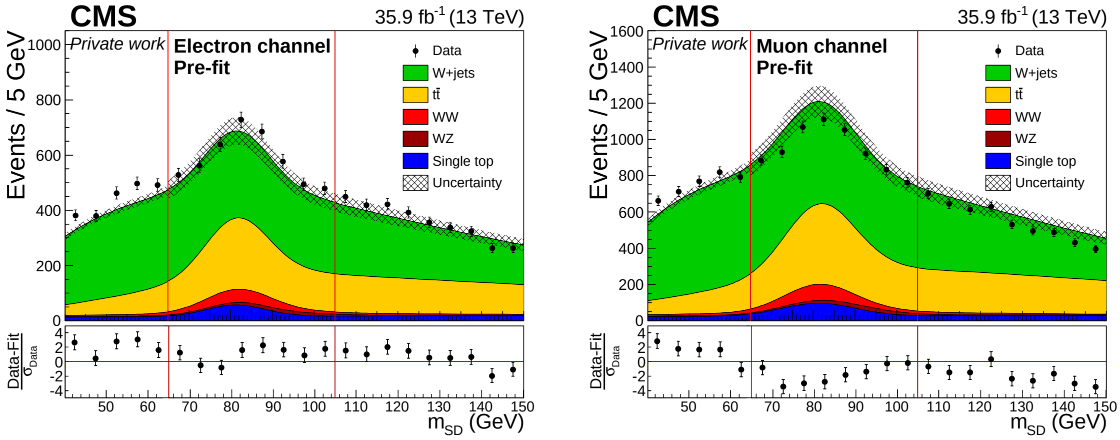

Figure 6.13: The complete m_{SD} background model derived from simulation, in the electron (left) and muon (right) channels, compared to data before the final fit. W+jets and $\mathrm{t\bar{t}}$ contributions are derived from data in the final fit.

Background m_{WV} distribution

The m_{WV} distribution for the background contributions in the signal region is modelled using the following functions:

- **W+jets:** $F_{\text{W+jets}}(m_{\mathrm{WV}}) = e^{k_{\mathrm{ET11}} m_{\mathrm{WV}} + k_{\mathrm{ET12}}/m_{\mathrm{WV}}}$
- **$\mathbf{t\bar{t}}$:** $F_{\mathrm{t\bar{t}}}(m_{\mathrm{WV}}) = e^{k_{\mathrm{ET21}} m_{\mathrm{WV}} + k_{\mathrm{ET22}}/m_{\mathrm{WV}}}$
- **SM diboson:** $F_{\mathrm{WV}}(m_{\mathrm{WV}}) = e^{k_{\mathrm{ET31}} m_{\mathrm{WV}} + k_{\mathrm{ET32}}/m_{\mathrm{WV}}}$ (6.13)
- **Single t:** $F_{\mathrm{t}}(m_{\mathrm{WV}}) = e^{k_{\mathrm{E1}} m_{\mathrm{WV}}}$,

where the parameter subscripts E and ET denote exponential and exponential with a tail, respectively. A table summarising the values of the parameters extracted from the fits to simulation is given in Appendix A.7. Simulated m_{WV} distributions, along with the extracted fit functions, for the signal region in both the electron and muon channels are shown in Figure 6.14.

For the sideband regions, similar functions are used, with the exception of the diboson contribution, which has a much smaller contribution in the sidebands as compared to the signal region, and is modelled using a simple decaying exponential function. Simulated m_{WV} distributions, along with the extracted fit functions, for the sideband region are given

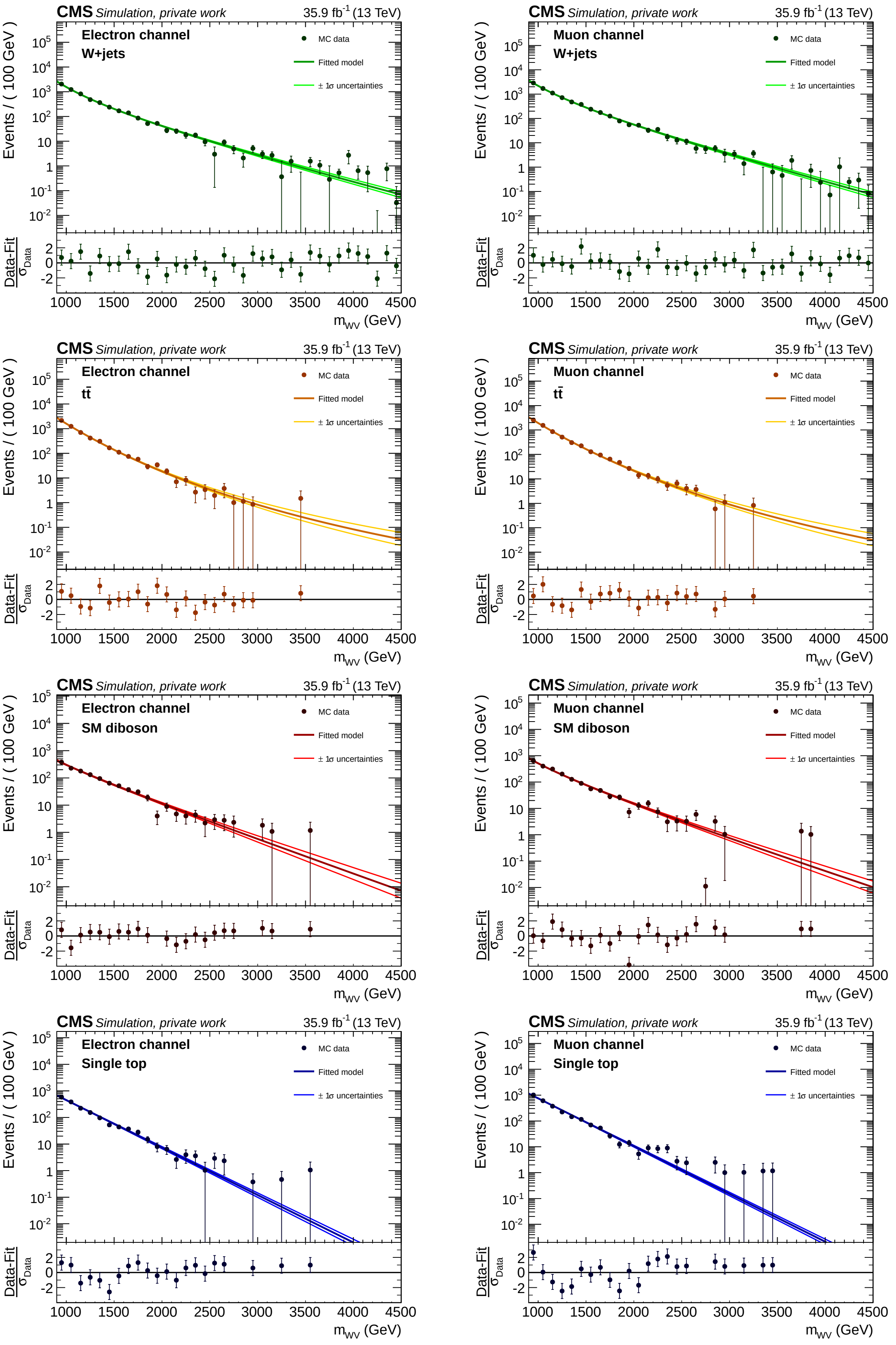

Figure 6.14: Simulated events and fitted parametric functions for the W+jets, $t\bar{t}$, SM diboson, and single top quark (top to bottom, respectively) m_{WV} distributions in the signal region. The electron channel is shown on the left, whilst the muon channel is shown on the right.

in Appendix A.7.

The extracted W+jets functions in the signal and sideband regions are used to construct a transfer function that is used, in combination with fits to data in the sideband regions, to get the final estimate of the W+jets contribution in the signal region. The transfer function method is discussed in detail in the following section. Similar to the W+jets m_{SD} distribution, an alternative fit function is also used for m_{WV} to avoid bias from the selection of the specific form of the function. For the m_{WV} distribution, the used alternative fit function is:

$$F^{\text{alt}}_{\text{W+jets}}(m_{\text{WV}}) = e^{m_{\text{WV}}/(k_{\text{ET41}}+k_{\text{ET42}}m_{\text{WV}})}. \tag{6.14}$$

The uncertainty arising from the use of the alternative fit function is propagated to the final transfer function, discussed in the following section. The pre-fit background m_{WV} model in the signal region is shown in Figure 6.15 for both the electron and muon channels.

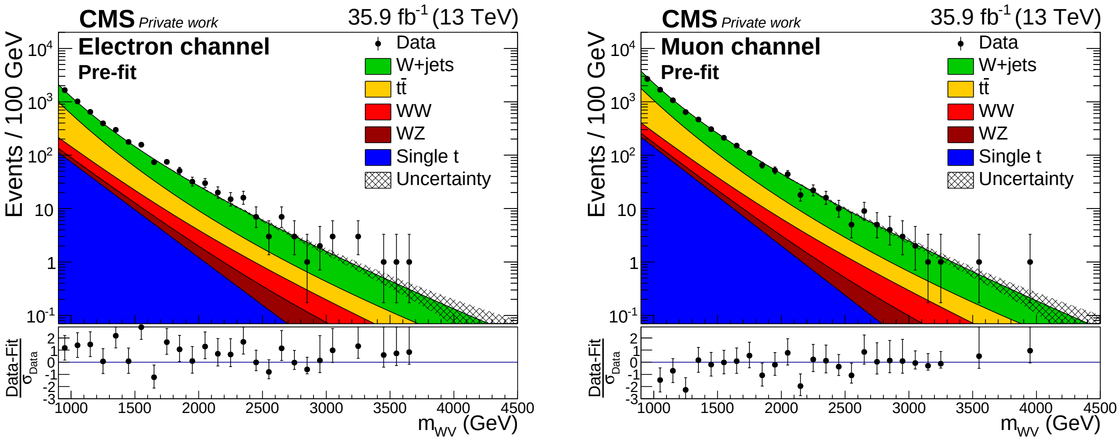

Figure 6.15: The complete m_{WV} background model for the signal region, derived from simulation, in the electron (left) and muon (right) channels, compared to data before the final fit. The W+jets contribution is estimated from sideband data using a transfer function in the final fit.

6.2.4 Two-dimensional fit and estimation of W+jets contribution

The contribution of the W+jets process is estimated from a two-dimensional fit to data, which is designed to extract the signal as well as background contributions fixed from data. The topology of the two-dimensional fit is demonstrated in Figure 6.16. The fit is performed in the $(m_{\text{SD}}, m_{\text{WV}})$-plane, and owing to the lack of prior knowledge about modelling m_{WV} shape parameters as a function of m_{SD} continuously, the fit is modified from a usual two-dimensional fit. The phase space is divided into sideband and signal regions along m_{SD}, and while performing the fit, the m_{WV} shape parameters within one region are kept constant with respect to m_{SD}. The background shape parameters in the sideband region are obtained by fitting to data, since the contamination from signal is negligible; in the signal region, the data is used to extract the signal.

In order to derive the W+jets contribution in the signal region, the α ratio (transfer function) method [170, 171] is used. A demonstration of the α ratio method is shown in Figure 6.17. The method works on the assumption that although the simulation may not accurately

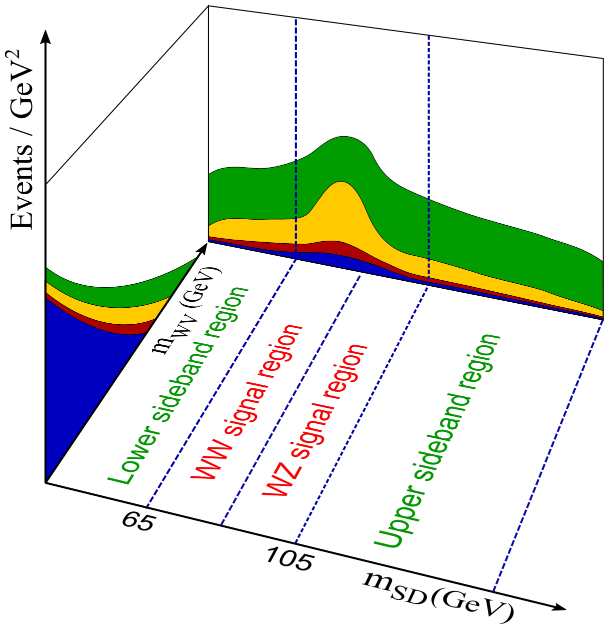

Figure 6.16: Topology of the final two-dimensional fit to data to fix background contributions and extract the signal. The fit is performed in the $(m_{\mathrm{SD}}, m_{\mathrm{WV}})$-plane, with the phase space being split into signal and sideband regions along m_{SD}.

describe the shape of the W+jets distribution in the signal region, it does accurately predict the ratio of distributions in the signal and sideband regions. A ratio of the simulated m_{WV} distributions in the signal and sideband regions is thus used to transfer the W+jets m_{WV} distribution in the sideband, extracted from data, to the signal region, thereby encoding the dependence of m_{WV} on m_{SD}. The total background m_{WV} contribution in the signal region can therefore be expressed as:

$$\begin{aligned} F^{\mathrm{SR}}_{\mathrm{bkg}}(m_{\mathrm{WV}}) &= F^{\mathrm{SB,\ data}}_{\mathrm{W+jets}} \alpha^{\mathrm{MC}}(m_{\mathrm{WV}}) + F^{\mathrm{SR}}_{\mathrm{t\bar{t}}} + F^{\mathrm{SR}}_{\mathrm{single\ t}} + F^{\mathrm{SR}}_{\mathrm{diboson}}, \\ \alpha^{\mathrm{MC}}(m_{\mathrm{WV}}) &= \frac{F^{\mathrm{SR,\ MC}}_{\mathrm{W+jets}}}{F^{\mathrm{SB,\ MC}}_{\mathrm{W+jets}}}, \end{aligned} \tag{6.15}$$

with F representing the parametric functions corresponding to the various contributions in the signal (SR) and sideband (SB) regions. The α function in the electron and muon channels, derived using both the sideband regions and the full signal region, is shown in Figure 6.18.

While performing the fit, different constraints are placed on the normalisation and m_{SD} and m_{WV} shape parameters of the various contributions, depending on the significance of the contribution and the uncertainty in its modelling. The W+jets contribution is derived from data, with the normalisation and m_{SD} shape parameters being allowed to vary without constraint, in order to account for possible mismodelling. The m_{WV} shape parameters are determined from sideband data and the transfer function α^{MC}, with constraints being placed according to the uncertainties in simulation propagated to α^{MC}. For the $\mathrm{t\bar{t}}$ con-

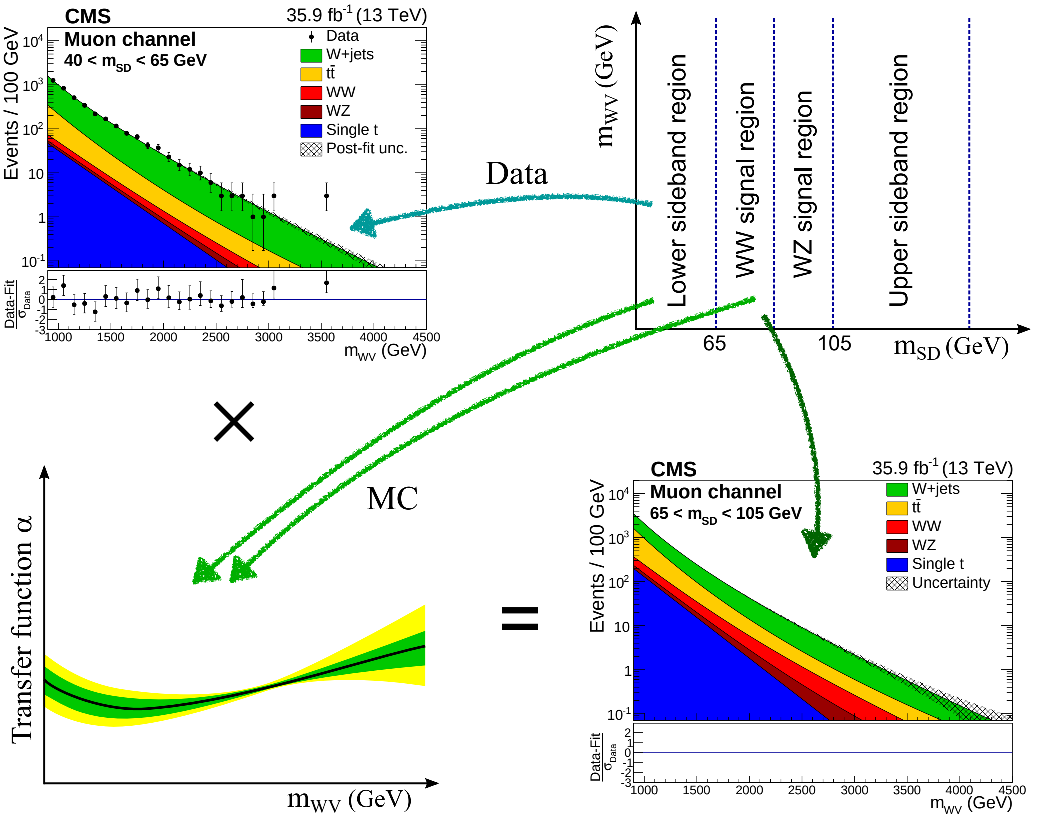

Figure 6.17: Demonstration of the transfer function method to estimate the contribution of W+jets background in the signal region. A transfer function α, derived from simulated distributions in the signal and sideband regions, is used to transfer the W+jets m_{WV} distribution in sidebands to the signal region.

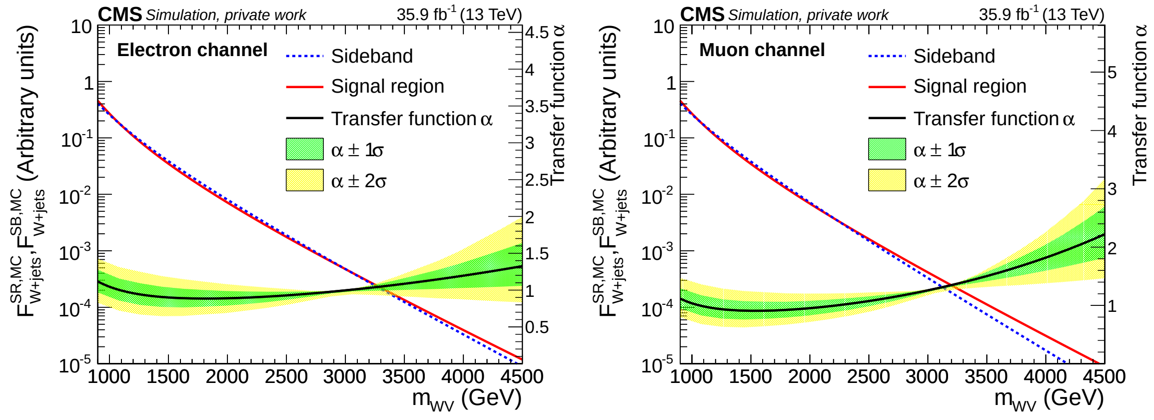

Figure 6.18: Alpha function used to transfer the W+jets m_{WV} distribution from sidebands to the signal region in the electron (left) and muon (right) channels. The alpha function is defined as a ratio of the m_{WV} distribution of simulated events in the signal region to the sideband regions.

tribution, the normalisation and m_{WV} shape parameters are allowed to vary within their respective uncertainties, whilst the m_{SD} shape is kept fixed. The shape parameters of the SM diboson contribution are also kept fixed; however, the normalisation is allowed to vary within 100% in order to cover its systematic uncertainty, as well as to allow a significant contribution from aTGC processes, within the sensitivity of this analysis. The normalisation of the single top quark contribution is allowed to vary within its uncertainty, whilst the m_{SD} and m_{WV} shape parameters are kept fixed. Details of the uncertainties used as constraints are discussed in the following section.

The normalisations of background contributions before and after the fit are listed in Table 6.3. Before fitting to data, consistency checks are carried out by utilising Asimov data. One of the checks is a closure test, wherein the two-dimensional fit is performed on Asimov data corresponding to zero aTGC parameters, verifying that the fitted model complies with the SM Asimov data. Results of the closure test are shown in Figure A.18 in Appendix A.8. Other checks include signal injection tests, wherein the fit is performed on Asimov data corresponding to the signal scenario where an aTGC parameter is set to a nonzero value. Results of signal injection tests with Asimov data corresponding to $c_{\mathrm{WWW}}/\Lambda^2 = 3.6\ \mathrm{TeV}^{-2}$ and $c_{\mathrm{B}}/\Lambda^2 = 20\ \mathrm{TeV}^{-2}$ are shown in Figures A.19 and A.20, respectively. The former case refers to the scenario with enhanced WW and WZ contributions, while the latter refers to the scenario where only the WW contribution is enhanced, and the WZ contribution remains unchanged. In both the cases, the signal is identified accurately without any bias. Final results of the two-dimensional fit to data are presented in Chapter 7, following a discussion of the statistical model and the procedure used to extract limts.

Table 6.3: Pre-fit and post-fit normalisations of the background contributions compared to data. The uncertainties in the pre-fit yields are used as constraints in the fit, whilst uncertainties in the post-fit yields are the corresponding total post-fit uncertainties. Since the normalisation of the W+jets process is allowed to vary freely in the fit, there are no corresponding pre-fit uncertainties. This table has been published in Reference [1].

	Electron channel			Muon channel		
	Pre-fit	Post-fit	Scale factor	Pre-fit	Post-fit	Scale factor
W+jets	2421	3036 ± 123	1.25	4319	4667 ± 182	1.08
$\mathrm{t\bar{t}}$	1491 ± 324	1127 ± 119	0.76	2632 ± 570	1978 ± 202	0.75
Single t	271 ± 39	242 ± 26	0.89	509 ± 69	449 ± 43	0.88
Diboson	314 ± 314	267 ± 102	0.85	552 ± 552	465 ± 162	0.84
Total	4497	4672 ± 201	1.04	8012	7559 ± 319	0.94
Data		4691			7568	

6.2.5 Impact of uncertainties

The effect of systematic uncertainties from the sources discussed in Section 5.6 is propagated to the estimates of the background contributions. Estimated normalisation uncertainties for the various background contributions derived from simulation are summarised in Table 6.4. The dominant contributions come from theory and uncertainty in identification of vector bosons. The effect of lepton and jet uncertainties on $p_{\mathrm{T}}^{\mathrm{miss}}$ is included in the corresponding lepton and jet uncertainty rows, while the $p_{\mathrm{T}}^{\mathrm{miss}}$ row only quotes the uncertainty arising from unclustered energy deposits. All uncertainties are included as nuisance parameters in the final fit to data.

Table 6.4: Estimated normalization uncertainties (%) for background processes derived from simulation. The dominant sources of uncertainty include vector boson identification and theoretical uncertainties.

	Electron channel				Muon channel			
Uncertainty source	$\mathrm{t\bar{t}}$	WW	WZ	t	$\mathrm{t\bar{t}}$	WW	WZ	t
PDF	2.79	1.93	2.44	0.22	2.71	1.78	2.54	0.25
μ_{F}, μ_{R}	17.99	5.77	4.82	0.94	17.74	5.99	4.26	1.06
Luminosity	2.5	2.5	2.5	2.5	2.5	2.5	2.5	2.5
Pileup	0.59	0.90	1.40	0.29	0.40	0.82	0.67	0.41
Lepton identification	2.12	2.30	2.26	2.22	1.81	2.55	2.42	2.04
Lepton energy scale	0.80	1.53	0.94	1.45	0.68	1.72	1.19	1.14
Lepton energy resolution	0.26	0.11	0.21	1.22	0.02	0.14	0.33	0.27
Jet energy scale	4.41	4.26	2.44	4.94	3.54	3.75	2.50	2.97
Jet energy resolution	1.79	1.85	2.69	3.44	0.85	0.62	2.92	0.91
V tag	14	14	14	14	14	14	14	14
b tag	1.05	0.04	0.08	0.85	1.04	0.03	0.08	0.84
b mistag	0.04	0.02	0.04	0.05	0.05	0.03	0.04	0.05
$p_{\mathrm{T}}^{\mathrm{miss}}$	0.91	1.01	0.64	1.50	0.59	0.24	0.17	0.99
Total	23.74	16.44	15.91	15.84	23.30	16.31	15.80	14.85

The uncertainties in shape parameters of the major background contributions are also taken into account. For the W+jets shape, the uncertainty in simulation is propagated via the transfer function. The effect of the alternative fit function is also included by inflating the parameter uncertainties to cover the estimate from the alternative function. For the $\mathrm{t\bar{t}}$ contribution, the uncertainty is estimated using the uncertainties in the shape parameters of the parametric function from the fit to simulation. The shape uncertainties are also included as nuisance parameters in the final fit to data.

It is interesting to note that differential corrections from higher order, NNLO QCD [172,173] and NLO electroweak [174], contributions can be considerable at higher values of m_{WV}. However, the two corrections have opposite signs, and partially cancel out. Furthermore, the influence of these corrections has not been fully investigated for processes with anomalous couplings. Therefore, they are not included as additional sources of uncertainty.

The aim of science is not to open the door to infinite wisdom, but to set a limit to infinite error.

……

– Bertolt Brecht

7

Limits on anomalous gauge coupling parameters

A befitting result —

This chapter reveals the outcome of the analysis presented in this thesis. Mathematical framework of the statistical model and details of the limit setting procedure are discussed, before giving out results from the two-dimensional fit to data. The chapter concludes by presenting one- and two-dimensional limits on anomalous triple gauge coupling parameters, comparing them with the limits obtained from other measurements.

While searching for physics beyond the SM, it is customary to derive limits on cross sections and quantities characterising the new physics, in case no deviations from the SM predictions are observed. For the analysis presented in this thesis, confidence intervals are constructed for anomalous triple gauge coupling parameters using the diboson mass distribution. In order to do so, the profile likelihood ratio is used as a test statistic. Using the profile likelihood ratio, confidence intervals are constructed for single parameters as well as combinations of two parameters simultaneously.

7.1 Statistical model

Given a probability density function $f(x|\mu)$ for the random variable associated with x, and characterised by a parameter μ, the likelihood is defined by flipping the quantity of interest from the random variable to the parameter:

$$L(\mu|x) = f(x|\mu). \tag{7.1}$$

For n independent measurements of the random variable, the combined likelihood is given by:

$$L(\mu|\vec{x}) = \prod_{i=1}^{n} f(x_i|\mu), \tag{7.2}$$

with the maximum likelihood estimate of the parameter μ corresponding to maximising the joint probability density function.

For the analysis presented in this thesis, an unbinned likelihood is constructed using the signal and background modelling functions presented in Chapter 6. In this case, the total m_{WV} probability density, characterised by an aTGC parameter c_i, is given by:

$$f(m_{\mathrm{WV}}|c_i) = \frac{F_{\mathrm{signal}}(m_{\mathrm{WV}}|c_i) + \sum_p F_{\mathrm{bkg},p}(m_{\mathrm{WV}})}{N_{\mathrm{signal}}(c_i) + \sum_p N_{\mathrm{bkg},p}}, \tag{7.3}$$

where F_{signal} and N_{signal} are the signal model and normalisation, respectively, defined in Section 6.1; $F_{\mathrm{bkg},p}$ is the background function for the p-th process, defined in Section 6.2, now including the corresponding normalisation; and $N_{\mathrm{bkg},p}$ is the normalisation of the p-th background contribution. For n independent measurements of m_{WV}, the likelihood can be written as:

$$L(c_i|\vec{m}_{\mathrm{WV}}) = \frac{e^{-\lambda}\lambda^n}{n!} \prod_{j=1}^{n} f(m_{\mathrm{WV},j}|c_i), \tag{7.4}$$

where $m_{\mathrm{WV},j}$ is the measurement of m_{WV} for the j-th event, and the Poisson factor accounts for the rate of observation in the experiment, given an expectation, with λ being the expected yield as appearing in the denominator of Equation 7.3:

$$\lambda = N_{\mathrm{signal}}(c_i) + \sum_p N_{\mathrm{bkg},p}. \tag{7.5}$$

Furthermore, since events are categorised into four categories corresponding to the WW and WZ sensitive regions in the electron and muon channels, the likelihood is modified to:

$$L(c_i|\vec{m}_{\mathrm{WV}}) = \prod_{k=1}^{4} \left(\frac{e^{-\lambda}\lambda^{n_k}}{n_k!} \prod_{j=1}^{n_k} f(m_{\mathrm{WV},j}|c_i) \right). \tag{7.6}$$

Finally, including the nuisance parameters corresponding to systematic uncertainties, the eventual form of the likelihood becomes:

$$L(c_i, \vec{\theta} | \vec{m}_{\mathrm{WV}}) = \pi(\vec{\theta}) \prod_{k=1}^{4} \left(\frac{e^{-\lambda} \lambda^{n_k}}{n_k!} \prod_{j=1}^{n_k} f(m_{\mathrm{WV},j} | c_i, \vec{\theta}) \right), \tag{7.7}$$

where θ denotes a nuisance parameter, and $\pi(\theta)$ is the corresponding prior probability.

Normalisation uncertainties are incorporated via a log-normal distribution, where an expected yield N is modified to $Ne^{\theta \ln \epsilon}$, with the nuisance parameter θ having a Gaussian distribution with mean zero and standard deviation one:

$$\begin{aligned} N &\to Ne^{\theta \ln \epsilon}, \\ \pi(\theta) &= \frac{1}{\sqrt{2\pi}} e^{-\theta^2/2}. \end{aligned} \tag{7.8}$$

The parameter ϵ marks the size of the uncertainty; for instance, a 15% normalisaton uncertainty corresponds to the transformation $N \to Ne^{\theta \ln 1.15}$.

Uncertainties in shape are incorporated by modifying the shape parameter using a nuisance parameter, which has a Gaussian distribution with mean zero and standard deviation proportional to the uncertainty. For instance, to incorporate the shape uncerainty into the parameter a in the signal shape function:

$$\begin{aligned} a &\to a + \theta, \\ \pi(\theta) &= \frac{1}{\sqrt{2\pi\sigma}} e^{-\theta^2/2\sigma^2}, \end{aligned} \tag{7.9}$$

with σ being fixed by the size of the uncertainty.

The best-fit value of the anomalous coupling parameter of interest can be obtained by globally maximising the likelihood given in Equation 7.7. In order to derive confidence intervals, the profile likelihood ratio, also called the LHC test statistic, is constructed:

$$2\Delta\mathrm{NLL}(c_i) = -2 \ln \left(\frac{L(c_i, \hat{\hat{\vec{\theta}}}(c_i) | \vec{m}_{\mathrm{WV}})}{L(\hat{c}_i, \hat{\vec{\theta}} | \vec{m}_{\mathrm{WV}})} \right), \tag{7.10}$$

where $\hat{c}_i$ and $\hat{\vec{\theta}}$ represent parameters that globally maximise L, whilst $\hat{\hat{\vec{\theta}}}(c_i)$ corresponds to the nuisance parameters that maximise L for a given value of c_i.

The Wilks' theorem [175], derived by Samuel Wilks, states that the profile likelihood ratio distribution approaches a chi-squared distribution with the corresponding degrees of freedom as the sample size becomes very large. Therefore, confidence intervals with a specific confidence level can be constructed as loci of all the points in the parameter space where the profile likelihood ratio of Equation 7.10 is smaller than the critical value of the chi-squared distribution with the corresponding degrees of freedom and confidence level.

7.2 Fit results

In order to perform the two-dimensional fit to data, discussed in Chapter 6, and derive limits on aTGC parameters using the model discussed in the preceeding section, a framework developed in the context of Higgs boson analysis [176] is used. While performing the fit, m_{WV} is constrained to the interval $900 < m_{\mathrm{WV}} < 4500$ GeV, where the lower limit is the minimum selection requirement on m_{WV}, and the upper limit is chosen based on data observed in the control regions. The upper limit on m_{WV} is placed to stay comfortably below the threshold where the EFT is no longer valid. Further discussion on the EFT validity and unitarity consideration in this analysis is given in the following section. Results of the two-dimensional fit are shown in Table 7.1 and Figures 7.1 and 7.2.

Table 7.1: Summary of background, signal, and data yields for the WW and WZ categories in each lepton channel. The anomalous diboson yields are predictions of the signal model, with anomalous coupling parameters set to the indicated values, including the standard model and anomalous contributions, along with the relevant interference terms. Nuisance parameters have been set to their post-fit values for this prediction. This table has been published in Reference [1].

	Electron channel		Muon channel	
	WW	WZ	WW	WZ
W+jets	1618 ± 66	1418 ± 57	2529 ± 99	2138 ± 83
$\mathrm{t\bar{t}}$	600 ± 63	526 ± 56	1040 ± 106	938 ± 96
Single top quark	145 ± 16	97 ± 10	264 ± 25	185 ± 18
Diboson (SM)	144 ± 52	122 ± 52	265 ± 88	200 ± 79
Total expected (SM)	2507 ± 106	2163 ± 96	4098 ± 172	3461 ± 151
Diboson ($c_{\mathrm{WWW}}/\Lambda^2 = 3.6$ TeV^{-2})	193 ± 15	185 ± 15	334 ± 26	287 ± 22
Diboson ($c_{\mathrm{W}}/\Lambda^2 = 4.5$ TeV^{-2})	163 ± 14	154 ± 15	283 ± 23	237 ± 21
Diboson ($c_{\mathrm{B}}/\Lambda^2 = 20$ TeV^{-2})	188 ± 21	144 ± 14	322 ± 33	221 ± 20
Data	2456	2235	3996	3572

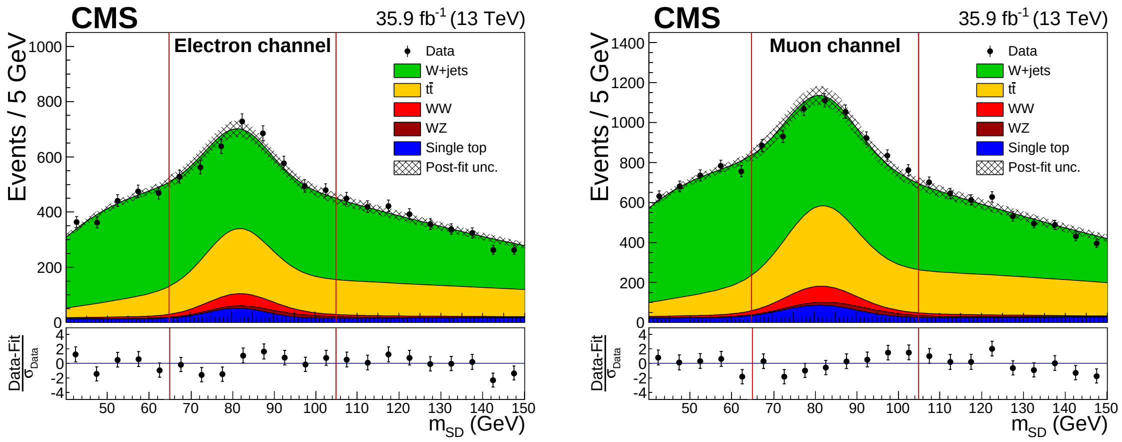

Figure 7.1: Result of the final two-dimensional fit to data, showing the m_{SD} distribution. The electron channel is shown on the left, while the muon channel is shown on the right. The red vertical lines indicate the boundaries between signal and sideband regions. This figure has been published in Reference [1].

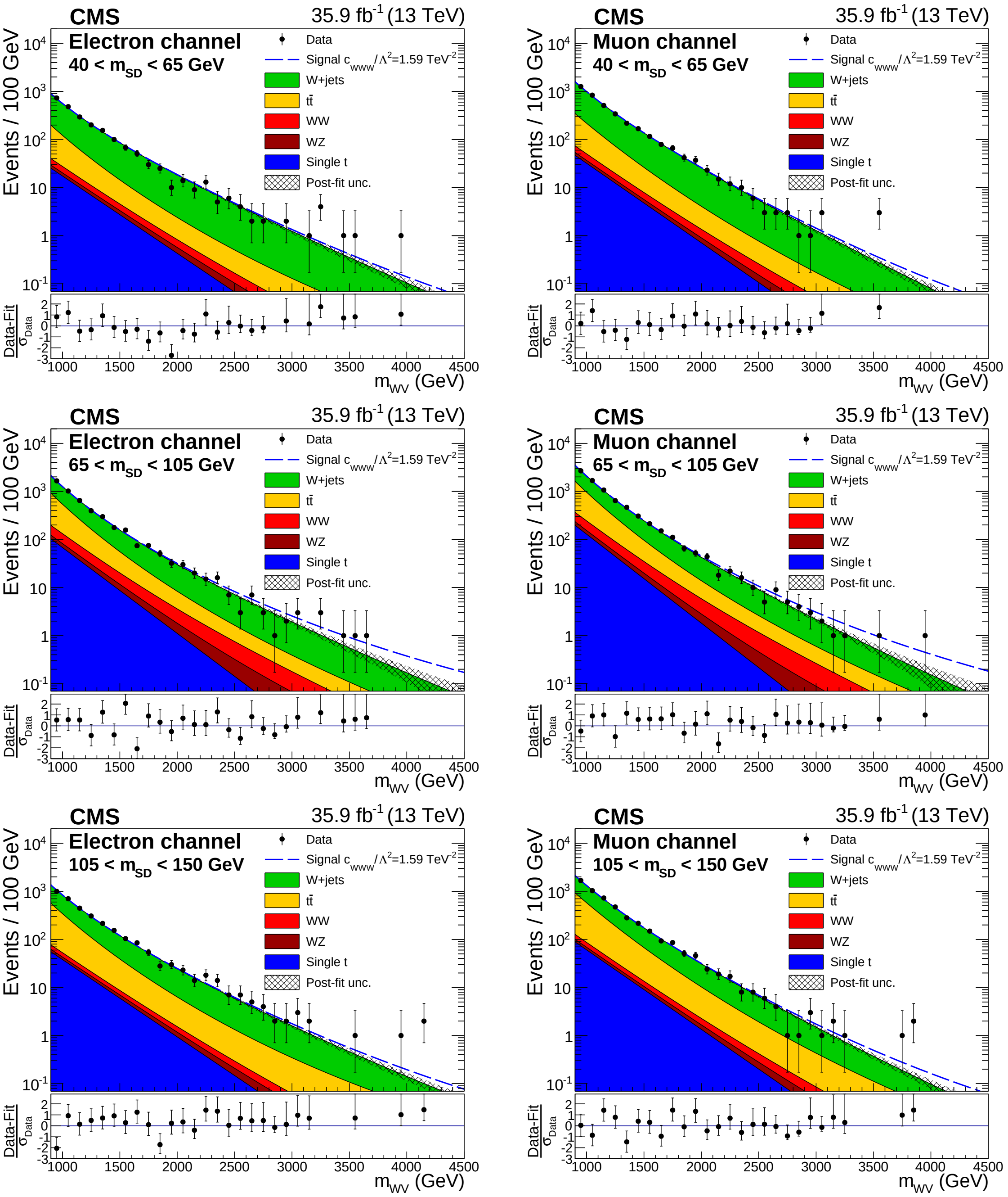

Figure 7.2: Result of the final two-dimensional fit to data, showing the m_{WV} distributions in the lower sideband (top), signal (middle), and upper sideband (bottom) regions. The electron channel is shown on the left, while the muon channel is shown on the right. An example of the excluded signal ($c_{\mathrm{WWW}}/\Lambda^2 = 1.59\ \mathrm{TeV}^{-2}$) is indicated by the dashed line. This figure has been published in Reference [1].

Table 7.1 quotes the final event yields of the various background processes for the WW and WZ categories in both the electron and muon channels. The total background yield is compared with data. In addition, predicted diboson yields with anomalous coupling parameters set to their respective working points are also quoted. The signal diboson yields comprise all contributions, including the contributions from the standard model scenario and anomalous couplings, along with the relevant interference terms, with the nuisance parameters being set to their post-fit values. No significant deviation from the standard model predictions is observed in the yields.

Figure 7.1 shows the final m_{SD} distribution as a result of the two-dimensional fit, whilst Figure 7.2 depicts the m_{WV} distribution in the lower sideband, signal, and upper sideband regions. In both figures, the hashed area represents the combined post-fit uncertainty on the background contributions. The dashed magenta line in Figure 7.2 corresponds to the predicted diboson m_{WV} distribution, with the anomalous coupling parameter c_{WWW} set to its extracted limit value of 1.59 TeV^{-2}. Analogous to the event yields, no significant deviation from the standard model predictions is observed in the shapes of the m_{SD} and m_{WV} distributions.

7.3 Extracted limits on aTGC parameters

Since there is no observed deviation from the SM predictions, confidence intervals are constructed on single aTGC parameters as well as combintions of two parameters simultaneously.

7.3.1 One-dimensional limits

Confidence intervals for single aTGC parameters are constructed by forming the profile likelihood ratio distribution as a function of one aTGC parameter, while explicitly fixing the others to their SM value of zero. Profile likelihood ratio distributions for all aTGC parameters are given in Appendix A.9. Each profile likelihood ratio distribution is then used to set one-dimensional limits on the respective aTGC parameter, using the method outlined in Section 7.1. Limits are derived in both the EFT and LEP parametrisations presented in Chapter 1. To obtain the limits in the LEP parametrisation, the signal is reparametrised using the relationships in Equation 1.52, and the limit setting procedure is repeated.

The derived expected and observed one-dimensional limits on aTGC parameters at 95% CL — which corresponds to $\chi^2 = 3.84$ with one degree of freedom — in both the parametrisations, are quoted in Table 7.2. The expected limits are derived by performing pseudoexperiments in simulation. Observed limits from Run 1 at a centre-of-mass energy of 8 TeV [30] are also quoted to demonstrate the improvement, where the limit on $\Delta\kappa_{\gamma}$ has been converted to a limit on $\Delta\kappa_{Z}$ using Equation 1.52.

The limits obtained from this analysis on all the aTGC parameters are the most stringent constraints on the parameters to date. There is an especially significant improvement in the measured limits on c_{B} and $\Delta\kappa_{Z}$ over any previous measurement. A chart comparing the limits obtained from this analysis to other contemporary and historical measurements is given in Figure 9.1 in the concluding chapter.

In order to ensure that the limits are extracted from an m_{WV} region well below the threshold where the EFT is no longer valid and unitarity is violated, a constraint is placed on the maximum value of m_{WV} used in the fit. This constraint is $m_{\mathrm{WV}} < 4.5$ TeV, based on the observation the maximum m_{WV} for events in the control regions. It is also customary to quote limits with different cutoff values of the closest reference to the scale of the process

Table 7.2: Expected and observed limits at 95% CL on single anomalous triple gauge coupling parameters, along with observed best fit values. Limits are derived in both the EFT and LEP parametrisations, and for each coupling, all other coupling parameters are explicitly set to zero. In order to demonstrate the improvement, observed limits from Run 1 at 8 TeV [30] are also quoted. This table has been published in Reference [1].

Param.	aTGC	Expected limit	Observed limit	Best-fit	8 TeV limit
EFT	$c_{\mathrm{WWW}}/\Lambda^2$ (TeV^{-2})	$[-1.44, 1.47]$	$[-1.58, 1.59]$	-0.26	$[-2.7, 2.7]$
	c_{W}/Λ^2 (TeV^{-2})	$[-2.45, 2.08]$	$[-2.00, 2.65]$	1.21	$[-2.0, 5.7]$
	c_{B}/Λ^2 (TeV^{-2})	$[-8.38, 8.06]$	$[-8.78, 8.54]$	1.07	$[-14, 17]$
LEP	λ_{Z}	$[-0.0060, 0.0061]$	$[-0.0065, 0.0066]$	-0.0010	$[-0.011, 0.011]$
	Δg_1^{Z}	$[-0.0070, 0.0061]$	$[-0.0061, 0.0074]$	0.0027	$[-0.009, 0.024]$
	$\Delta\kappa_{\mathrm{Z}}$	$[-0.0074, 0.0078]$	$[-0.0079, 0.0082]$	-0.0010	$[-0.018, 0.013]$

in an analysis. For this analysis, m_{WV} is a direct representation of the scale of the process; therefore, limits are rederived multiple times, lowering the value of the cutoff threshold on m_{WV} at each step. Figures depicting the limits as a function of the cutoff threshold on m_{WV} for all the aTGC parameters are given in Appendix A.10.

7.3.2 Two-dimensional limits

In order to extract limits on two aTGC parameters simultaneously, two-dimensional profile likelihood ratio distributions are formed as a function of two parameters, while explicitly fixing the third to its SM value of zero. Expected and observed two-dimensional limits on pairwise combinations of aTGC parametes are constructed at 95% CL — which corresponds to $\chi^2 = 5.99$ with two degrees of freedom — in both the EFT and LEP parametrisations.

The limits are represented in the form of contours in the parameter space of the respective parameters, shown in Figure 7.3 for the EFT parametrisation, and 7.4 for the LEP parametrisation. In addition to the 95% CL contours, the best-fit and SM points and the 68 and 99% CL contours are also shown. It is evident from the figures that the observed results are compatible with the standard model scenario. A comparison between the two-dimensional confidence regions for the aTGC parameters obtained from this analysis at a centre-of-mass energy of 13 TeV and the ones obtained from Run 1 at a centre-of-mass energy of 8 TeV [30] is presented in Chapter 8, after discussing preliminary further improvement by inclusion of more data collected during 2017 and 2018.

It is interesting to note that in principle, it is possible to derive simultaneous limits on all three considered aTGC parameters. However, since the three-dimensional profile likelihood ratio distribution is a 3-manifold, and the constructed limit at a certain confidence level is a locus of points in three dimensions, a useful and intuitive visualisation is hard to construct. Furthermore, no new information is obtained from such a construction since there is no term in the expression for the cross section that contains all the three coupling parameters. Therefore, it is customary to only present one- and two-dimensional confidence regions for the parameters as results of experimental high-energy physics analyses aimed at probing the anomalous coupling parameters.

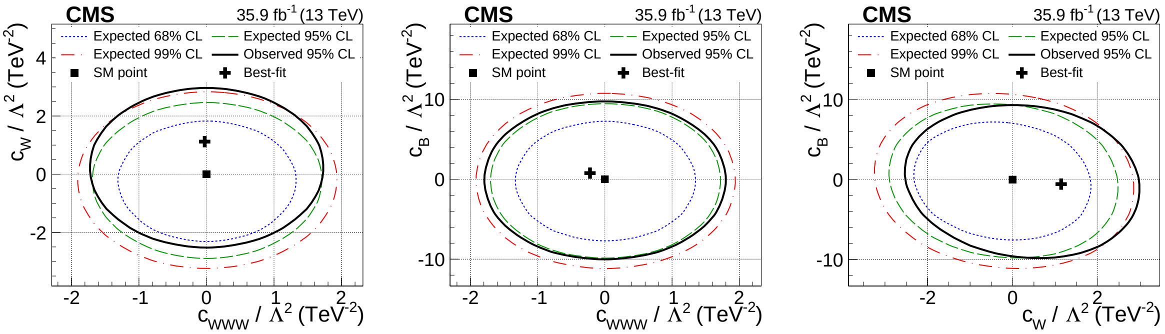

Figure 7.3: Simultaneous limits on two aTGC parameters, in the EFT parametrisation, with the third being fixed to zero. Limits for the combinations c_{WWW}/Λ^2–c_W/Λ^2 (left), c_{WWW}/Λ^2–c_B/Λ^2 (centre), and c_W/Λ^2–c_B/Λ^2 (right) are shown. Expected 95% CL contours are shown in dashed green, whilst the dotted blue and dot-dashed red represent the 68 and 99% CL contours, respectively. Contours for the observed 95% CL are shown in solid black. The SM expectation is marked with the black squares, while the observed best-fit points are shown by the black crosses. This figure has been published in Reference [1].

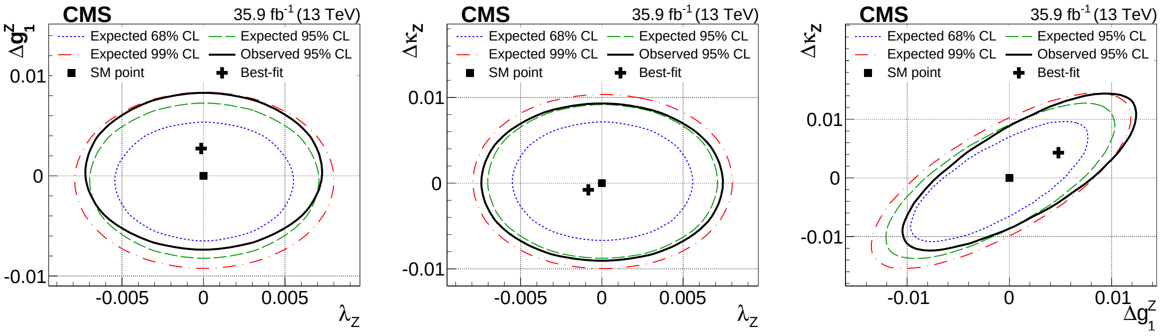

Figure 7.4: Simultaneous limits on two aTGC parameters, in the LEP parametrisation, with the third being fixed to zero. Limits for the combinations λ_Z–Δg_1^Z (left), λ_Z–$\Delta\kappa_Z$ (centre), and Δg_1^Z–$\Delta\kappa_Z$ (right) are shown. Expected 95% CL contours are shown in dashed green, whilst the dotted blue and dot-dashed red represent the 68 and 99% CL contours, respectively. Contours for the observed 95% CL are shown in solid black. The SM expectation is marked with the black squares, while the observed best-fit points are shown by the black crosses. This figure has been published in Reference [1].

All life is an experiment. The more experiments you make the better.

……

– Ralph Waldo Emerson

Extension to full Run 2 data

The more the merrier —

This chapter extends the published results of the analysis to full Run 2 data, making some simplifications in the process. Analysis with 2017 and 2018 data is described, along with the used data sets. The chapter concludes by presenting one- and two-dimensional limits obtained by utilising all the data collected during Run 2 of the LHC operation, corresponding to 137 fb^{-1}.

8

The results of this analysis presented so far have been derived using data collected in proton-proton collisions during 2016, corresponding to an integrated luminosity of 35.9 fb^{-1}. The extent of the extracted confidence intervals is primarily governed by the amount of available data events, whilst systematic uncertainties only play a minor role. As an illustration, eliminating the consideration of systematic uncertainties from the analysis entirely results in a change of only ~5% in the extracted limits. On the other hand, the factor by which the limits improve by increasing luminosity is approximately proportional to the fourth-root of the factor by which the luminosity is increased. For instance, a four-fold increase in luminosity results in limits being improved by a factor of $\sqrt{2}$.

These considerations motivate the extension of the published analysis to utilise all the data collected during Run 2 of the LHC operation. It should, however, be kept in mind that in order to extend the analysis to data collected during 2017 and 2018, certain assumptions and simplifications are made, and the results are preliminary, serving to demonstrate further improvement in the already established world-leading limits from this analysis.

For the preliminary results of the extended analysis, as a simplification, no new simulated samples are produced. This is justified by the fact that the major backgrounds, W+jets entirely and $\mathrm{t\bar{t}}$ in part, are already derived from data, while some of the nuisance parameters calculated from simulation also have enough wiggle room to accommodate small changes in shape. Furthermore, the estimates of the systematic uncertainties are also taken from the published analysis. While performing the analysis with data collected during 2017 and 2018, the distributions derived from simulation are rescaled to normalise them to the luminosity corresponding to the respective years.

8.1 Analysis with 2017 data

During 2017 data taking, a similar amount of data to 2016 was collected. Data corresponding to an integrated luminosity of 41.5 fb^{-1} of the collected data is utilised for this analysis. The used data sets, along with the corresponding luminosity and number of events in each data set, are listed in Table 8.1. Single electron and single muon data sets from run pe-

Table 8.1: Data sets used from 2017 data taking, along with the corresponding luminosity and number of events. The data accumulated in these data sets corresponds to an integrated luminosity of 41.5 fb^{-1}.

Data set	Luminosity (fb^{-1})	Number of events
/SingleElectron/Run2017B-17Nov2017-v1	4.79	60,537,490
/SingleElectron/Run2017C-17Nov2017-v1	9.63	136,637,888
/SingleElectron/Run2017D-17Nov2017-v1	4.25	51,526,710
/SingleElectron/Run2017E-17Nov2017-v1	9.31	102,121,689
/SingleElectron/Run2017F-17Nov2017-v1	13.54	128,467,223
/SingleMuon/Run2017B-17Nov2017-v1	4.79	136,300,266
/SingleMuon/Run2017C-17Nov2017-v1	9.63	165,652,756
/SingleMuon/Run2017D-17Nov2017-v1	4.25	70,361,660
/SingleMuon/Run2017E-17Nov2017-v1	9.31	154,630,534
/SingleMuon/Run2017F-17Nov2017-v1	13.54	242,140,980

riods B to F are used, which have been compiled in the MINIAOD format following the "November 2017" re-reconstruction. The runs containing events selected for analysis are required to pass quality assessment from the data quality monitoring (DQM).

Figure 8.1 shows the obtained post-fit m_{WV} distribution in the signal region, which is used to extract confidence intervals for the aTGC parameters. The derived one-dimensional confidence intervals, along with their respective best-fit values, obtained utilising 2017 data are listed in Table 8.2. For comparison, the published observed limits from the 2016 analysis are also quoted. Since the amounts of data collected during 2016 and 2017 were not drastically different, the final limits are also similar in general, with the limits from the 2017 data on the parameters c_{WWW} and c_{W} being slightly better, and c_{B} being slightly worse compared with the limits from the 2016 data.

Two-dimensional confidence regions for pairwise combinations of the aTGC parameters in the EFT and LEP parametrisations are shown in Figures 8.2 and 8.3, respectively. Additional figures depicting profile likelihood ratio distributions used to derive the one-dimensional confidence regions are given in Appendix A.11.

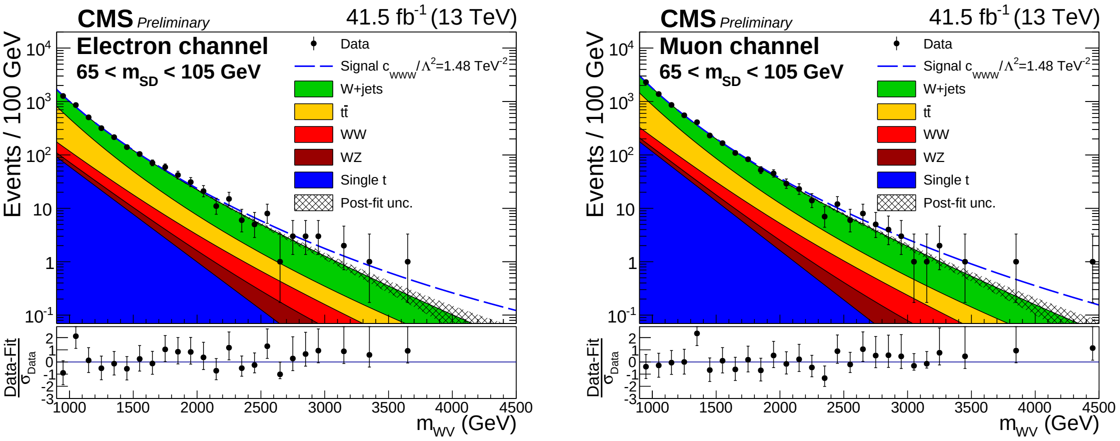

Figure 8.1: Result of the two-dimensional fit in the electron (left) and muon (right) channels for the analysis using data collected during 2017. The m_{WV} distribution in the signal region is shown; an example of the excluded signal ($c_{\mathrm{WWW}}/\Lambda^2 = 1.48\ \mathrm{TeV}^{-2}$) is indicated by the dashed line.

Table 8.2: Expected and observed single aTGC limits at 95% CL, along with observed best fit values, from the analysis using data collected during 2017. Limits are derived in both the EFT and LEP parametrisations. Observed limits from the 2016 analysis are also quoted for comparison.

Param.	aTGC	Expected limit	Observed limit	Best-fit	2016 limit
EFT	$c_{\mathrm{WWW}}/\Lambda^2$ (TeV^{-2})	$[-1.41, 1.44]$	$[-1.42, 1.48]$	0.28	$[-1.58, 1.59]$
	c_{W}/Λ^2 (TeV^{-2})	$[-2.42, 2.06]$	$[-2.7, 0.92]$	-1.38	$[-2.00, 2.65]$
	c_{B}/Λ^2 (TeV^{-2})	$[-8.26, 7.94]$	$[-10.06, 9.22]$	-4.58	$[-8.78, 8.54]$
LEP	λ_Z	$[-0.0059, 0.0060]$	$[-0.0059, 0.0061]$	0.0012	$[-0.0065, 0.0066]$
	Δg_1^Z	$[-0.0068, 0.0060]$	$[-0.0083, 0.0036]$	-0.0044	$[-0.0061, 0.0074]$
	$\Delta\kappa_Z$	$[-0.0050, 0.0054]$	$[-0.0085, 0.0094]$	0.0043	$[-0.0079, 0.0082]$

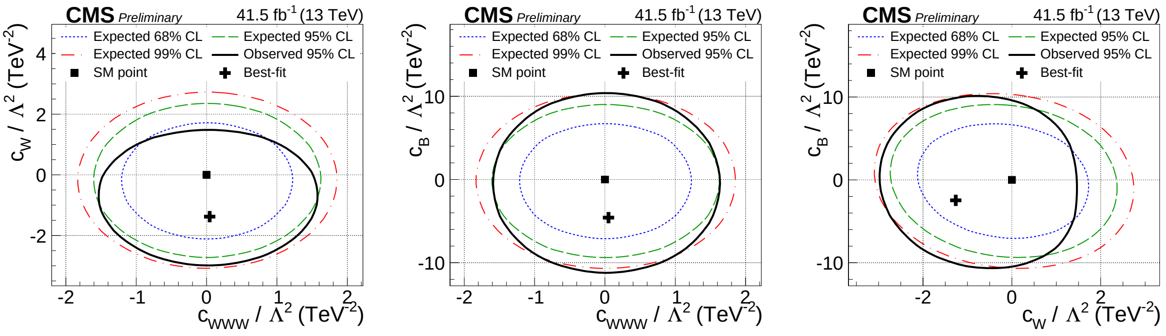

Figure 8.2: Simultaneous limits on two aTGC parameters, in the EFT parametrisation, from the analysis using data collected during 2017. Limits for the combinations c_{WWW}/Λ^2–c_W/Λ^2 (left), c_{WWW}/Λ^2–c_B/Λ^2 (centre), and c_W/Λ^2–c_B/Λ^2 (right) are shown. Observed 95% CL contours are shown in solid black, whilst contours for expected 68, 95, and 99% CL are shown in dotted blue, dashed green, and dot-dashed red, respectively. The SM expectation is marked with the black squares, while the observed best-fit points are indicated by the black crosses.

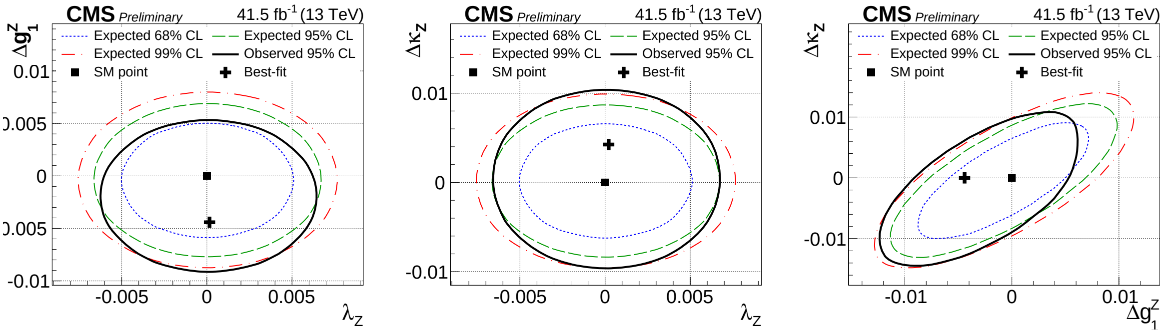

Figure 8.3: Simultaneous limits on two aTGC parameters, in the LEP parametrisation, from the analysis using data collected during 2017. Limits for the combinations λ_Z–Δg_1^Z (left), λ_Z–$\Delta\kappa_Z$ (centre), and Δg_1^Z–$\Delta\kappa_Z$ (right) are shown. Observed 95% CL contours are shown in solid black, whilst contours for expected 68, 95, and 99% CL are shown in dotted blue, dashed green, and dot-dashed red, respectively. The SM expectation is marked with the black squares, while the observed best-fit points are indicated by the black crosses.

8.2 Analysis with 2018 data

Until 2018, the running conditions at the centre-of-mass energy of 13 TeV had been understood and established very well. Therefore, significantly more data was collected during 2018 than 2016 and 2017. 59.9 fb^{-1} of the collected data is utilised for this analysis. The used data sets, along with the corresponding luminosity and number of events, are listed in Table 8.3. EGamma and single muon data sets from run periods A to D, which have been compiled in the MINIAOD format, are used. For run periods A to C, the data sets correspond to the “September 2018” re-reconstruction, whilst for run period D, data sets

Table 8.3: Data sets used from 2018 data taking, along with the corresponding luminosity and number of events. The data accumulated in these data sets corresponds to an integrated luminosity of 59.9 fb^{-1}.

Data set	Luminosity (fb^{-1})	Number of events
/EGamma/Run2018A-17Sep2018-v2	14.03	327, 843, 843
/EGamma/Run2018B-17Sep2018-v1	7.07	153, 822, 427
/EGamma/Run2018C-17Sep2018-v1	6.90	147, 827, 904
/EGamma/Run2018D-PromptReco-v2	31.75	738, 976, 078
/SingleMuon/Run2018A-17Sep2018-v2	14.03	241, 608, 232
/SingleMuon/Run2018B-17Sep2018-v1	7.07	119, 918, 017
/SingleMuon/Run2018C-17Sep2018-v1	6.90	110, 032, 072
/SingleMuon/Run2018D-PromptReco-v2	31.75	506, 717, 754

compiled with prompt reconstruction during data taking are employed, since there was no end-of-year reconstruction for them owing to the upcoming legacy reprocessing. Similar to 2016 and 2017, only runs passing quality assessment from DQM are selected.

Figure 8.4 shows the obtained post-fit m_{WV} distribution in the signal region, using which confidence intervals for the aTGC parameters are extracted. The derived one-dimensional confidence intervals, along with their respective best-fit values, obtained utilising 2018 data are listed in Table 8.4. For comparison, the published observed limits from the 2016 analysis are also quoted. Since the amount of data collected during 2018 was significantly larger than 2016 and 2017, the limits derived on all the parameters are improved noticably.

Two-dimensional confidence regions for pairwise combinations of the aTGC parameters in the EFT and LEP parametrisations are shown in Figures 8.5 and 8.6, respectively. Additional figures depicting profile likelihood ratio distributions used to derive the one-dimensional confidence regions are given in Appendix A.12.

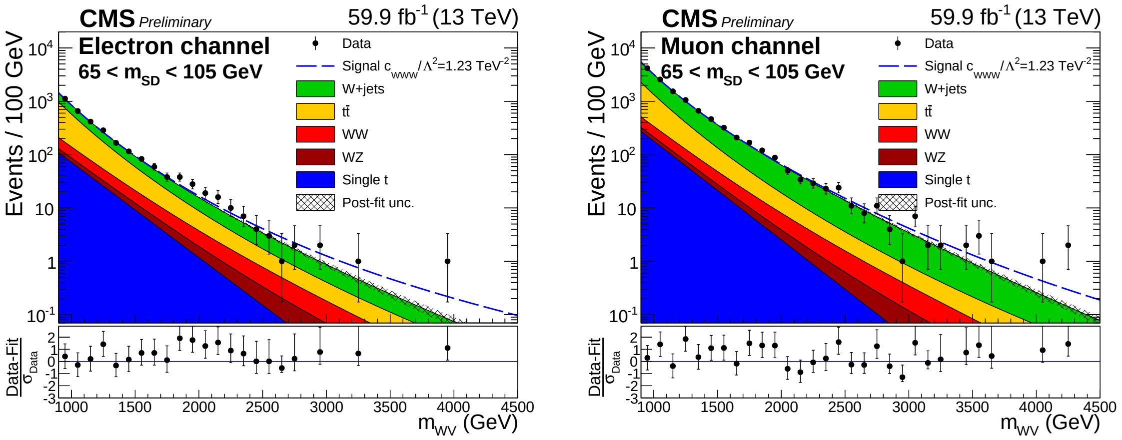

Figure 8.4: Result of the two-dimensional fit in the electron (left) and muon (right) channels for the analysis using data collected during 2018. The m_{WV} distribution in the signal region is shown; an example of the excluded signal ($c_{\mathrm{WWW}}/\Lambda^2 = 1.23\ \mathrm{TeV}^{-2}$) is indicated by the dashed line.

Table 8.4: Expected and observed single aTGC limits at 95% CL, along with observed best fit values, from the analysis using data collected during 2018. Limits are derived in both the EFT and LEP parametrisations. Observed limits from the 2016 analysis are also quoted for comparison.

Param.	aTGC	Expected limit	Observed limit	Best-fit	2016 limit
EFT	$c_{\mathrm{WWW}}/\Lambda^2$ (TeV^{-2})	$[-1.27, 1.29]$	$[-1.22, 1.23]$	-0.01	$[-1.58, 1.59]$
	c_{W}/Λ^2 (TeV^{-2})	$[-2.17, 1.81]$	$[-2.15, 1.63]$	-0.33	$[-2.00, 2.65]$
	c_{B}/Λ^2 (TeV^{-2})	$[-7.34, 7.06]$	$[-7.46, 7.94]$	0.74	$[-8.78, 8.54]$
LEP	λ_{Z}	$[-0.0052, 0.0053]$	$[-0.0050, 0.0051]$	0.0000	$[-0.0065, 0.0066]$
	Δg_1^{Z}	$[-0.0061, 0.0054]$	$[-0.0061, 0.0053]$	-0.0004	$[-0.0061, 0.0074]$
	$\Delta\kappa_{\mathrm{Z}}$	$[-0.0065, 0.0069]$	$[-0.0073, 0.0069]$	-0.0007	$[-0.0079, 0.0082]$

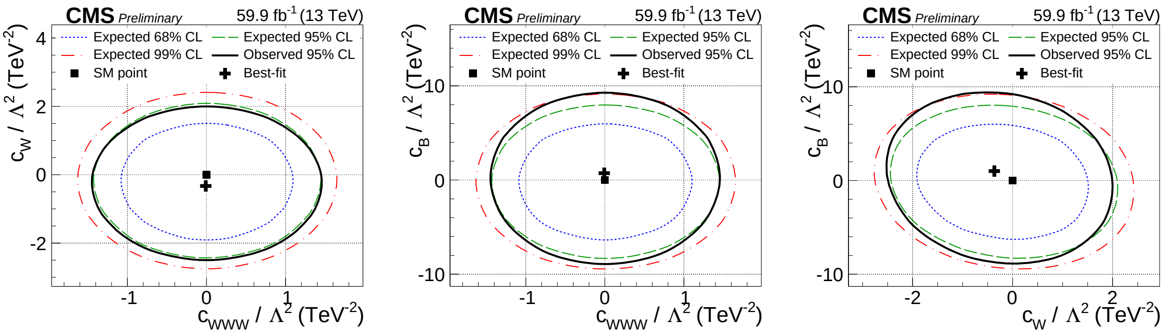

Figure 8.5: Simultaneous limits on two aTGC parameters, in the EFT parametrisation, from the analysis using data collected during 2018. Expected 68, 95, and 99% CL and observed 95% CL limits for the combinations $c_{\mathrm{WWW}}/\Lambda^2$–$c_{\mathrm{W}}/\Lambda^2$ (left), $c_{\mathrm{WWW}}/\Lambda^2$–$c_{\mathrm{B}}/\Lambda^2$ (centre), and c_{W}/Λ^2–c_{B}/Λ^2 (right) are shown, along with the respective best-fit and SM points.

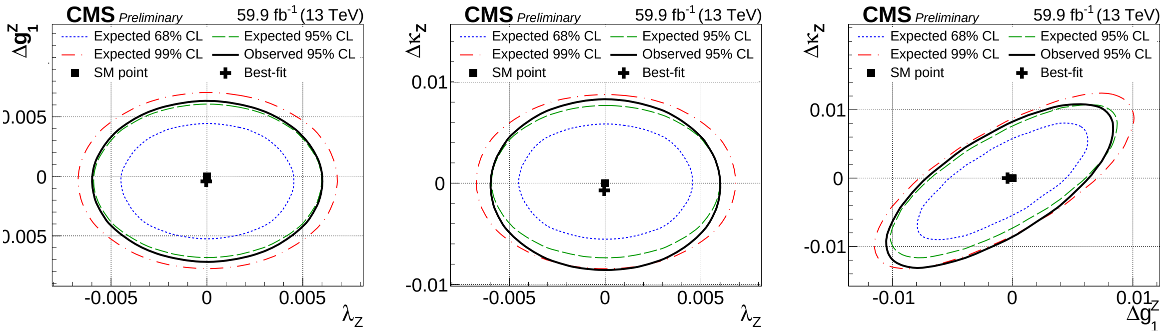

Figure 8.6: Simultaneous limits on two aTGC parameters, in the LEP parametrisation, from the analysis using data collected during 2018. Expected 68, 95, and 99% CL and observed 95% CL limits for the combinations λ_{Z}–Δg_1^{Z} (left), λ_{Z}–$\Delta\kappa_{\mathrm{Z}}$ (centre), and Δg_1^{Z}–$\Delta\kappa_{\mathrm{Z}}$ (right) are shown, along with the respective best-fit and SM points.

8.3 Limits using full Run 2 data

Extremely stringent constraints on the aTGC parameters can be established by combining data from all the years. To this end, the final fit is performed on the combined data, corresponding to 137 fb^{-1} at a centre-of-mass energy of 13 TeV. Figure 8.7 shows the final post-fit m_{WV} distribution in the signal region for the 137 fb^{-1} of data. The corresponding one-dimensional confidence intervals, along with their respective best-fit values, are listed in Table 8.5. Observed limits on the same parameters from proton-proton collision data from Run 1 at a centre-of-mass energy of 8 TeV [30] are also quoted to demonstrate the improvement in this analysis at a centre-of-mass energy of 13 TeV.

Similar comparisons between the two-dimensional confidence regions from Run 1 and Run 2 for pairwise combinations of the aTGC parameters in the EFT and LEP parametrisations are shown in Figures 8.8 and 8.9, respectively. Comparing the observed 95% CL contours from this analysis with the ones from the analysis utilising 8 TeV data highlights the extensive improvement in this analysis.

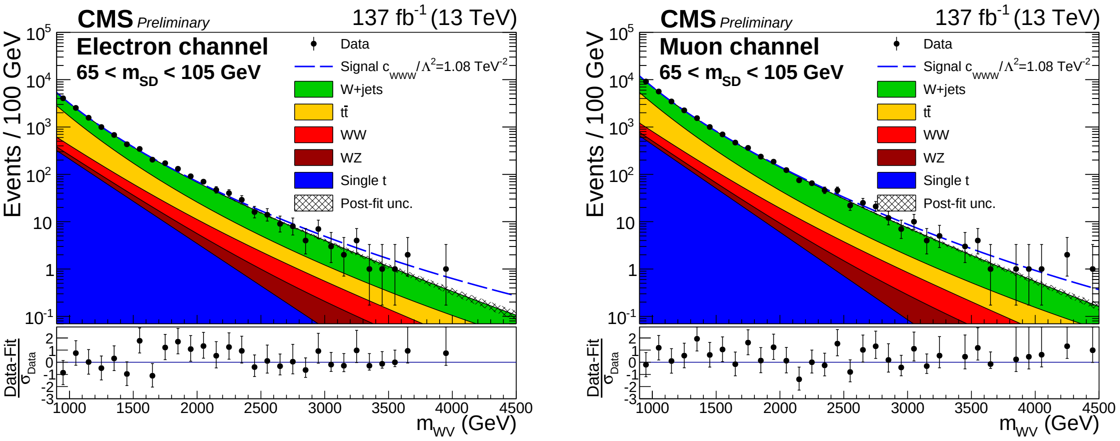

Figure 8.7: Result of the two-dimensional fit in the electron (left) and muon (right) channels for the analysis using full Run 2 data. The m_{WV} distribution in the signal region is shown; an example of the excluded signal ($c_{\mathrm{WWW}}/\Lambda^2 = 1.08\ \mathrm{TeV}^{-2}$) is indicated by the dashed line.

Table 8.5: Expected and observed single aTGC limits at 95% CL, along with observed best fit values, from the analysis using full Run 2 data. Limits are derived in both the EFT and LEP parametrisations. In order to demonstrate the improvement in limits from Run 1 to Run 2, observed limits from Run 1 [30] are also quoted.

Param.	aTGC	Expected limit	Observed limit	Best-fit	8 TeV limit
EFT	$c_{\mathrm{WWW}}/\Lambda^2\ (\mathrm{TeV}^{-2})$	$[-1.09, 1.11]$	$[-1.04, 1.08]$	0.07	$[-2.7, 2.7]$
	$c_{\mathrm{W}}/\Lambda^2\ (\mathrm{TeV}^{-2})$	$[-1.87, 1.51]$	$[-1.99, 0.688]$	-1.01	$[-2.0, 5.7]$
	$c_{\mathrm{B}}/\Lambda^2\ (\mathrm{TeV}^{-2})$	$[-6.26, 5.98]$	$[-6.98, 6.42]$	-2.34	$[-14, 17]$
LEP	λ_Z	$[-0.0045, 0.0046]$	$[-0.0043, 0.0044]$	0.0003	$[-0.011, 0.011]$
	Δg_1^Z	$[-0.0052, 0.0049]$	$[-0.0057, 0.0027]$	-0.0029	$[-0.009, 0.024]$
	$\Delta\kappa_Z$	$[-0.0055, 0.0058]$	$[-0.0059, 0.0065]$	0.0021	$[-0.018, 0.013]$

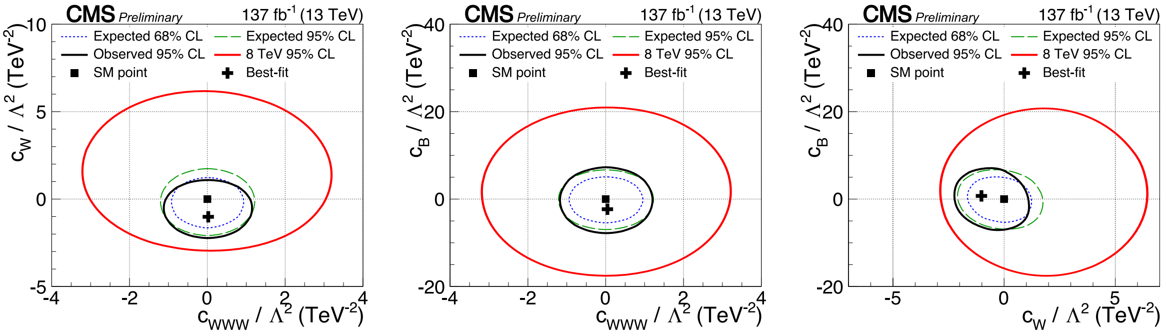

Figure 8.8: Comparison of simultaneous limits on two aTGC parameters, in the EFT parametrisation, from Run 2 with the ones from Run 1. Limits for the combinations c_{WWW}/Λ^2–c_W/Λ^2 (left), c_{WWW}/Λ^2–c_B/Λ^2 (centre), and c_W/Λ^2–c_B/Λ^2 (right) are shown. Run 1 limits are shown in solid red, whilst the improved Run 2 limits are shown in solid black. Expected 68 and 95% CL contours for Run 2 are shown in dotted blue and dashed green, respectively. The SM expectation is marked with the black squares, while the observed best-fit points are indicated by the black crosses.

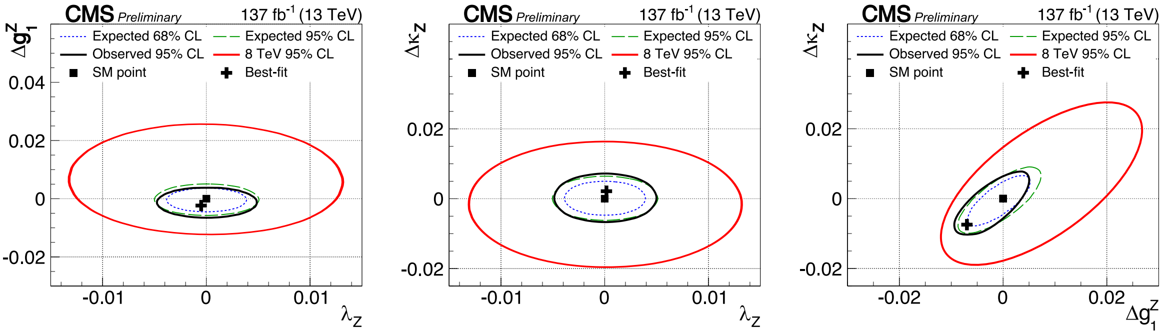

Figure 8.9: Comparison of simultaneous limits on two aTGC parameters, in the LEP parametrisation, from Run 2 with the ones from Run 1. Limits for the combinations λ_Z–Δg_1^Z (left), λ_Z–$\Delta\kappa_Z$ (centre), and Δg_1^Z–$\Delta\kappa_Z$ (right) are shown. Run 1 limits are shown in solid red, whilst the improved Run 2 limits are shown in solid black. Expected 68 and 95% CL contours for Run 2 are shown in dotted blue and dashed green, respectively. The SM expectation is marked with the black squares, while the observed best-fit points are indicated by the black crosses.

Once you eliminate the impossible, whatever remains, no matter how improbable, must be the truth.

……

– Arthur Conan Doyle,
Sherlock Holmes

9

Conclusion and future prospects

To an end, and beyond —

This concluding chapter summarises the analysis presented in this thesis, and makes recommendations for future work on the topic.

The standard model (SM) of particle physics has been serving as an epitome of human understanding about the constituents of matter for many decades. However, keeping in view the theoretical and experimental shortcomings of the SM, myriads of beyond SM (BSM) models and extensions have been proposed. Many of these models add new physics at scales beyond the reach of our current particle colliders. Therefore, despite the earnest efforts of the particle physics community, no direct evidence of any of the BSM models has emerged. Considering the abundance of the BSM models and a limited reach compared with the scale of the new physics introduced, our best bet is to search for consequent deviations in the SM interactions in a model-independent approach. To this end, an effective quantum field theory has been proposed, wherein the impact of the BSM physics is parametrised by adding higher-order operators to the SM Lagrangian.

In this thesis, a search for anomalous $WW\gamma$ and WWZ triple gauge couplings (aTGCs) in the effective field theory (EFT) framework was presented. The search utilised data recorded by the Compact Muon Solenoid (CMS) experiment at the CERN LHC in proton-proton collisions during 2016, corresponding to an integrated luminosity of 35.9 fb^{-1}. WW and WZ events were considered for the analysis, with a W boson decaying into a charged lepton and the corresponding neutrino, and a W or Z boson decaying into hadrons. This semileptonic final state has a perfect balance between purity and efficiency compared with the fully leptonic and hadronic final states. Since the search was targeted towards highly boosted vector bosons, the hadronically decaying vector boson was reconstructed as a single, large-radius jet, and jet substructure techniques were used to improve sensitivity to gauge boson decays and suppress background processes.

A multitude of Monte Carlo (MC) event generators, comprising various components in proton-proton collisions, were used to simulate the signal and background processes. In order to reconstruct events in data and simulation, both standard and analysis-specific reconstruction techniques were used, incorporating simulation corrections and sources of systematic uncertainties. W+jets, top quark pair, SM diboson, and single top quark production processes were considered as background processes for the analysis. Carefully optimised selection requirements were imposed to enrich the selection of signal events while suppressing the background processes.

The signal and background processes were modelled using parametric functions, with the signal function accounting for contributions from different aTGCs and their interference, as well as the interference between the SM contribution and each aTGC. The background processes were estimated using a mix of simulation and data-driven techniques. In particular, the dominant background process, W+jets, was estimated in the signal region by transferring normalisation and shape of the contribution from a W+jets-enriched sideband region, using a transfer function derived from simulation. The final background estimation and signal extraction was carried out in a two-dimensional fit in the $(m_{\mathrm{SD}}, m_{\mathrm{WV}})$-plane. The m_{WV} distribution in the signal region was utilised to derive one- and two-dimensional confidence regions on the aTGC parameters in the EFT and LEP parametrisations.

The results of this analysis have been published in Reference [1]. The obtained 95% confidence intervals, $-1.58 < c_{\mathrm{WWW}}/\Lambda^2 < 1.59\ \mathrm{TeV}^{-2}$, $-2.00 < c_{\mathrm{W}}/\Lambda^2 < 2.65\ \mathrm{TeV}^{-2}$, and $-8.78 < c_{\mathrm{B}}/\Lambda^2 < 8.54\ \mathrm{TeV}^{-2}$, are the strictest bounds on these parameters to date. In order to demonstrate the improvement obtained in this analysis, a comparison with other contemporary and historical measurements is shown in Figure 9.1 in the LEP parametrisation, which has been used historically to present these results. The measurements include those performed at the LEP [65], DØ [66], CMS [11, 14, 26, 29, 30, 67], and ATLAS [19, 20, 22, 23, 27, 28, 31, 32, 177, 178] experiments. The limits from this analysis are significantly better than any other previous measurement, with an improvement by up to a factor of ~3 from the next best measurement in case of one of the parameters, $\Delta\kappa_Z$.

Moving forward, there are a number of further improvements that can be made to this analysis. Since the results from the analysis depend primarily on the amount of available data events, a significant improvement in the limits on the anomalous coupling parameters was already demonstrated by extending the results of the published analysis to 137 fb^{-1} of collision data taken at a centre-of-mass energy of 13 TeV. Owing to time constraints and unavailability of some simulated samples, certain simplifications had to be made for this extension. The simplifications, although justified, warrant further work before the results with the 137 fb^{-1} of data can be published. In particular, all the signal and background MC simulated samples for 2017 and 2018 data taking, with the corresponding conditions and simulation corrections, need to be implemented in the analysis to extract the contributions derived from simulation with greater accuracy for the analyses with 2017 and 2018 data.

One of the other major improvements to this analysis is the inclusion of angular variables characterising a diboson event [179]. Details of the characterising angles and a preliminary study to improve the limits on the aTGC parameters by introducing an optimised selection requirement on the variable $|\cos\theta^*|$ are given in Appendix A.13. The study already demonstrates a significant improvement in the size of the confidence intervals. The results can be further refined by better incorporating the angular variables into the analysis, and using m_{SD}, τ_{21}, and $|\cos\theta^*|$ simultaneously to distinguish between signal and background events. A multivariate machine learning technique may be used, with the aforementioned and other variables as input, to enhance the distinguishing capability.

In order to further reduce the contribution of the background processes, methodological enhancements can be implemented. For instance, the contribution of the W+jets background can be reduced by utilising additional jet substructure variables, including quark/gluon likelihood, subjet quark/gluon likelihood, energy correlations functions, Q-jet volatility, jet pull angle, and jet pull magnitude [180]. Similarly the contribution of the $\mathrm{t\bar{t}}$ background can be suppressed by employing top jet tagging [181].

In terms of theoretical accuracy, investigation has to be carried out regarding the impact and validity of differential corrections from higher order, NNLO QCD [172, 173] and NLO electroweak [174], contributions to the signal process with anomalous gauge couplings. These corrections need to be incorporated into the simulated samples for further analyses, since their effects can be particularly large at higher values of m_{WV}.

As with any scientific endeavour, it is imperative that this search for physics beyond the SM in the vector boson sector is carried on with persistence. With significantly more data from the upcoming data-taking runs of the LHC, and the high-luminosity LHC, and novel improvements in analysis techniques, we shall either obtain extremely precise measurements, cementing our understanding of the elementary particles, or observe a deviation that is the harbinger of the next scientific revolution.

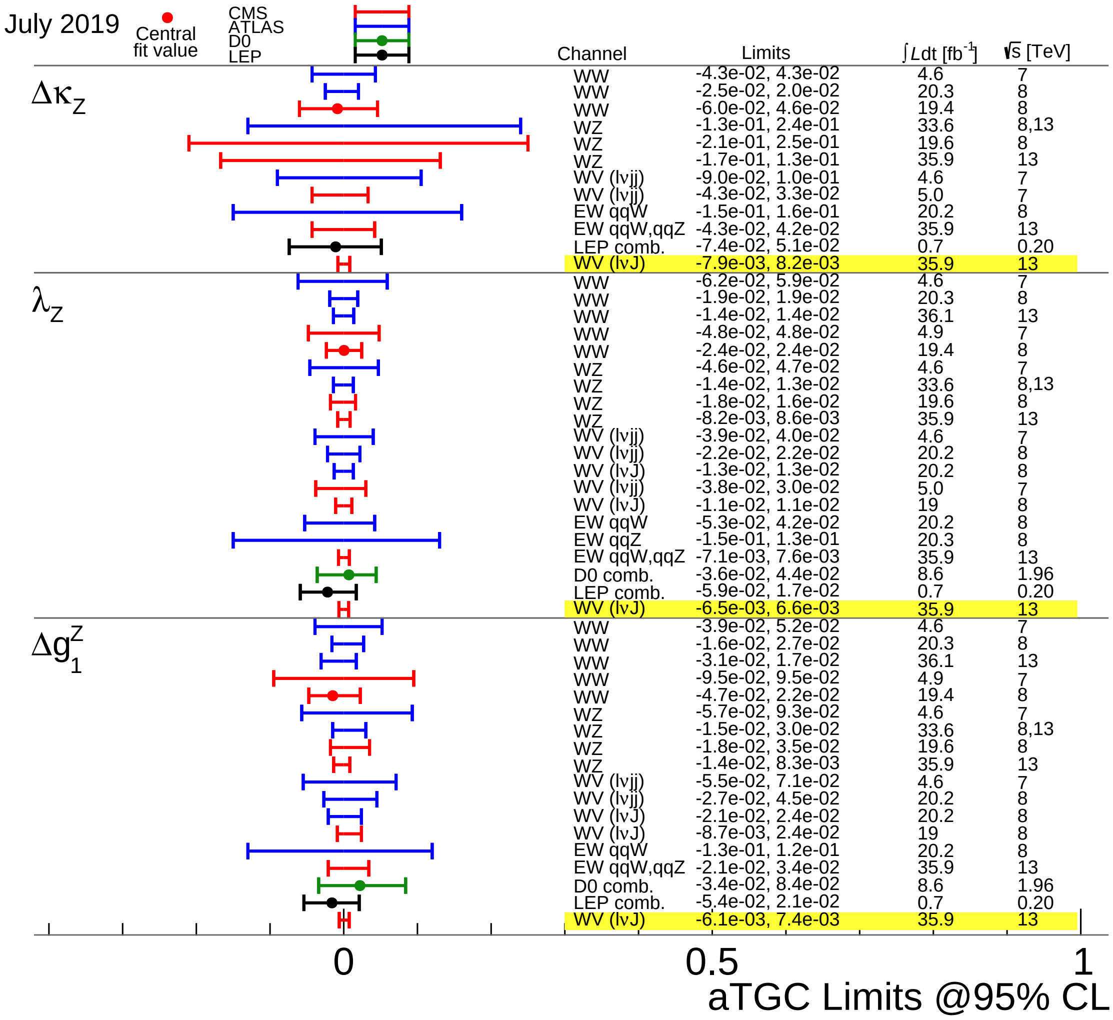

	Channel	Limits	$\int L dt$ [fb^{-1}]	$\sqrt{s}$ [TeV]
$\Delta\kappa_Z$	WW	-4.3e-02, 4.3e-02	4.6	7
	WW	-2.5e-02, 2.0e-02	20.3	8
	WW	-6.0e-02, 4.6e-02	19.4	8
	WZ	-1.3e-01, 2.4e-01	33.6	8,13
	WZ	-2.1e-01, 2.5e-01	19.6	8
	WZ	-1.7e-01, 1.3e-01	35.9	13
	WV (lνjj)	-9.0e-02, 1.0e-01	4.6	7
	WV (lνjj)	-4.3e-02, 3.3e-02	5.0	7
	EW qqW	-1.5e-01, 1.6e-01	20.2	8
	EW qqW,qqZ	-4.3e-02, 4.2e-02	35.9	13
	LEP comb.	-7.4e-02, 5.1e-02	0.7	0.20
	WV (lνJ)	-7.9e-03, 8.2e-03	35.9	13
λ_Z	WW	-6.2e-02, 5.9e-02	4.6	7
	WW	-1.9e-02, 1.9e-02	20.3	8
	WW	-1.4e-02, 1.4e-02	36.1	13
	WW	-4.8e-02, 4.8e-02	4.9	7
	WW	-2.4e-02, 2.4e-02	19.4	8
	WZ	-4.6e-02, 4.7e-02	4.6	7
	WZ	-1.4e-02, 1.3e-02	33.6	8,13
	WZ	-1.8e-02, 1.6e-02	19.6	8
	WZ	-8.2e-03, 8.6e-03	35.9	13
	WV (lνjj)	-3.9e-02, 4.0e-02	4.6	7
	WV (lνjj)	-2.2e-02, 2.2e-02	20.2	8
	WV (lνJ)	-1.3e-02, 1.3e-02	20.2	8
	WV (lνjj)	-3.8e-02, 3.0e-02	5.0	7
	WV (lνJ)	-1.1e-02, 1.1e-02	19	8
	EW qqW	-5.3e-02, 4.2e-02	20.2	8
	EW qqZ	-1.5e-01, 1.3e-01	20.3	8
	EW qqW,qqZ	-7.1e-03, 7.6e-03	35.9	13
	D0 comb.	-3.6e-02, 4.4e-02	8.6	1.96
	LEP comb.	-5.9e-02, 1.7e-02	0.7	0.20
	WV (lνJ)	-6.5e-03, 6.6e-03	35.9	13
Δg_1^Z	WW	-3.9e-02, 5.2e-02	4.6	7
	WW	-1.6e-02, 2.7e-02	20.3	8
	WW	-3.1e-02, 1.7e-02	36.1	13
	WW	-9.5e-02, 9.5e-02	4.9	7
	WW	-4.7e-02, 2.2e-02	19.4	8
	WZ	-5.7e-02, 9.3e-02	4.6	7
	WZ	-1.5e-02, 3.0e-02	33.6	8,13
	WZ	-1.8e-02, 3.5e-02	19.6	8
	WZ	-1.4e-02, 8.3e-03	35.9	13
	WV (lνjj)	-5.5e-02, 7.1e-02	4.6	7
	WV (lνjj)	-2.7e-02, 4.5e-02	20.2	8
	WV (lνJ)	-2.1e-02, 2.4e-02	20.2	8
	WV (lνJ)	-8.7e-03, 2.4e-02	19	8
	EW qqW	-1.3e-01, 1.2e-01	20.2	8
	EW qqW,qqZ	-2.1e-02, 3.4e-02	35.9	13
	D0 comb.	-3.4e-02, 8.4e-02	8.6	1.96
	LEP comb.	-5.4e-02, 2.1e-02	0.7	0.20
	WV (lνJ)	-6.1e-03, 7.4e-03	35.9	13

Figure 9.1: Comparison of the observed limits on aTGC parameters from different measurements. The highlighted rows represent the limits obtained from the measurement presented in this thesis. This figure has been published in Reference [1].

I have discovered a truly remarkable proof of this proposition which this margin is too narrow to contain.

— Pierre de Fermat

Appendices

The devil in the detail —

This section presents supplementary material, which contains useful details, but was too disruptive or extensive to put in the main text. The thesis concludes with lists of figures and tables, a bibliography, and closing remarks.

A.1 Additional figures for b tagging efficiencies

A.1.1 WW signal

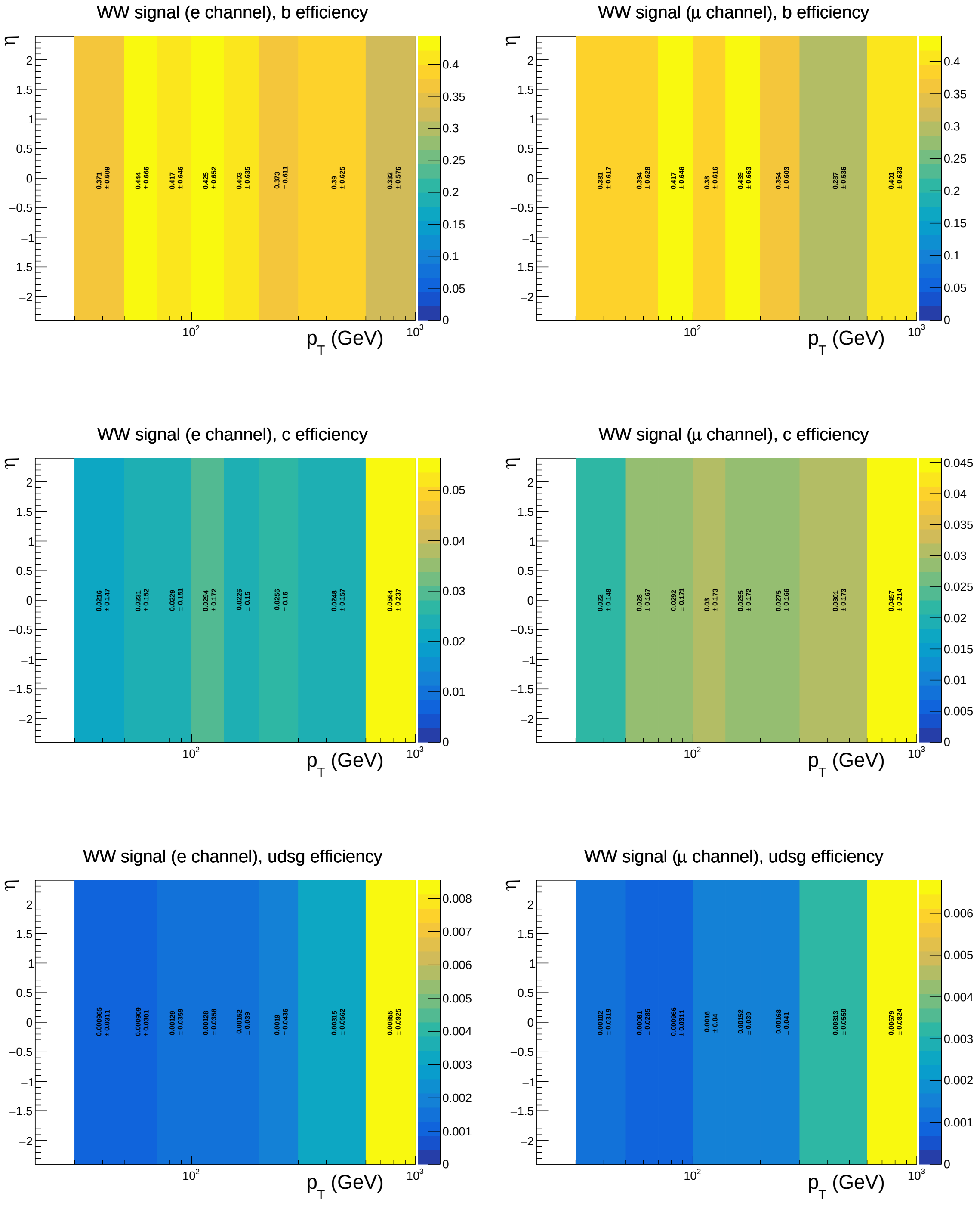

Figure A.1: b tagging efficiencies as a function of p_T and η for the simulated WW signal sample in the electron (left) and muon (right) channels. b tagging efficiencies for b jets, and mistagging efficiencies for c and light jets are shown on the top, middle, and bottom, respectively.

A.1.2 WZ signal

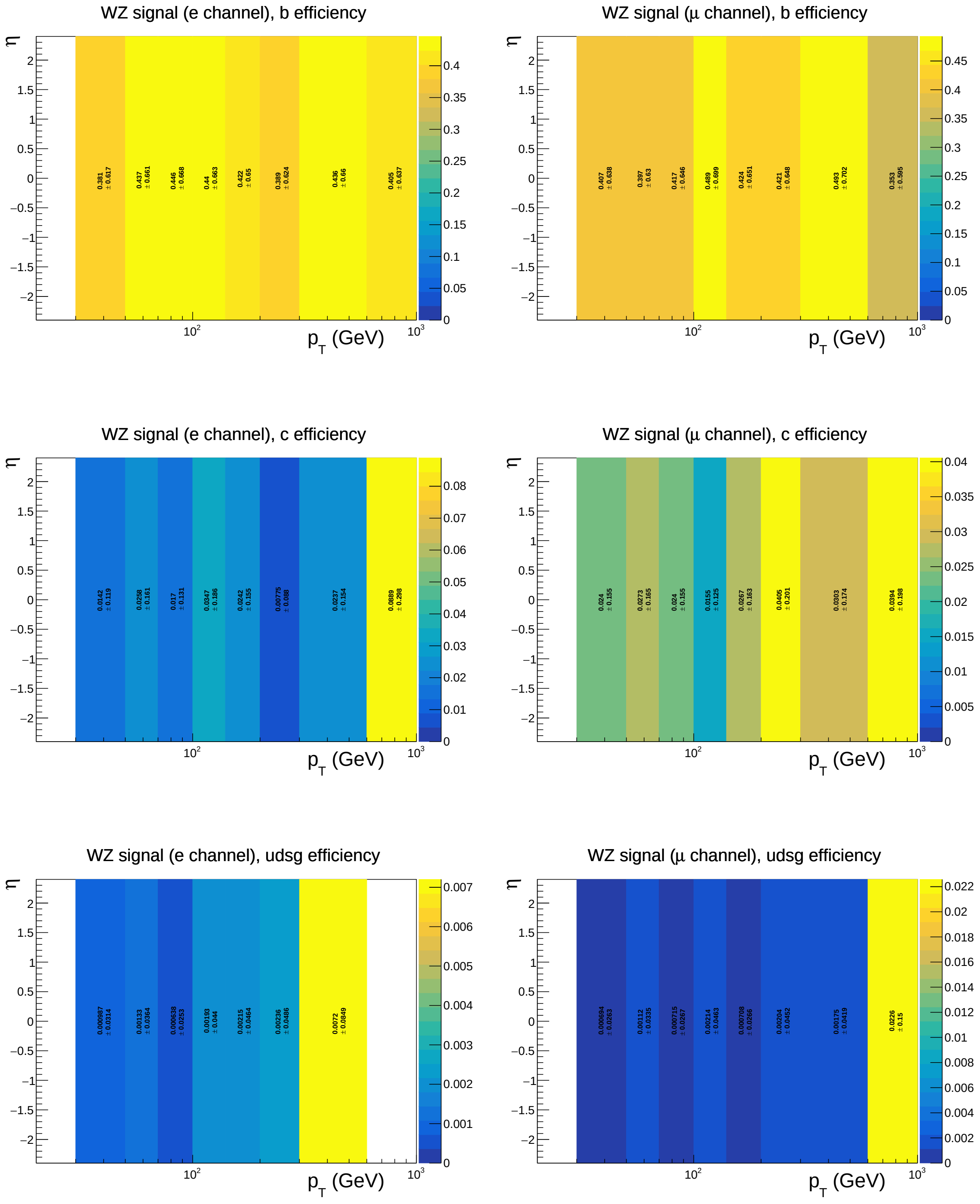

Figure A.2: b tagging efficiencies as a function of p_T and η for the simulated WZ signal sample in the electron (left) and muon (right) channels. b tagging efficiencies for b jets, and mistagging efficiencies for c and light jets are shown on the top, middle, and bottom, respectively.

A.1.3 W+jets

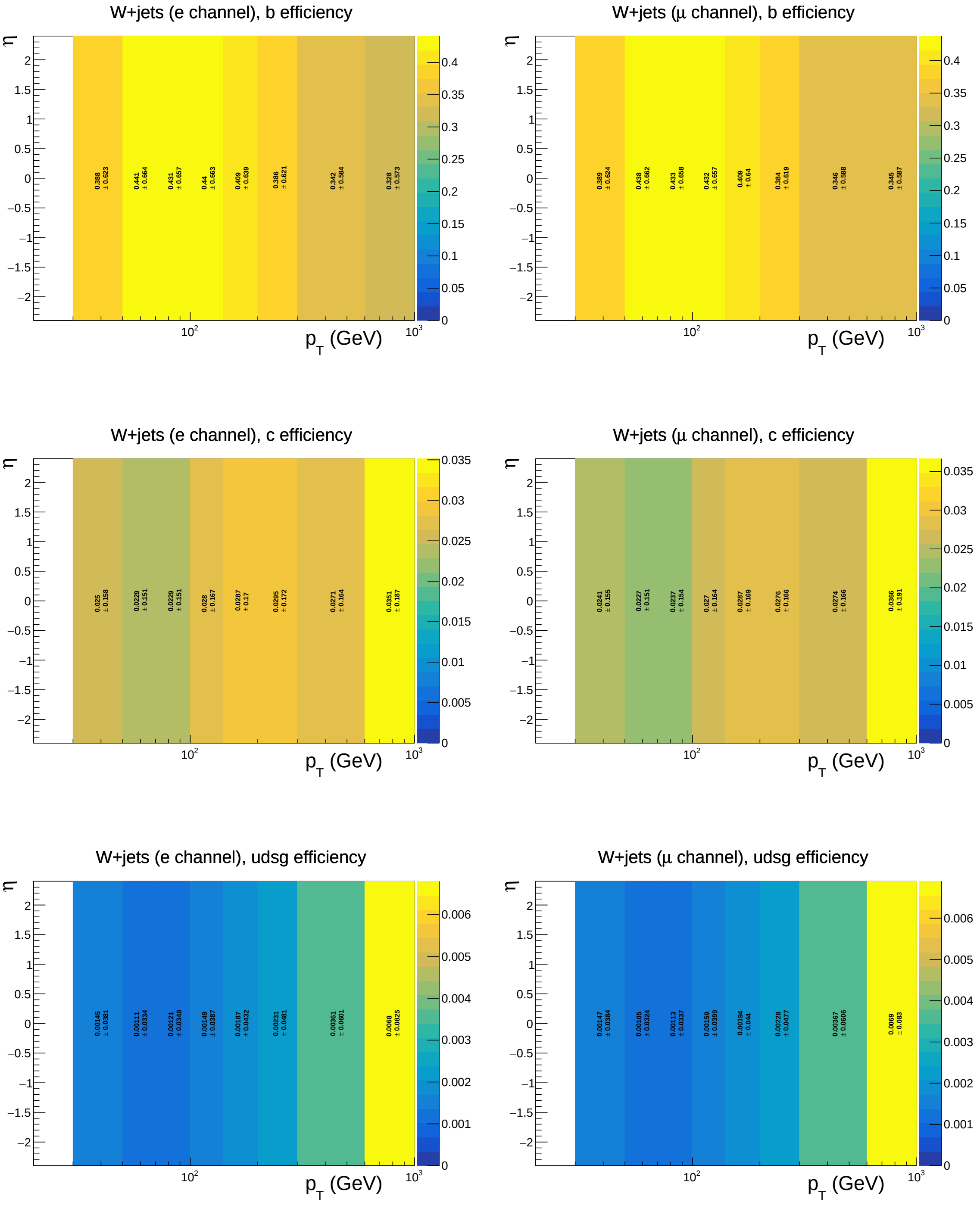

Figure A.3: b tagging efficiencies as a function of p_T and η for the simulated W+jets sample in the electron (left) and muon (right) channels. b tagging efficiencies for b jets, and mistagging efficiencies for c and light jets are shown on the top, middle, and bottom, respectively.

A.1.4 SM WW

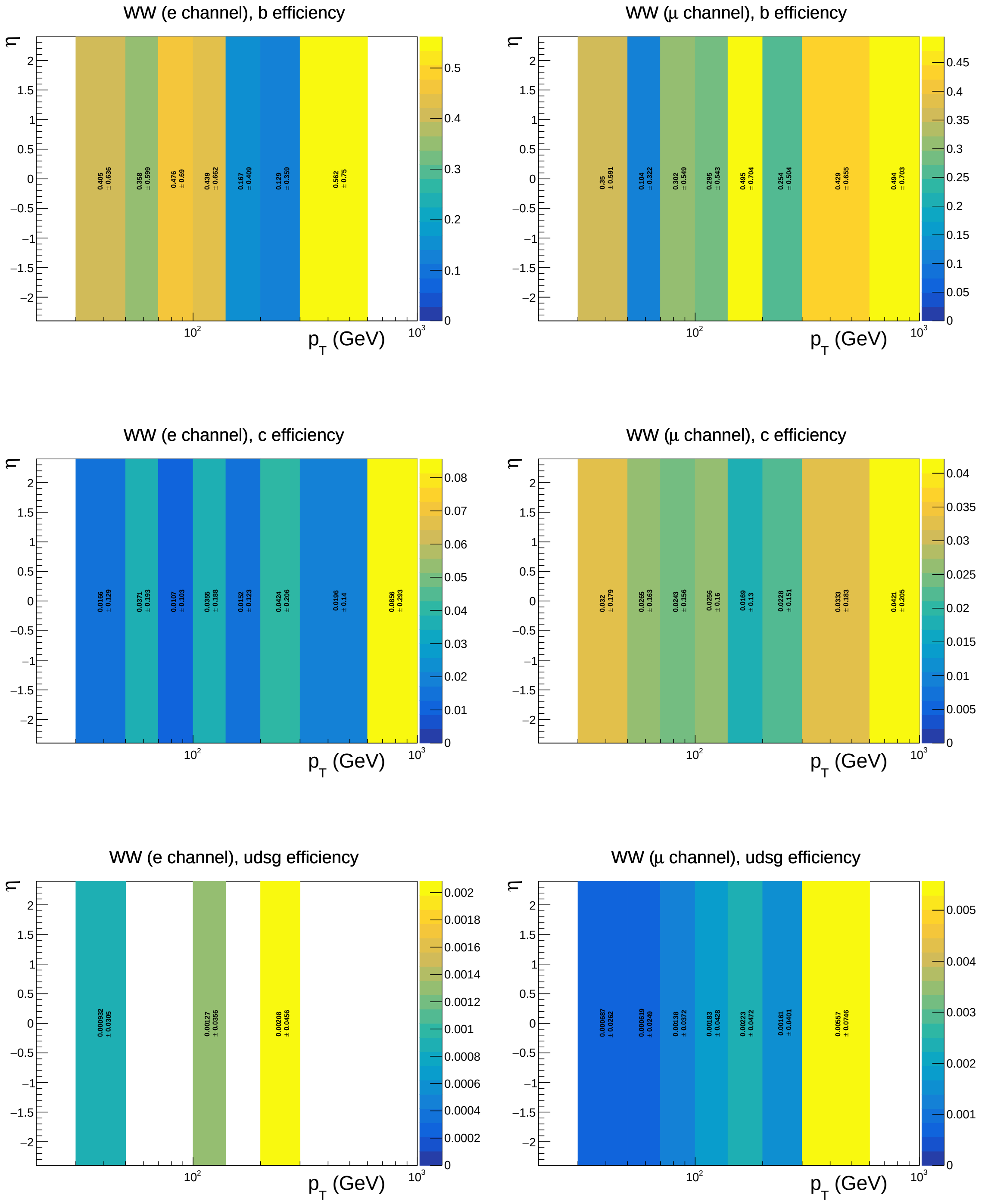

Figure A.4: b tagging efficiencies as a function of p_T and η for the simulated SM WW sample in the electron (left) and muon (right) channels. b tagging efficiencies for b jets, and mistagging efficiencies for c and light jets are shown on the top, middle, and bottom, respectively.

A.1.5 SM WZ

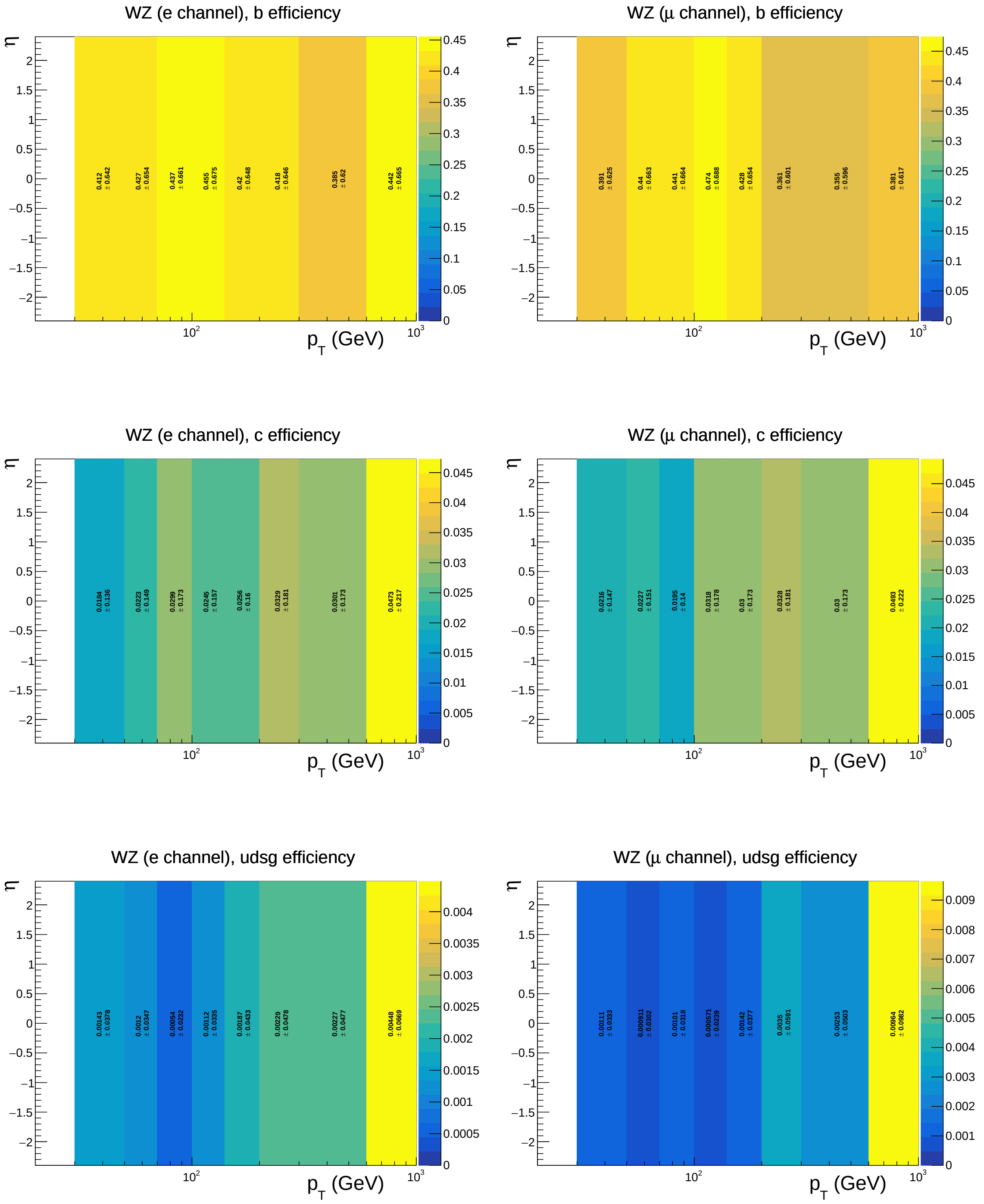

Figure A.5: b tagging efficiencies as a function of p_{T} and η for the simulated SM WZ sample in the electron (left) and muon (right) channels. b tagging efficiencies for b jets, and mistagging efficiencies for c and light jets are shown on the top, middle, and bottom, respectively.

A.1.6 Single top quark

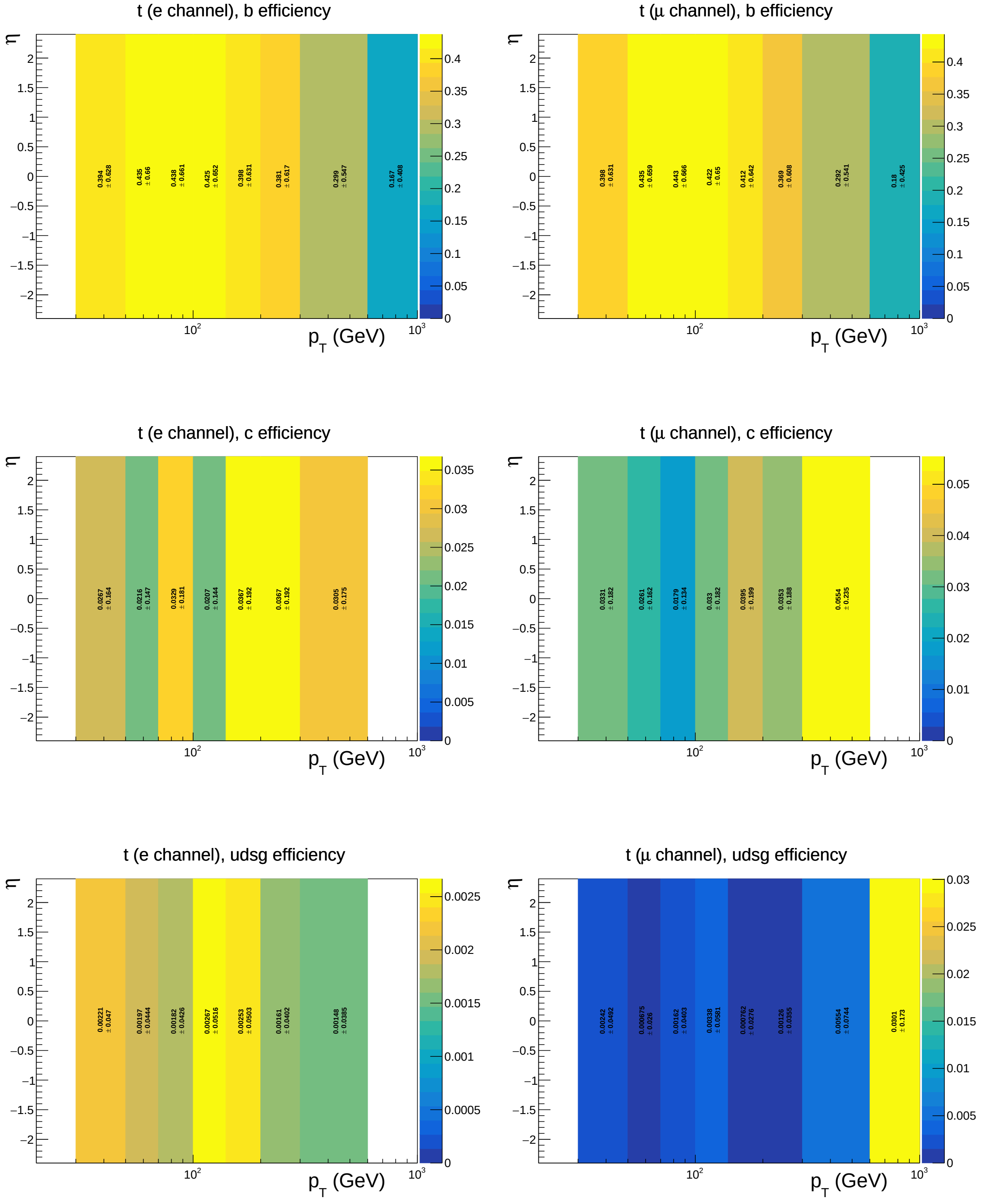

Figure A.6: b tagging efficiencies as a function of p_T and η for simulated single top quark samples in the electron (left) and muon (right) channels. b tagging efficiencies for b jets, and mistagging efficiencies for c and light jets are shown on the top, middle, and bottom, respectively.

A.2 Additional figures for impact of nonzero aTGCs

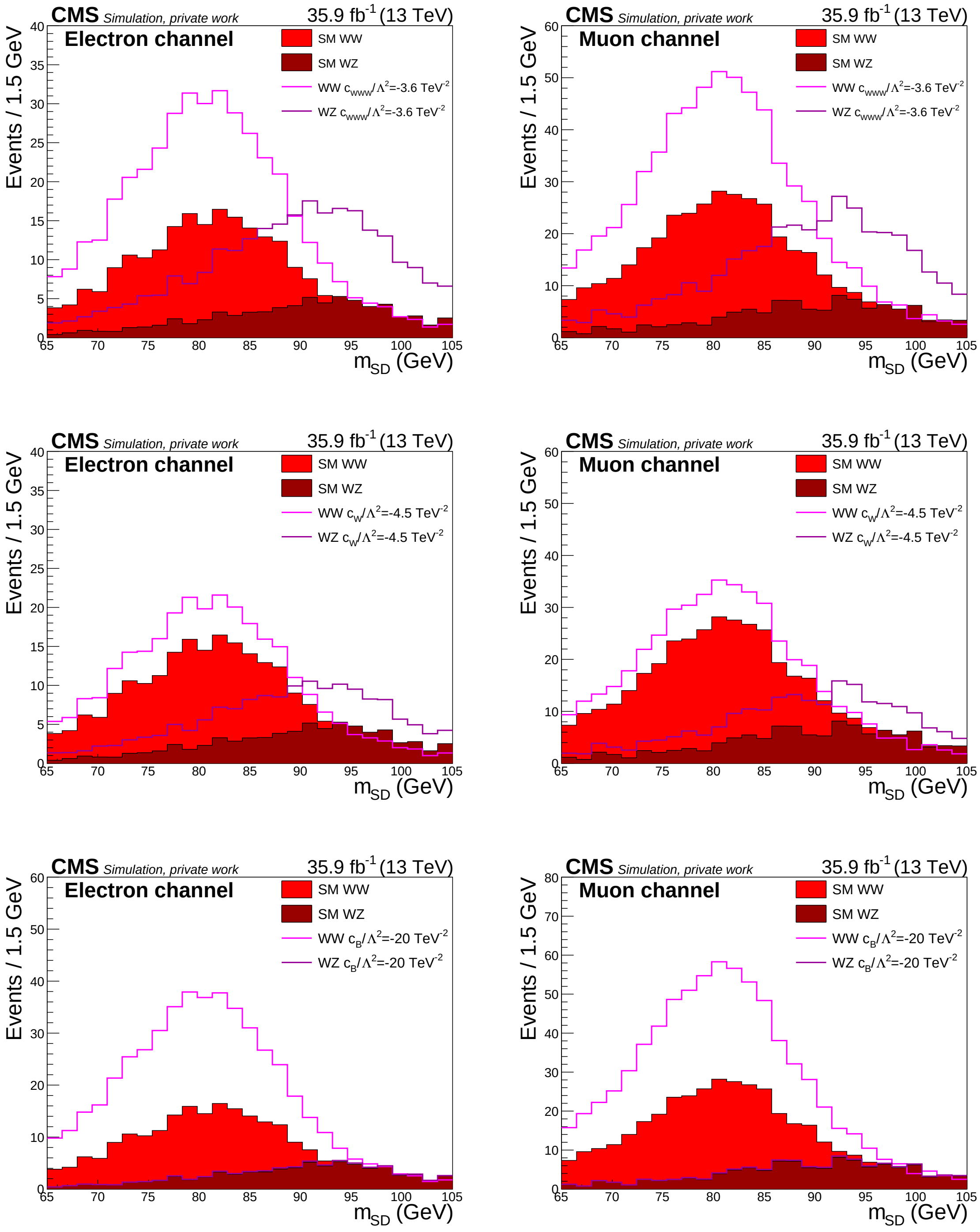

Figure A.7: Impact of nonzero aTGCs on signal m_{SD} distributions in the electron (left) and muon (right) channels. The impact of $c_{\mathrm{WWW}}/\Lambda^2 = -3.6\ \mathrm{TeV}^{-2}$, $c_{\mathrm{W}}/\Lambda^2 = -4.5\ \mathrm{TeV}^{-2}$, and $c_{\mathrm{B}}/\Lambda^2 = -20\ \mathrm{TeV}^{-2}$ is shown on the top, middle, and bottom, respectively.

A.3 Additional figures for signal modelling

A.3.1 WW category

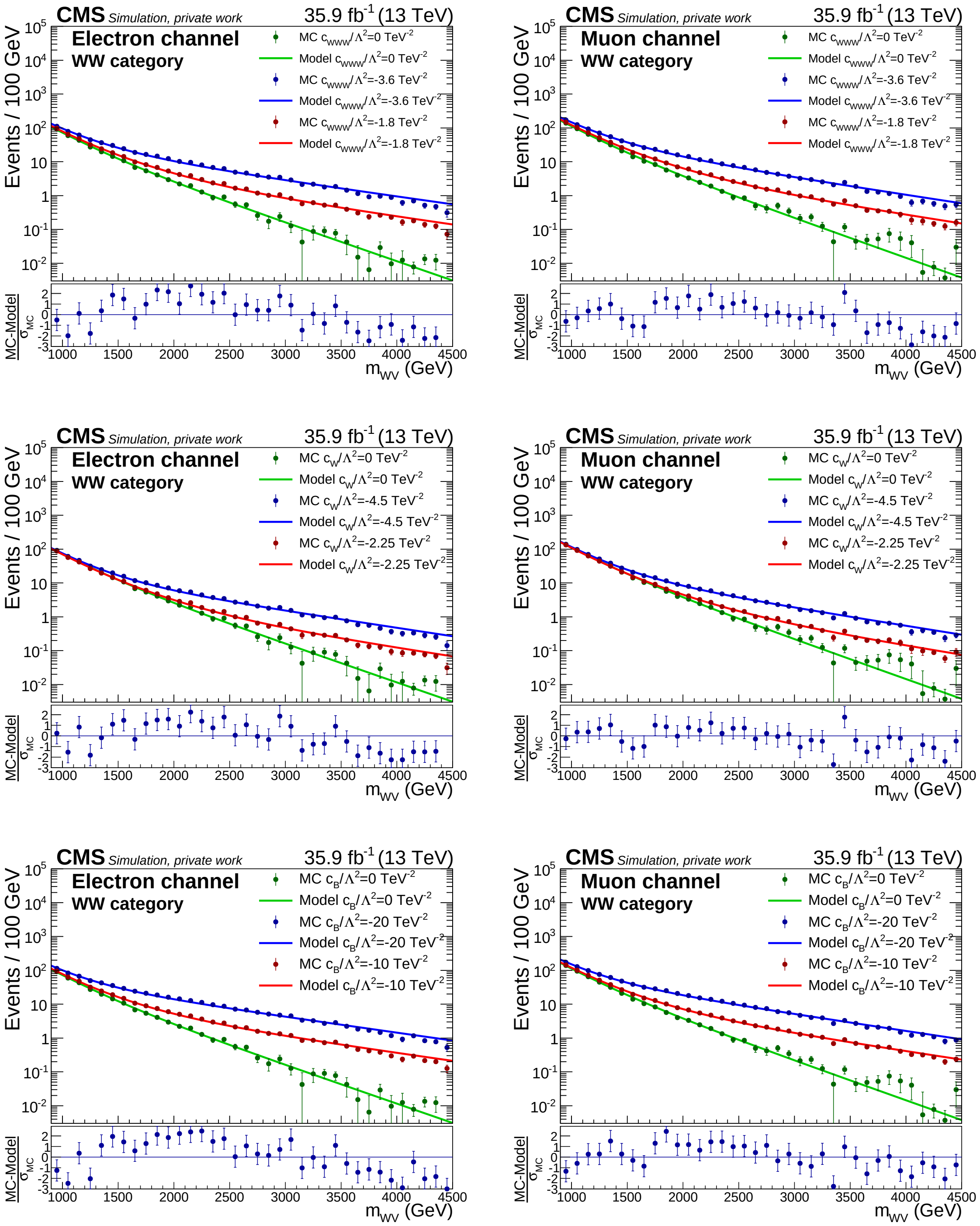

Figure A.8: Simulated events (points) and signal model (solid curves) in the electron (left) and muon (right) channels for the WW category. Events and model are shown for zero, negative working point, and an intermediate aTGC value in green, blue, and red, respectively.

A.3.2 WZ category

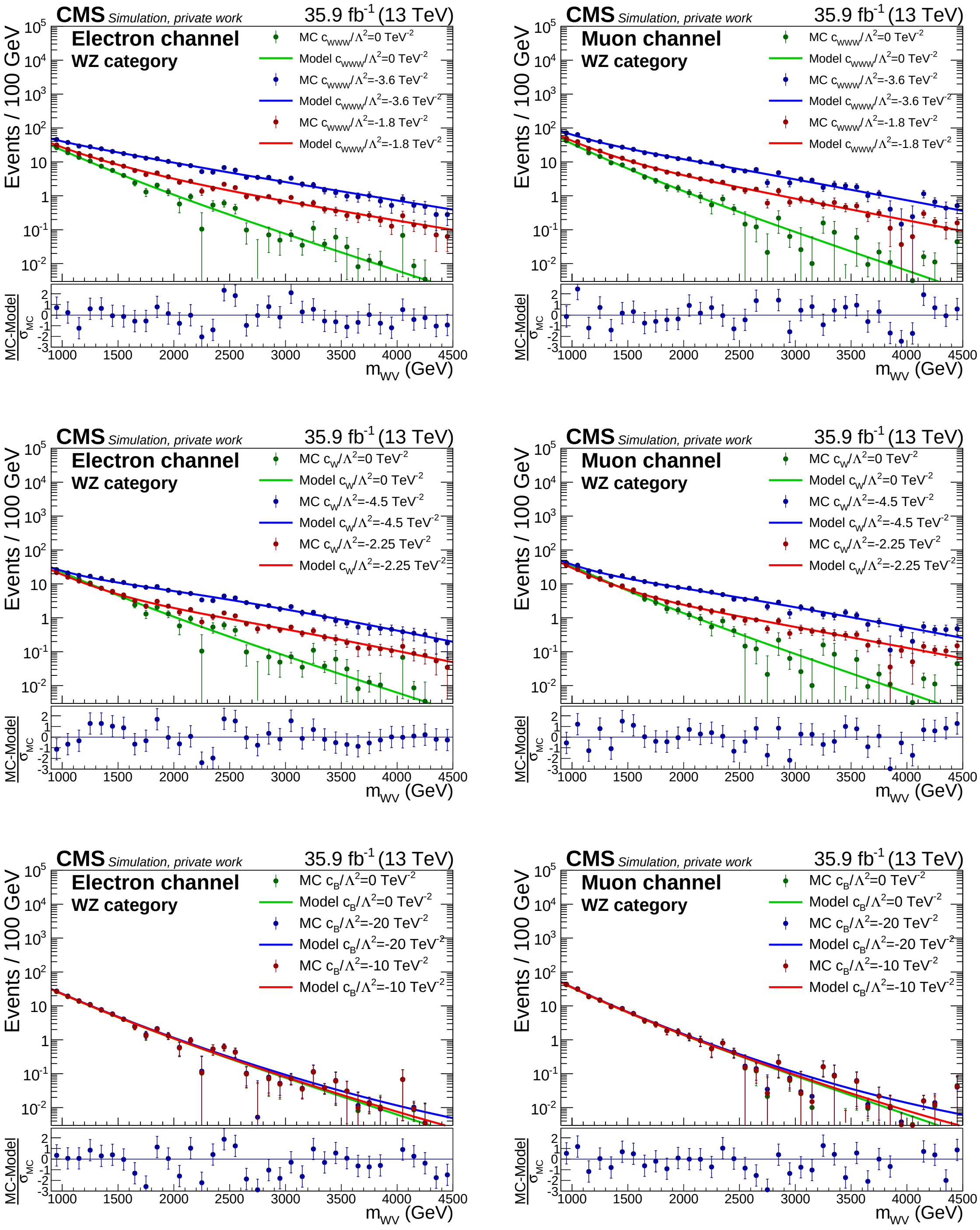

Figure A.9: Simulated events (points) and signal model (solid curves) in the electron (left) and muon (right) channels for the WZ category. Events and model are shown for zero, negative working point, and an intermediate aTGC value in green, blue, and red, respectively.

A.4 Details for signal shape systematic uncertainties

A.4.1 Impact of individual sources

Table A.1: Impact (%) of individual sources of systematic uncertainty on signal shape parameters. The effect of a source is calculated by refitting the signal model to the corresponding simulation variations. The impact on signal shape is dominated by theory uncertainties, with smaller contributions from experimental sources.

	WW category					
	Electron channel			Muon channel		
Uncertainty source	$a_{c_{\mathrm{WWW}}}$	$a_{c_{\mathrm{W}}}$	$a_{c_{\mathrm{B}}}$	$a_{c_{\mathrm{WWW}}}$	$a_{c_{\mathrm{W}}}$	$a_{c_{\mathrm{B}}}$
PDF	3.62	2.84	1.63	4.47	4.76	1.40
μ_{F}, μ_{R}	3.06	2.76	2.47	1.88	1.59	1.45
Pileup	0.19	0.19	0.15	0.33	0.27	0.18
Lepton identification	1.20	1.02	1.13	0.28	0.51	0.50
Lepton energy scale	0.14	0.46	0.45	1.34	0.59	0.19
Lepton energy resolution	0.13	0.25	0.32	0.13	0.42	0.07
Jet energy scale	0.77	1.06	0.28	0.54	0.47	0.39
Jet energy resolution	1.32	0.83	0.80	1.21	0.42	0.07
b tag	0.01	0.01	0.01	0.01	0.01	0.01
b mistag	0.00	0.00	0.00	0.01	0.01	0.00
$p_{\mathrm{T}}^{\mathrm{miss}}$	0.51	0.21	0.47	1.01	0.26	0.08
Total	5.11	4.19	3.35	5.05	5.08	2.35

	WZ category					
	Electron channel			Muon channel		
Uncertainty source	$a_{c_{\mathrm{WWW}}}$	$a_{c_{\mathrm{W}}}$	$a_{c_{\mathrm{B}}}$	$a_{c_{\mathrm{WWW}}}$	$a_{c_{\mathrm{W}}}$	$a_{c_{\mathrm{B}}}$
PDF	5.86	4.81	2.57	3.60	2.98	2.21
μ_{F}, μ_{R}	2.46	2.12	2.35	2.22	1.18	2.71
Pileup	0.37	0.56	0.31	0.08	0.23	0.26
Lepton identification	1.18	0.92	1.07	0.23	0.46	0.51
Lepton energy scale	0.50	0.67	0.81	1.34	0.60	0.81
Lepton energy resolution	0.35	0.05	0.31	0.38	0.47	0.75
Jet energy scale	1.26	2.02	2.85	2.02	2.12	3.04
Jet energy resolution	0.60	0.82	1.97	0.51	1.21	0.26
b tag	0.00	0.00	0.01	0.00	0.01	0.00
b mistag	0.01	0.01	0.00	0.01	0.01	0.01
$p_{\mathrm{T}}^{\mathrm{miss}}$	0.54	0.06	0.33	0.31	0.37	0.84
Total	6.55	5.43	5.05	4.37	3.68	4.56

A.4.2 Figures for WW category

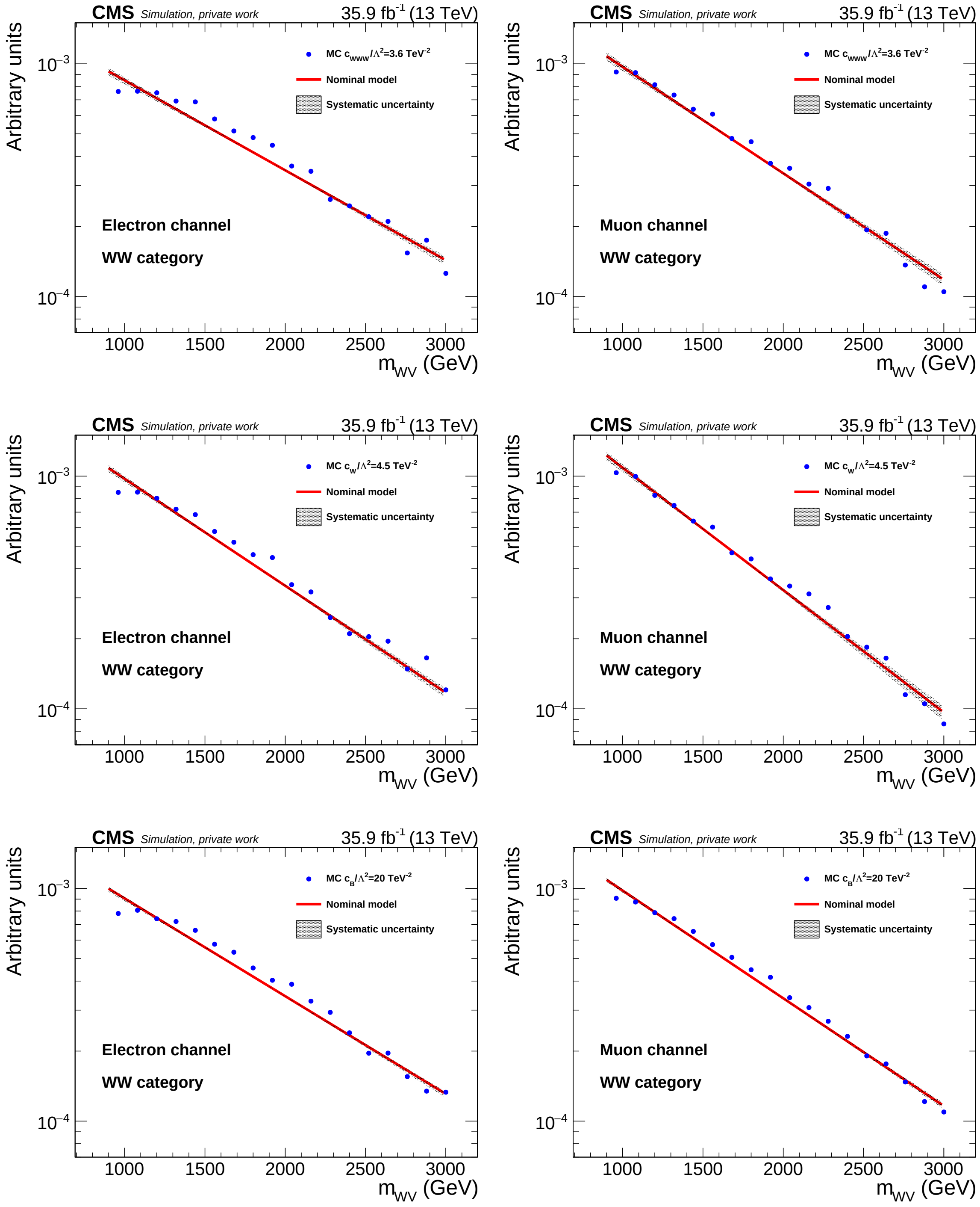

Figure A.10: Impact of systematic uncertainties on the shape of the signal model in the electron (left) and muon (right) channels for the WW category. The nominal model is shown by the red line, whilst the shaded area represents the uncertainty band.

A.4.3 Figures for WZ category

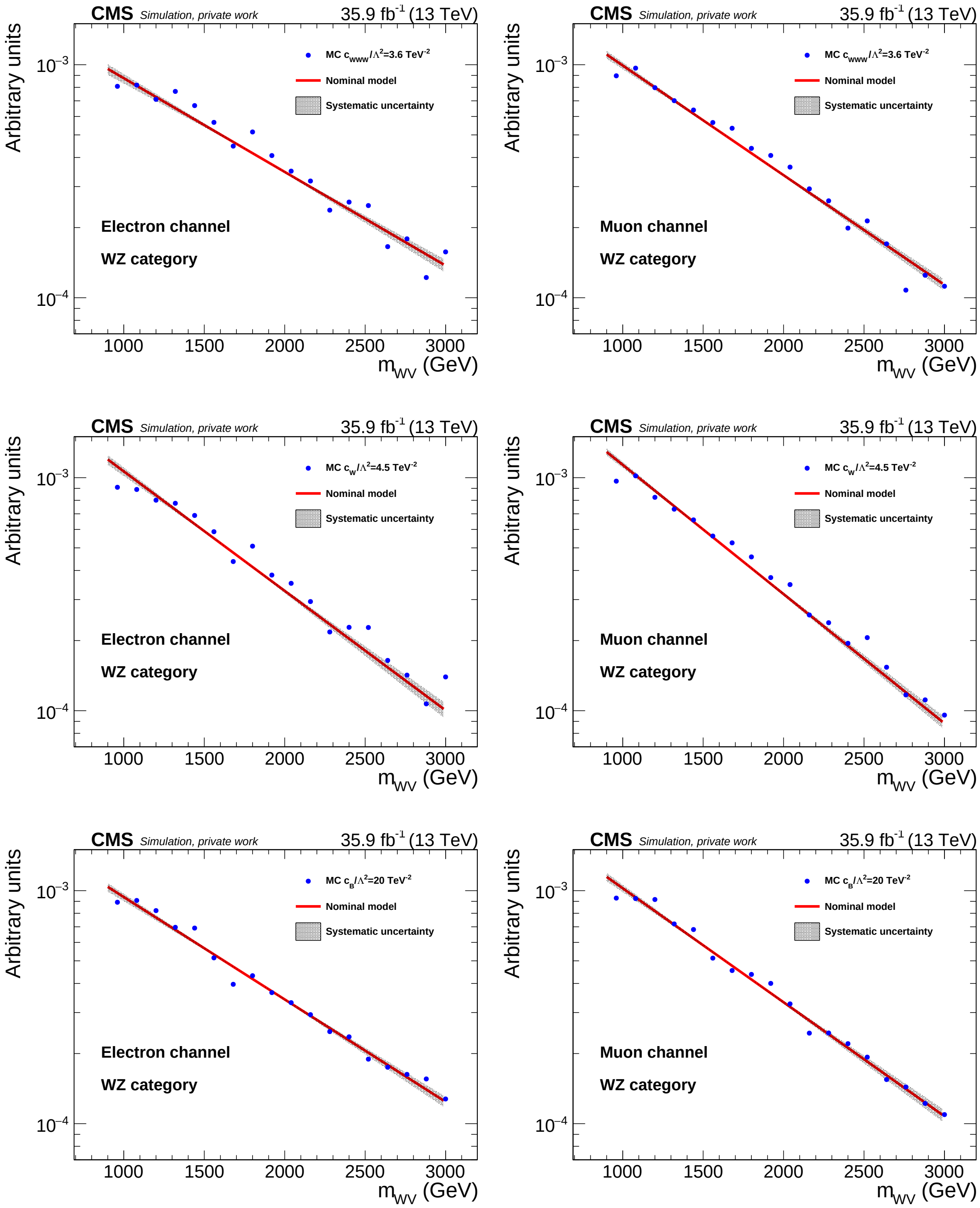

Figure A.11: Impact of systematic uncertainties on the shape of the signal model in the electron (left) and muon (right) channels for the WZ category. The nominal model is shown by the red line, whilst the shaded area represents the uncertainty band.

A.5 Additional control region comparisons

A.5.1 W+jets control region

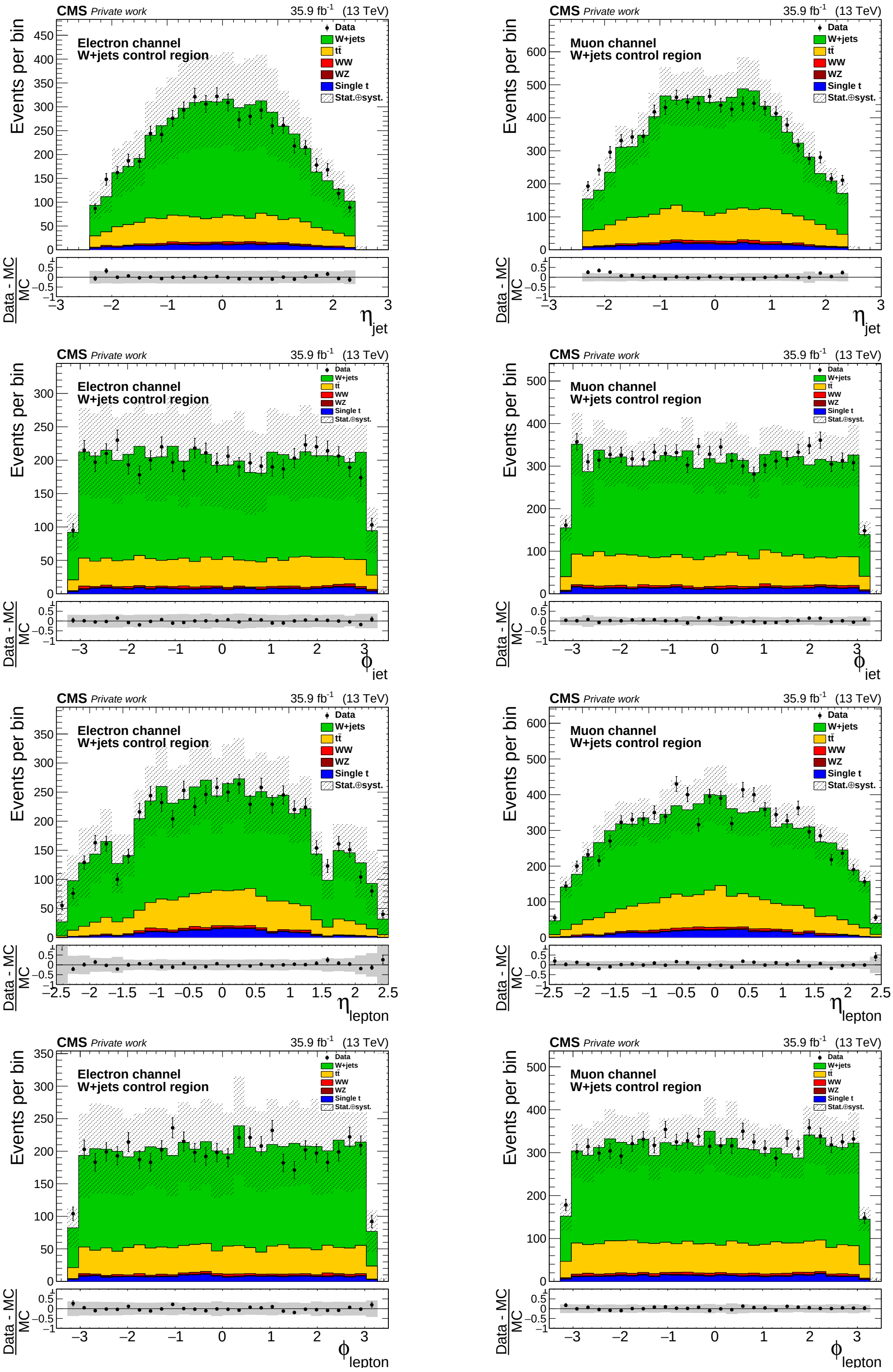

Figure A.12: Comparison between data and simulation for the η_{jet}, ϕ_{jet}, η_{lep}, and ϕ_{lep} distributions in the W+jets control region.

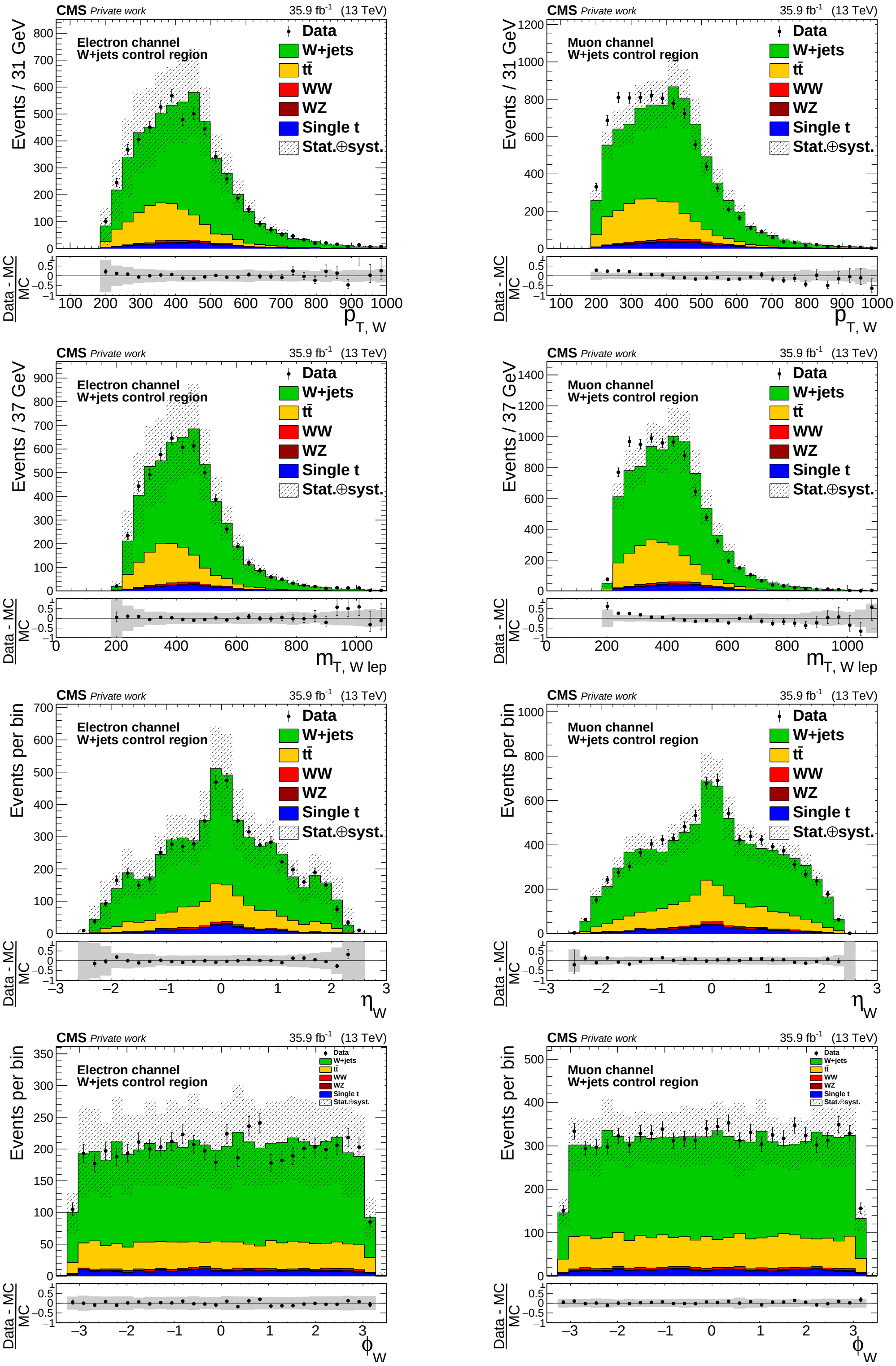

Figure A.13: Comparison between data and simulation for the $p_{\mathrm{T,W}}$, $m_{\mathrm{T,W}}$, η_{W}, and ϕ_{W} distributions in the W+jets control region.

A.5.2 $t\bar{t}$ control region

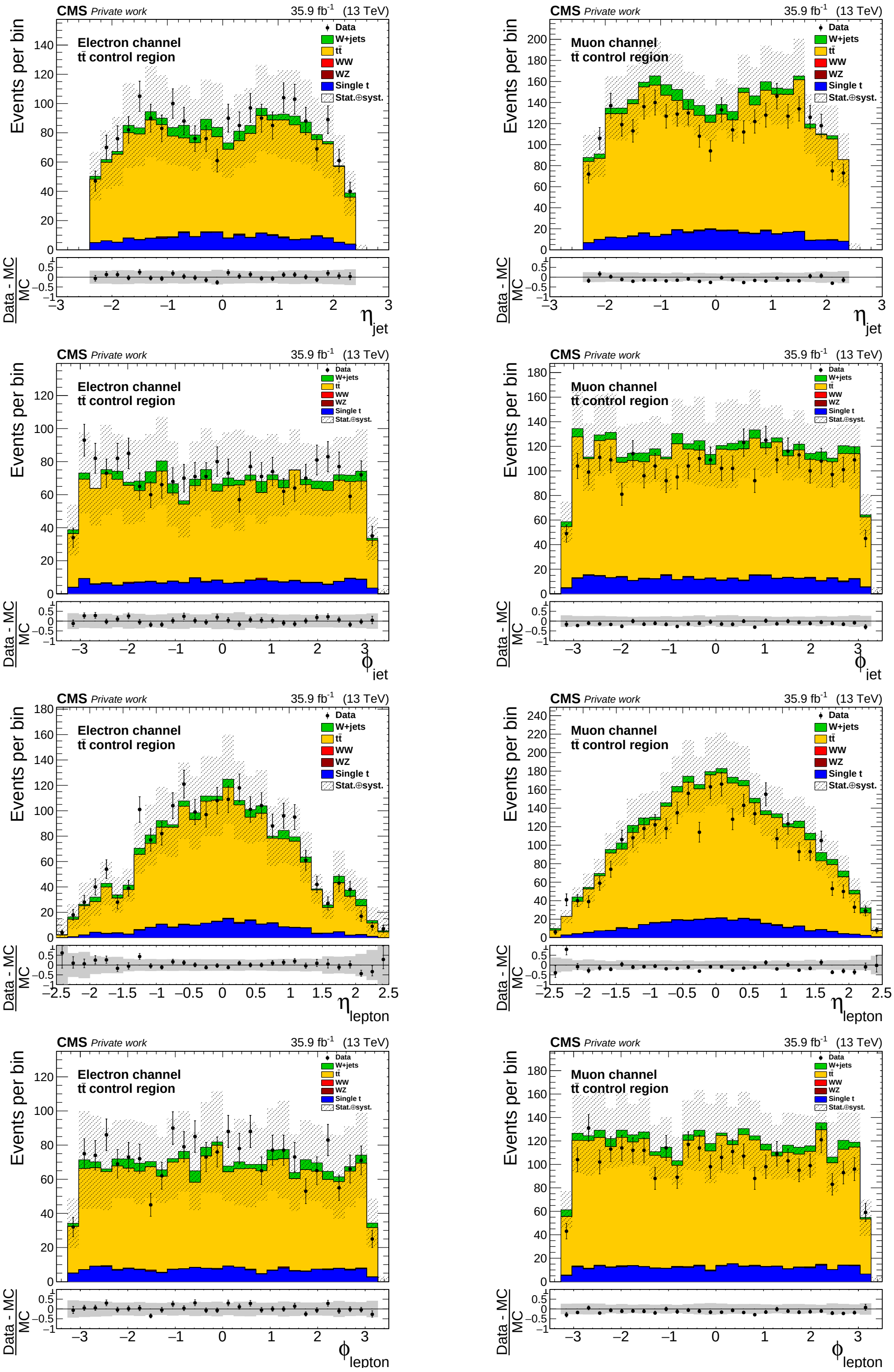

Figure A.14: Comparison between data and simulation for the η_{jet}, ϕ_{jet}, η_{lep}, and ϕ_{lep} distributions in the $t\bar{t}$ control region.

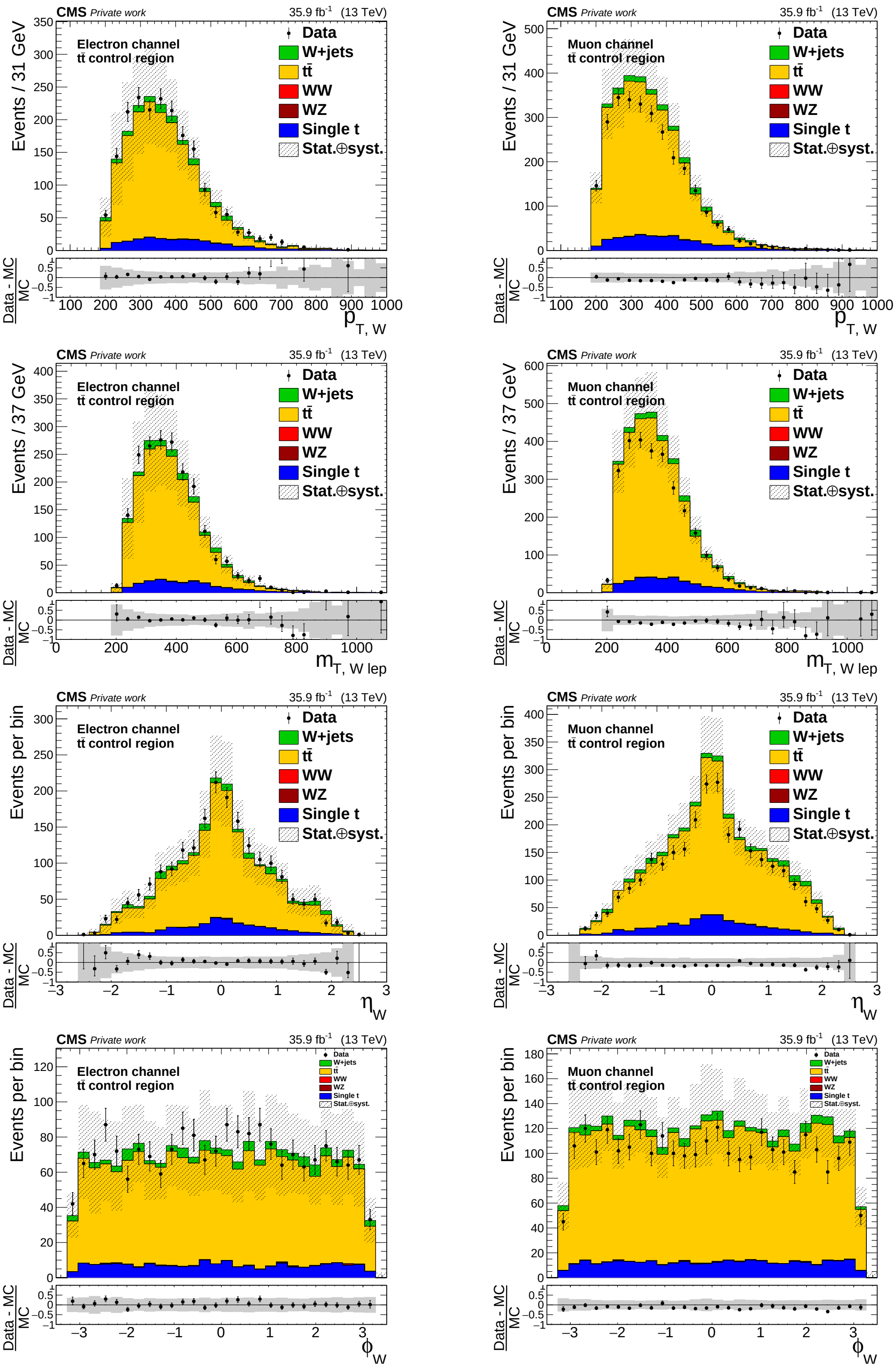

Figure A.15: Comparison between data and simulation for the $p_{\mathrm{T,W}}$, $m_{\mathrm{T,W}}$, η_{W}, and ϕ_{W} distributions in the t$\bar{\mathrm{t}}$ control region.

A.6 Additional figures for validation of negligible backgrounds

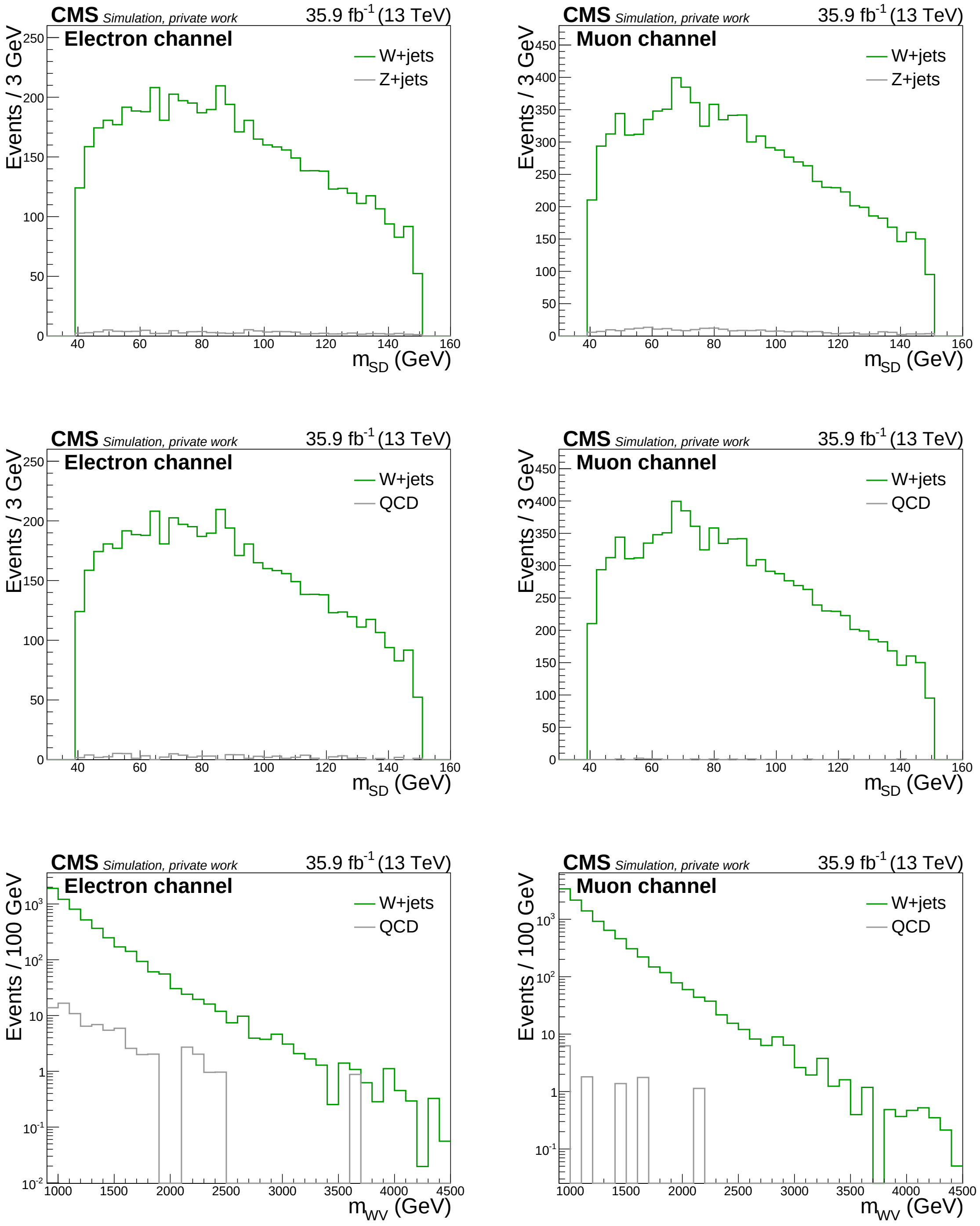

Figure A.16: Comparison between simulated W+jets and negligible contributions in the electron (left) and muon (right) channels. Z+jets m_{SD} and very loosely selected QCD m_{SD} and m_{WV} distributions are shown on the top, middle, and bottom, respectively.

A.7 Details for background modelling

A.7.1 Fit parameters for background functions

Table A.2: Extracted background function parameter values from the fit to simulation for the m_{SD} distribution. Bold parameters are kept floating in the final two-dimensional fit to data.

Process	Parameter	Electron channel	Muon channel
W+jets	$\boldsymbol{k}_{\mathbf{CS1}}$	21.33 ± 2.71	23.79 ± 3.17
	$\boldsymbol{k}_{\mathbf{CS2}}$	$(-2.25 \pm 0.08) \cdot 10^{-2}$	$(-2.43 \pm 0.13) \cdot 10^{-2}$
$\mathrm{t\bar{t}}$	k_{EEG1}	$(-6.41 \pm 1.67) \cdot 10^{-3}$	$(-7.82 \pm 1.95) \cdot 10^{-3}$
	k_{EEG2}	62.99 ± 3.79	68.51 ± 4.33
	k_{EEG3}	34.79 ± 3.71	43.08 ± 0.73
	k_{EEG4}	$(8.38 \pm 0.17) \cdot 10^{-1}$	$(8.12 \pm 0.12) \cdot 10^{-1}$
	k_{EEG5}	82.64 ± 0.47	83.00 ± 0.39
	k_{EEG6}	7.78 ± 0.65	8.72 ± 0.45
SM diboson	k_{DG1}	82.02 ± 0.37	81.13 ± 0.29
	k_{DG2}	8.13 ± 0.39	7.83 ± 0.31
	k_{DG3}	$(5.48 \pm 0.26) \cdot 10^{-1}$	$(5.36 \pm 0.21) \cdot 10^{-1}$
	k_{DG4}	5.01 ± 2.49	5.68 ± 1.81
	k_{DG5}	4.95 ± 0.02	4.95 ± 0.01
Single t	k_{EG1}	$(7.06 \pm 0.16) \cdot 10^{-1}$	$(6.46 \pm 0.15) \cdot 10^{-1}$
	k_{EG2}	$(3.52 \pm 0.74) \cdot 10^{-3}$	$(2.54 \pm 0.66) \cdot 10^{-3}$
	k_{EG3}	82.53 ± 0.40	82.47 ± 0.37
	k_{EG4}	7.49 ± 0.48	9.34 ± 0.45

Table A.3: Extracted background function parameter values from the fit to simulation for the m_{WV} distribution in the signal region. The quoted W+jets parameters are not used; instead, the final parameters are determined from sideband data using a MC-derived transfer function in the final two-dimensional fit.

Process	Parameter	Electron channel	Muon channel
W+jets	k_{ET11}	$(-2.26 \pm 0.12) \cdot 10^{-3}$	$(-2.37 \pm 0.12) \cdot 10^{-3}$
	k_{ET12}	2738 ± 221	2603 ± 206
$\mathrm{t\bar{t}}$	k_{ET21}	$(-3.13 \pm 0.35) \cdot 10^{-2}$	$(-3.03 \pm 0.33) \cdot 10^{-3}$
	k_{ET22}	113.3 ± 14.5	115.8 ± 13.5
SM diboson	k_{ET31}	$(-2.86 \pm 0.30) \cdot 10^{-3}$	$(-2.75 \pm 0.24) \cdot 10^{-3}$
	k_{ET32}	814.4 ± 542.0	1557.2 ± 432.0
Single t	k_{E1}	$(-4.11 \pm 0.10) \cdot 10^{-3}$	$(-4.26 \pm 0.08) \cdot 10^{-3}$

A.7.2 Additional figures for sideband regions

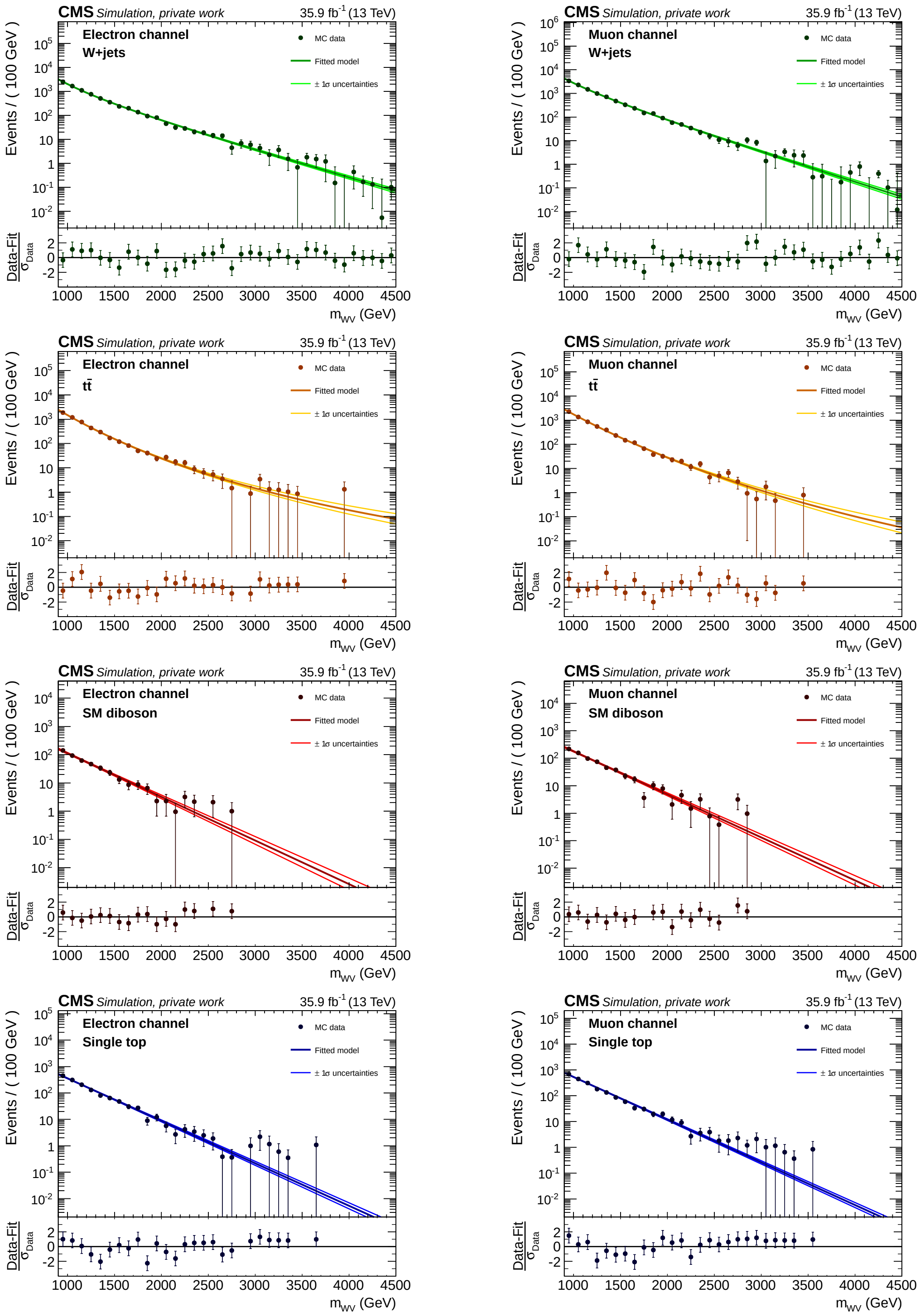

Figure A.17: Simulated events and fitted parametric functions for the W+jets, $t\bar{t}$, SM diboson, and single top quark (top to bottom, respectively) m_{WV} distributions in the sideband regions. The electron channel is shown on the left, whilst the muon channel is shown on the right.

A.8 Fit results for Asimov data

A.8.1 SM scenario

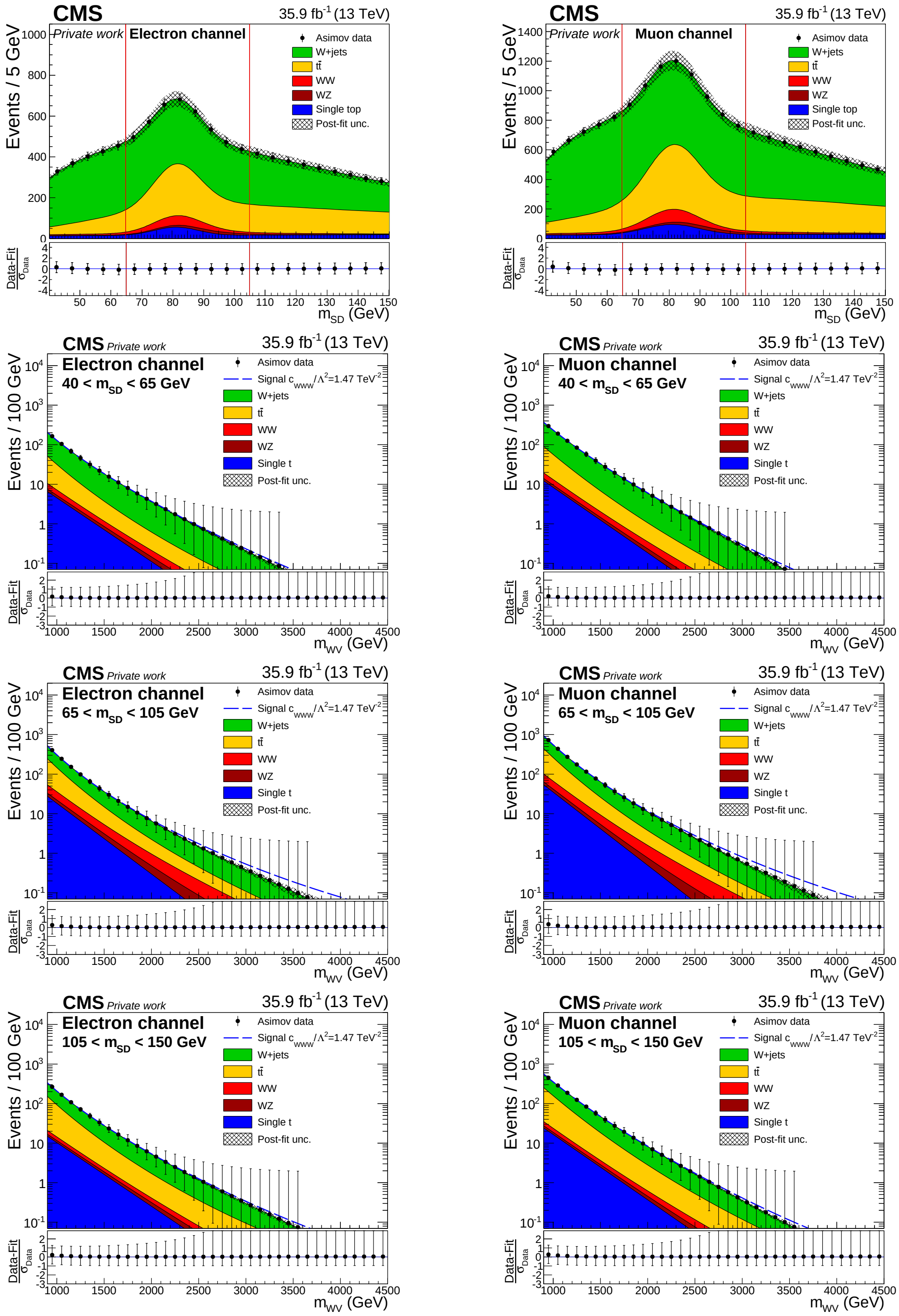

Figure A.18: Result of the two-dimensional fit to SM Asimov data in the electron (left) and muon (right) channels, showing the m_{SD}, and lower-sideband, signal, and upper-sideband m_{WV} distributions. An example of the expected excluded signal is indicated by the dashed line.

A.8.2 c_{WWW}/Λ^2 signal injection

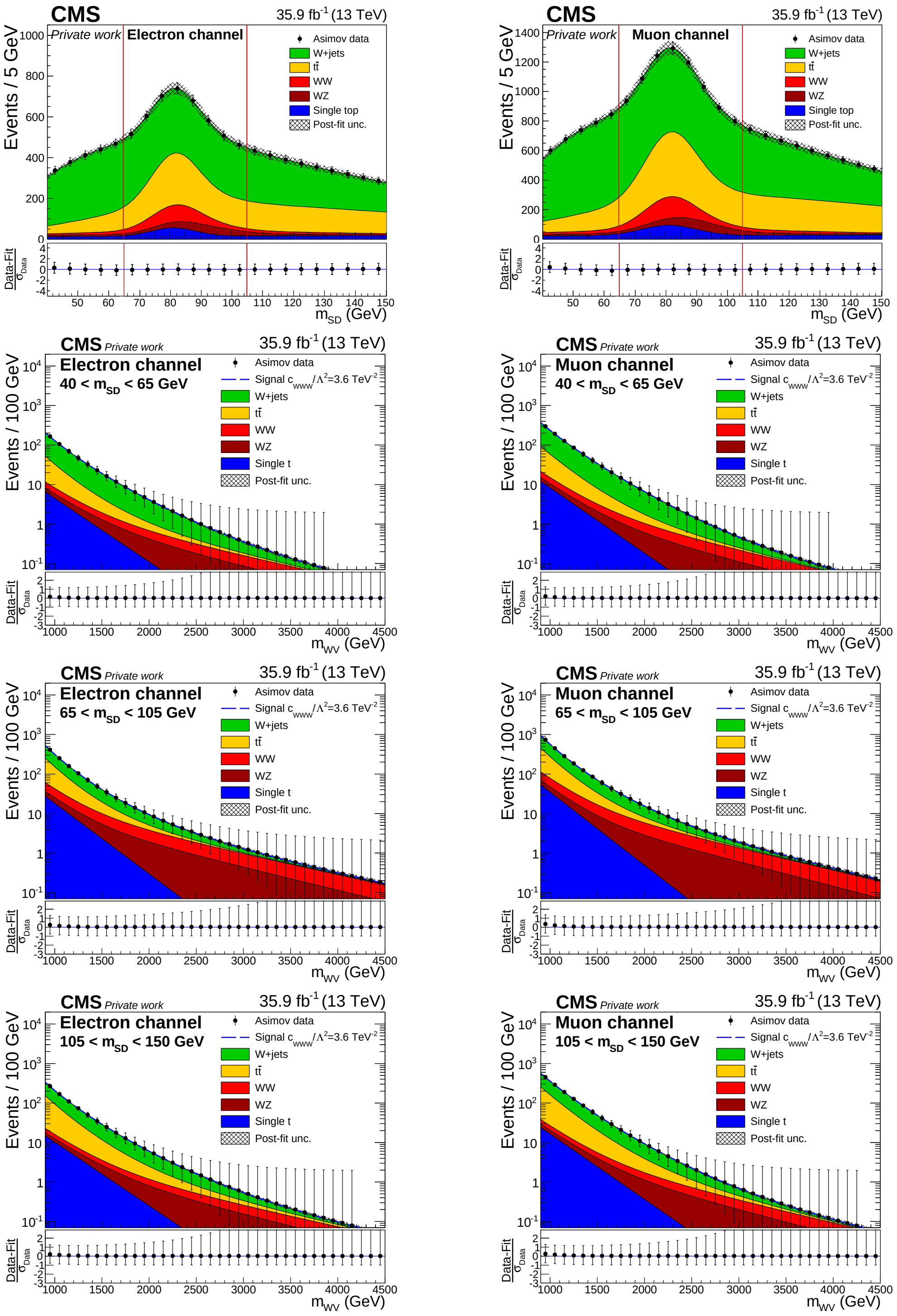

Figure A.19: Result of the signal injection test with Asimov data corresponding to $c_{WWW}/\Lambda^2 = 3.6\ \text{TeV}^{-2}$ in the electron (left) and muon (right) channels, showing the m_{SD}, and lower-sideband, signal, and upper-sideband m_{WV} distributions. Both the WW and WZ contributions are enhanced significantly, and the signal is extracted without any bias.

A.8.3 c_B/Λ^2 signal injection

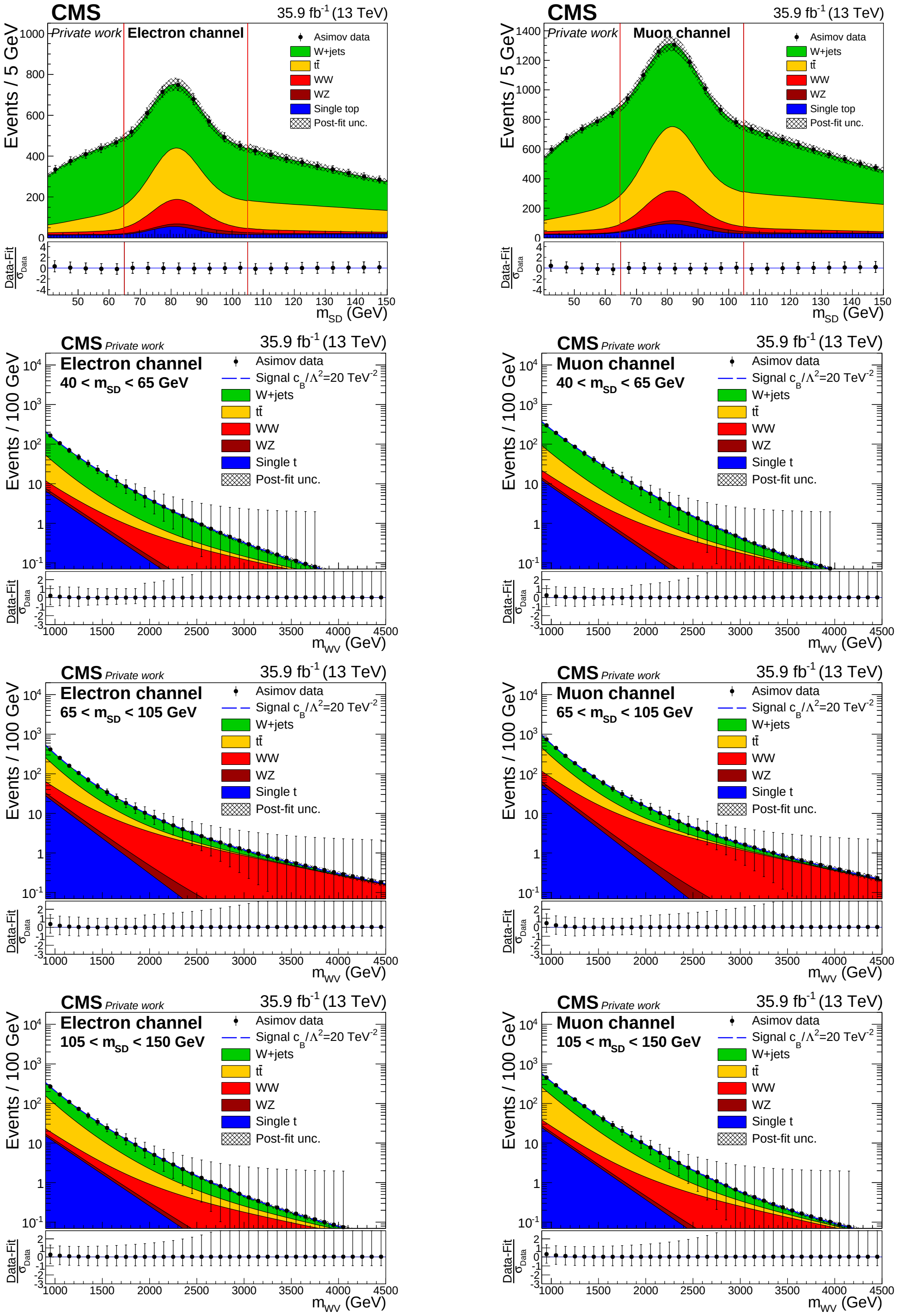

Figure A.20: Result of the signal injection test with Asimov data corresponding to $c_B/\Lambda^2 = 20\ \text{TeV}^{-2}$ in the electron (left) and muon (right) channels, showing the m_{SD}, and lower-sideband, signal, and upper-sideband m_{WV} distributions. There is a significant enhancement in the WW contribution, whilst the WZ contribution remains unchanged.

A.9 Additional figures for one-dimensional aTGC limits

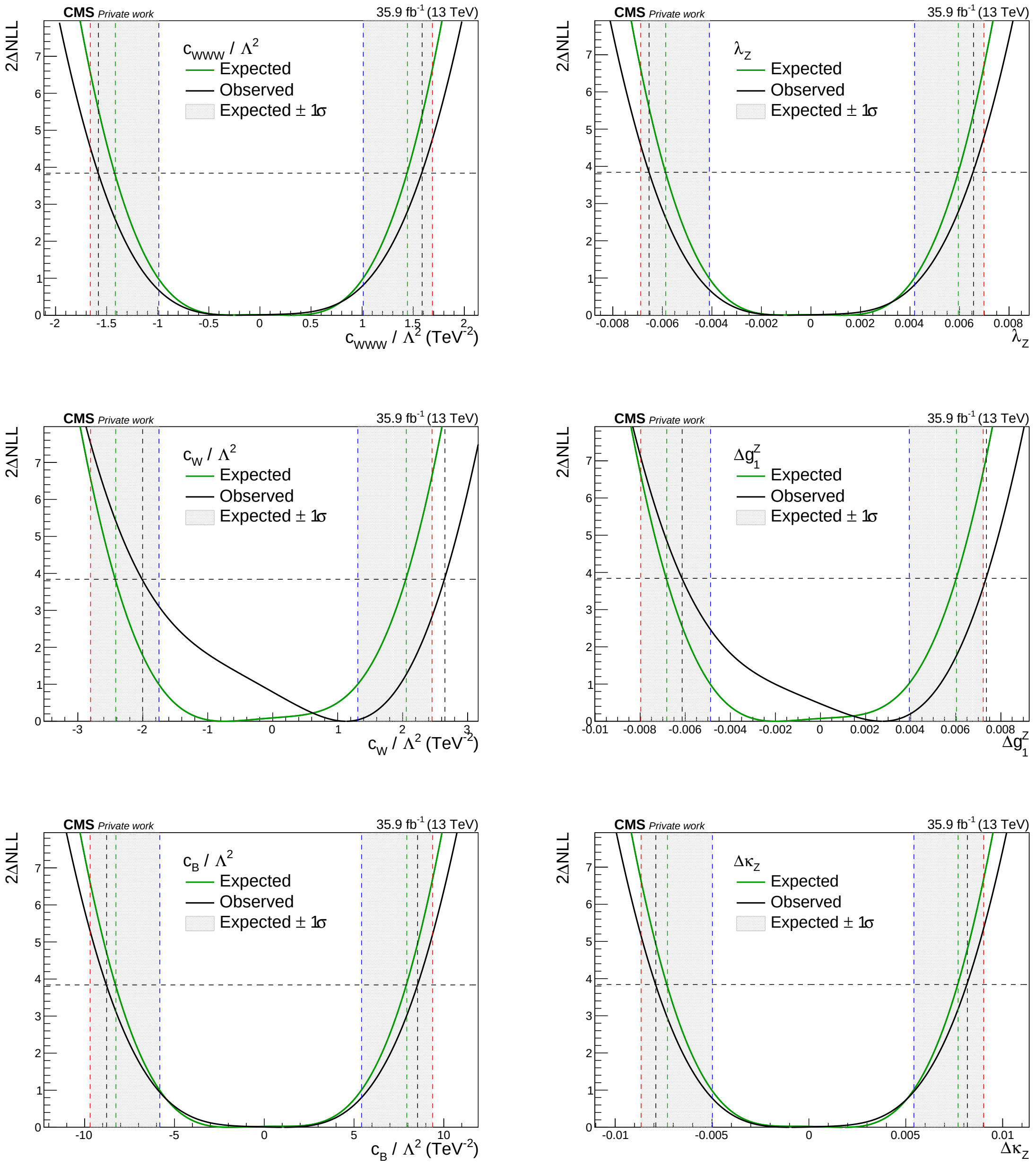

Figure A.21: Profile likelihood ratio distribution for the aTGC parameters in the EFT (left) and LEP (right) parametrisations. Each distribution corresponds to one varying parameter, with the other two parameters in the parametrisation being set to zero. The solid green and black lines represent the expected and observed distributions, respectively. Projecting the intersection points between the curves and the horizontal dashed line gives the 95% CL limits, whilst the region between 68 and 99% CL around the expected 95% CL limit is marked by the shaded bands.

A.10 aTGC limits as a function of diboson mass cutoff

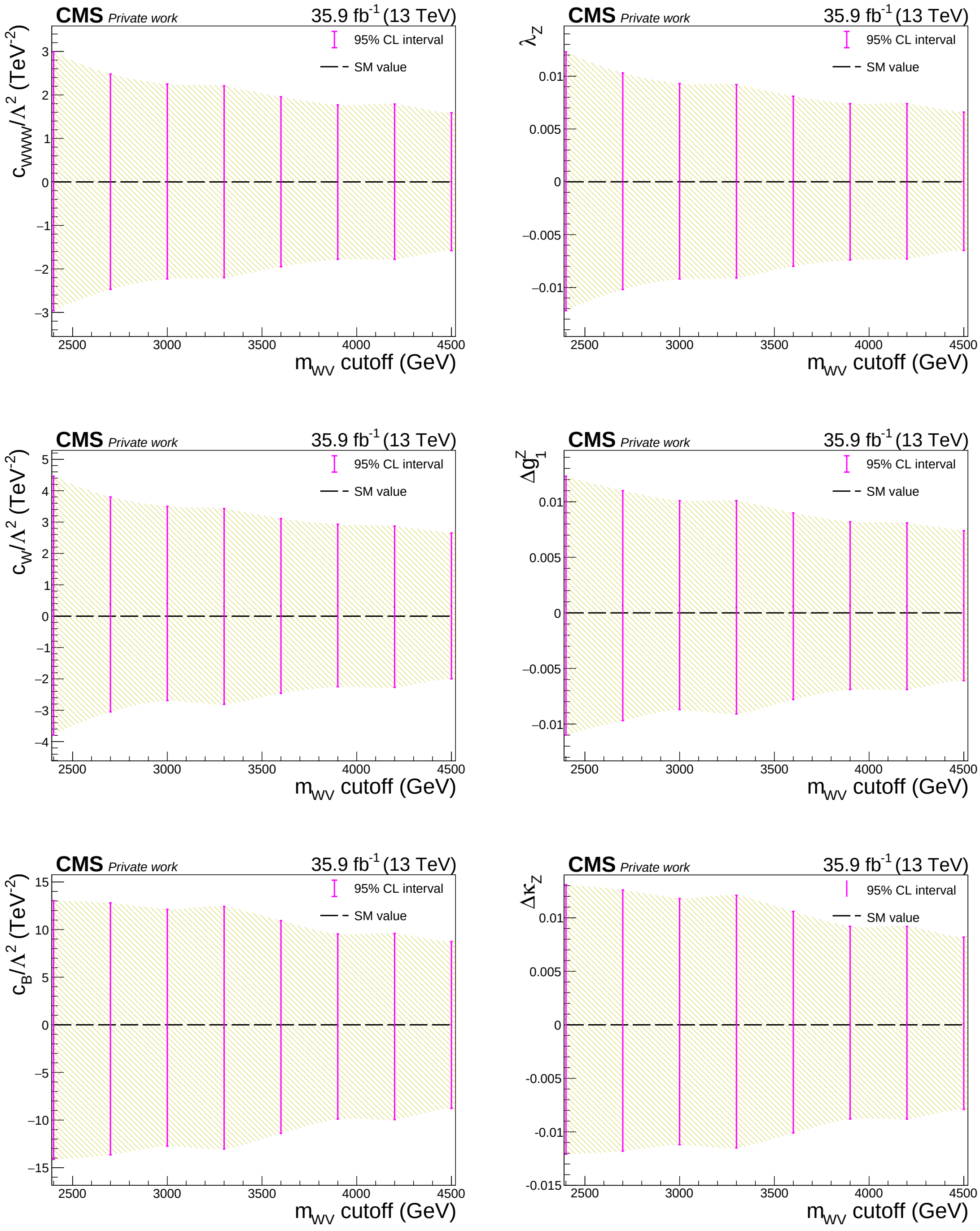

Figure A.22: Limits on aTGC parameters in the EFT (left) and LEP (right) parametrisations as a function of cutoff on the diboson mass scale. The main results from this analysis correspond to a cutoff of $m_{\mathrm{WV}} < 4.5$ TeV. Limits for cutoff scales smaller than 2.4 TeV are not considered to avoid extrapolating to aTGC values larger than the ones studied in simulation.

A.11 Additional figures for limits with 2017 data

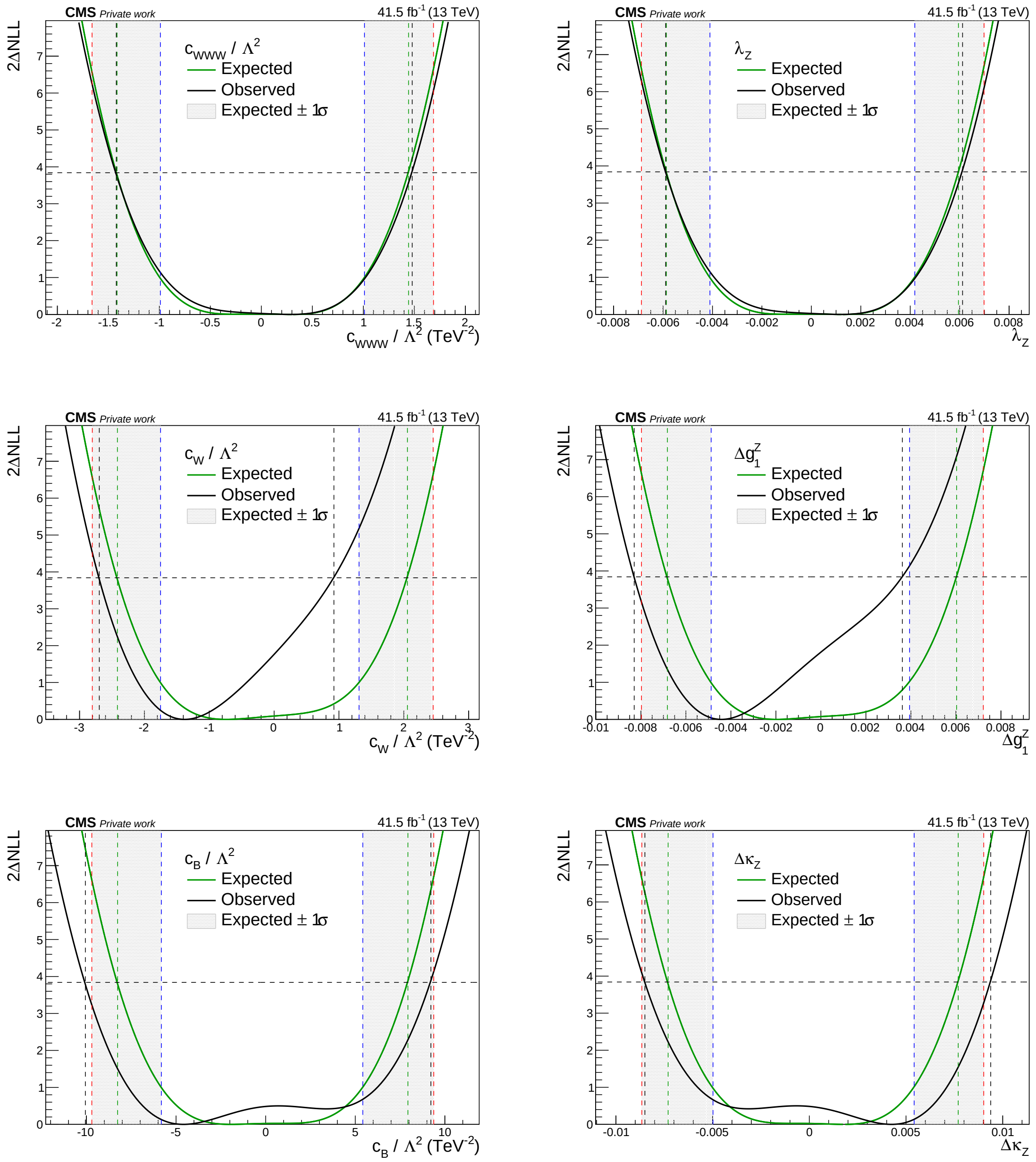

Figure A.23: One-dimensional profile likelihood ratio distribution for the aTGC parameters in the EFT (left) and LEP (right) parametrisations for the analysis using 2017 data. The expected and observed distributions are shown in green and black, respectively. The observed distribution is especially asymmetric for c_W/Λ^2, and correspondingly Δg_1^Z, owing to a significant contribution from the linear term. The 95% CL limits are calculated by projecting the intersection between the curves and the horizontal dashed line onto the parameter axis.

A.12 Additional figures for limits with 2018 data

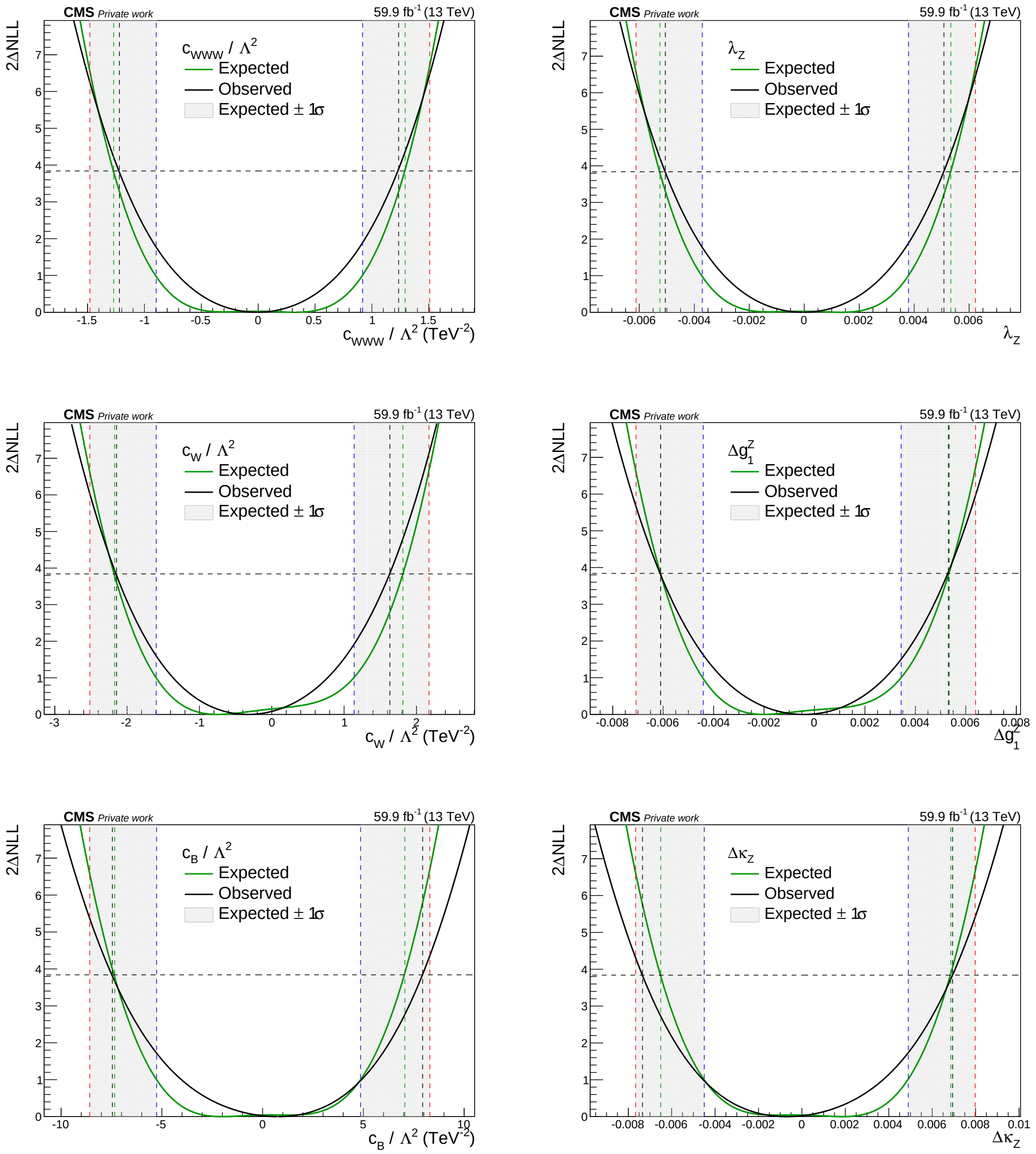

Figure A.24: One-dimensional profile likelihood ratio distribution for the aTGC parameters in the EFT (left) and LEP (right) parametrisations for the analysis using 2018 data. The expected and observed distributions are shown in green and black, respectively. Expected and observed 95% CL limits are calculated by projecting the intersection between the green and black curves and the horizontal dashed line onto the parameter axis. The shaded bands represent the region between 68 and 99% CL around the expected 95% CL limit.

A.13 Details for inclusion of angular variables

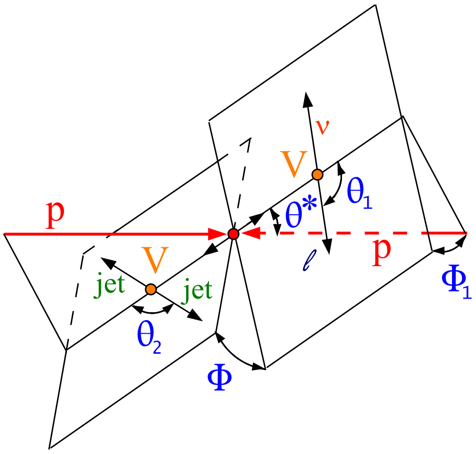

Figure A.25: A schematic showing decay angles characterising a diboson event, with the five angles being shown in blue. $\cos\theta^*$ is a good discriminator between signal and background processes.

Table A.4: Expected and observed aTGC limits at 95% CL after applying an optimal requirement of $|\cos\theta^*| < 0.8$. To demonstrate the improvement, limits without this requirement are also shown.

	$\lvert\cos\theta^*\rvert < 0.8$		$\lvert\cos\theta^*\rvert \leq 1$
aTGC parameter (TeV^2)	Expected limit	Observed limit	Observed limit
c_{WWW}/Λ^2	$[-1.11, 1.13]$	$[-1.02, 1.03]$	$[-1.58, 1.59]$
c_W/Λ^2	$[-1.95, 1.54]$	$[-1.66, 1.51]$	$[-2.00, 2.65]$
c_B/Λ^2	$[-6.58, 6.14]$	$[-6.10, 5.42]$	$[-8.78, 8.54]$

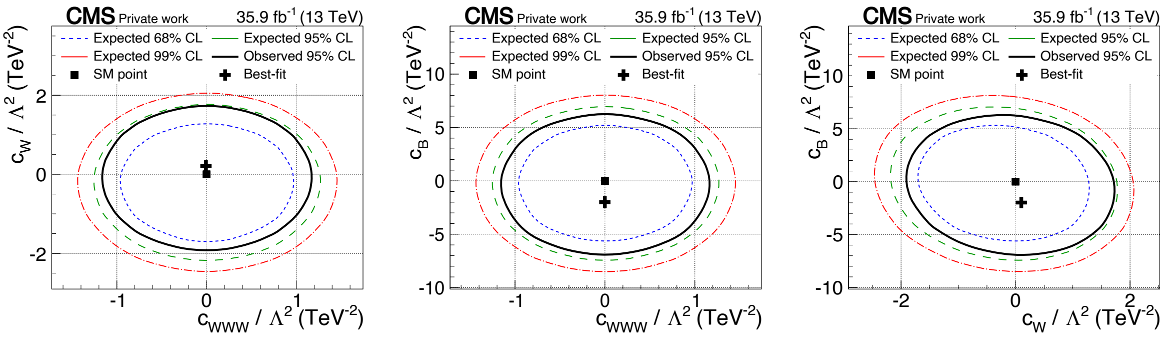

Figure A.26: Simultaneous limits on two aTGC parameters after applying an optimal requirement of $|\cos\theta^*| < 0.8$. Contours for the expected 68, 95, and 99% CL are shown in dotted blue, dashed green, and dot-dashed red, respectively, whilst contours for the observed limits are shown in solid black.

List of figures

List of tables

Bibliography

[1] **CMS** Collaboration, “Search for anomalous triple gauge couplings in WW and WZ production in lepton + jet events in proton-proton collisions at $\sqrt{s} = 13$ TeV”, *JHEP* **12** (2019) 62.

[2] F. Zwicky, “Republication of: The redshift of extragalactic nebulae”, *Gen. Relativ. Gravit.* **41** (2009) 207–224.

[3] V. C. Rubin and W. K. Ford, “Rotation of the andromeda nebula from a spectroscopic survey of emission regions”, *Astrophys. J.* **159** (1970) 379.

[4] A. G. Riess *et al.*, “Observational evidence from supernovae for an accelerating universe and a cosmological constant”, *Astronom. J.* **116** (1998) 1009–1038.

[5] S. Perlmutter *et al.*, “Measurements of Ω and Λ from 42 high-redshift supernovae”, *Astrophys. J.* **517** (1999) 565–586.

[6] **Planck** Collaboration, “Planck 2015 results - XIII. Cosmological parameters”, *A&A* **594** (2016) A13.

[7] A. de Gouvêa, D. Hernández, and T. M. P. Tait, “Criteria for natural hierarchies”, *Phys. Rev. D* **89** (2014) 115005.

[8] M. Gonzalez-Garcia and M. Maltoni, “Phenomenology with massive neutrinos”, *Phys. Rep.* **460** (2008) 1–129.

[9] L. Canetti, M. Drewes, and M. Shaposhnikov, “Matter and antimatter in the universe”, *New J. Phys.* **14** (2012) 095012.

[10] **CMS** Collaboration, “Measurement of the ZZ production cross section and search for anomalous couplings in $2\ell2\ell'$ final states in pp collisions at $\sqrt{s} = 7$ TeV”, *JHEP* **01** (2013) 063.

[11] **CMS** Collaboration, “Measurement of the W^+W^- cross section in pp collisions at $\sqrt{s} = 7$ TeV and limits on anomalous WWγ and WWZ couplings”, *Eur. Phys. J. C* **73** (2013) 2610.

[12] **CMS** Collaboration, “Measurement of the pp $\rightarrow$ ZZ production cross section and constraints on anomalous triple gauge couplings in four-lepton final states at $\sqrt{s} =$ 8 TeV”, *Phys. Lett. B* **740** (2015) 250.

[13] **CMS** Collaboration, “Measurement of the W^+W^- cross section in pp collisions at $\sqrt{s} = 8$ TeV and limits on anomalous gauge couplings”, *Eur. Phys. J. C* **76** (2016) 401.

[14] **CMS** Collaboration, “Measurement of the WZ production cross section in pp collisions at $\sqrt{s} = 7$ and 8 TeV and search for anomalous triple gauge couplings at $\sqrt{s} = 8$ TeV”, *Eur. Phys. J. C* **77** (2017) 236.

[15] **CMS** Collaboration, "Measurements of the pp $\rightarrow$ ZZ production cross section and the Z $\rightarrow 4\ell$ branching fraction, and constraints on anomalous triple gauge couplings at $\sqrt{s} = 13$ TeV", *Eur. Phys. J. C* **78** (2018) 165.

[16] **ATLAS** Collaboration, "Measurement of the $W^{\pm}Z$ production cross section and limits on anomalous triple gauge couplings in proton-proton collisions at $\sqrt{s} = 7$ TeV with the ATLAS detector", *Phys. Lett. B* **709** (2012) 341.

[17] **ATLAS** Collaboration, "Measurement of the ZZ production cross section and limits on anomalous neutral triple gauge couplings in proton-proton collisions at $\sqrt{s} = 7$ TeV with the ATLAS detector", *Phys. Rev. Lett.* **108** (2012) 041804.

[18] **ATLAS** Collaboration, "Measurement of the WW cross section in $\sqrt{s} = 7$ TeV pp collisions with the ATLAS detector and limits on anomalous gauge couplings", *Phys. Lett. B* **712** (2012) 289.

[19] **ATLAS** Collaboration, "Measurement of WZ production in proton-proton collisions at $\sqrt{s} = 7$ TeV with the ATLAS detector", *Eur. Phys. J. C* **72** (2012) 2173.

[20] **ATLAS** Collaboration, "Measurement of W^+W^- production in pp collisions at $\sqrt{s} = 7$ TeV with the ATLAS detector and limits on anomalous WWZ and $WW\gamma$ couplings", *Phys. Rev. D* **87** (2013) 112001.

[21] **ATLAS** Collaboration, "Measurement of ZZ production in pp collisions at $\sqrt{s} = 7$ TeV and limits on anomalous ZZZ and $ZZ\gamma$ couplings with the ATLAS detector", *JHEP* **03** (2013) 128.

[22] **ATLAS** Collaboration, "Measurement of total and differential W^+W^- production cross sections in proton-proton collisions at $\sqrt{s} = 8$ TeV with the ATLAS detector and limits on anomalous triple-gauge-boson couplings", *JHEP* **09** (2016) 029.

[23] **ATLAS** Collaboration, "Measurements of $W^{\pm}Z$ production cross sections in pp collisions at $\sqrt{s} = 8$ TeV with the ATLAS detector and limits on anomalous gauge boson self-couplings", *Phys. Rev. D* **93** (2016) 092004.

[24] **ATLAS** Collaboration, "Measurement of the ZZ production cross section in proton-proton collisions at $\sqrt{s} = 8$ TeV using the $ZZ \rightarrow \ell^-\ell^+\ell'^-\ell'^+$ and $ZZ \rightarrow \ell^-\ell^+\nu\bar{\nu}$ channels with the ATLAS detector", *JHEP* **01** (2017) 099.

[25] **ATLAS** Collaboration, "$ZZ \rightarrow \ell^+\ell^-\ell'^+\ell'^-$ cross-section measurements and search for anomalous triple gauge couplings in 13 TeV pp collisions with the ATLAS detector", *Phys. Rev. D* **97** (2018) 032005.

[26] **CMS** Collaboration, "Measurements of the pp $\rightarrow$ WZ inclusive and differential production cross section and constraints on charged anomalous triple gauge couplings at $\sqrt{s} = 13$ TeV", *JHEP* **04** (2019) 122.

[27] **ATLAS** Collaboration, "Measurement of the $W^{\pm}Z$ boson pair-production cross section in pp collisions at $\sqrt{s} = 13$ TeV with the ATLAS detector", *Phys. Lett. B* **762** (2016) 1–22.

[28] **ATLAS** Collaboration, "Measurement of fiducial and differential W^+W^- production cross-sections at $\sqrt{s}$ =13 TeV with the ATLAS detector", *Eur. Phys. J. C* **79** (2019) 884.

[29] **CMS** Collaboration, "Measurement of the sum of WW and WZ production with W+dijet events in pp collisions at $\sqrt{s} = 7$ TeV", *Eur. Phys. J. C* **73** (2013) 2283.

[30] **CMS** Collaboration, "Search for anomalous couplings in boosted WW/WZ $\to \ell\nu q\bar{q}$ production in proton-proton collisions at $\sqrt{s} = 8$ TeV", *Phys. Lett. B* **772** (2017) 21.

[31] **ATLAS** Collaboration, "Measurement of the WW + WZ cross section and limits on anomalous triple gauge couplings using final states with one lepton, missing transverse momentum, and two jets with the ATLAS detector at $\sqrt{\mathrm{s}} = 7$ TeV", *JHEP* **01** (2015) 049.

[32] **ATLAS** Collaboration, "Measurement of WW/WZ $\to \ell\nu qq'$ production with the hadronically decaying boson reconstructed as one or two jets in pp collisions at $\sqrt{s} = 8$ TeV with ATLAS, and constraints on anomalous gauge couplings", *Eur. Phys. J. C* **77** (2017) 563.

[33] A. Zannoni, "On the quantization of the monoatomic ideal gas", 1999, arXiv:cond-mat/9912229 [cond-mat.stat-mech].

[34] P. A. M. Dirac, "On the theory of quantum mechanics", *Proc. R. Soc. Lond. A* **112** (1926) .

[35] S. Bose, Theimer(translator), and B. Ram(translator), "The beginning of quantum statistics: A translation of 'Planck's law and the light quantum hypothesis'", *Am. J. Phys.* **44** (1976) 1056–1057.

[36] A. Einstein, "Quantentheorie des einatomigen idealen Gases", *Albert Einstein: Akademie Vorträge*, pp. 237–244. John Wiley & Sons, Ltd, 2006.

[37] **ATLAS** Collaboration, "Observation of a new particle in the search for the Standard Model Higgs boson with the ATLAS detector at the LHC", *Phys. Lett. B* **716** (2012) 1–29.

[38] **CMS** Collaboration, "Observation of a new boson at a mass of 125 GeV with the CMS experiment at the LHC", *Phys. Lett. B* **716** (2012) 30–61.

[39] **LHCb** Collaboration, "Observation of $J/\psi p$ resonances consistent with pentaquark states in $\Lambda_b^0 \to J/\psi K^- p$ decays", *Phys. Rev. Lett.* **115** (2015) 072001.

[40] **Particle Data Group** Collaboration, "Review of particle physics", *Phys. Rev. D* **98** (2018) 030001.

[41] F. Englert and R. Brout, "Broken symmetry and the mass of gauge vector mesons", *Phys. Rev. Lett.* **13** (1964) 321–323.

[42] P. W. Higgs, "Broken symmetries and the masses of gauge bosons", *Phys. Rev. Lett.* **13** (1964) 508–509.

[43] S. L. Glashow, "Partial-symmetries of weak interactions", *Nucl. Phys.* **22** (1961) 579–588.

[44] S. Weinberg, "A model of leptons", *Phys. Rev. Lett.* **19** (1967) 1264–1266.

[45] A. Salam, "Weak and electromagnetic interactions", *Selected Papers of Abdus Salam*, pp. 244–254. World Scientific, 1994.

[46] **UA1** Collaboration, "Experimental observation of isolated large transverse energy electrons with associated missing energy at $\sqrt{s} = 540$ GeV", *Phys. Lett. B* **122** (1983) 103–116.

[47] **UA2** Collaboration, "Observation of single isolated electrons of high transverse momentum in events with missing transverse energy at the CERN pp collider", *Phys. Lett. B* **122** (1983) 476–485.

[48] **UA1** Collaboration, "Experimental observation of lepton pairs of invariant mass around 95 GeV/c^2 at the CERN SPS collider", *Phys. Lett. B* **126** (1983) 398–410.

[49] **UA2** Collaboration, "Evidence for $Z \rightarrow e^+e^-$ at the CERN pp collider", *Phys. Lett. B* **129** (1983) 130–140.

[50] R. P. Feynman, *QED: The Strange Theory of Light and Matter*. Princeton University Press, 2014.

[51] C. S. Wu, E. Ambler, R. W. Hayward, D. D. Hoppes, and R. P. Hudson, "Experimental test of parity conservation in beta decay", *Phys. Rev.* **105** (1957) 1413–1415.

[52] **ATLAS** Collaboration, "Observation of Higgs boson production in association with a top quark pair at the LHC with the ATLAS detector", *Phys. Lett. B* **784** (2018) 173–191.

[53] **CMS** Collaboration, "Observation of $t\bar{t}H$ Production", *Phys. Rev. Lett.* **120** (2018) 231801.

[54] **ATLAS** Collaboration, "Observation of $H \rightarrow b\bar{b}$ decays and VH production with the ATLAS detector", *Phys. Lett. B* **786** (2018) 59–86.

[55] **CMS** Collaboration, "Observation of Higgs boson decay to bottom quarks", *Phys. Rev. Lett.* **121** (2018) 121801.

[56] P. A. M. Casares, "A review on Loop Quantum Gravity", 2018, arXiv:1808.01252 [gr-qc].

[57] U. Danielsson, "Introduction to string theory", *Rep. Prog. in Phys.* **64** (2000) 51–96.

[58] R. N. Mohapatra and G. Senjanović, "Neutrino mass and spontaneous parity nonconservation", *Phys. Rev. Lett.* **44** (1980) 912–915.

[59] **KATRIN** Collaboration, "Improved upper limit on the neutrino mass from a direct kinematic method by KATRIN", *Phys. Rev. Lett.* **123** (2019) 221802.

[60] T. Blum, A. Denig, I. Logashenko, E. de Rafael, B. L. Roberts, T. Teubner, and G. Venanzoni, "The muon (g-2) theory value: Present and future", 2013, arXiv:1311.2198 [hep-ph].

[61] **Muon g−2** Collaboration, "Muon (g-2) technical design report", 2015, arXiv:1501.06858 [physics.ins-det].

[62] B. Capdevila, A. Crivellin, S. Descotes-Genon, J. Matias, and J. Virto, "Patterns of new physics in $b \rightarrow s\ell^+\ell^-$ transitions in the light of recent data", *JHEP* **01** (2018) 93.

[63] K. Hagiwara, S. Ishihara, R. Szalapski, and D. Zeppenfeld, “Low energy effects of new interactions in the electroweak boson sector”, *Phys. Rev. D* **48** (1993) 2182–2203.

[64] C. Degrande, N. Greiner, W. Kilian, O. Mattelaer, H. Mebane, T. Stelzer, S. Willenbrock, and C. Zhang, “Effective field theory: A modern approach to anomalous couplings”, *Ann. Phys.* **335** (2013) 21–32.

[65] **LEP** Collaboration, “Electroweak measurements in electron–positron collisions at W-boson-pair energies at LEP”, *Phys. Rep.* **532** (2013) 119–244.

[66] **D∅** Collaboration, “Limits on anomalous trilinear gauge boson couplings from WW, WZ and Wγ production in p$\overline{\text{p}}$ collisions at $\sqrt{s} = 1.96$ TeV”, *Phys. Lett. B* **718** (2012) 451–459.

[67] **CMS** Collaboration, “Electroweak production of two jets in association with a Z boson in proton-proton collisions at $\sqrt{s} = 13$ TeV”, *Euro. Phys. J. C* **78** (2018) 589.

[68] **CERN**, “The CERN accelerator complex. Complexe des accélérateurs du CERN”, Dec 2008, https://cds.cern.ch/record/1260465.

[69] **CERN**, “Linear accelerator 2”, Dec 2019, https://home.cern/science/accelerators/linear-accelerator-2.

[70] **CERN**, “The Proton Synchrotron Booster”, Dec 2019, https://home.cern/science/accelerators/proton-synchrotron-booster.

[71] **CERN**, “The Proton Synchrotron”, Dec 2019, https://home.cern/science/accelerators/proton-synchrotron.

[72] **CERN**, “The Super Proton Synchrotron”, Dec 2019, https://home.cern/science/accelerators/super-proton-synchrotron.

[73] **CERN**, “Cross section of an LHC dipole in the tunnel.”, Jul 2011, https://cds.cern.ch/record/1365795.

[74] **CMS** Collaboration, “Public CMS luminosity information”, Dec 2019, https://twiki.cern.ch/twiki/bin/view/CMSPublic/LumiPublicResults.

[75] T. Sakuma and T. McCauley, “Detector and event visualization with SketchUp at the CMS experiment”, *J. Phys.: Conf. Ser.* **513** (2014) 022032.

[76] **CMS** Collaboration, “Interactive slice of the CMS detector”, Aug 2016, https://cds.cern.ch/record/2205172.

[77] A. Dominguez *et al.*, “CMS technical design report for the pixel detector upgrade”, Tech. Rep. CERN-LHCC-2012-016, CMS-TDR-11, Sep 2012, https://cds.cern.ch/record/1481838.

[78] Autodesk, “3ds Max overview”, Dec 2019, https://www.autodesk.com/products/3ds-max.

[79] **CMS** Collaboration, “The CMS experiment at the CERN LHC”, *JINST* **3** (2008) S08004.

[80] **CMS** Collaboration, “The CMS ECAL performance with examples”, Tech. Rep. CMS-CR-2013-430, CERN, Geneva, Nov 2013, https://cds.cern.ch/record/1632384.

[81] **CMS** Collaboration, “Energy resolution of the barrel of the CMS electromagnetic calorimeter”, *JINST* **2** (2007) P04004.

[82] **CMS** Collaboration, “Measurement of the pion energy response and resolution in the CMS HCAL Test Beam 2002 Experiment”, Tech. Rep. CMS-NOTE-2004-020, CERN, Geneva, Sep 2004, https://cds.cern.ch/record/800406.

[83] **CMS** Collaboration, “Precise mapping of the magnetic field in the CMS barrel yoke using cosmic rays”, *JINST* **5** (2010) T03021.

[84] **CMS** Collaboration, “The Phase-2 upgrade of the CMS muon detectors”, Tech. Rep. CERN-LHCC-2017-012. CMS-TDR-016, CERN, Geneva, Sep 2017, https://cds.cern.ch/record/2283189.

[85] **CMS** Collaboration, “Performance of the CMS muon detector and muon reconstruction with proton-proton collisions at $\sqrt{s} = 13$ TeV”, *JINST* **13** (2018) P06015.

[86] **CMS** Collaboration, “The performance of the CMS muon detector in proton-proton collisions at $\sqrt{s} = 7$ TeV at the LHC”, *JINST* **8** (2013) P11002.

[87] M. Abbrescia *et al.*, “Preliminary results of resistive plate chambers operated with eco-friendly gas mixtures for application in the CMS experiment”, *JINST* **11** (2016) C09018.

[88] **CMS** Collaboration, “The CMS trigger system”, *JINST* **12** (2017) P01020.

[89] **CMS** Collaboration, “CMS data processing workflows during an extended cosmic ray run”, *JINST* **5** (2010) T03006.

[90] **CMS** Collaboration, “Data parking and data scouting at the CMS experiment”, Tech. Rep. CMS-DP-2012-022, CERN, Geneva, Sep 2012, https://cds.cern.ch/record/1480607.

[91] K. Bos *et al.*, *LHC computing Grid: Technical Design Report. Version 1.06*. Technical Design Report LCG. CERN, Geneva, 2005.

[92] **CMS** Collaboration, “CMS computing model”, Jul 2018, https://twiki.cern.ch/twiki/bin/view/CMSPublic/WorkBookComputingModel.

[93] E. Martelli and S. Stancu, “LHCOPN and LHCONE: Status and future evolution”, *J. Phys.: Conf. Ser.* **664** (2015) 052025.

[94] **CMS** Collaboration, “Alignment of the CMS tracker with LHC and cosmic ray data”, *JINST* **9** (2014) P06009.

[95] V. Blobel and C. Kleinwort, “A new method for the high-precision alignment of track detectors”, 2002, arXiv:hep-ex/0208021 [hep-ex].

[96] **CMS** Collaboration, “Welcome to CMS and CMSSW”, Dec 2019, https://cms-sw.github.io/.

[97] G. Cerminara and B. van Besien, "Automated workflows for critical time-dependent calibrations at the CMS experiment", *J. Phys.: Conf. Ser.* **664** (2015) 072009.

[98] **CMS** Collaboration, "CMS tracker performance results for full Run 2 legacy reprocessing", Tech. Rep. CMS-DP-2020-012, Feb 2020, https://cds.cern.ch/record/2713208.

[99] S. Weinzierl, "Introduction to Monte Carlo methods", 2000, arXiv:hep-ph/0006269 [hep-ph].

[100] **NNPDF** Collaboration, "Parton distributions for the lhc run II", *JHEP* **04** (2015) .

[101] **NNPDF** Collaboration, "Parton distributions from high-precision collider data", *Eur. Phys. J. C* **77** (2017) 663.

[102] V. Sudakov, "Vertex parts at very high energies in quantum electrodynamics", *JETP* **3** (1956) 65.

[103] A. Sen, "Asymptotic behavior of the Sudakov form factor in quantum chromodynamics", *Phys. Rev. D* **24** (1981) 3281–3304.

[104] S. Hoeche *et al.*, "Matching parton showers and matrix elements", *HERA and the LHC: A workshop on the implications of HERA for LHC physics: Proceedings part A* (2006) 12.

[105] R. Frederix and S. Frixione, "Merging meets matching in MC@NLO", *JHEP* **12** (2012) 61.

[106] B. Andersson, G. Gustafson, G. Ingelman, and T. Sjöstrand, "Parton fragmentation and string dynamics", *Phys. Rep.* **97** (1983) 31–145.

[107] B. Andersson, "The Lund model", *Camb. Monogr. Part. Phys. Nucl. Phys. Cosmol.* **7** (1997) 1–471.

[108] D. Amati and G. Veneziano, "Preconfinement as a property of perturbative QCD", *Phys. Lett. B* **83** (1979) 87–92.

[109] J. Alwall *et al.*, "A standard format for Les Houches event files", *Comput. Phys. Commun.* **176** (2007) 300–304.

[110] J. Alwall *et al.*, "The automated computation of tree-level and next-to-leading order differential cross sections, and their matching to parton shower simulations", *JHEP* **07** (2014) 79.

[111] P. Nason, "A new method for combining NLO QCD with shower Monte Carlo algorithms", *JHEP* **11** (2004) 040.

[112] S. Frixione, P. Nason, and C. Oleari, "Matching NLO QCD computations with parton shower simulations: the POWHEG method", *JHEP* **11** (2007) 070.

[113] S. Alioli, P. Nason, C. Oleari, and E. Re, "A general framework for implementing NLO calculations in shower Monte Carlo programs: the POWHEG BOX", *JHEP* **06** (2010) 43.

[114] T. Sjöstrand *et al.*, "High-energy-physics event generation with PYTHIA 6.1", *Comput. Phys. Commun.* **135** (2001) 238–259.

[115] T. Sjöstrand *et al.*, "An introduction to PYTHIA 8.2", *Comput. Phys. Commun.* **191** (2015) 159–177.

[116] **CMS** Collaboration, "Event generator tunes obtained from underlying event and multiparton scattering measurements", *Eur. Phys. J. C* **76** (2016) 155.

[117] **CMS** Collaboration, "Investigations of the impact of the parton shower tuning in Pythia 8 in the modelling of $t\bar{t}$ at $\sqrt{s} = 8$ and 13 TeV", Tech. Rep. CMS-PAS-TOP-16-021, CERN, Geneva, 2016, https://cds.cern.ch/record/2235192.

[118] S. Agostinelli *et al.*, "Geant4 — a simulation toolkit", *Nucl. Instrum. Meth. A* **506** (2003) 250–303.

[119] J. Allison *et al.*, "Geant4 developments and applications", *IEEE Trans. Nucl. Sci.* **53** (2006) 270–278.

[120] **CMS** Collaboration, "Particle-flow event reconstruction in CMS and performance for jets, taus, and MET", Tech. Rep. CMS-PAS-PFT-09-001, CERN, Geneva, Apr 2009, https://cds.cern.ch/record/1194487.

[121] **CMS** Collaboration, "Commissioning of the particle-flow event reconstruction with the first LHC collisions recorded in the CMS detector", Tech. Rep. CMS-PAS-PFT-10-001, 2010, https://cds.cern.ch/record/1247373.

[122] **CMS** Collaboration, "Particle-flow reconstruction and global event description with the CMS detector", *JINST* **12** (2017) P10003.

[123] R. Frühwirth, "Application of Kalman filtering to track and vertex fitting", *Nucl. Instrum. Meth. A* **262** (1987) 444–450.

[124] P. Billoir, "Progressive track recognition with a Kalman-like fitting procedure", *Comput. Phys. Commun.* **57** (1989) 390–394.

[125] P. Billoir and S. Qian, "Simultaneous pattern recognition and track fitting by the Kalman filtering method", *Nucl. Instrum. Meth. A* **294** (1990) 219–228.

[126] T. Miao, N. Leioatts, H. Wenzel, and F. Yumiceva, "Beam position determination using tracks", Tech. Rep. CMS-NOTE-2007-021, CERN, Geneva, Aug 2007, https://cds.cern.ch/record/1061285.

[127] K. Rose, "Deterministic annealing for clustering, compression, classification, regression, and related optimization problems", *Proceedings of the IEEE* **86** (1998) 2210–02239.

[128] W. Waltenberger, R. Frühwirth, and P. Vanlaer, "Adaptive vertex fitting", *J. Phys. G* **34** (2007) N343–N356.

[129] W. Adam, R. Frühwirth, A. Strandlie, and T. Todorov, "Reconstruction of electrons with the Gaussian-sum filter in the CMS tracker at the LHC", *J Phys. G* **31** (2005) N9–N20.

[130] **CMS** Collaboration, "Performance of electron reconstruction and selection with the CMS detector in proton-proton collisions at $\sqrt{s} = 8$ TeV", *JINST* **10** (2015) P06005.

[131] R. Atkin, "Review of jet reconstruction algorithms", *J. Phys.: Conf. Ser.* **645** (2015) 012008.

[132] G. P. Salam and G. Soyez, "A practical seedless infrared-safe cone jet algorithm", *JHEP* **05** (2007) 086.

[133] S. D. Ellis and D. E. Soper, "Successive combination jet algorithm for hadron collisions", *Phys. Rev. D* **48** (1993) 3160–3166.

[134] M. Cacciari, G. P. Salam, and G. Soyez, "The anti-k_T jet clustering algorithm", *JHEP* **04** (2008) 063.

[135] Y. Dokshitzer, G. Leder, S. Moretti, and B. Webber, "Better jet clustering algorithms", *JHEP* **08** (1997) 001.

[136] **CMS** Collaboration, "Determination of jet energy calibration and transverse momentum resolution in CMS", *JINST* **6** (2011) P11002.

[137] **CMS** Collaboration, "Jet energy scale and resolution in the CMS experiment in pp collisions at 8 TeV", *JINST* **12** (2017) P02014.

[138] **CMS** Collaboration, "Pileup removal algorithms", Tech. Rep. CMS-PAS-JME-14-001, CERN, Geneva, 2014, https://cds.cern.ch/record/1751454.

[139] D. Bertolini, P. Harris, M. Low, and N. Tran, "Pileup per particle identification", *JHEP* **10** (2014) 59.

[140] **CMS** Collaboration, "Identification of b-quark jets with the CMS experiment", *JINST* **8** (2013) P04013.

[141] **CMS** Collaboration, "Identification of heavy-flavour jets with the CMS detector in pp collisions at 13 TeV", *JINST* **13** (2018) P05011.

[142] **CMS** Collaboration, "Performance of missing energy reconstruction in 13 TeV pp collision data using the CMS detector", Tech. Rep. CMS-PAS-JME-16-004, CERN, Geneva, 2016, http://cds.cern.ch/record/2205284.

[143] D. Krohn, J. Thaler, and L. T. Wang, "Jet trimming", *JHEP* **2** (2010) 84.

[144] S. D. Ellis, C. K. Vermilion, and J. R. Walsh, "Recombination algorithms and jet substructure: Pruning as a tool for heavy particle searches", *Phys. Rev. D* **81** (2010) 094023.

[145] S. D. Ellis, C. K. Vermilion, and J. R. Walsh, "Techniques for improved heavy particle searches with jet substructure", *Phys. Rev. D* **80** (2009) 051501.

[146] A. J. Larkoski, S. Marzani, G. Soyez, and J. Thaler, "Soft drop", *JHEP* **5** (2014) 146.

[147] M. Dasgupta, A. Fregoso, S. Marzani, and G. P. Salam, "Towards an understanding of jet substructure", *JHEP* **09** (2013) 29.

[148] J. M. Butterworth, A. R. Davison, M. Rubin, and G. P. Salam, "Jet substructure as a new Higgs-search channel at the Large Hadron Collider", *Phys. Rev. Lett.* **100** (2008) 242001.

[149] J. Thaler and K. Van Tilburg, "Identifying boosted objects with N-subjettiness", *JHEP* **03** (2011) 15.

[150] **ATLAS** Collaboration, "Searches for new physics using jet substructure in ATLAS and CMS", Tech. Rep. ATL-PHYS-PROC-2018-163, CERN, Geneva, Nov 2018, https://cds.cern.ch/record/2648893.

[151] T. Gehrmann *et al.*, "W^+W^- production at hadron colliders in next to next to leading order QCD", *Phys. Rev. Lett.* **113** (2014) 212001.

[152] M. Grazzini, S. Kallweit, D. Rathlev, and M. Wiesemann, "WZ production at hadron colliders in NNLO QCD", *Phys. Lett. B* **761** (2016) 179–183.

[153] J. Campbell, R. K. Ellis, and D. Rainwater, "Next-to-leading order QCD predictions for $W + 2$-jet and $Z + 2$-jet production at the CERN LHC", *Phys. Rev. D* **68** (2003) 094021.

[154] M. Czakon and A. Mitov, "Top++: A program for the calculation of the top-pair cross-section at hadron colliders", *Comput. Phys. Commun.* **185** (2014) 2930–2938.

[155] M. Aliev, H. Lacker, U. Langenfeld, S. Moch, P. Uwer, and M. Wiedermann, "HATHOR – HAdronic Top and Heavy quarks crOss section calculatoR", *Comput. Phys. Commun.* **182** (2011) 1034–1046.

[156] **CMS** Collaboration, "Work in progress (evolving results) and dedicated studies from PAGs", Aug 2018, https://twiki.cern.ch/twiki/bin/view/CMS/MuonWorkInProgressAndPagResults.

[157] **CMS** Collaboration, "MET filter recommendations for Run II", Jul 2019, https://twiki.cern.ch/twiki/bin/view/CMS/MissingETOptionalFiltersRun2.

[158] **CMS** Collaboration, "Utilities for accessing pileup information for data", Dec 2019, https://twiki.cern.ch/twiki/bin/viewauth/CMS/PileupJSONFileforData.

[159] "Search for a heavy resonance decaying to a pair of vector bosons in the lepton plus merged jet final state at $\sqrt{s} = 13$ TeV", *JHEP* **5** (2018) 88.

[160] **CMS** Collaboration, "EGamma ID recipes Run 2", Feb 2020, https://twiki.cern.ch/twiki/bin/view/CMS/EgammaIDRecipesRun2.

[161] **CMS** Collaboration, "Reference muon ID, isolation and trigger efficiencies for Run-II", Apr 2019, https://twiki.cern.ch/twiki/bin/view/CMS/MuonReferenceEffsRun2.

[162] **CMS** Collaboration, "Jet energy resolution", Mar 2020, https://twiki.cern.ch/twiki/bin/view/CMS/JetResolution.

[163] **CMS** Collaboration, "W/Z-tagging of jets", Apr 2020, https://twiki.cern.ch/twiki/bin/view/CMS/JetWtagging.

[164] **CMS** Collaboration, "Methods to apply b-tagging efficiency scale factors", Apr 2020, https://twiki.cern.ch/twiki/bin/view/CMS/BTagSFMethods.

[165] **CMS** Collaboration, “Usage of b/c tag objects for 13 TeV Data in 2016 and 80X MC”, Mar 2017, https://twiki.cern.ch/CMS/BtagRecommendation80XReReco.

[166] **CMS** Collaboration, “MET corrections and uncertainties for Run-II”, Nov 2019, https://twiki.cern.ch/twiki/bin/viewauth/CMS/MissingETRun2Corrections.

[167] **CMS** Collaboration, “MET-phi corrections for data Run B–F, data Run GH, and MC 80X”, Mar 2017, https://github.com/cms-met/MetTools/blob/master/MetPhiCorrections/python/tools.

[168] J. Butterworth *et al.*, “PDF4LHC recommendations for LHC run II”, *J. Phys. G* **43** (2016) 023001.

[169] **CMS** Collaboration, “CMS luminosity measurements for the 2016 data taking period”, Tech. Rep. CMS-PAS-LUM-17-001, CERN, Geneva, 2017, https://cds.cern.ch/record/2257069.

[170] **CMS** Collaboration, “Search for massive resonances decaying into WW, WZ or ZZ bosons in proton-proton collisions at $\sqrt{s} = 13$ TeV”, *JHEP* **03** (2017) 162.

[171] **CMS** Collaboration, “Search for massive resonances decaying into pairs of boosted bosons in semi-leptonic final states at $\sqrt{s} = 8$ TeV”, *JHEP* **08** (2014) 174.

[172] M. Grazzini, S. Kallweit, S. Pozzorini, D. Rathlev, and M. Wiesemann, “W^+W^- production at the LHC: fiducial cross sections and distributions in NNLO QCD”, *JHEP* **08** (2016) 140.

[173] M. Grazzini, S. Kallweit, D. Rathlev, and M. Wiesemann, “$W^\pm Z$ production at the LHC: fiducial cross sections and distributions in NNLO QCD”, *JHEP* **05** (2017) 139.

[174] S. Kallweit, J. M. Lindert, S. Pozzorini, and M. Schönherr, “NLO QCD+EW predictions for $2\ell 2\nu$ diboson signatures at the LHC”, *JHEP* **11** (2017) 120.

[175] S. S. Wilks, “The large-sample distribution of the likelihood ratio for testing composite hypotheses”, *Ann. Math. Statist.* **9** (1938) 60–62.

[176] **CMS** Collaboration, “Higgs analysis combined limit tool”, Mar 2020, https://cms-analysis.github.io/HiggsAnalysis-CombinedLimit.

[177] **ATLAS** Collaboration, “Measurement of the electroweak production of dijets in association with a Z-boson and distributions sensitive to vector boson fusion in proton-proton collisions at $\sqrt{s} = 8$ TeV using the ATLAS detector”, *JHEP* **4** (2014) 31.

[178] **ATLAS** Collaboration, “Measurements of electroweak Wjj production and constraints on anomalous gauge couplings with the ATLAS detector”, *Eur. Phys. J. C* **77** (2017) 474.

[179] K. Hagiwara, R. Peccei, D. Zeppenfeld, and K. Hikasa, “Probing the weak boson sector in $e^+e^- \to W^+W^-$”, *Nucl. Phys. B* **282** (1987) 253–307.

[180] **CMS** Collaboration, “V tagging observables and correlations”, Tech. Rep. CMS-PAS-JME-14-002, CERN, Geneva, 2014, https://cds.cern.ch/record/1754913.

[181] D. E. Kaplan, K. Rehermann, M. D. Schwartz, and B. Tweedie, “Top tagging: A method for identifying boosted hadronically decaying top quarks”, *Phys. Rev. Lett.* **101** (2008) 142001.

Acknowledgements

I vividly remember the long summer evening my parents gifted a three-year-old me my first stationery, including a graphite pencil and strawberry-shaped eraser. I felt ecstatic. The effort and devotion put into my education growing up resulted in me excelling at all the stages of my academic career. It is a debt I have carried to this day, and can never think of paying off. My parents, **Dr. and Mrs. Iqbal**, are hence the rightful receipients of my deepest gratitude on the completion of my PhD.

I would also want to appreciate the unending support and encouragement from my loving wife **Komal**, who stood by me through thick and thin, regarding matters related to my PhD, and otherwise.

As I look back at the three years of my PhD, I want to acknowledge the contribution of the following people:

- **Prof. Thomas Müller:** They say your PhD supervisor is your mentor for life; now I can understand why. He was the best I could have ever asked for. Thank you for giving me the opportunity to work at the Institute of Experimental Particle Physics (ETP) at KIT. Thank you also for offering insightful scientific guidance and elegant advice, providing relentless support whenever I needed, and of course, travelling 6000 kilometres to attend my wedding in Islamabad.

- **Ashfaq Ahmad:** Thank you for co-supervision of my PhD, and recommending me to pursue a PhD at KIT in the first place. You have always been a great mentor, a trustworthy advisor, and a good friend.

- **Matthias Mozer:** Thank you for your technical guidance, and teaching me about vector bosons and analysis techniques in general. I owe a lot of what I know about the subject to you.

- **Thorsten Chwalek:** Thank you for your kind support in a lot of matters, especially in helping with administrative issues since the very start, when I did not speak a word of German.

I would like to thank my collaborators **Andreas Hinzmann** and **Robin Cameron Aggleton** from the University of Hamburg for a very fruitful collaboration, and **Ivan Shvetsov** for helping me set up the analysis in the start.

I am obliged to all my colleagues at the Institute of Experimental Particle Physics at KIT for establishing a very productive research environment. In no particular order, I would like to thank the following colleagues for the academic, and otherwise, support: **Nils Faltermann**, **Denise Müller**, **Johann Rauser**, **Kevin Flöh**, **Soureek Mitra**, and my officemates **Daniela Schäfer**, **Max Neukum**, and **David Seith**. Furthermore, thank you all for taking the time out to proofread this thesis.

I am highly grateful to the Karlsruhe School for Particle and Astroparticle Physics: Science and Technology (KSETA) for financial support through the GSSP programme of the German Academic Exchange Service (DAAD). In particular, I would like to thank the KSETA spokesperson, **Prof. Ulrich Nierste**, for his support in bureaucratic matters, and sharing my profound interest of football and co-arranging the institute summer football sessions.

I would also like to acknowledge **Dagmar Beerwerth** from DAAD for being an excellent contact person, and making persistent effort to ensure that the issues of the scholarship holders are resolved promptly, and the ETP and KSETA secretaries **Bärbel Bräunling** and **Barbara Lepold**, respectively, for handling administrative issues seemlessly.

Like all good things in life, my time as a PhD student is coming to an end. It was an amazing journey, and would not have been possible without the backing of the above mentioned people. You are all remarkable, and I hope to work with you again in the future, on one project or another.

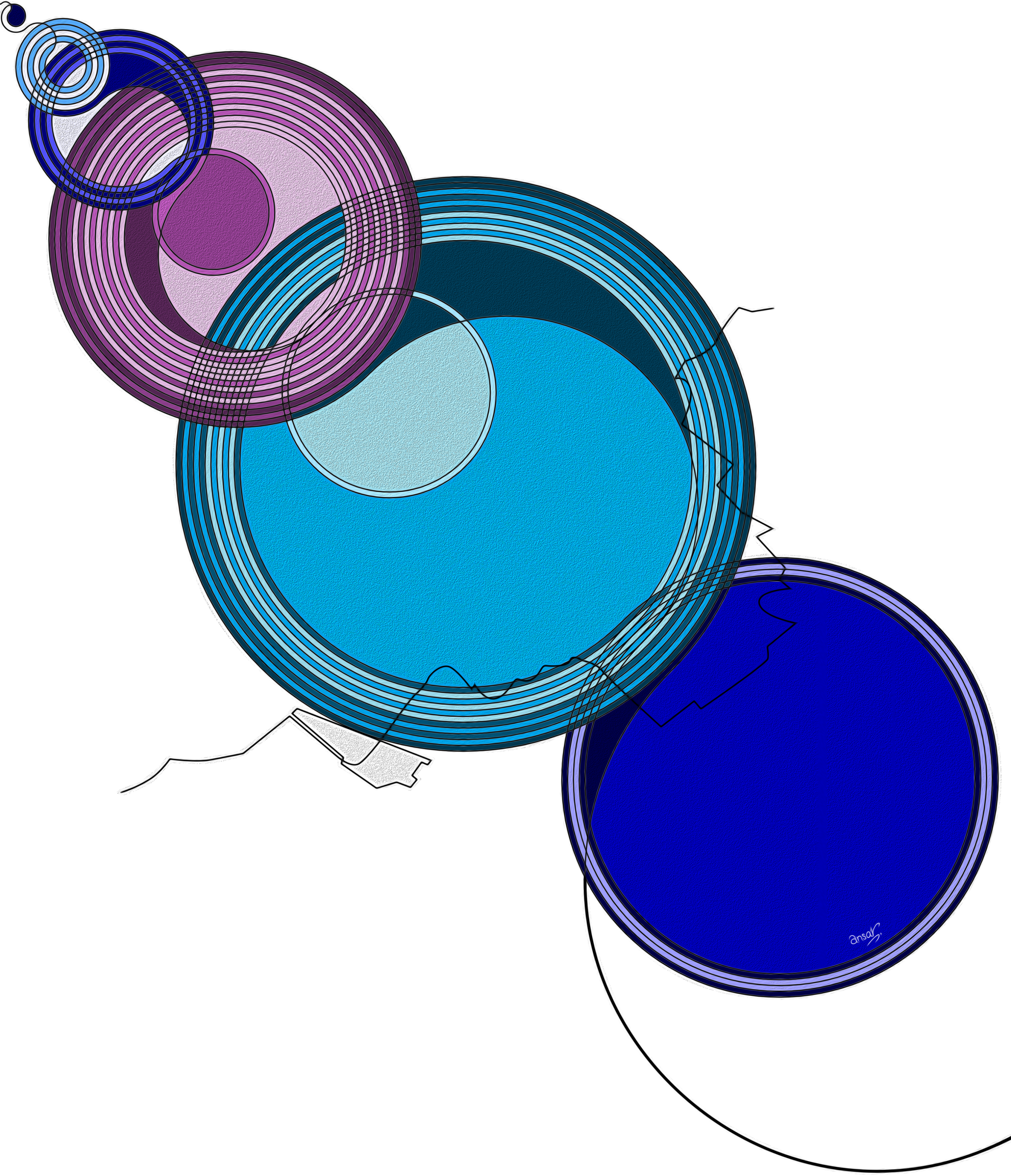
ansar

Analysis poster

The analysis described in this thesis was presented in the form of oral and poster presentations at various national and international conferences. The following poster was shown in the European Physical Society Conference on High Energy Physics (EPS-HEP), held in Ghent, Belgium, during 10–17 July 2019.

Search for anomalous triple gauge couplings in semileptonic WW and WZ decays with CMS

CMS-PAS-SMP-18-008

Muhammad Ansar Iqbal[1], Matthias Mozer[1], Robin Aggleton[2], Andreas Hinzmann[2]

[1] Institute for Experimental Particle Physics (ETP), Karlsruhe Institute of Technology (KIT), Germany
[2] Institute for Experimental Physics, University Hamburg (UHH), Germany

Effective Field Theory

The SM Lagrangian is expanded by adding higher dimensional operators:

$$\mathcal{L}_{\text{eff}} = \mathcal{L}_{\text{SM}} + \frac{1}{\Lambda}\mathcal{L}_1 + \frac{c_{\text{WWW}}}{\Lambda^2}\mathcal{O}_{\text{WWW}} + \frac{c_{\text{W}}}{\Lambda^2}\mathcal{O}_{\text{W}} + \frac{c_{\text{B}}}{\Lambda^2}\mathcal{O}_{\text{B}} + \ldots$$

in the region $E/\Lambda << 1$, where the six-dimensional operators are:

$$\mathcal{O}_{\text{WWW}} = \text{Tr}[W_{\mu\nu}W^{\nu\rho}W^{\mu}_{\rho}]$$
$$\mathcal{O}_{\text{W}} = (D_\mu\Phi)^\dagger W^{\mu\nu}(D_\nu\Phi)$$
$$\mathcal{O}_{\text{B}} = (D_\mu\Phi)^\dagger B^{\mu\nu}(D_\nu\Phi)$$

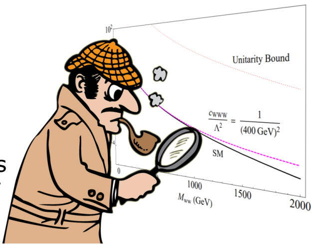

Anomalous triple gauge couplings $\{c_{\text{WWW}}, c_{\text{W}}, c_{\text{B}}\}$ control the size of each new contribution.

Signal process and event selection

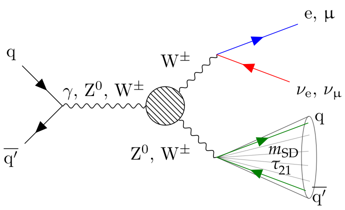

Exactly one lepton passing selection criteria, no additional loose leptons (single lepton triggers)

Missing transverse momentum p_T^{miss}

At least one AK8 “fat jet” passing quality requirements (boosted topology techniques are used)

Selection Cut	e channel	μ channel
Lepton p_T >	50 GeV	53 GeV
Lepton $\|\eta\|$ <	2.5	2.4
CHS jet p_T >	200 GeV	200 GeV
CHS jet $\|\eta\|$ <	2.4	2.4
Jet τ_{21}^{PUPPI} <	0.55	0.55
Jet m_{SD} ∈	[40, 150] GeV	[40, 150] GeV

Selection Cut	e channel	μ channel
p_T^{miss} >	110 GeV	40 GeV
$W_{lep} p_T$ >	200 GeV	200 GeV
m_{WV} >	900 GeV	900 GeV
$\Delta R(\text{jet}, \text{lep})$ >	$\pi/2$	$\pi/2$
$\Delta\phi(\text{jet}, \vec{p}_T^{miss})$ >	2.0	2.0
$\Delta\phi(\text{jet}, W_{lep})$ >	2.0	2.0

Backgrounds

- W+jets
- Top pair production ($t\bar{t}$)
- SM diboson production (WW, WZ)
- Single top processes

Parametric functions are used to model m_{SD} and m_{WV} distributions for all background contributions, which are then combined to form the background PDF

$$F_{background}(m_{SD}, m_{WV})$$

Analysis strategy

- Control regions are used to validate modelling of main backgrounds (W+jets and $t\bar{t}$).
- Shape of W+jets is obtained from sideband data by using alpha-ratio method.
- Systematic uncertainties are taken into account as nuisance parameters in the final two-dimensional fit.

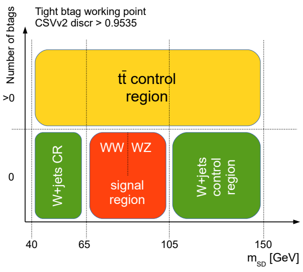

- One- and two-dimensional limits are extracted from profile likelihood distributions.

Signal model

$$F_{signal}(m_{WV})$$

$$= N_{SM}(e^{a_0 m_{WV}} + e^{a_{corr} m_{WV}})$$

SM contribution

$$+ \sum_i (N_{c_i,1}.c_i^2.e^{a_{i,1} m_{WV}}.\frac{1+Erf((m_{WV}-a_{0,i})/a_{w,i})}{2}$$

pure aTGC term

$$+ N_{c_i,2}.c_i.e^{a_{i,2} m_{WV}})$$

SM-aTGC interference

$$+ \sum_{i<j} (N_{c_i,c_j}.c_i.c_j.e^{a_{ij} m_{WV}})$$

aTGC-aTGC interference

where c_i are the various anomalous triple gauge coupling parameters and Erf is the error function

Final fit results

Final background estimation and signal extraction is performed via a (modified) two-dimensional fit in the (m_{SD}, m_{WV}) plane.

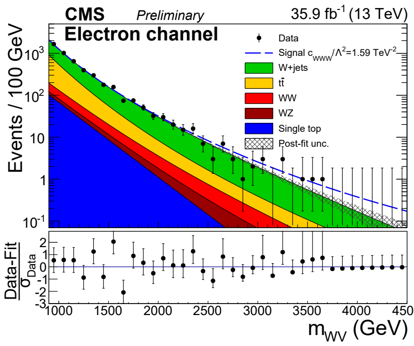

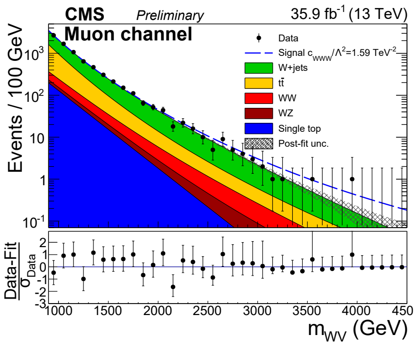

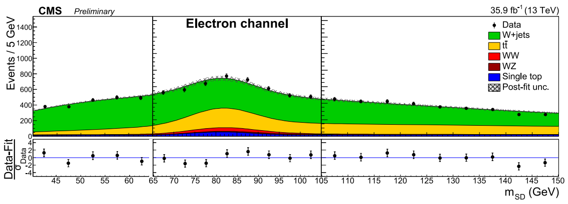

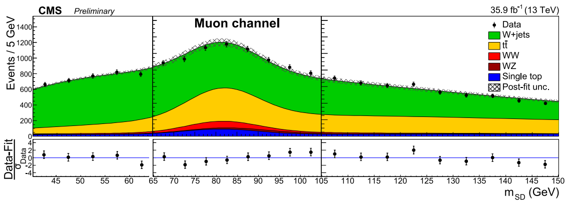

Limits on aTGC parameters

Parametrization	aTGC	Expected limit	Observed limit	Run I limit
EFT	c_{WWW}/Λ^2 (TeV^{-2})	[-1.44, 1.47]	[-1.58, 1.59]	[-2.7, 2.7]
	c_W/Λ^2 (TeV^{-2})	[-2.45, 2.08]	[-2.00, 2.65]	[-2.0, 5.7]
	c_B/Λ^2 (TeV^{-2})	[-8.38, 8.06]	[-8.78, 8.54]	[-14, 17]
LEP	λ_Z	[-0.0060, 0.0061]	[-0.0065, 0.0066]	[-0.011, 0.011]
	Δg_1^Z	[-0.0070, 0.0061]	[-0.0061, 0.0074]	[-0.009, 0.024]
	$\Delta\kappa_Z$	[-0.0074, 0.0078]	[-0.0079, 0.0082]	[-0.018, 0.013]

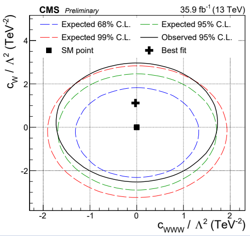

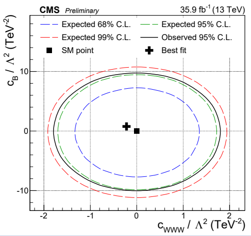

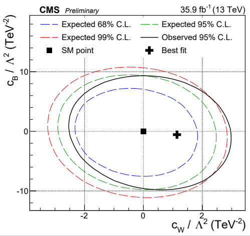

Conclusion

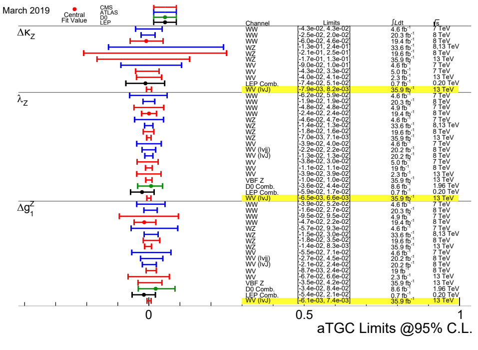

Strictest bounds on these aTGC parameters from direct measurements so far!

EPS-HEP, Ghent, 2019

muhammad.ansar.iqbal@cern.ch